UNIVERSITÀ DEGLI STUDI
DI TRENTO

DEPARTMENT OF INFORMATION ENGINEERING AND COMPUTER SCIENCE
IECS Information Engineering and Computer Science

Next-Generation Space Communications Technologies for Building Future Mars Connectivity

Stefano Bonafini

Advisor

Prof. Claudio Sacchi

Università degli Studi di Trento

December 2022

Abstract

This decade will hopefully see the first human stepping on the Martian soil. Thus, supporting and enhancing the life quality of a future crew should be the driving theme for accomplishing manned missions on Mars. In this regard, an on-demand, ubiquitous, reliable, wideband, and low-latency connectivity seems of vital importance, both for in-situ and deep-space communications. Hence, this PhD dissertation aims to introduce innovation on this multi-faceted topic, to propose a new set of solutions which we refer to as Next Generation Communications on Mars (NGC-M). First, we discuss through extensive simulations the viability of an Extraterrestrial Long Term Evolution (E-LTE) porting, where a lander and a rover are re-allocated to compose a wireless local mobile network as the base station (BS) and user equipment (UE), respectively. Next, in order to model realistic Martian channels for further solid evaluations, we present a study on large and small-scale phenomena through a three-dimensional (3D) ray-tracing algorithm executed over 3D tile-based rendering of high-resolution Digital Elevation Model (DEM) of the "Red Planet" surface. Then, we formulate a framework for the design of heterogeneous ground-to-space multi-layered (3D) networks implementing Cloud Radio Access Networks (C-RAN) for "Towards 6G" Martian connectivity. The results will spread from simulations of the so-called splitting options, for the virtualization of baseband functionalities on non-dedicated hardware, to end-to-end (E2E) network emulations and on-hardware assessments. Finally, a decode-and-forward (DF) optical wireless multi-relay network (OWmRN), based on satellites orbiting the Lagrangian points (LPs), will be proposed for wideband exchanges of data between Mars and Earth. Data rate over time will be measured with respect to the selected shortest-path for relaying. The analysis of the various techniques, performed in a holistic and systemic view, focuses on viability and performance, taking into account trade-offs and constraints inherent to the unusual and challenging Martian application environment.

Keywords
Mars, Connectivity, RF Propagation, 3D Networks, Towards 6G

Contents

Acronyms

2G	Second Generation.
3D	3-Dimensional.
3G	Third Generation.
4G	Fourth Generation.
5G	Fifth Generation.
6G	Sixth Generation.
ACK	Acknowledgment.
AEO	Areostationary Orbits.
AF	Amplify-and-Forward.
AFE	Analog Front-End.
APD	Avalanche Photodiodes.
AR	Augmented Reality.
Ar*	Argon.
ASIC	Application-Specific Integrated Circuit.
AWGN	Additive White Gaussian Noise.
BBU	Baseband Unit.
BER	Bit Error Rate.
BPF	Band Pass Filter.
BPP	Binomial Point Process.
BS	Base Station.
C-BER	Coded Bit Error Rate.
C-RAN	Cloud Radio Access Network.
C02	Carbon Dioxide.
CAPEX	Capital Expenditure.
CD	Contact Distance.
CDF	Cumulative Density Function.
CDL	Clustered Delay Line.
CDL-C	Clustered Delay Line Channel Model of type C.
CEO	Chief Executive Officer.
CF	Compress-and-Forward.
CP	Cyclic Prefix.
CPE	Common Phase Error.
CPRI	Common Public Radio Interface.
CRC	Cyclic Redundancy Check.
CS	CubeSat.
CSI	Channel State Information.
CSMA/CA	Carrier Sense Multiple Access with Collision Avoidance.
CU	Centralized Unit.
DC	Direct Current.
DEM	Digital Elevation Model.
DF	Decode-and-Forward.
DFT	Discrete Fourier Transform.
DL-SCH	Downlink Shared Channel.

DM-RS	Demodulation Reference Signal.
DPU	Data Processing Unit.
DSH	Deep Space Habitat.
DSN	Deep Space Network.
DST	Deep Space Transport.
DT	Direct Transmission.
DTN	Delay Tolerant Network.
DU	Distributed Unit.
E-LTE	Extraterrestrial Long Term Evolution.
E-S	Earth-Sun.
E2E	End-to-End.
EDL	Entry, Descent and Landing.
EHF	Extremely High Frequency.
EM	Electromagnetic.
EMC	Evolvable Mars Campaign.
EPC	Evolved Packet Core.
ESA	European Space Agency.
FDE	Frequency Domain Equalization.
FEC	Forward Error Correction.
FFT	Fast Fourier Transform.
FH	Front-Haul.
FOD	Foreign Object Debris.
FSO	Free Space Optics.
GA1	Gale Crater - Area 1.
GA2	Gale Crater - Area 2.
HAPS	High-Altitude Pseudo-Satellites.
HARQ	Hybrid Automatic Repeat Request.
HF	High Frequency.
HPS	Hybrid Propulsion System.
HSS	Home Subscriber Server.
I-DFT	Inverse Discrete Fourier Transform.
I-FDMA	Interleaved Frequency Division Multiple Access.
I-FFT	Inverse Fast Fourier Transform.
IC	Instruction Count.
IM/DD	Intensity Modulated/Direct Detection.
IoT	Internet of Things.
IPC	Instructions Per Cycle.
ISS	International Space Station.
ITU	International Telecommunication Union.
JAXA	Japan Aerospace Exploration Agency.
JN	Jetson Nano.
JPL	Jet Propulsion Laboratory.
KPI	Key Performance Indicator.
L-FDMA	Localized Frequency Division Multiple Access.
LDPC	Low-Density Parity-Check.
LEO	Low Earth Orbit.

LMO	Low Martian Orbit.
LoRa	Long Range.
LOS	Line-of-Sight.
LP	Lagrangian Points.
LTE	Long Term Evolution.
LTE-A	Long Term Evolution Advanced.
LTP	Licklider Transmission Protocol.
M2M	Machine-to-Machine.
MAHD	Mid-Air Helicopter Delivery.
MarCO	Mars Cube One.
MAVEN	Mars Atmosphere and Volatile EvolutioN.
MDS	Minimum Detectable Signal.
MHS	Mars Helicopter Scout.
MIMO	Multiple-Input Multiple-Output.
MIPS	Mega Instructions Per Second.
MISO	Multiple-Input Single-Output.
ML	Multi-Layered.
MME	Mobility Management Entity.
MMSE	Minimum Mean Square Error.
MMX	Martian Moons Exploration.
MOPA	Master Oscillator Power Amplifier.
MOXIE	Mars Oxygen In-Situ Resource Utilization Experiment.
MPCV	Multi-Purpose Crew Vehicle.
Mr-S	Mercury-Sun.
MRO	Mars Reconnaissance Orbiter.
Ms-S	Mars-Sun.
MSH	Mars Science Helicopter.
N	Nitrogen.
NACK	Negative-Acknowledgment.
NASA	National Aeronautics and Space Administration.
NEP	Nuclear Electric Propulsion.
NFV	Network Function Virtualization.
NGC	Next Generation Core.
NGC-M	Next Generation Communications on Mars.
NLOS	Non-Line-of-Sight.
NN	Nearest-Neighbor.
NR	New Radio.
NTN	Non-Terrestrial Networks.
NTP	Nuclear Thermal Propulsion.
O2	Oxygen.
OAI	OpenAirInterface.
OB	Orbiter.
OFDM	Orthogonal Frequency Division Multiplexing.
OFDMA	Orthogonal Frequency Division Multiple Access.
OOK	On-Off Keying.
OPEX	Operational Expenditure.

OWmRN	Optical Wireless Multi-Relay Network.
P-GW	Packet Gateway.
PAPR	Peak-to-Average Power Ratio.
PDCP	Packet Data Convergence Protocol.
PDF	Probability Density Function.
PDP	Power Delay Profile.
PDSCH	Physical Downlink Shared Channel.
PHY	Physical.
PSK	Phase Shift Keying.
PT-RS	Phase Tracking Reference Signal.
QAM	Quadrature Amplitude Modulation.
QoE	Quality of Experience.
QoS	Quality of Service.
RB	Resource Block.
RF	Radio-Frequency.
RLC	Radio Link Control.
RMA	Reliability, Maintainability, Availability.
RMS	Root Mean Square.
ROCC	Rover Operation Control Center.
RP	Raspberry Pi.
RP*	Reflection Point.
RRC	Radio Resource Control.
RRH	Remote Radio Head.
RRM	Radio Resource Management.
RS	Reed-Solomon.
RTT	Round-Trip-Time.
RU	Radio Unit.
RX	Receiver.
S-GW	Serving Gateway.
SA	Sub Area.
SAM	Sample Analysis at Mars.
SC-FDMA	Single-Carrier Frequency Division Multiple Access.
SCF	Small Cell Forum.
SDR	Software Defined Radio.
SEP	Solar Electric Propulsion.
SIMO	Single-Input Multiple-Output.
SISO	Single-Input Single-Output.
SLS	Space Launch System.
SNR	Signal to Noise Ratio.
SOI	Sphere of Influence.
SOLACOS	Solid State Laser Communications in Space.
SSPA	Solid-State Power Amplifier.
SWaP-C	Size, Weight, Power and Cost.
TCP	Transmission Control Protocol.
TDL	Tapped Delay Line.
TE	Transverse Electric.
TM	Transverse Magnetic.
TX	Transmitter.
U	Unit.
UAV	Unmanned Aerial Vehicle.

UDP	User Datagram Protocol.
UE	User Equipment.
UHF	Ultra High Frequency.
URSS	Union of Soviet Socialist Republics.
USA	United States of America.
USD	US Dollar.
V-LMO	Very-LMO.
V-S	Venus-Sun.
VR	Virtual Reality.
VXLAN	Virtual Extensible LAN.
WLAN	Wireless Local Area Network.
WSN	Wireless Sensor Network.
ZF	Zero Forcing.

List of Figures

List of Tables

Part I

Introduction and State-of-the-Art

Chapter 1

Introduction

The PhD dissertation begins here with introducing the general framework and motivations around our work. Sect.1.2 shows the main contributions and novelties brought by our studies, and sect.1.3 summarizes the content of each chapter.

1.1 General Framework and Motivations

TRY to make sense of what you see and wonder about what makes the universe exist. Be curious." is, probably, the most famous quote of the inspiring and never forgotten scientist Stephen William Hawking. This would be enough to justify all the attempts and costs to be met in order to successfully reach, explore and live on Mars.

The "Red Planet", which owes the name to its reddish appearance, is the Earth's most similar planet in the whole Solar System. Despite being a harsh yet probably dying environment, studies reveal that it could have been a flourishing planet with waterways and a thicker atmosphere [1]. From here, it is trivial to suppose that there could have been some kind of life presence on its surface. However, evidences physically taken are necessary to demonstrate it. Moreover, the set of experiences, that would be gathered as a consequence of manned missions on Mars, is fundamental to further push the boundaries towards a far-future, probably unmanned, exploration of Jupiter, Saturn and all the other celestial objects composing our Solar System and, by extension, our universe.

There is another reason for being enthusiastic about Mars and its unrevealed secrets. As it was during 60s with the first "Space Race" towards the Moon, which disruptively changed our history, this kind of apparently unattainable missions leave breakthrough technologies for mankind on Earth. They become the engine of a renewed technological advancement that, directly impacts on people's lives. Insulin pump, heat-resistant suits for firefighters, anti-scratch lenses, photovoltaic cells and even the computer mouse are some of the innovations coming, especially, from the National Aeronautics and Space Administration (NASA) struggles in making humans surviving in the outer space [2]. As we enter in what we easily call the "Space Race 2.0", or better "Mars Race", we can assume that we will witness to the same appreciable positive side effects, which will repay for all the efforts spent. However, we still have a long path ahead to pave the way to the human landing on Mars and, again, we shall travel it through, sometimes, small innovative steps demanding huge dedication.

Exploring Mars means to sustain a several months long travel just for a round trip, assuming to wait for the minimum cost transfer window: around nine months to reach the planet, at least other three months to wait for the proper positioning of Earth and Mars, and the remaining nine months for the return [3]. As imaginable, such a long time implies a profoundly strict scheduling and a phased mission approach. The Evolvable Mars Campaign (EMC) details three stages, that will culminate with the first human crew leaving footprints on the "Red Planet" terrain [4]. It has already begun with the Phase 0 at the International Space Station (ISS) in Low Earth orbit (LEO), which studies the effects on the body of a long term exposure to zero gravity [5]. Indeed, one of the main concerns around life in the deep space regards atrophy of muscles and brittle bones due to the weightless condition [3].

Phase 1, also referred to as "Earth Reliant", started during November of this year in the context of the unmanned Artemis 1 mission, whose goal is to test the reliability of both the Space Launch System (SLS) and the Orion Multi-Purpose Crew Vehicle (MPCV), carried by the SLS. The Orion MPCV arrived in the vicinity of the Moon, inserted in and orbited the Lunar retrograde orbit, and will finally move back to Earth within these days. This should be the trailblazer to the next Moon landing. Indeed, in the late 20s of this century, later well Eugene Cernan[1] in 1972, a manned mission is expected to bring a human crew on the Earth's natural satellite.

Thus, Phase 2, or "Proving Ground", should mark the construction of the Deep Space Transport (DST) vehicle, composed of a Deep Space Habitat (DSH) and an hybrid propulsion system (HPS). Phase 2 is aimed at sim-

---

[1] Eugene Andrew Cernan (March 14, 1934 – January 16, 2017) was an American astronaut, famously known for having been "The last man on the Moon".

ulating the arrival on Mars through an analog mission around the Moon. Fast and slow transfer operations, maintenance and maneuvers will be validated to assess the DST with an emphasis on the DSH, where the crew should live and work for a very long time. Authors in [5] theorize a possible launch around 2026, however, it is more convincing to assume the starting point of Phase 2 at the beginning of the next decade.

After, hopefully, multiple successful missions, the "Earth Independent" Phase 3 will be a cornerstone of space explorations leading to the descent of humans on Mars. Still, there is no certainty about a departure date. Some quite recent forecasts stated it around 2028 [6], CEO Elon Musk, on behalf of SpaceX, hints about 2029, while others assume a more solid and wider timeline in which a Mars surface mission should start in 2039 and end three years later in 2042 [7]. What comes next would be to set up a base on Mars. Potter et al., for instance, talk about "growing capabilities" gathered in a time span roughly going from 2019 and 2097, which could lead to a permanent base constituted by a 50-person crew [7]. Thus, let us go deep inside these growing knowledge, technologies and solutions to be acquired for instantiating human communities on Mars.

First, the propulsion system is key to quickly reach and leave Mars [8]. Several options are currently under study, from the nuclear electric propulsion (NEP) and nuclear thermal propulsion (NTP) [8], where both of them are based on nuclear fission, or the solar electric propulsion (SEP), in which electricity is harvested through solar arrays [5]. The latter is capable of reducing the propellant mass of ~ 10 times with respect to the one exploited by usual chemical propulsion systems currently used in today's space shuttles. Hybrid systems based on SEP and hypergolic propulsion, i.e. no-ignition propellant based on fuel and oxidizer, were proposed for deep space coasting and insertion burns, and orbit departure, respectively [9, 10].

Secondly, the engineering of a shield, which should guarantee the safe landing of the DST, or part of it, on the Martian surface, has to be taken into account with particular attention. NASA is actively working on an inflatable heat shield, within the project Low-Earth Orbit Flight Test of an Inflatable Decelerator (LOFTID) [11], that will reduce the volume occupation on the rocket, thus expanding and inflate during the entry, descent and landing (EDL) phase [12].

Spacesuits are high-priority equipment too. They shall be optimized for a maximum flexibility to allow Earth-like movements. On Mars, the significant thermal variation of the day, and throughout the year too, makes

it mandatory to design spacesuits able to protect both from freezing and overheating [12].
Once landed on the "Red Planet", installing a base is a primary concern. Even though a modular base seems preferable to host dozens of people, the principal idea revolves around the development of a pressurized home on wheels, which will shift location to let astronauts collect samples from disparate areas.
Then, uninterrupted power resources will make a huge difference for living on another planet. Nuclear fission power systems are most probably the designated ones since dust-storms, lasting for months, unluckily decrease the efficiency of solar arrays.
Common to all the stages and substages of a manned mission to Mars is the paramount need of connectivity. A strong back-haul link to Earth will be necessary from the departure phase to the travelling time, from EDL to actually living on Mars. Connectivity has to be efficient, reliable, maintainable and always-available, but distances, which primarily influence each aspect of deep space missions, are a serious natural bottleneck. As known, the whole design of network infrastructures and communication systems is directly dependent on the distance from the communicating nodes, trivially, from transmitter (TX) to receiver (RX), both for wired and wireless links. Precisely, the shortest distance from Mars to Earth is 54.6×10^6km, the average one 229×10^6km, the longest is around 401.4×10^6km. This translates into a delay amounting to, in order, 3min and 2s, 12min and 42s and 22min and 19s [13]. For what concerns on-travel communications, latency from Earth is acceptable to some extents, being each crew member physically locked in the same DSH, within the DST vehicle. Simply, instructions, commands and any kind of data will arrive on-board and, vice-versa, will be received on Earth delayed in time. Instead, on the Martian terrain, astronauts, cosmonauts, taikonauts or even parastronauts, whose presence in space was announced few days ago by the European Space Agency (ESA) with the selection of the British John McFall in the context of the Parastronaut Feasibility Project [14], should rely on on-demand, ubiquitous, low-latency, wideband and robust connectivity. This will be achieved in order to transfer *in-situ* large amount of information related to critical messages or emergency messages, for post-processing purposes or even for remote control of machines such as unmanned aerial vehicles (UAVs). Examples are multiple: maintaining a supportive real-time link from the base to a crew subgroup conducting experiments outside, sharing

data with rovers and landers deployed in faraway places, or again control UAVs to gather data through sensors from those dangerous or unreachable zones such as mountains, deep craters or (active?) volcanoes. In addition, several works demonstrated that undesirable side effects might arise if an isolated group is settled over a remote environment, such as the Martian surface. Many potential psychological issues affecting mental health have been highlighted in view of this situation [15]. Therefore, socialization between people living in the deep space should be pursued, also to increase the success probability of deep space missions. The insufficiency of old-fashioned narrowband and high-latency connectivity is strengthened by experiments and interviews conducted by NASA on crew members of the International Space Station, which demonstrated that a proper communication infrastructure, guaranteeing low delays and large bandwidth availability, will create a positive mood among the astronauts, while increasing their performance in terms of autonomy and interactions [16]. On the contrary, frustration and general bad feelings can be perceived in presence of a poor quality communication, where "being understood by others" was individuated as the major contributor to the quality of experience (QoE) [16].

Supposing RF communications with bandwidth centered at GHz frequencies, which is mandatory to achieve reasonable data rates, the large scale attenuation is in the order of hundreds of dB when Earth and Mars are just in inferior conjunction. The communication system has to counteract through an over-dimensioning with respect to terrestrial systems, which results into huger, heavier, lower bandwidth, power demanding systems that could not fit deep space applications. Moreover, the superior conjunction, happening when Mars and Earth are obscured between each other by the presence of Sun in the middle of them, completely blocks all the communications for a couple of weeks every two years. Clearly, we should counteract such phenomena to continuously support the crew's lives and scientific work.

For all the reasons mentioned above, assuring connectivity on Mars is a two-fold topic, that this research will seek to address, thus divided:

- Development of a mobile infrastructure for wireless *in-situ* connectivity.
- Setup of wideband continuous interplanetary long-haul links.

The literature is not so abundant when speaking about planet surface communications. Later on, we will see a review of all the proposals found in the state-of-the-art for each faced topic, while highlighting their advantages and drawbacks with respect to the application they serve. Interesting would be to analyze the current protocols adopted by machines, already deployed on Mars, to forward and receive data to and from Earth. Unfortunately, little is published about this. Instead, we exactly know that, for instance, the Perseverance rover transmits at 2Mbps through an ultra-high frequency (UHF) antenna at a carrier frequency of 400MHz in direction of the Mars orbiters acting as a relay-node (RN), at $160 - 500$bps thanks to an X-band high gain antenna pointed towards the Deep Space Network (DSN)'s 34m antenna on Earth, or at $800-3000$bps via an X-band low gain antenna to/from the DSN's 70m antenna [17]. Supposing a crew composed of several persons, the allowed data rate appears to be poor for the amount of information that would be generated and processed in perspective. This does not consider that the human personnel is, surely, mass and power-constrained. More easily, the same radio equipment mounted on rovers cannot be endured by a human being. Thus, the quality-of-service (QoS) and the overall data rate would clearly and unacceptably be reduced.

1.2 Thesis Contributions

We try to investigate viable and innovative solutions for broadband Martian connectivity, to formulate a new paradigm and a set of potential disruptive technologies which we refer to as "Next Generation Communications on Mars" (NGC-M). Here below, a brief discussion introduces the main novel contributions of this thesis:

1. We propose an Extraterrestrial Long Term Evolution (E-LTE) porting for local mobile networks on the Martian surface. Moving the usual LTE terrestrial infrastructures, like multiple truss towers and huge hardware within their cabinets, seem to be of difficult realization, both from a physical, systemic, energetic to an economic perspective. Indeed, bringing there large and weighing equipments through DST vehicles exponentially increases, at least, mission times and costs. For this reason, landers could be re-used to embark baseband equipment to furnish access to an LTE-based network. The generated network cells would interconnect rovers, and in the future, humans, while maintaining back-hauls with other landers or even satellites deployed in various

orbits. As we will appreciate, our evaluations points out the feasibility of such a solution when referring to short range communications. On the contrary, the rocky Martian environments and larger distances hopelessly affect the system QoS.

2. Our preliminary analysis highlighted also a scarcity in the state-of-the-art around replicable channel models for selected Martian locations. Indeed, even though communication systems are usually tested in the exact locations where they are going to be installed for network access provisioning, as understandable, the same cannot be done in the context of deep space communications, where we need to be previously certain about the perfect functioning of our system. Thus, it becomes fundamental to solidly simulate performance for the system parametrization and dimensioning, especially, because, for the same reason, it is non-trivial to determine how a RF signal would propagate over the Martian terrain. Thus, we build a 3D tile-based structure upon the use of high-resolution Digital Elevation Models of Mars. Through a 3D ray tracing algorithm customized to fit the obtained 3D rendering, we estimate the path loss exponent, shadowing effect, blockage probability and again multipath propagation for precise Martian terrains. Realistic statistical Martian channels are then computed for further simulations.

3. A global network coverage could be necessary for future colonies and remote machines, respectively, living and operating in disparate Martian areas. However, assuring it through thousands of incredibly complex landers is unfeasible. As mentioned above, the E-LTE porting suffers from limited radio resources and large coverage. It is based on fixed BSs, which translates into fixed small cells, thus limiting also the mobility of people on Mars. Moreover, LTE energy efficiency, throughput, handover and latency are firmly surpassed and revolutionized by technologies of fifth generation (5G).
   Recently, non-terrestrial networks (NTN) were integrated in the “5G & Beyond” vision towards a future definition of sixth generation (6G) mobile networks. However, NTN, at their first stage, assumes to leave all the computational complexity at the side of LEO constellations, when satellites are not treated as merely transparent relaying nodes forwarding data to an on-ground gateway [18]. On a hand, this means an increased power consumption, huger solar arrays for energy har-

vesting and processing units (PUs) for processing complexity, higher satellite volume and weight, which reflect on missions' overall costs. On the other, fixed and bigger radio equipment is necessary on-ground, which could reduce a lot the degrees of freedom of such a choice. Instead, 6G technologies will change the communication network architecture from two to three dimensions, indeed, they will seamlessly merge satellite, aerial and terrestrial networks in a joint terrestrial-network (TN) and non-terrestrial networks (NTN) cluster, a unique dynamic and adaptive infrastructure [19].

From here, we formulate multi-layered (ML), or better three-dimensional (3D), networks composed of heterogeneous nodes, i.e. UAVs and CubeSats (CS), to create an autonomous yet reconfigurable space ecosystem on Mars. 5G New Radio (NR) functions are virtualized on heterogeneous nodes, such as UAVs and CubeSats, i.e. small satellite platforms. Both UAVs and CSs host computational and energy resources. This means processing units (PUs), solar panels and batteries, as well as radio equipment and antennas for connectivity purposes. Eventually, scientific payload could also be accommodated. More precisely, the UAV and CS binomial composes the Cloud Radio Access Network architecture, which takes in charge of the 5G NR processing. Roughly speaking, the UAV is the remote radio head (RRH), the CS represents the baseband unit (BBU) and the wireless mid-haul interfacing them is based on the Common Public Radio Interface (CPRI) standard. Splitting options are operated to divide and optimize the usage of resources on UAV and CS. We suppose to move the core network, or Next Generation Core (NGC), into a higher Low Mars Orbit (LMO) constellation of satellites.

Thanks to simulations, we first demonstrate the feasibility of 3D Networks implementing C-RAN on Mars by meeting strict latency and bandwidth requirements to split the baseband processing between UAV and CS. Then, a deep analysis is made to encompass the most important trade-offs appearing between mechanic, systemic and networking parameters. For instance, satellite lifetime and coverage with respect to communication delays and bandwidth. E2E evaluations show the achievable performance in terms of E2E packet loss, throughput and delay. Concluding, on-hardware tests allow predicting the computational and energy resources needed on UAVs to maintain the service continuity and quality.

4. Being the back-haul of the space ecosystem on Mars, which shall accomplish the delivering and receiving of tremendously high amount of data to and from Earth, we introduce here an optical relaying network based on satellites orbiting around the Lagrangian points. Optical frequencies exponentially raise the bandwidth to be occupied and optical transceivers benefits from their narrow beams, which incredibly reduces the power losses for the long distances occurring in this scenario. However, path losses and the interrupted service continuity, due to the superior conjunction, oblige a non-direct link for the Mars-to-Earth long-haul. For this reason, we suppose to deploy satellites in the LPs for relaying signals through a decode-and-forward (DF) strategy to maximize the overall E2E throughput. Results will show, depending on the optimal selection of relaying LP nodes constructing the shortest-path, the achievable data rate on the route from Earth to Mars and vice-versa.

1.3 Thesis Structure

This manuscript is composed of 8 self-sufficient but correlated chapters, which are subdivided into an incipit and other sections and subsections showing the methodologies, results and chapter-related conclusions. The summaries of the thesis chapters are reported in the following subsections.

1.3.1 Chapter 2: Brief Story of Mars Exploration: from Background Knowledge to our Future in the Deep Space

Our analyses cannot ignore the scenarios, which surrounds them by. Thus, a particular focus shall be paid to the background knowledge about Mars and to the past unmanned missions towards its future exploration. Mars is the fourth planet, coming from the Sun, of our Solar System. We will spend some time in detailing its orbit around the Sun, which will be taken into account for the optical relaying network based on LPs for the long-haul link.

Mars is a heavily cratered planet, allegedly due to its thin atmosphere, which does not sufficiently protect it from the meteorites impact. As we will see later, the Martian atmosphere plays a major role in the dimensioning of 3D Networks because it reflects a lower drag force expressed on possible orbiting satellites, thus a higher service lifetime.

The reddish appearance depends on the dryness of its environment. The terrain electrical properties modelled through a Martian soil replicant, as the JSC Mars-1, will affect the large and small scale phenomena study, later discussed. It is still unknown if we can claim the inactivity of Mars. However, many evidences showed an ancient volcanic activity over its surface [20].

Our proposals rely on machines to be likely found or to be, somehow easily, deployed on Mars, like rovers, landers, UAVs, CubeSats and bigger satellites. Thus, knowing the story of successful past missions, which we will narrate in this chapter, is important to recognize the key elements that will play a major role for a future Martian connectivity.

1.3.2 Chapter 3: The Current Picture of Martian Connectivity versus New Trends of Non Terrestrial Networks

This dissertation treats the same big issue, i.e. guaranteeing reliable connectivity on Mars, but from four main perspectives. Chronologically going, we have the on-ground E-LTE porting and its analysis, the study on large and small-scale phenomena through 3D ray tracing and 3D tile-based rendering of DEMs, the wide framework on 3D Networks implementing C-RAN and the reasoning around long-haul connections through FSO and a relaying infrastructure in the deep space. Thus, before arriving to the discussion of the realized methodologies to face the just mentioned sub-topics, we describe here the reviewed literature, that enabled our investigation and findings.

1.3.3 Chapter 4: Long Term Evolution Porting: Extraterrestrial Mobile Connectivity

Solutions regarding the connectivity on Mars revolved around, in a first instance, the idea of porting the terrestrial LTE by reusing the radio equipment on landers and rovers to create static network cells. Depending on on-board energy and processing resources, landers take in charge of performing base station (BS) tasks, meaning remote radio head (RRH) and BBU functionalities. Rovers are on the same plane as humans, indeed, both of them are treated as UEs of the network cell, thus giving an anthropomorphic characterization to them, as suggested in [21].

Performance is evaluated on the basis of orthogonal frequency-division multiple access (OFDMA) for downlink communications and single-carrier frequency-division multiple access (SC-FDMA) for uplink ones. The latter has been tested upon a localized (L-FDMA) and interleaved (I-FDMA) allocation of the sub-carriers. The Martian channels are modelled thanks to few samples found in the literature, regarding the received power of delayed signal replicas over the Gusev crater. This has also driven us to the formulation of more realistic and replicable Martian channel models for further analysis (see next subsection and Chapter 5). A link budget computation reveals the reachable data rate at the cell border for a given QoS through Turbo channel coding. Common metrics, such as bit error rate (BER), coded-BER (C-BER), signal-to-noise ratio (SNR), and capacity are exploited for our evaluations.

1.3.4 Chapter 5: A Reliable and Replicable Martian Propagation Model based on 3D Ray Tracing and Digital Elevation Model

To the best of our knowledge, models for estimating various RF propagation impairments are not replicable or not present in the state-of-the-art. Instead, other contributions derive heuristic, empirical and overall approximated analysis. From here, we suggest taking advantage from the high-resolution DEMs made available by NASA. Each pixel is a tile with side length the DEM's resolution. The tiles are interpolated to construct walls of a 3D structure representing, in our case, the Gale crater. We estimate through the Cole-Cole equations the dielectric permittivity of the Martian replicant soil JSC Mars-1 for few selected frequencies. The obtained electrical properties are associated to each tile, comprising the walls. A 3D ray tracing algorithm is developed to track all the paths followed by the line-of-sight (LOS), first and second signal reflections, which are generated by an isotropic radiator over the tile-based 3D rendering of the Gale crater. By collecting the received power and the time of arrival of each signal replicas over precise Gale areas, we derive large-scale phenomena such as path losses, shadowing, blockage probability and small-scale phenomena such as multipath fading, thus power delay profiles (PDPs). To conclude, we add considerations about atmospheric and dust-storms attenuation.

1.3.5 Chapter 6: “Towards 6G” Martian Connectivity: a Space Ecosystem Providing Connectivity from Above

3D Networks are composed of three segments: the *on-ground layer*, which is constituted of UEs in the form of sensors, rovers, landers and humans acquiring and forwarding data from or to other end-users, the *aerial layer* where UAVs or HAPS reside and the *space layer* with orbiting CubeSats and in higher altitudes orbiters, that can serve as the Next Generation Core (NGC) network. The binomial, vertically and wirelessly linking a Cubesat and a UAV, takes in charge of all the C-RAN functionalities typically performed by 5G virtual BBU pools. The result is a drone providing access to the UE, acting as radio unit (RU) and (adaptively) operating splitting options to detach the processing chain of the BBU - distributed unit (DU) plus centralized unit (CU) functionalities - and optimize the resources need and utilization of both communicating nodes. This, as later shown, has an effective impact on the system design and maintainability over time.

The full-bodied chapter introduced by this small preamble will move from theory to simulations, from emulations to hardware test. We will tackle 3D Networks implementing C-RAN from the inner requirements of the splitting options and Common Public Radio Interface (CPRI) to be met, to the mechanical, systemic and networking aspects. An in-depth analysis will show trade-offs arising from desired system Key Performance Indicator (KPI) in terms of satellite lifetime and propulsion, delay and goodput, service time and coverage. E2E delays, packet loss and throughput will be assessed thanks to an OpenAirInterface (OAI) emulator of the C-RAN in 3D Networks, while the computational load and performance with respect to the selected splitting option are obtained through an implementation of the Downlink Shared Channel (DL-SCH) and Physical Downlink Shared Channel (PDSCH) on Raspberry Pi (RP) 3B+ and 4B. Finally, a dimensioning of resources to be hosted on UAVs will conclude the discussion.

1.3.6 Chapter 7: Advanced Optical-based Relaying Network for Mars-to-Earth Long-Haul

Critical and emergency information, data related to missions aspects, data gathered and post processed *in-situ*, but also data for the entertainment will strongly characterize the flows from Mars-to-Earth, and vice versa. And that being the case, current direct transmissions (DT) from the surface or orbit of Mars to the NASA's DSN are not suitable to maintain the demanded data rates. Envisioning the arrival of human on Mars, it is so of dramatic importance to find better ways to interplanetary exchange data. Therefore, we argue about a possible futuristic multi-relays optical network deployed on LPs for broadband communications in the deep space. The network is constructed upon relaying satellites orbiting around the LPs. The orbiters mount optical transceivers in favor of an extremely huge available spectrum and an increased gain due to a strongly reduced beam divergence. The signal is relayed from Earth-to-Mars, or vice versa, following the shortest-path, whose selection mostly depends on the minimization of the distances to be travelled with respect to the position of Mercury-Sun (Mr-S), Venus-Sun (V-S), Earth-Sun (E-S) and Mars-Sun (Ms-S) LPs. Data rates over time and the occurrence probability of each LPs within the shortest-path will be detailed.

1.3.7 Chapter 8: Final Considerations and Future Trends: What Comes Next?

Finally, Chapter 8 will resume the key points of this piece of research, while comparing the presented solutions and evidence their strengths and weaknesses. We will suggest some industrial opportunities for eventual terrestrial applications partly exploiting the content of this thesis. To conclude, suggestions about future works and open issues will be given to clarify further steps for a connected Martian environment.

The thesis structure and logical flow is punctually described in Fig.1.1.

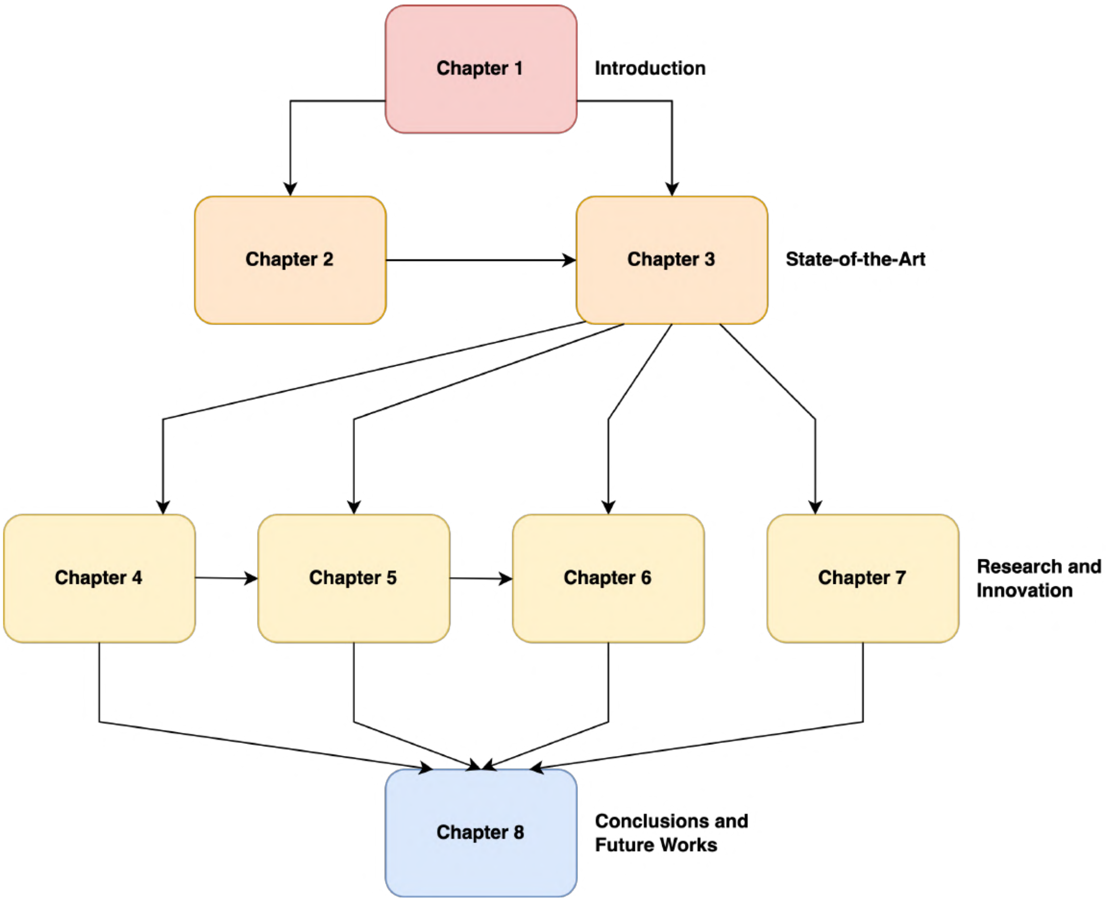

Figure 1.1: Thesis flowchart logically connecting the chapters across the parts.

Chapter 2

Brief Story of Mars Exploration: from Background Knowledge to our Future in the Deep Space

The following is a complete overview of the knowledge gained by the scientific community in more than sixty years of unmanned missions towards the discovery of Mars. The narration is not for its own sake but, rather, it contextualizes the analysis and developed solutions, that will be presented later on. Sect.2.1 defines the planetary habitability and sect.2.2 deals with the revolution and rotation of Mars around the Sun. The atmospheric composition and the absence of a magnetosphere are described in sect.2.3, while sect.2.4 focuses on the Martian environment. Sect.2.5 finalizes the chapter by illustrating past, present and future Martian missions.

2.1 Overview of Mars and Planetary Habitability

MARS is a terrestrial, or of rocky type, planet, like Earth and Venus, and this is a point in favor to the possible presence of lifeforms on it [22]. In fact, it is unlikely to find, among other reasons, complex organisms on gaseous worlds as they are Jupiter, Saturn and Uranus. The "Red Planet" (see Fig.2.1) is the fourth planet from the Sun, after Mercury, Venus and Earth, and it is the eighth biggest heavenly body in our Solar System. There are many similarities between Mars and Earth, such as being located in the Goldilocks' zones, i.e. habitable zone of the Solar System depicted as a yellow strip in Fig.2.2. In simple words, the definition of habitable zone is "the area around a star where it is not too hot and

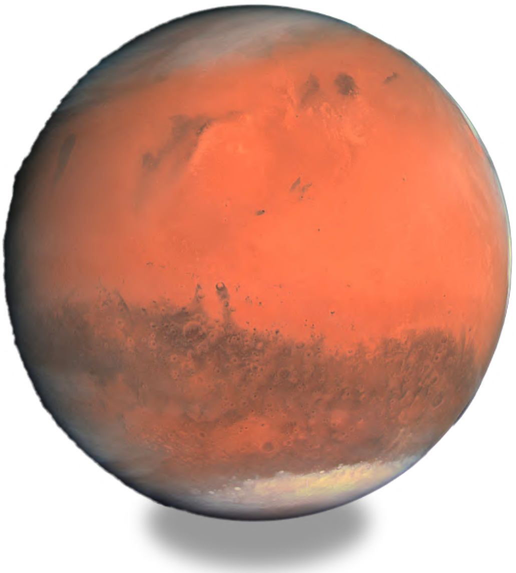

Figure 2.1: True color view of Mars taken by Rosetta's OSIRIS camera on February 23, 2007. Credit: ESA/MPS for OSIRIS Team, MPS/UPD/LAM/IAA/RSSD/INTA/UPM/DASP/IDA

not too cold for liquid water to exist" [23]. Similarly to what happened on Earth, we suppose liquid water to be the necessary condition for life. In addition, just a little amount of light, less than the 10^{-5} of the solar flux on Earth, and oxygen are required for the photosynthesis and multicellular organisms [24]. Moreover, Mars and Earth share the same layered composition, made of an atmosphere, a crust, a mantle and a core [22]. Precisely, although Mars has a current thin atmosphere, which as mentioned above could be the cause of its cratered environment, especially thanks to the Mars Atmosphere and Volatile EvolutioN (MAVEN) mission, researchers theorized and found confirmation that it could have been way thicker in early stages of the planet's history. The solar wind could have been the primary culprit for the atmospheric loss [22].
However, let us expand a bit this general overview about Mars here below. We start from the orbit, to arrive at the atmosphere and magnetosphere and, finally, to land on ground detailing important bulk characteristics and morphology aspects.

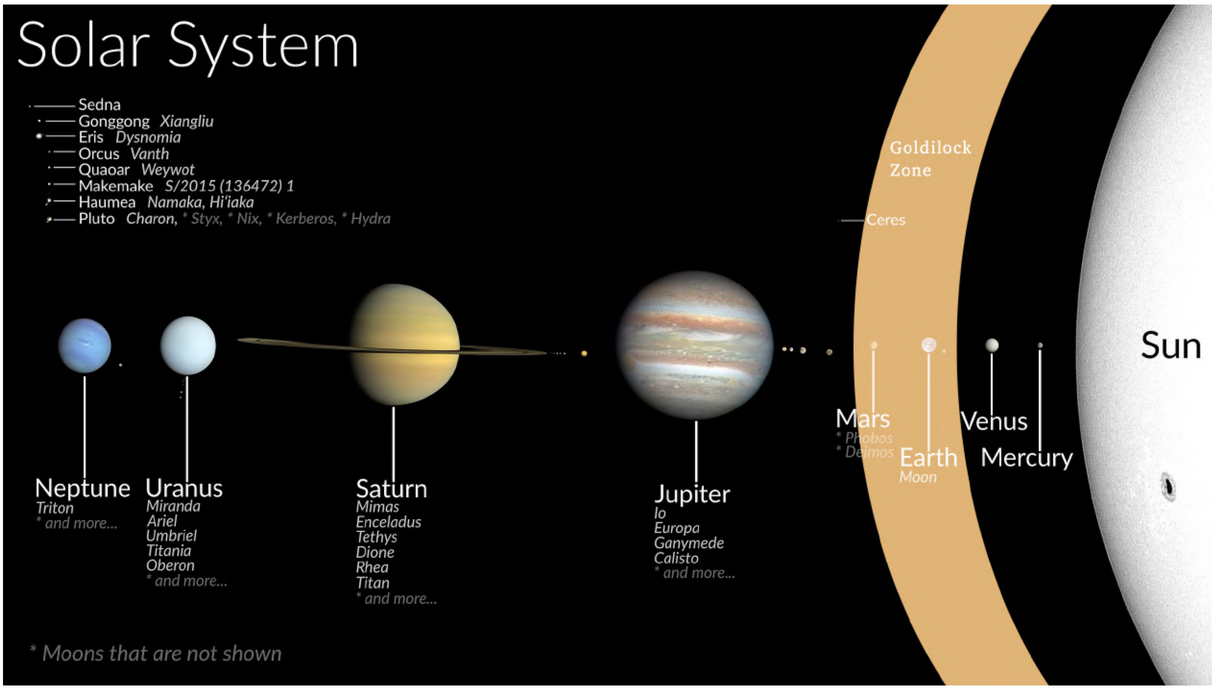

Figure 2.2: True sizes and order of the Solar Systems' planets. The Goldilocks zone, or habitable region, is colored in orange. Credit: NASA/ESA

Table 2.1: Mars vs. Earth Orbit Characterization

	Semi-major axis a (10^6km)	Perihelion (10^6km)	Aphelion (10^6km)	Eccentricity	Equatorial Inclination °	Day (hrs)
Mars	$\sim$ 227.96	$\sim$ 206.65	$\sim$ 249.26	0.0935	25.19	$\sim$ 24.66
Earth	$\sim$ 149.6	$\sim$ 147.1	$\sim$ 152.1	0.0167	23.44	24.0

2.2 Revolution and Rotation

Most of the orbital parameters characterizing the revolution of Mars around the Sun are included in Tab.2.1. Comparing terrestrial and Martian orbits, the semi-major axis of the latter highlights the increased distance from the Sun with respect to the former. The apsides clearly show how the Sun, even though it is mostly centered into the ellipse representing the Earth's orbit, is shifted of more than 42×10^6km. The orbit eccentricity is higher for Mars, which leads to a huger variation of its orbital velocity. From here, seasons have variable duration on Mars, i.e. spring and summer are longer than fall and winter, considering the northern hemisphere [25]. Spring, or autumn for the southern hemisphere, lasts 194sols, while summer 178sols, or winter for the southern hemisphere. Instead, autumn, or spring for the southern hemisphere, lasts 142sols, winter, or summer for the southern hemisphere,

Table 2.2: Mars vs. Earth Atmospheric Data

	Surface Pressure (mb)	Surface density ρ ($\frac{kg}{m^3}$)	Scale Height H (km)	Atm. Mass (kg)	Atm. Composition (%)	Temperature T (K)
Mars	6.36	~ 0.020	11.1	$\sim 2.5 \cdot 10^{16}$	$95.1\,CO_2$, $2.59\,N_2$, $1.94\,Ar$, $0.16\,O_2$, $0.06\,CO$	~ 210
Earth	1014	~ 1.217	8.5	$\sim 5.1 \cdot 10^{18}$	$78.08\,N_2$, $20.95\,O_2$	~ 288

lasts 154sols for a total amount of 668sols per each revolution [25].
The vertical axis, around which Mars rotates, is tilted of 25.19°and one rotation is completed within 24.6hrs (Martian days are called Sols), that is slightly longer than the Earth's rotation.
Mars has two small potato-shaped natural satellites, Phobos and Deimos [26]. Their particular form is due to their little mass, which translates into a low gravity that cannot shape them as a spheroid. Evidences suggest many analogies with the asteroids in the outer asteroids belt. It is believed that they were caught into the Martian orbit by the planet's sphere of influence (SOI). While Phobos orbits close to Mars (the orbital period is 0.32sols) and it is estimated that in 50×10^6years it will crush on its surface, Deimos is two and a half times farther away than Phobos with an orbital period of 1.26days.

2.3 Atmosphere and Magnetosphere

It is commonly known that the Mars' atmospheric pressure is roughly $\approx 0.6\%$ of the terrestrial one [22]. This, as we will see later, will be a key parameter for our discussion around 3D Networks on Mars. The atmospheric composition is mainly based on very sparse elements and molecules, such as carbon dioxide (CO2), nitrogen (N), and argon gases (Ar*). Oxygen (02) is only the 0.16% of the whole atmosphere, while on Earth it is the second most predominant element (see Tab.2.2.

The lack of a thick atmosphere turns into a dispersion of the heat from the surface of Mars to the space. The average temperature is ≈ -63°C [13], almost -78°C lower than the one on Earth [27], however, the variation around the mean can range between the upper bound of 20°C and a lower one around -153°C [25]. That is why the spacesuits' material need to be carefully selected to repair for the wide thermal excursion.
Dust storms can pervade the whole atmosphere and cover Mars for a period lasting months or years. They are harmful for scientific tools, for instance, solar panels and cameras can be completely obscured, thus blocking their operations. In 2018, we lost the communications with the rover Opportu-

Table 2.3: Mars vs. Earth Bulk Parameters

	Mass M (10^{24}kg)	Volume (10^{10}km^3)	Equatorial radius r (km)	Surface gravity g (m/s^2)
Mars	~ 0.64	~ 16.32	~ 3396.2	3.71
Earth	~ 5.97	~ 108.32	~ 6378.14	9.78

nity due to a “Dust Devil”. A recent article states that one of the driving causes behind dust storms on Mars could be the energy imbalance between Mars’ seasons, which is the amount of energy absorbed from the Sun that is different from the one re-emitted by the planet in the form of heat [28]. If on Earth it is measured to be the 0.4%, on Mars it is around the 15.3%. This could cause the giant dust storms that we can appreciate on the “Red Planet”.

As far as magnetic perturbations are concerned, no magnetic field surrounds Mars. The magnetic field is usually a protection from galactic cosmic rays and solar winds, that could cause not only sterilizing effects, the atmospheric loss and serious health damages, in case of human presence, but also the malfunctioning of satellites accelerating their orbit decay or compromising their payload [29,30]. There are traces of it over the crust in the southern hemisphere, that could denote a past global magnetic field, probably dating back to 4.12 to 4.14billion years ago [25,26]. The dynamo theory, saying that the heat flowing in a planet’s core, which creates circulating currents in the outer core, generates a global magnetic field [29], should apply for Mars too, however, it is still not clear what happened on Mars.

2.4 Bulk Characteristics and Morphology

The diameter of the “Red Planet” is the 53% of the terrestrial one, as can be seen from Tab.2.3. Its form is an oblate spheroid, indeed, the equator circumference is 21343km, but the one around the poles is 21244km. Thus, as Earth, it results a bit squashed at the poles.

The Mars/Earth mass ratio is the 11%, which induces a gravity of 3.71 $\frac{m}{s^2}$, which is the 62% less than the gravity on Earth. For this reason, being directly proportional to local gravity and planet’s radius, the escape velocity on Mars is way lower too, measured to be 5.03km/s, thus halving the escape velocity on Earth [13]. We can imagine how this would positively affect the departure phase of rockets there.

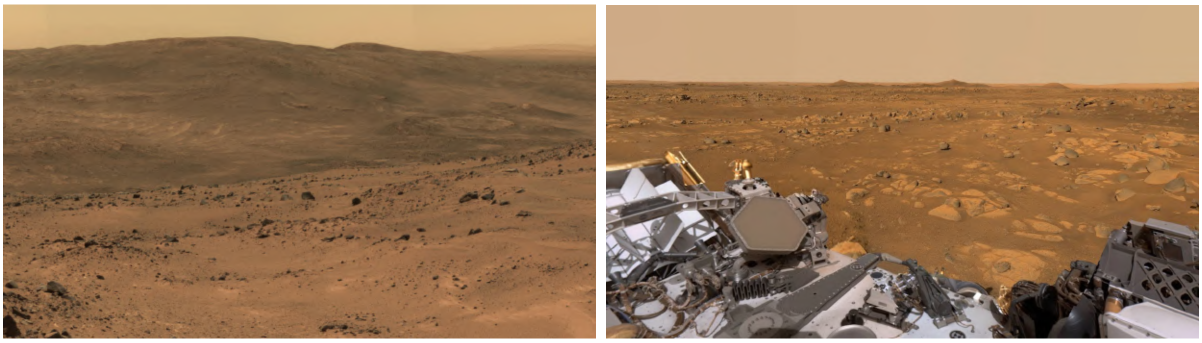

(a) Spirit view (b) Perseverance view

Figure 2.3: (a) Sight from the "Husband Hill" photographed by NASA's Mars Exploration Rover Spirit back in 2005 through the 360-degree panoramic camera (Pancam). Credit: NASA/JPL-Caltech/Cornell Univ. (b) Sight of the Martian site "Van Zyl Overlook" taken by the Perseverance Rover's Mastcam-Z. Credit: NASA/JPL-Caltech/ASU/MSSS

The planet is mostly known for its famous reddish color, which is a mix of brown gold and tan, due to the rusting of iron in its rocks, soil (regolith) and dust (see Fig.2.3 and 2.4) [26]. The morphology of Mars is one of the most interesting of the whole Solar System. The Martian landscape is characterized by enormous volcanoes, mountains, valleys, flat areas and deep depressions or craters. Olympus Mons is the Solar System's highest volcano, reaching $\approx$ 26km of height, but also tremendously wide with a diameter of almost $\approx$ 601km [26]. Large canyons can extend for hundreds of kilometers, like the Valles Marineris of about $\approx$ 320km at its largest point and $\approx$ 7km of depth [26].

The hemispheres are topologically different. The northern one is composed of plains and its crust estimated thickness is $\approx$ 30km, while on the southern one lays mountains and volcanoes and the crust thickness raises up to $\approx$ 100km. Leone et al. hypothesized and modelled possible giant impact scenarios, where a Moon-sized object could have collided with Mars leading to a deep thermal anomaly, thus causing the onset of volcanism in the southern highlands [31].

Thanks to meteorites and satellite examinations, we know the basaltic composition of the Martian rocks. The ALH84001 Martian meteorite, found in Antarctica, is made of orthopyroxenite and other minerals, whose creation is supposed to be due to the reaction between the original material and water [22]. Olivine, pyroxene, amphiboles, feldspar, carbonates, sulfates, silica, phyllosilicates, phosphates, and hematite, which also composes the soil in the Meridiani Planum (landing site of Opportunity), are typical

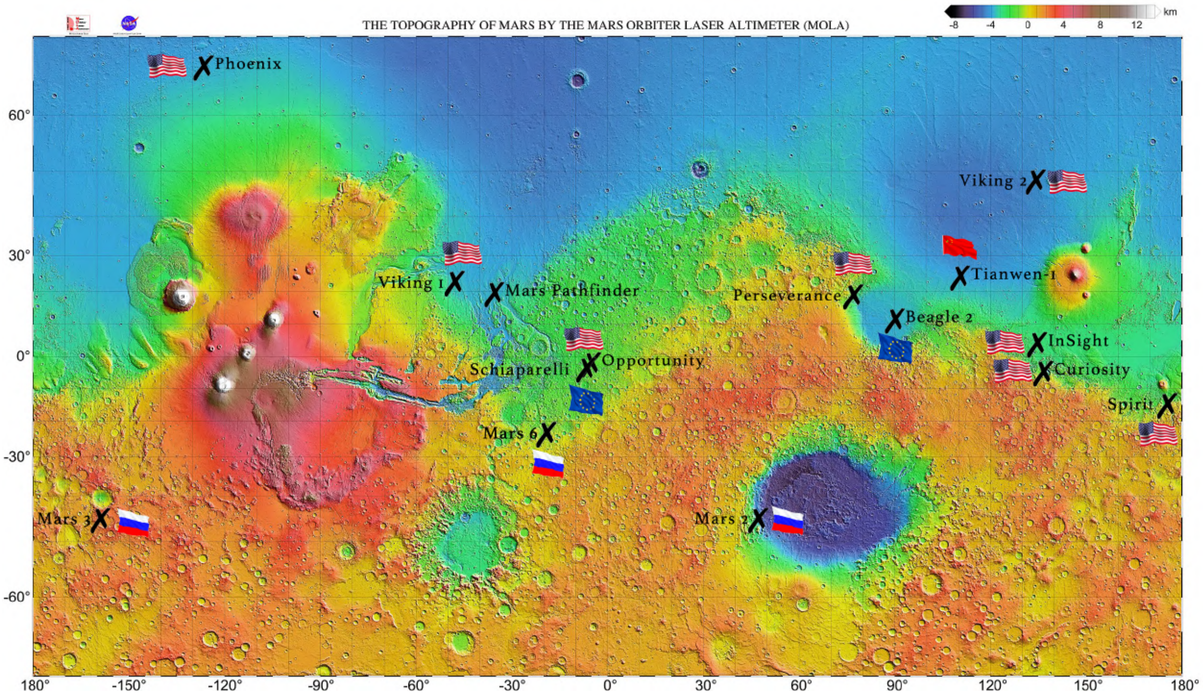

Figure 2.4: Top view of Mars showing the topography of the planet and the landing sites of unmanned Martian missions led by different countries. Photo captured by the Mars Orbiter Laser Altimeter (MOLA). Credit: NASA/JPL/USGS

minerals in Martian rocks [22].

Iced water is currently present at the poles. Once upon a time, the atmosphere was thick enough to keep the globe warm and the water in liquid form. In the next section, we will talk about the Opportunity's findings regarding the hematite concretions, which are firmly linked with flowing water in some ancient era. River valley networks, deltas, and lakebeds, such as, allegedly, the Gusev crater [32], are now dry, but their presence is still marked on the Martian environment. Many outflow channels, which are kilometers-long sinuous incisions with variable depths [33], were discovered on Mars. Their existence is due to some sort of liquid carving them in the crust of the planet. Even though they can be associated with lava flows, which for sure occurred, they seem more similar to our rivers and could suggest intense flooding of water.

To conclude, few words about the Martian sub-surface. Right now, Mars does not exhibit an active plate tectonic system. However, many surface and sub-surface lava flows were spotted through the processing of radar acquisitions. Sub-surface lava flows are also called lava tubes. Last year, HiRISE discovered the mouth of a lava tube, a 50m pit in the equatorial

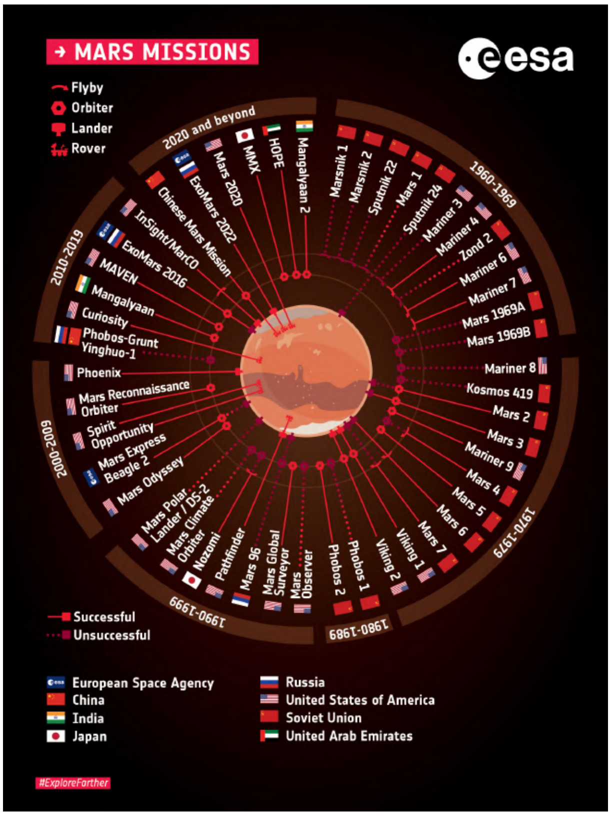

Figure 2.5: Portrait of Martian missions conducted in the last 62 years. Credit: ESA

Arsia Mons region [34]. Recently, they gained particular interest because they can serve as shelters for future colonies on Mars. Human could be protected from cosmic rays and solar winds, dust storms, and large temperature fluctuations, thus allowing longer missions while being a prime location for the search of life [35].

2.5 Past Present and Future of Martian Missions

The first "Space Race" began during the "Cold War" between the United States of America (USA) and the Union of Soviet Socialist Republics (URSS) in the 60s, where the researchers started to focus their attention not only on the Moon but also to the exploration of Mars. Indeed, several missions were planned to reach the Martian orbit. After some failures, as shown in Fig.2.5, in 1965 the NASA's flyby Mariner 4 was finally able to send back to Earth 22 images of Mars taken from the orbit [36]. Curiously, the impatient NASA's telecommunications team, in order to not wait for the post-processing of data, hand-painted the photo over strips of paper matching a reddish color-map to pixel matrices received from the probe [37].

Over time, almost 50 trials between flybys, orbiters, landers and rovers under different nations flags, were attempted to explore Mars from the orbit to its surface. Approximately, the 60% of them succeeded in their mission goals.

With the attempt of finding lifeforms or, at least, signs of them (and to prove a certain scientific superiority against the enemy faction), soviets sent the Mars 2 and Mars 3 landers in 1971 [38]. The Mars 2 failed the EDL phase, however, Mars 3 went out twenty seconds after a completed soft-landing. Later on, NASA successfully arrived on Mars with the lander Viking 1 in 1976. Thanks to its on-board camera, it photographed for the first time the Martian landscape, revealing its desert and rocky nature [36]. This mission was the precursor of other unmanned missions, that brought to the Martian surface many vehicles equipped with instrumentation to analyze the planet.

The last two decades were characterized by a growing importance of smaller and mobile vehicles, namely: the rovers, able at moving around the Martian surface - on the contrary landers are semi-static vehicles. Rovers are platforms based on highly technological mechatronic concepts. They represent a human sensorial extension on Mars given their robotic components, that act as human body parts under human will [21]. Among them, we need to cite the “Sojourner”, which is the first rover, landed in 1997, on Mars in the context of the Mars Pathfinder mission, which allowed, for example, to study the “Dust Devils”, compute the planet’s radius and see some ice clouds in the atmosphere. “Spirit” and “Opportunity” landed in 2004, respectively, in the Gusev crater and Meridiani Planum. Researchers selected these two areas because, from images captured by satellites, the Gusev crater was thought to be a dry lake, as cited above, while the Meridian Planum was the perfect flat spot to land on [39]. The outstanding revelation was the Opportunity’s finding of hematite-based spherules or concretions, probably formed by aqueous rain [40]. This strengthened the scientists convictions about the presence of water, thus indirectly of lifeforms, in the Mars distant history. Consequently, other missions were launched bringing rovers to the Martian surface, such as “Curiosity” in 2012, whose landing site was a big depression called Gale crater. “Curiosity” is equipped, among the other modules, with the Sample Analysis at Mars (SAM) instrument suite, which is one of the most powerful astrobi-

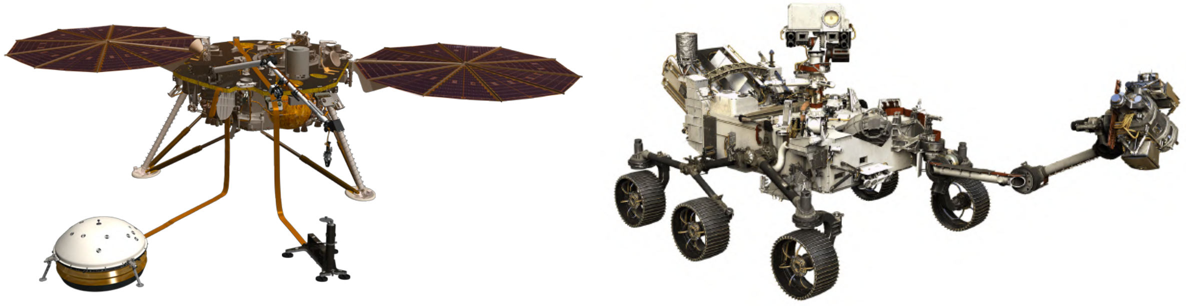

(a) Insight lander (b) Perseverance rover

Figure 2.6: (a) Image of the Martian Insight lander. The drill HP^3 and the seismometer SEIS instrument are visible in the front, as well as the horn antennas, the robotic arm and the other sensors mounted on the body and the big circular solar arrays on the side. Credit: NASA/JPL/ESA. (b) Photo of the Perseverance rover. The robotic arm is equipped with the ultraviolet SHERLOC and X-ray PIXL spectrometers. Above, the anthropomorphic head is composed of the SuperCam, which records audio, analyzes minerals and takes images, and two zoomable panoramic cameras called Mastcam-Z. Credit: NASA/JPL/ESA.

ology instruments ever engineered by NASA [41]. Thanks to it, important discoveries around the presence of water and lifeforms in some Martian era were carried out, such as the detection of organic molecules, the methane variability in the atmosphere and the presence of jarosite. Lately, two missions brought to Mars disruptive advancements in the regards of unmanned missions in the deep space.

The InSight lander (see Fig.2.6a), in the late 2018, was accompanied by two CubeSats, that served as communication relays during the EDL phase [36]. The recent development of Mars Cube One (MarCO) mission, targeted at sending swarms of CubeSats to Mars, designed small satellites supplied by solar panels (see Fig.2.7). Their size and weight were suitable to host advanced payloads. Indeed, MarCO's design is a six-unit (6U) CubeSat. Each of the two platforms has a stowed size of 36.6 centimeters by 24.3 centimeters and by 11.8 centimeters [42]. So far, the results of the MarCO mission have been contrasting. MarCOs satellites, named EVE and WALL-E, served as communication relays during the InSight rover landing, beaming back data at each stage of its descent to the Martian surface in near-real-time [43]. WALL-E sent some remarkable images of Mars, while EVE performed other radio science experiments. The last contact with the MarCO pair was in early 2019. The NASA mission team investigated the reasons for why they have not been able to contact the pair. WALL-E should have experienced problems due to a leaky thruster

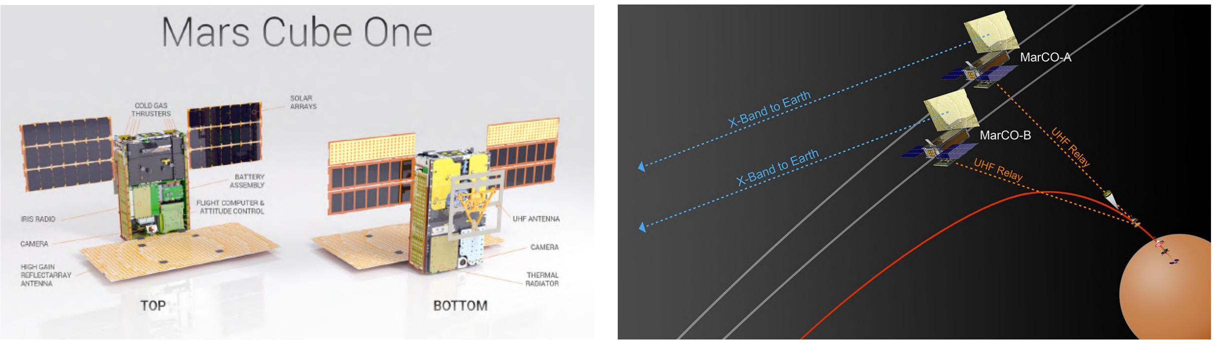

(a) MarCO details

(b) Mission illustration

Figure 2.7: (a) MarCO CubeSats schematic detailing the on-board scientific units. Credit: NASA/JPL-Caltech (b) Mission illustration presenting the communication links to support the entry, descent and landing (EDL) phase of perseverance and to deliver data to Earth. Credit: NASA

along with some control issues. Moreover, the brightness sensors that allow the CubeSats to stay pointed at the Sun and recharge their batteries could have been another failure point. However, as claimed in [43], the mission was always about pushing the limits of miniaturized technology and seeing just how far it could have taken. MarCO satellites demonstrated to be capable of orbiting and transmitting/receiving signals. Future versions are expected to go farther in advanced radio system experimentation.
The Mars Perseverance rover started its operations in 2021 (see Fig.2.6b). Despite being the most complex scientific machine ever launched on Mars, its brightest achievement was the first powered flight of a UAV, the so-called Mars Helicopter Scout (MHS) or “Ingenuity”, in a world beyond Earth. The MHS is capable of flying over a distance of $\approx$ 300m at a height of $\approx$ 4.6m for no more than 90s, consuming 350W and taking 24hours to re-charge its batteries through solar panels [44]. Of particular interest is the 33rd flight of the MHS, during which a small foreign object debris (FOD) was seen to be attached for a while, before drifting away, to an MHS leg [45]. Even though the MHS was meant as a mere demonstration, it left the clear awareness that envisioning other UAVs on Mars, characterized by an augmented efficiency, an increased flight time and equipped with considerable complex payload and radio resources to absolve scientific objectives, could be a realistic opportunity to support future manned missions [46].
Indeed, the preliminary concepts of the next Martian UAV has already been presented in [47]. The Mars Science Helicopter (MSH), depicted in

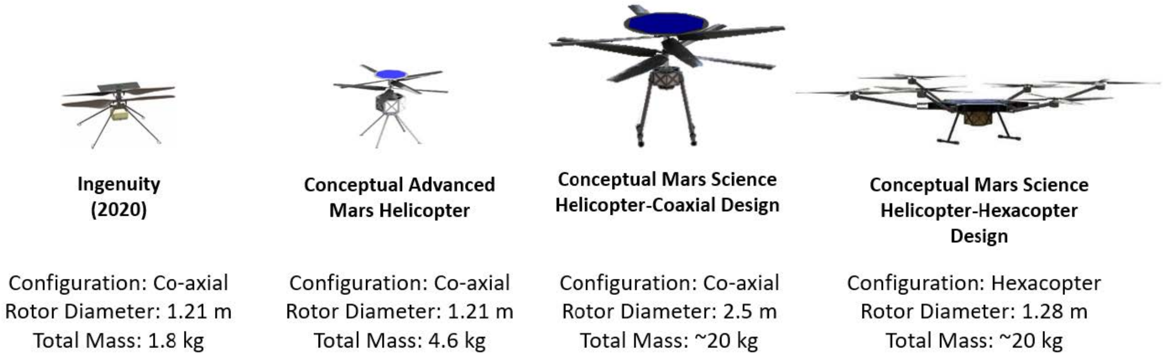

Figure 2.8: Research progress on future payload-equipped UAVs to be deployed on Mars. Credit: [49]

Fig.2.8, would be released by a mid-air helicopter delivery (MAHD) [48]. The MAHD would complete the EDL phase and release the rotorcraft, equipped with a jetpack, in mid-air. The jetpack should detach after having stabilized the MSH. At the end, the MSH would land on Mars. This approach is key to increase the stowed volume to accommodate larger rotors, that means higher lift capabilities. Thus, the MSH is designed to host a $2-5$kg payload, assuring $\approx$ 7mins of flight time [47]. This is a noticeable step ahead with respect to the MHS.

Lastly, this decade will see other probes and machines on the Martian orbit and surface, like the Martian Moons Exploration (MMX) probe from the Japan Aerospace Exploration Agency (JAXA), whose launch should happen in 2025 and that is aimed at landing on Phobos, collecting samples and delivering them to Earth in 2029.

Again, private companies, which are more free from restrictions of public companies, are dreaming about reaching Mars with some space travels before the 30s of this century. SpaceX realized the “Falcon 9” and “Starship” launch vehicles, which are and will be the first ever partially/completely, respectively, reusable spacecraft for beyond Earth missions [50]. A potential new business might even arise from these lofty utopian aspirations, as partially demonstrated from Blue Origin, for instance, having just brought tourists outside the Kármán line to experiment the zero gravity [51].

Chapter 3

The Current Picture of Martian Connectivity versus New Trends of Non Terrestrial Networks

Hereinafter, we take a snapshot of the state-of-the-art dealing with Martian communications. The discussion will move from proposed surface (sect.3.1) and space (sect.3.2) infrastructures for Martian connectivity to algorithms for deriving Martian channel models (sect.3.3), thus understanding the RF propagation on the planet. Later on, in sect.3.4, NTN networks and 3D Networks, C-RAN infrastructures and functional splits opportunities for terrestrial applications will be widely reviewed, as well as solutions for designing a long-haul linking Mars and Earth in sect.3.5.
This part of the thesis is partly retrieved from published journals and conference papers [1].

3.1 On-Ground Martian Communications

VERY few works deal with providing connectivity over the Martian surface and, most of them, only consider the presence of unmanned vehicles and unmanned sensors. Pucci et al. in [52] studied the performance of a network based on IEEE 802.15.4 standard. The Wireless Sensor Network (WSN) transmission is simulated under an empirically-modelled Martian channel. The flat region is represented by a Ricean channel, while, the rocky region is modelled as a Rayleigh channel. Moreover, large-scale attenuation phenomena (path loss, shadowing, attenuation due to dust storms) are modelled upon terrestrial criteria. For instance, a 3rd order

---

[1] Part of this chapter appears in [193, 197, 199, 201, 202]

path loss exponent is considered, that is typical of terrestrial rocky terrains. On the other hand, in [53], Daga et al. analyzed the IEEE 802.11a and b wireless local area network (WLAN) standards under the Martian propagation conditions of Gusev crater and Meridian Planum. In order to realistically simulate the performance of the standards, they expanded the work done in [54], where the authors exploited the digital elevation model (DEM) of the Gusev crater and Meridian planum with a resolution of 11m/px as input for a proprietary ray-tracing software, in order to derive a realistic channel model for the S-band. In [53] and [54], the values of the received power are given for a variety of distances between TX and RX. Although this work is very solid, it does not provide a replicable channel model able to analyze the propagation impairments occurring on different regions of the Martian surface and for different carrier frequencies. We will better dig into it in sect3.3. In [55], Hong et al. investigate the energy consumption of Mars sensor networks, considering multi-hop *ad-hoc* setups connecting the sensors to the rovers. Another work lists the challenges of proximity WSNs operating on Mars and suggests new strategies based on Delay Tolerant Network (DTN) concepts in order to implement intelligent and adaptive network protocols able at operating autonomously on Mars [56] . Other studies evaluate the performance of a network composed of tumbleweed rovers propelled by wind and able to collect and share environmental data [57]. Such a solution is proposed for two working frequencies, i.e. $f = 400$MHz and $f = 2.4$GHz, considering a transmit power of 100mW. It shows that, while for low data rates the probability of data loss, due for example to dust storms, is relatively acceptable, for the S-band, there is a 99% of probability of missing the link. This means that such an infrastructure cannot provide a reliable wideband connection.

3.2 Space Architectures for Martian Communications

As claimed in [58], it is expected that future Martian communications will be supported also by a stationary-orbit relay satellite. Stationary orbits around Mars, known as areostationary orbits (AEO), have similar characteristics as Earth's geostationary orbits. The AEO satellite is located at 17000km above the surface and is always in the same place with respect to the sky. Thus, it can receive data from the rovers and landers, LMO orbiters and CubeSats in the vicinity of Mars, providing relay to an Earth station or working as backbone for *in-situ* surface networks. In

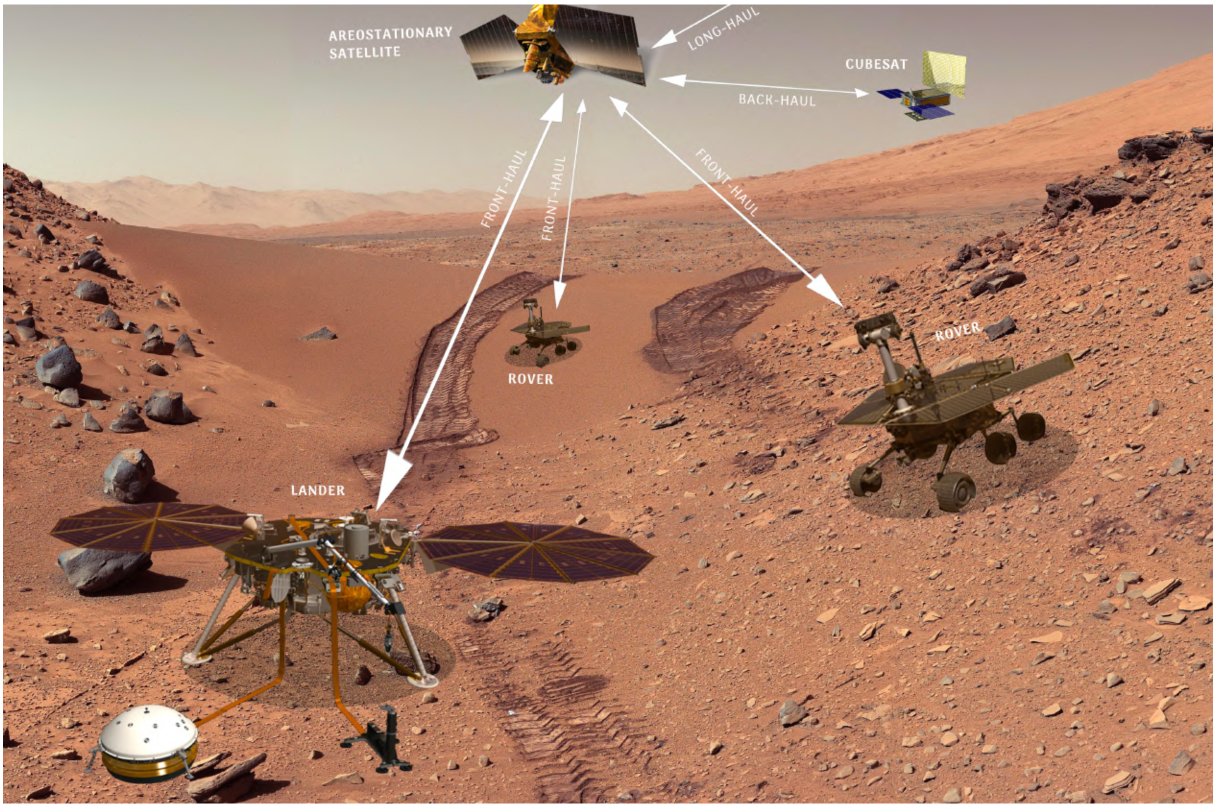

Figure 3.1: Snapshot of the current Martian communications among orbiting and surface devices. Inspired by: [58]

Fig.3.1, the picture of a (kind of) current scenario of Martian communications is drawn, as pictured also from Babuscia et al. in [58]. Instead, in a near-future scenario, CubeSats and orbiters could form a “sky layer” of a Martian network, that could work as relay and backbone for the rovers and the landers staying on the planet surface.
Again, it is expected that some communication payloads will orbit around Mars at different altitudes. These payloads are an obvious candidate to support future Martian connectivity with autonomy from Earth. A conceptual design of satellite-based Martian networking has been presented by Bell, Cesarone et al. in [59], where the overall infrastructure is pictorially represented in Fig.3.2a. The in-flight element of the network are an AEO satellite and a constellation of low-altitude microsatellites, these last regarded as the proximity connectivity providers for integrated navigation and communication services to Martian vehicles and human crews (the AEO satellite is used for back-haul of Martian nodes and long-haul to Earth). The microsatellites of [59] were targeted to 800km altitude, near

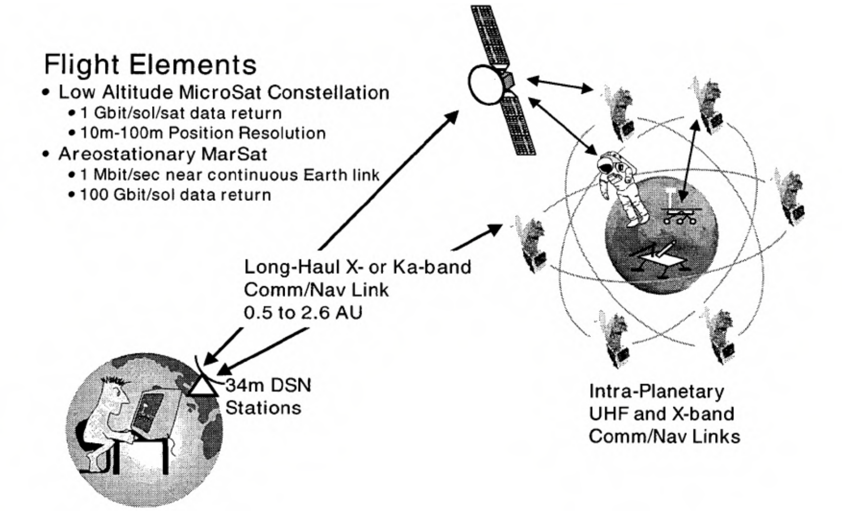

(a) Full-Satellite Martian Connectivity

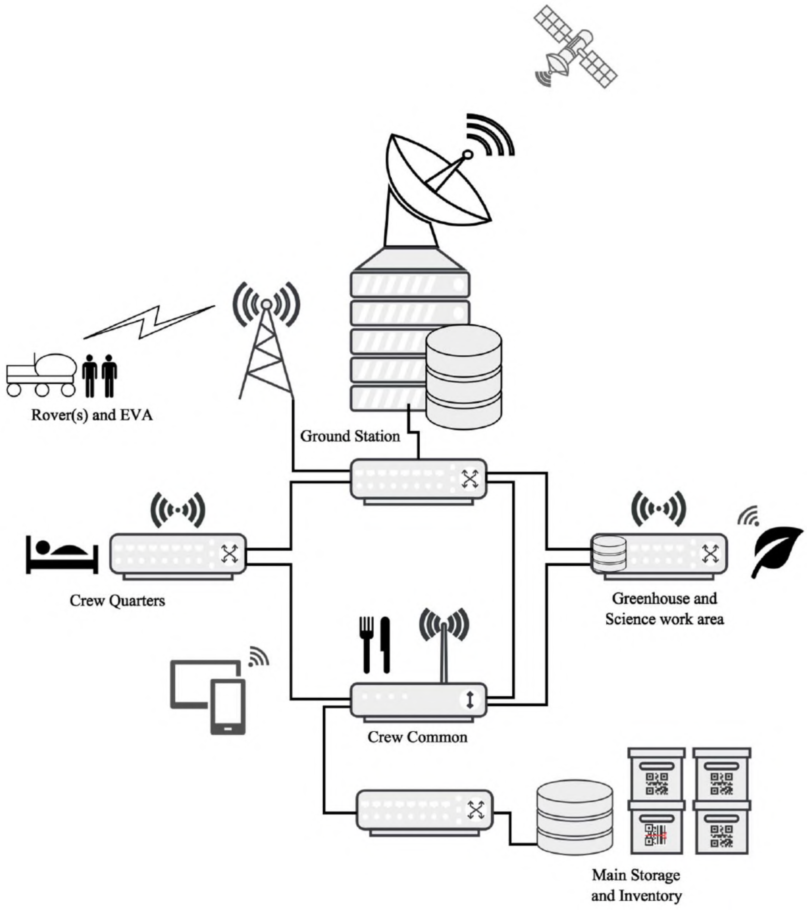

(b) Martian Network Topology

Figure 3.2: (a) Full-satellite based Martian infrastructure proposed by Bell at al. to achieve narrowband communications. Credit: [59] (b) Trans-planetary network topology proposed by Hill and Gagneja to interconnect devices, human personnel on Mars and Earth. Credit: [60]

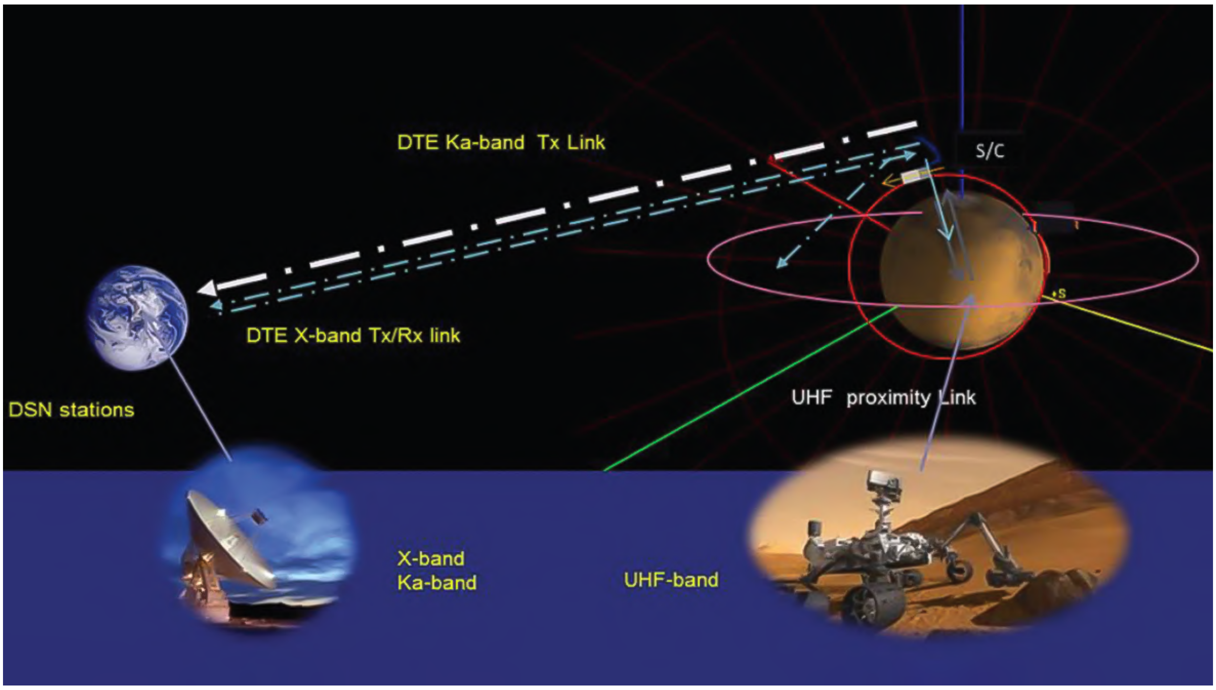

Figure 3.3: Architecture of a Martian communication system based on the Mars Reconnaissance Orbiter (MRO) as master network node. Credit: [61].

equatorial and high-inclination orbits. The constellation was designed to return 1Gbit per Sol, using 1W power and omnidirectional antennas. The reference bandwidths for transmission are UHF and X-band. The actual bit rate of such satellite connections is about 11.3Kbps, which is good to support voice, sensor data and localization data transmission.

A recent work dealing with satellite-based Martian connectivity [61] considers the use of Mars Reconnaissance Orbiter (MRO) as the space node providing both proximity link and relay to Earth. The related architecture, shown in Fig.3.3, looks simpler as compared to that of Fig.3.1 and easier to be managed. Data rate up to 2Mbps can be achieved by the MRO-rover link. The presence of astronauts on the Martian soil has not been considered in [61].

Authors of [60] (see Fig.3.2b) presented a more futuristic project for future Martian connectivity. In this paper, a physical network topology is described consisting of a high power ground station to communicate with orbiters. The ground station is then connected through a local wireless network to the manned installations on Mars. The units or habitats have Internet-like connections. Each of them has its own IPv6 router or switch, connected by Ethernet to multiple neighbors behind wall panels.

An additional wireless network connects wireless devices (usually personal crew devices, but may also include sensors) to the network. This 802.11 service is provided by access points from three routers opposite of each other [60]. The network configuration is clearly inspired by similar terrestrial satellite-based networks bringing connectivity to small buildings for indoor interactive TV or Internet services. Indeed, such an arrangement has been proposed for a future Mars science station, where the mobility is essentially of a nomadic kind.

3.3 Early Studies of Radio-Frequency Propagation Modelling on Mars

The literature is quite rich when dealing with the topic of RF propagation on Earth, along with all the analysis on attenuation which negatively affect the performance of communication systems at the physical (PHY)-layer side. Unfortunately, we cannot say the same for what concerns wireless communications on Mars. However, there are few pieces of research that have faced the problem.

The early works found in the state-of-the-art, which analyze the multipath propagation over some precise Martian locations, such as the Meridiani Planum - where the Mars Exploration Rover (MER) "Opportunity" landed to find evidence of liquid water in 2004 [62] - and the Gusev crater, which is probably an ancient lake [63] - where the second rover of the Mars Exploration Rover mission called "Spirit" landed, are the ones in [54] and [53]. The authors of [54], as well as the ones of [53], exploited the ICS telecom, a proprietary software by ATDI [64]. As we know, the environment, in which a communication occurs, sensibly affects the RF transmission, indeed, the objects in the middle of the path between TX and RX, which can move with a certain velocity, create reflections of the signal, thus multiple paths characterized by an intrinsic delay due to the increased distance with respect to the LOS. This brief explanation almost covers the so-called small-scale phenomena, i.e. multi-path propagation and Doppler effect, which is a frequency shift due to the motion of the transceiver.

Through the Longley-Rice, or also called “Irregular Terrain Model” (ITM), they presented few samples of received power and delay spread of simulated RF transmissions in the S-band ($f = 2.4$GHz). They considered DEMs of the two landing sites of the Mars Exploration Rover (MER) missions with a resolution of 11m/px. The results in [54] exhibit power delay profiles (PDP) for various distances in between the transceiver. For a 100m transmission, the 92% of the computed RMS delay spread values are lower than 0.72μs with the RMS maximum delay spread around 0.75μs, which on Earth can be compared to the delay spread experienced on an urban area [65]. As expected, by increasing the distance to 1000m, the percentage of RMS delay spread values below 0.72μs decreases to 72%, while the maximum RMS delay significantly increases to 3.08μs, which on Earth it could represent a mountainous area. Daga et al. in [53] concentrate more on the testing of the IEEE 802.11a and b PHY-layer over the MER landing areas. However, they presented also some more results regarding possible Martian PDPs, introducing also the 5GHz working frequency, by basically exploiting the methodology in [54].

It is interesting to see that, besides the fact that most of the time the received power and RMS delay spread values, respectively, decrease and increase with higher distances, some favorable terrain conditions lead to a Fresnel zone clearance, thus to better transmission conditions, i.e. higher received power and lower RMS delay spread.

These works probably lack in the description of the model, indeed, the arrangement used in order to estimate the PDPs is not detailed enough to be replicable. Moreover, the ITM, which is a radio propagation model that makes predictions on the signal attenuation expressed as a function of distance, exhibits shortcomings when dealing with knife-edge obstacles obstructing the propagation [66]. To conclude, the number of samples shown in both works does not allow to approximate realistic Martian channels, neither to understand the behavior of the so-called large-scale phenomena.

For what concerns large-scale phenomena, we can individuate terms that steady decrease the power of an RF signal (path loss), due to the distance between TX and RX, which fluctuates around the mean (shadowing) because of reflections and scattering during the transmission. To the best of authors' knowledge, in the literature we can find only a couple of works exposing such a topic for simulation purposes. To be precise in [67] and [52], where the small-scale phenomena are treated by representing a flat Martian area with a Ricean channel (LOS environment) and a rocky area with a Rayleigh channel (NLOS environment), the path loss is computed by assigning a 3^{rd} order exponent to the common free-space path loss (FPSL) in order to approximate for highly scatterers terrains (as seen before in sect.3.1). On the other hand, this evaluation is mostly empirical, thus it is difficult to know if this approximation could fit a Martian area, and if so,

which Martian area.
Even the atmosphere negatively impacts on the propagation of the signal by attenuating the received power. This happens mostly in the extremely high frequency (EHF)-band, indeed, at this level the wavelength of an EHF signal is comparable to the dimension of the molecules and elements composing the atmosphere. The “collision” between these two parties generates scattering and absorption, which causes attenuation [68]. As well as the atmosphere, dust storms, which are really frequent on the surface of Mars, and even clouds and fogs can act as attenuators. This is well explained in [69]. As reported, the troposphere, i.e. low atmosphere, is the main agent on the degradation of the RF signal. Furthermore, for high frequencies ($f > 10$GHz), it should be considered the attenuation due to clouds and fogs, which is not negligible. The last actor to be considered is the attenuation due to dust storms. As commonly known, they are remarkable features of the Martian surface, indeed, they were documented since the beginning of Mars explorations in the 60s [70]. Most of the spacecrafts and rovers sent to the "Red Planet" noticed such an event, which is really frequent in spring and summer. Dust clouds arise from the surface producing walls of sand with a spatial dimension that ranges between few kilometers to more than 2000km to even more, which creates a global dust storm encircling the whole planet. This can have a strong impact on RF propagation. From [70], the worst case, fixing a 10km dust storm, can reduce the received power of 3dBW for a 32GHz signal.

3.4 Non Terrestrial Networks for “5G & Beyond” Connectivity

While on Mars the only forms of current connectivity are satellite-based, in the last ten years, or so, mobile standards represented the main pillar of the terrestrial broadband connectivity. We passed from First Generation (1G) technologies with analog audio signals and Second Generation (2G) ones characterized by digital transmissions to Fifth Generation (5G) networks, whose global distribution started around 2019 [71]. This rapid evolution shed a new light on all the working fields, thus generating useful connected services to the areas inherent with the education and finance, politics and health, entertainment and environment protection. The technical and engineered innovations were numerous since the beginning of mobile standards and led to an exponential increase of supported data rates, reductions of delays, computational and energy resources optimization, and a general huge improvement of network reliability, maintainability and availability (RMA). However, there are still under-served or poorly-served regions, as well as other use-cases that we will treat in a while, demanding ubiquitous and continuous access to the network [18]. The reasons are manifold: low population density for harsh, disaster-hit, under-war environment, thus low income-generating opportunities, and a general poverty of people living in low- and middle-income countries (LMIC), thus less mobile internet usage, are just some of them.

To this aim, 3GPP started many Study Items (SI) to investigate inclusion of NTN into the 5G NR. For instance, 3GPP Release 15 mentioned the integration of NTN in the 5G NR standard. Hence, 3GPP, other organizations, academic researchers and companies are now looking towards the standardization of “5G & Beyond” (B5G) - sometimes called 5G Advanced (5G-A).

Even though, B5G will interface satellite networks with the mobile ones, on the long run, the goal is a perfect unification of NTN with common terrestrial networks (TN), as depicted in Fig.3.4a, to create a ground-to-space ecosystem. This would probably be one of the key enablers of next Sixth Generation (6G) technologies. The expected benefits are manifold. Guidotti et al. clearly outlined most of them [19]: serve users in under-served areas, serve users maintaining the needed QoS by off-loading traffic from a saturated on-ground network to the NTN, substitute failed TN due to natural disasters or malicious physical/cyber attacks, assure global coverage for narrowband IoT (NB-IoT) or enhanced machine-type communication (eMTC).

Now, if we consider single-layer NTN, they will be made by LEO constellations of satellites, most probably CubeSats. In this regard, authors in [73] supposed to extend broadband coverage of LTE networks through mega LEO constellations, where the satellites act as transparent regenerator for both an on-ground RN to Donor eNodeB, placed at the gateway, and an on-ground eNodeB to Evolved Packet Core (EPC) link. In line with this vision, Kodheli et al. considered the same architecture within the 5G NR standard [74].

NTN can be enlarged to embrace even more services if we take advantage from UAVs and HAPSs in the aerial segment, thus layering the network, and adding more constellations into various LEO or Medium Earth Orbit

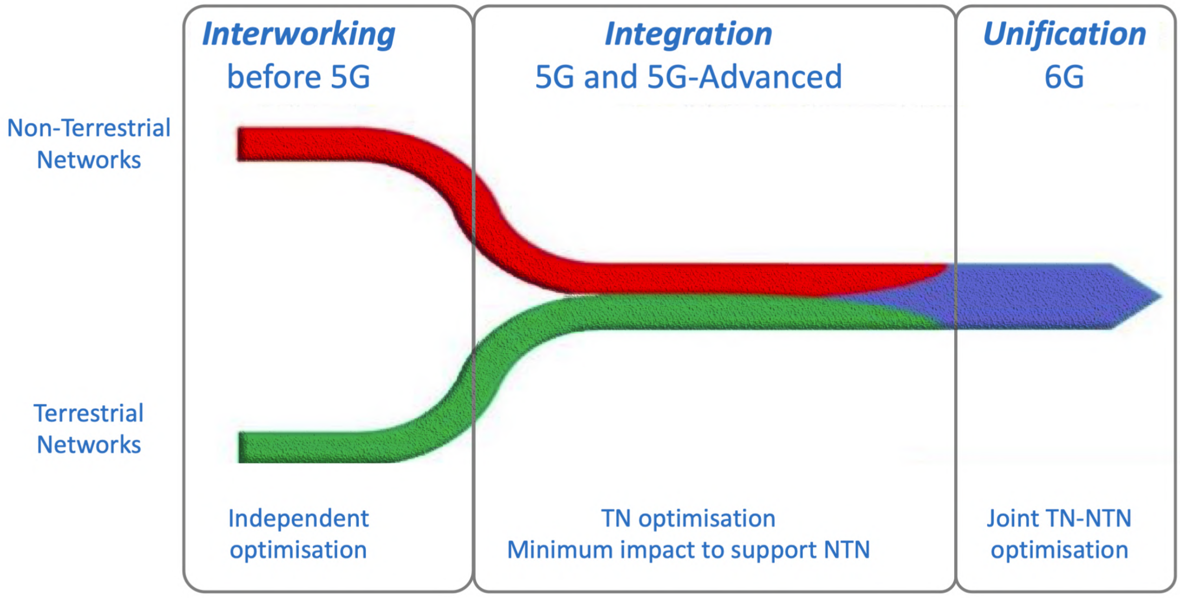

(a) Road to 6G

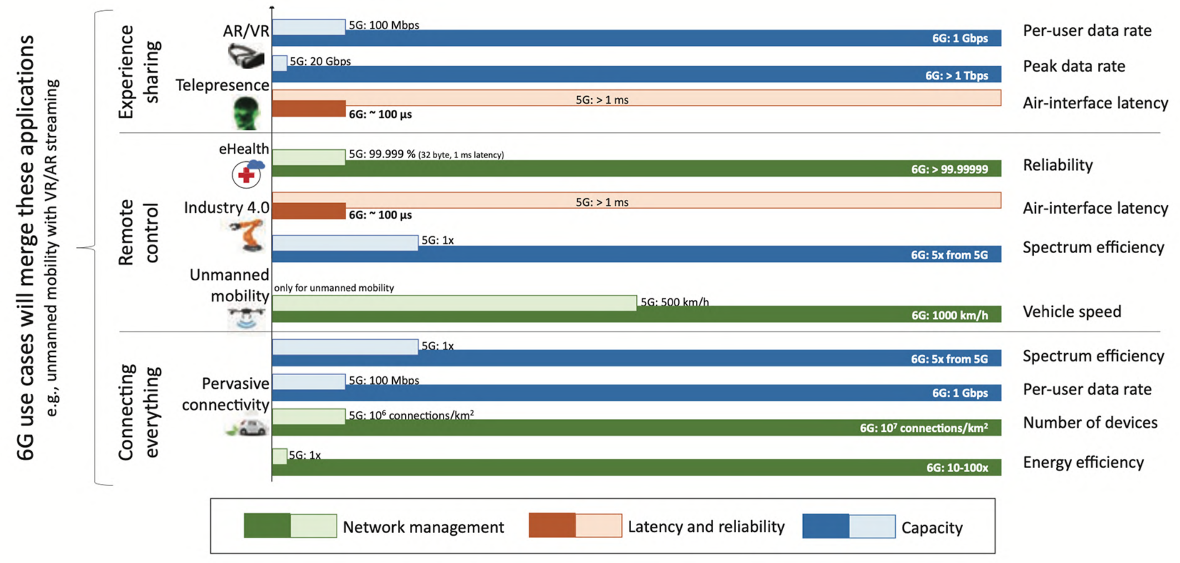

(b) 6G KPI and use-cases

Figure 3.4: (a) The 6G enabling vision expects TN to exactly dovetail NTN, thus constituting an autonomous ground-to-space ecosystem. Credit: [19] (b) 6G KPI compared to 5G ones. Several applications will be merged due to a renewed spectrum of use-cases. Credit: [72]

(MEO) altitudes as well as geostationary orbit (GEO) satellites. Authors in [75] define the most important features of ML NTN, meaning UAVs and HAPSs. Drones are flexible devices, which allow instantiating and deploying a network on-demand. HAPS, like airships, are huger flying nodes, which being at a higher height can cover wider areas for a longer service duration. However, NTNs are quite recent, and the literature has still to be widened to pave the way to a joint TN-NTN architecture. Very few works deal with design and performance evaluation of NTN. In [76], a link budget methodology is proposed to assure certain system level performance. Moreover, it is still not clear how NTN's layers should operate, which function should be processed at which node, and if it will be feasible to allocate the BBU load on small satellite platforms, when they are not acting as transparent RNs. For these reasons, functional splits are interesting concepts for enabling network function virtualization (NFV) on (ML) NTN. Let us deep down the knowledge about them.

3.4.1 Functional splits for network function virtualization: applications to "5G & Beyond" scenarios

Network function splitting and decomposition provide maximum flexibility for a distributed deployment of network functions, which was previously designed as a cumbersome monolithic system (see Fig.3.5). Splitting enables the monolithic system to be decoupled into sub-functions that can be designed as microservice or multi-agents. These smaller units can be deployed in distributed environments such as fog or edge or cloud-based computational resource provisioning environments. A recently published article in [78] proposed a multi-objective-based network function splitting considering 5G networks with a particular focus on network slicing. Focusing on different perspectives of a functional split between the radio access points and the edge/cloud platform, they presented a mixed integer quadratically constrained programming (MIQCP) framework for efficient placement of virtualized network functions (NVF) chains in future 5G systems. The authors detailed a deep performance analysis of split points between central cloud and distributed radio units. The work is mainly focused on the theoretical discussion of function splitting for 5G systems. In [79], a network function splitting and migration for SDN controller load balancing and overhead reduction is shown. Similarly, a micro-service-based full decomposition and containerization of SDN controller are dis-

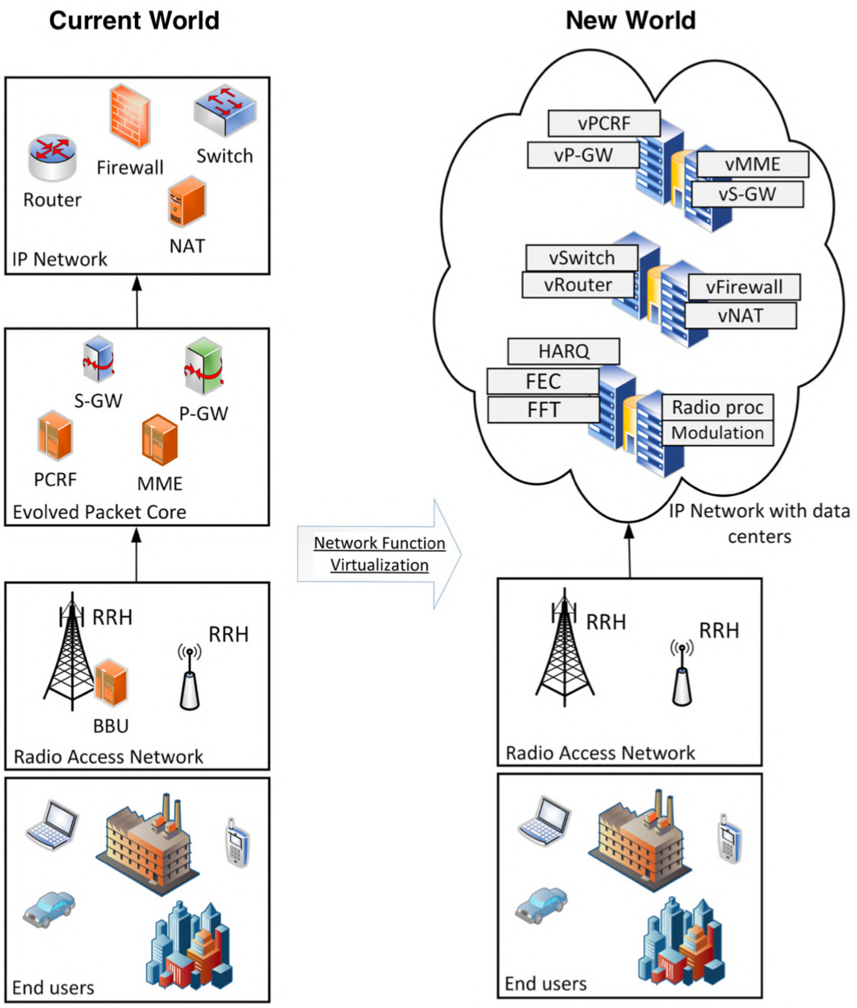

Figure 3.5: Transition to the newest network infrastructures is enabled by network function virtualization. Credit: [77]

cussed in [80]. The authors provided a decomposition framework for the design performance evaluation of a micro-service-based SDN controller. However, the authors did not consider a distributed and resource-constrained environment, which may affect the deployment of decomposed functions. The application of artificial intelligence (AI) for function splitting has also been studied. In [81] the authors discussed a deep reinforcement optimization for a virtualized radio access network function splitting. The author discussed how to optimize the exact placement and location of the decomposed RAN functions by developing a learning paradigm. The problem of placing functions either in a central (cloud) or a distributed environment is formulated to minimize the total network cost using constrained neural combinatorial reinforcement learning. The discussion is primarily on where to place functions in classic edge/fog versus cloud-based environment.

The work in [82] presented another complete decomposition of a monolithic network system towards achieving a zero-touch autonomous network. They used a multi-agent approach for service design. They proposed the functions to be designed as an atomic unit with autonomous capability of the smallest function. Using these units, which are agents, as a building, a fully autonomous network management system could be designed. The work in [83] is another interesting approach to virtual network function splitting.

Functional decomposition has a greater advantage in terms of flexibility, modularity, simplification of cellular sites, and improved coordination with a migration towards v-RAN. However, the classic back-haul network would not support the improvement required by 5G. Therefore, in 5G we are witnessing a transition from back-haul (including front-haul, mid-haul and back-haul) to xhaul to improve 4G's mobile back-haul considering higher data rates, lower latency, hard isolated slices, higher reliability, and dynamic connectivity targeting on-demand services, which consists of multiple physical and/or virtual components. To this aim, by exploiting splitting concepts, an E2E slicing to create a protected and dedicated path is shown in [84]. The proposed technique is to minimize the physical resource required for a given network slice. It provides reliability, improving a single node/link failure.

As a use-case analysis, the work in [85] presented a 5G network connectivity between the drone and the ground control station dimensioning the latency for ultra-reliable low latency (URLLC) applications with limited analysis for resource availability and energy consummation.

Returning to ML NTN, Bassoli et al. [86] preliminary formulated a ML or 3D Network for a border monitoring application divided into four main segments: sensors and peripherals on-ground acquiring data, fleets of hovering UAVs providing network resources and other cameras for monitoring, constellation of LEO CubeSats virtualizing network functionalities and a back-haul to the cloud or core network.

In particular, the Dynamic Architecture based on UAVs Monitoring for border Security and Safety (DAVOSS) project proposes the use of low-orbit CubeSats and hovering UAVs as host for the remote LTE BBU processing, which is divided thanks to a "Split D" operation [191, 192]. The DAVOSS logic diagram and the developed simulator are shown in Fig.3.6.

Such a solution is motivated by the favorable trade-off between reduced implementation and launch costs, flexibility and efficiency exhibited by these communication payloads. In the recent past, CubeSats hosting powerful CPU units for image processing have been successfully launched in orbit [87]. Therefore, nothing seriously hinders the installation on board of dedicated processors for BBU virtualization. Moreover, thanks to their low orbital altitude (ranging from 150 to 500km), CubeSats are characterized by another favorable trade-off between reduced latency and satisfactory visibility [88]. This last feature should allow coping with the stringent latency requirements of BBU splitting [192].

3.5 Technologies and Infrastructures for Mars-to-Earth Data Delivery

A preliminary study, which dates back to the early stage of this decade, predicted to 950Exabytes (EB) of newly-created data to be exchanged to Mars within 2050, leading to a data rate R_b of 30.1Tbps [89]. Due to the tremendous data rate size, still in [89], the author suggested creating a mirror database on Mars of the surface web by sending just 31.7 Petabytes (PB), which translates into a data rate R_b = 8Gbps. This assumption seems reasonable, even though such a prediction should be upward corrected given the unexpected augment of internet services happened during the 10s of this century. The Mars Laser Communications Demonstration (MLCD) was the first attempt made by NASA's Goddard Space Flight Center (GSFC), the Jet Propulsion Laboratory (JPL) and the Massachusetts Institute of Technology Lincoln Laboratory (MIT/LL) to forward a high amount of data from Mars to Earth through an optical free space link [90]. Back then, that project highlighted many challenges to be faced, indeed the power available was considered to be enough to transmit just 100bps. Since then, much advancement has been able to push the technological boundaries of optical communications.

In 2011, optical links were supposed both to exchange data between Mars and Earth and to interface machines on Martian ground to orbiters on orbit [89] [91]. In particular in [89], a precise link budget evaluation, done to transfer $R_b = 10Gbps$, was carried out. It seems also fascinating the idea of clusterizing the satellite system into one satellite exclusively dedicated to acquisition, tracking and pointing functions for the laser beams and another one gathering energy through solar panels, storing and process-

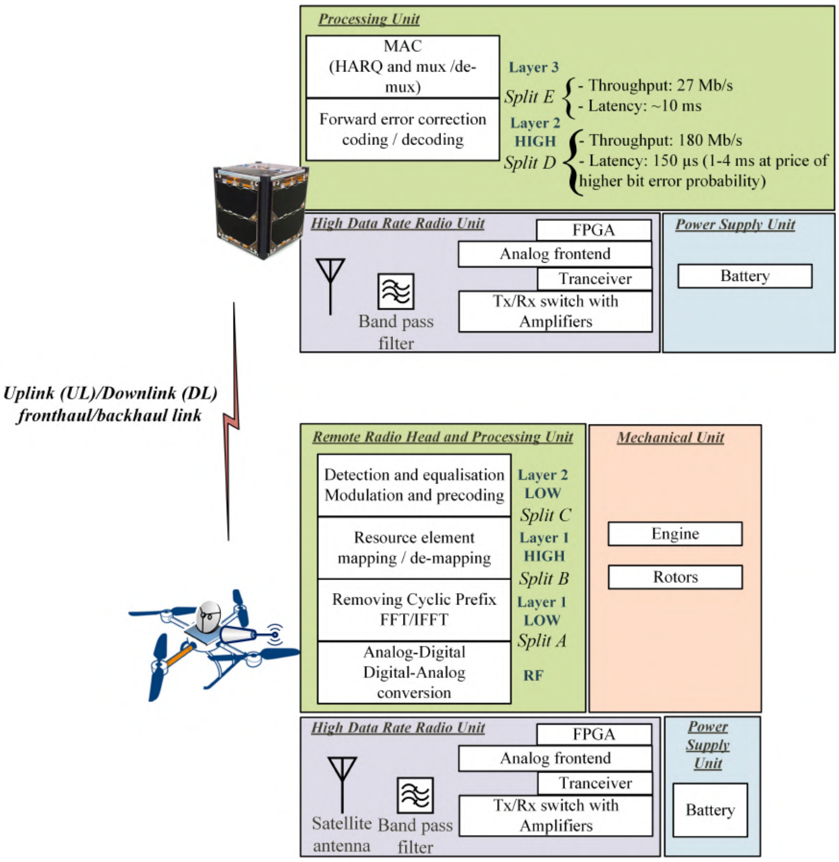

(a) DAVOSS Diagram

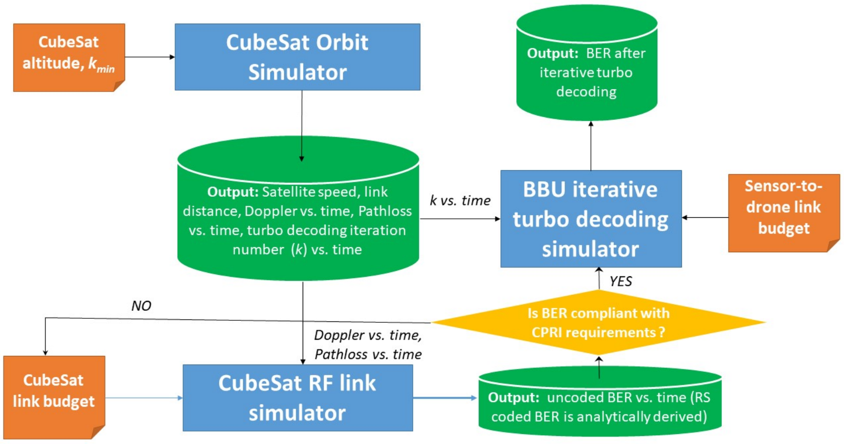

(b) DAVOSS Simulator

Figure 3.6: (a) The DAVOSS diagram shows a CubeSat and a UAV splitting BBU functionalities to provide on-ground connectivity. Credit: [191] (b) The DAVOSS simulator is comprehensive of interconnected MATLAB scripts and Simulink models for the system evaluation. Credit: [192]

ing signals and communicating with other relays in the deep space. Still in [89], the use of terrestrial Lagrangian points was suggested to eventually get rid of the Sun interference, that could be a background noise source of interference for optical systems.

Analysis related to the exploitation of Lagrangian points as “parking lots” for orbiters to relay data from Mars to Earth are quite recent. As per the state-of-the-art, they start with the work proposed by Malcolm Macdonald et al., who defined non-Keplerian orbits around the LPs to move orbiters in those unstable points that need propulsion force to perform station-keeping [92]. Then, the topology of a network constructed upon the LPs L4 and L5 of the Earth-Sun (E-S) system is presented in [93]. Through the 0-1 programming model constrained by total minimum throughput and connection time and having throughput as objective function, the authors created knowledge useful to select the proper routing strategies for such interplanetary networks [93]. Something more has been added to the work in [94], where the authors geometrically studied a relay network built upon many LPs findable in the Solar System. Some of them are related to the Moon-Earth system. However, here just delays considerations are raised, while E2E performance is not detailed.

Part II

Research and Innovation

Chapter 4

Long Term Evolution Porting: Extraterrestrial Mobile Connectivity

This fourth chapter opens the methodological storytelling of the set of solutions designed and developed to assure connectivity on the Martian surface, namely: Next Generation Communications on Mars (NGC-M). We will start with a brief frame introducing the scenario and motivations, then we will move on to sect.4.2 with the system description regarding the LTE porting on Mars. After that, in sect.4.3 and sect.4.4, a deepened overview on the LTE radio interface and channel modelling will be given. Sect.4.5 will analyze the results regarding the link performance and budget for system calibration. To conclude, sect.4.6 will resume the chapter, while highlighting advantages and drawbacks discovered throughout the work.
This part of the thesis is partly retrieved from published conference papers [1].

4.1 Scenario and Further Motivations

SPACE exploration has been advancing more and more lately, however, much has to be done for paving the way to a human long journey to discover Mars. As a matter of fact, space agencies brought machines on the planet surface, instead of humans, to reduce overall costs and risks. Still, as extensively discussed in sect.1.1, the final turning point for space explorations will be to set a human settlement on Mars. Thus, some sort of Martian connectivity is essential. Real-time communications between crew members, the exchange of post-processed data in the form of image, audio, video and distress calls require a robust and flexible network in-

---

[1] Part of this chapter appears in [190, 193]

frastructure to be deployed on the "Red Planet". To this aim, machines, somehow easily deployable, could be re-allocated to serve as access to a Martian network.

Rovers are small vehicles that collect different type of information, mostly geology and astrobiology-related data, in order to seek signs of past or present life. Their equipment is various, made of sensors, cameras, radars, drills and many others. For instance, Perseverance embarks the Mars Oxygen In-Situ Resource Utilization Experiment (MOXIE) tool for investigating the production of 02 from C02 on Mars. But beyond that, all these machines host radio and processing resources, solar panels, batteries and other (nuclear) power systems. The same does landers, even though they are usually bigger, with higher resource availability, and fixed on-ground, thus not having motion capabilities. For this reason, seeing landers as BS of a local network cell seems reasonable and heuristically practicable. Hereinafter, supposing bidirectional information exchange on the Martian surface, we propose an embryo of a mobile networking infrastructure operating on Mars, namely Extraterrestrial Long Term Evolution (E-LTE)[2]. The landers are treated as the eNodeB and the rovers represent the end-users, or UEs. The so-called E-LTE should support mobile *in-situ* connectivity with higher throughput as compared to conventional solutions for WSN. Moreover, multi-carrier techniques are more suitable to support high data rates than conventional single-carrier solutions or Code-Division Multiple Access (CDMA) solutions. Indeed, LTE and LTE-Advanced (LTE-A) are based on multi-carrier modulations – Orthogonal Frequency Division Multiple Access (OFDMA) for downlink and Single-Carrier Frequency Division Multiple Access (SC-FDMA) for uplink – that guarantee robustness, flexibility and adaptive radio resource management (RRM). The multiple access management, thanks to adaptive radio resource management (RRM), is more efficient than the Carrier Sense Multiple Access with Collision Avoidance (CSMA/CA) of IEEE 802.11a and b, as it allows to easily differentiate the QoS of the various radio terminals involved in the data exchange. The standard LTE uplink transmission, based on Single-Carrier Frequency Division Multiple Access (SC-FDMA) with Localized FDMA (L-FDMA) radio resource allocation, will be tested, but, in addition, it will be compared with the non-standard SC-FDMA using Interleaved-FDMA

---

[2] In 2019, LTE-M has been designed by the 3rd Generation Partnership Project (3GPP) as the acronym for a new narrowband 4G standard supporting Machine-to-Machine (M2M) and Internet-of-Things (IoT) [95]. That is why we introduce Extraterrestrial Long Term Evolution (E-LTE) to substitute the acronym LTE on Mars (LTE-M), that was neologized in our published works

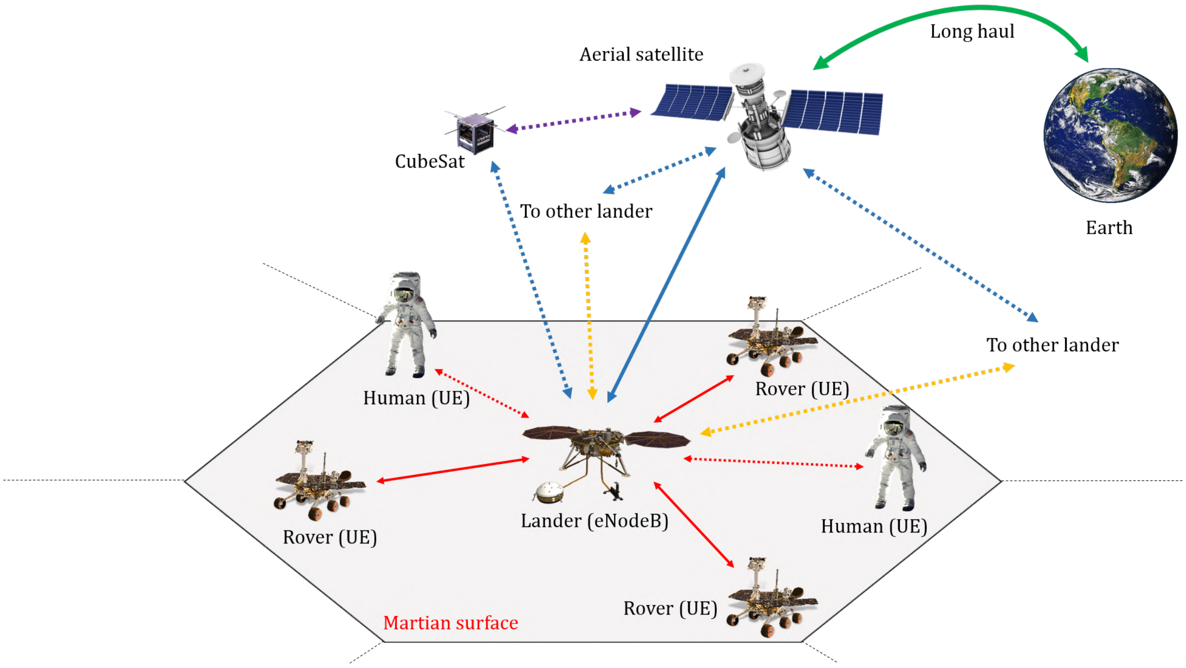

Figure 4.1: Pictorial image of the whole E-LTE infrastructure.

allocation. As compared to L-FDMA, I-FDMA is characterized by augmented robustness against multipath propagation [96], at the cost of an increased complexity of transmitter and receiver. Finally, the link budget and QoS analysis will explicitly consider the presence of turbo coding, typical of LTE standard, evaluating the total useful system capacity, that can be actually reached in the different Martian sites and for different cell dimensions. The outcomes of this analysis will discuss the adaptability of terrestrial LTE to the Martian environment, together with the necessary improvements to be planned for the future, concrete, utilization. We think that a mobile networking infrastructure readily available on Mars would represent a key facility for future manned missions.

4.2 E-LTE System Description

In Fig.4.1, the proposed LTE-based mobile wireless networking infrastructure operating on the Mars surface is shown. The claimed objective of this architecture is to achieve superior capacity and support mobility in data exchange between the vehicles present on Mars and, in the near future, with a human crew.

Rovers, humans and landers exchange information in a Martian communication cell. Landers, as the InSight one, are fed by big solar panels and high capacity batteries, and they are considered to be the eNodeB, or base transceiver station, of the LTE-based network cell, while rovers and, in the future, astronauts will be equipped with reduced-size (and weight) user terminals (UEs). The red lines of Fig.4.1 show the exchange of information between UEs (mounted on the rovers or handled by humans) and the eNodeB installed on the lander. The aerial satellite has been considered for long-haul connection to Earth (green curved arrow) and for the Martian back-haul of lander eNodeBs. Such a solution, directly inspired by [58], is highlighted in Fig.4.1 by the blue lines. Eventually, CubeSats can be considered in order to support Martian back-haul operations (dotted blue line), possibly in conjunction with the aerial satellite (violet dot line). Such a solution would reduce latency and definitely increase network performance. Satellite long-haul and back-haul links may be operated in the X-band, as indicated in [58], or they may consider the use of higher frequency bands like Ka-band or mm-Wave bands in order to exploit the availability of larger spectrum portions. As an alternative to satellite (or orbiter) back-haul, the challenging solution of a direct wireless back-haul between the Martian landers might deserve interest, as it would reduce delays and overall improve the network efficiency. This last option has been depicted in Fig.4.1 by the yellow-dot lines. However, in-band back-haul solutions would subtract precious resources to cellular uplink and downlink, while out-of-band solutions, like the one suggested for terrestrial LTE-A [97], would require additional hardware complexity and increased power consumption to the lander.

Differently than in other published works, data transmission on the Martian surface is entirely and autonomously managed by the LTE-based cell. Thanks to the capabilities of LTE protocols, rovers, landers and, hopefully, humans could exchange information as in a terrestrial mobile network.

4.3 The E-LTE radio interface

The starting point of the radio interface design for the LTE-based Martian mobile transmission system is the terrestrial LTE physical (PHY)-layer solution, based on multi-carrier modulation. OFDMA and, more in general, multi-carrier transmissions represented a step-ahead of terrestrial Fourth

Generation (4G) standard with respect to the previous ones (2G and 3G), all based on single-carrier solutions. The advantages of multi-carrier versus single-carrier in mobile communications are well-known and can be listed as follows [96]:

- *Improved resilience against multipath propagation*: inter-symbol interference can be rejected by inserting a Cyclic Prefix (CP) of proper length. Moreover, single-tap Frequency Domain Equalization (FDE) allows at efficiently counteracting fading effects by spending a modest computational burden.

- *Orthogonal multiple access is allowed*, avoiding the issue of multi-user interference affecting CDMA systems.

- *Flexible RRM enabled*, with controlled QoS for the different users.

The implementation of multi-carrier transmission systems is fully viable in the baseband domain, thanks to the utilization of the Fast Fourier Transform (FFT) digital signal processing tools.
In terrestrial LTE, two distinct multi-carrier techniques are used for uplink and downlink, namely: SC-FDMA and OFDMA respectively. OFDMA is the multi-user version of the Orthogonal Frequency Division Multiplexing (OFDM), where blocks of M orthogonal sub-carriers are allocated to K separated users ($M = N/K$, N being the total number of sub-carriers used for transmission). The block diagram of the OFDMA system used by LTE is shown in Fig.4.2a. The system relies on efficient and robust turbo coding in order to correct channel errors [98]. The choice of M-ary Quadrature Amplitude Modulation (QAM) has been suggested by the augmented robustness of these constellations, as compared to M-ary Phase Shift Keying (PSK), for numbers of levels higher than 4 [99].
Despite the name, SC-FDMA is actually a multi-carrier modulation scheme that, counterintuitively, looks as a single carrier when transmitted onto the channel [96]. The block diagram of the SC-FDMA transmission system used for the terrestrial LTE uplink is reported in Fig.4.2b. The evident difference between OFDMA and SC-FDMA is the presence of the Discrete Fourier Transform (DFT) pre-coding of the M-size information symbol block transmitted by the UE and the dual Inverse DFT (I-DFT) decoding, present at the receiver side. For this reason, SC-FDMA can be regarded as either a DFT-precoded OFDMA or a cyclic-prefixed single-carrier transmission system with orthogonal multiple access managed in the discrete

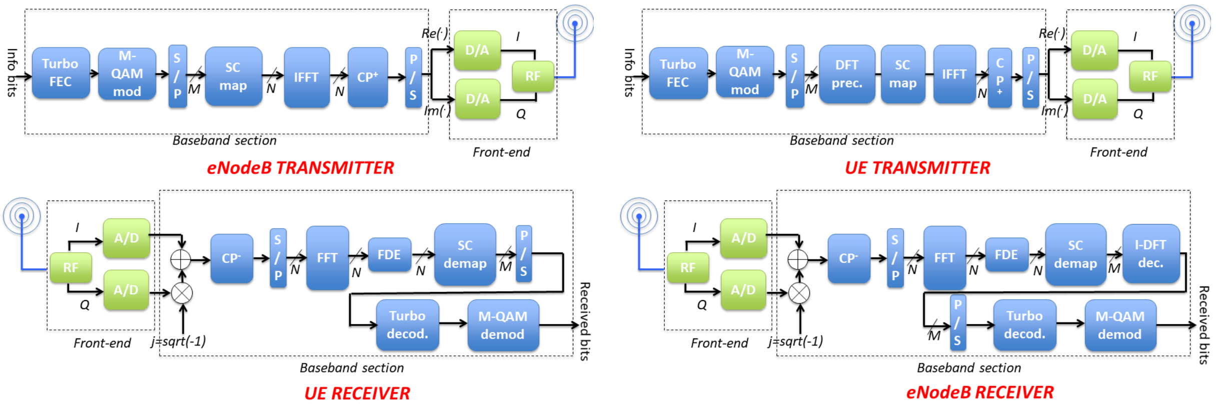

(a) OFDMA radio interface

(b) SC-FDMA radio interface

Figure 4.2: (a) Block diagram of the OFDMA-based radio interface used by the downlink of terrestrial LTE. (b) Block diagram of the SC-FDMA-based radio interface used by the uplink of terrestrial LTE.

frequency domain [96].
In terrestrial networking, the uplink is generally characterized by a power-constrained link budget, because the UE cannot transmit at high RF power due to size, weight and energy consumption constraints. This is the reason why SC-FDMA has been preferred to OFDMA for the LTE uplink. Indeed, as compared to OFDMA, SC-FDMA is characterized by:

- *reduced Peak-to-Average-Power Ratio (PAPR)*. This allows to reduce the amplifier back-off and to exploit better the (scarce) power resources.

- *increased diversity gain due to FDE*. Indeed, the received SC-FDMA signal is, before I-DFT decoding, actually a single-carrier signal. Therefore, the diversity gain is increased, with respect to the OFDMA, by a factor equal to the FFT size N [96].

As experimentally observed in [100], the performance improvement yielded by SC-FDMA is paid by a dramatic increase of the computational complexity required, in particular, for the receiver synchronization. This is the motivation why 3GPP standardization committee considered SC-FDMA only for the uplink.
The uplink multiple access is managed by LTE with Localized FDMA (L-FDMA) sub-carrier allocation. This means that chunks of adjacent sub-carriers of size M are assigned to each of the K users. Such a sub-carrier

allocation strategy is very similar to that of OFDMA.
However, the uplink multiple access might be made more efficient and robust against multipath propagation by using the Interleaved FDMA (I-FDMA) sub-carrier allocation. I-FDMA is based on the interleaving of users' sub-carriers, yielding to a kind of spectrum spreading, for which it is possible to quantify a processing gain equal to K [96]. I-FDMA has not been considered by 3GPP standardization committee for terrestrial uplink, due to its high computational complexity (user signal bandwidth and required TX sampling rate are K times those of L-FDMA). However, I-FDMA might be regarded as a valuable alternative to L-FDMA in Martian applications, as the UEs used on Mars might be not so constrained in terms of size, weight and cost as the terrestrial counterparts.

4.4 Martian Channel Modelling

The communication channel has been modelled by analyzing in detail small-scale and large-scale propagation phenomena occurring on the Martian surface. Like in terrestrial environment, the modality of signal propagation depends, mostly, on the morphology and on the inner electrical properties (permittivity) of the test site. For what concerns our dealing, we considered as Martian test site the Gusev crater. This site corresponds to a crater located at 14.5deg S 175.4deg E and is in the Aeolis quadrangle [101]. The crater is about 166km in diameter and formed approximately 3-4 billion years ago. It was named in honor of Russian astronomer Matvei Gusev (1826-1866) in 1976. Fig 4.3a and 4.3b show two different views of the Gusev crater region. The panoramic view of the region, photographed by Spirit in Fig.4.3a, shows a very vast and only apparently flat area. This first impression is fully confirmed by the landform map of Fig.4.3b, that clearly evidences the presence of climbs and rocky zones.

4.4.1 Analysis and modelling of Martian small-scale propagation

In the UHF bands, the dominant small-scale propagation impairment present on the Martian surface is multipath fading. Other small-scale propagation phenomena, like phase dispersion in the Martian ionosphere occurring during reflections from the Mars surface [102], considerably affect signals transmitted in lower high frequency (HF) band and can be neglected in

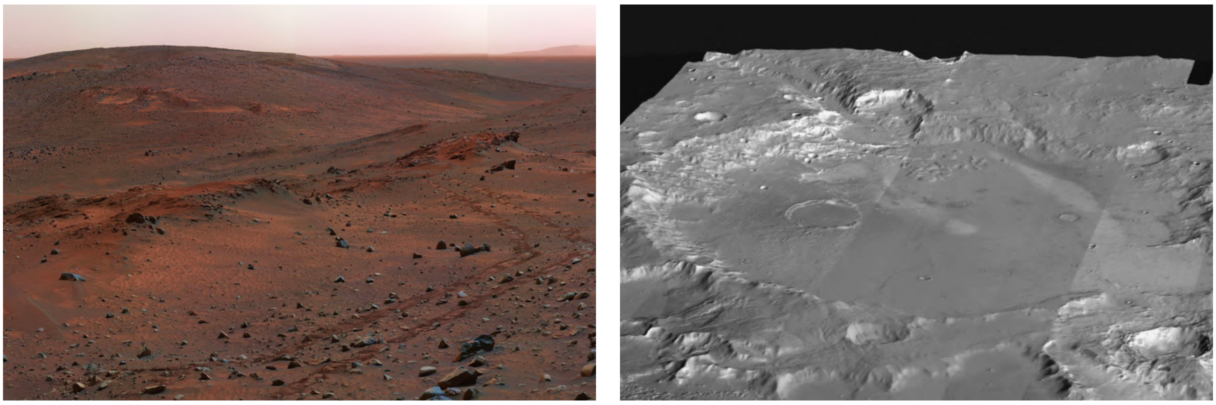

(a) Gusev crater panorama

(b) Gusev crater top view

Figure 4.3: (a) Panoramic view of the Gusev crater region photographed by the rover Spirit. Credit: NASA/JPL (b) Topography data of the Gusev crater from the Mars Global Surveyor. Credit: NASA/JPL-Caltech/Arizona State University

Table 4.1: Root Mean Square (RMS) Delay Spread and Received Power vs. Distance between TX and RX

Distance (m)	Site	RMS Delay Spread (μs)
100	"Gusev1, Site1"	0.155
	"Gusev1, Site3"	0.065
1000	"Gusev1, Site1"	1.864
	"Gusev1, Site3"	0.718

Note: 1W radiated power.

the frequency range considered for our tests.

The multipath channel has been supposed of Rayleigh type. Such a model looks reasonable, at least in the considered scenario, as the rocky terrain, with high climbs, and the low heights of UE antennas seem to reduce the probability of measuring a strong LOS component. This hypothesis, assumed also in [52], can be regarded, at least, as a typical worst-case scenario.

Following the approach suggested by [53], we adopted the usual tapped-delay line model also for the Martian multipath channel. In order to provide a reliable parametrization of such a model for the Gusev crater region, we have considered the values of the RMS delay spread associated to TX-RX distances $d_{TX-RX} = 100$m and $d_{TX-RX} = 1000$m respectively, reported in [53] and shown in Tab.4.1 for the "Gusev1, Site1" and "Gusev1, Site3" areas. In the absence of precise information about the power delay pro-

file (PDP) of Martian channels, we assumed, accepting some degree of approximation, the validity of the Jake's exponential PDP model, widely used in terrestrial Rayleigh-fading channels [103]. A deepened investigation of Martian multipath channels is left to Chapter 5.
Fig.4.4 shows the frequency responses for "Gusev1, Site1" and "Gusev1, Site3" multipath channels. The frequency selectivity of the channel response increases as the delay spread increases, as clearly confirmed by Tab.4.1 compared to Fig.4.4a, Fig.4.4b, Fig.4.4c and Fig.4.4d. It is important to highlight, once again, that the frequency selectivity of the channel depends on the morphology and electrical properties of the environment, for example path scattering due to rocks, and not on the mere increase of distance between TX and RX.

4.4.2 Analysis and modelling of Martian large-scale propagation

Large-scale propagation phenomena active on Mars are related to distance path loss and additional attenuation due to dust storms. For the Martian terrain, characterized by a medium-high density of rocks and numerous scatterers, a 3rd-order exponent path loss model is considered in [52] and we adopt it also for our assessments.

$$L(d) = \left(\frac{4\pi d_{TX-RX}}{\lambda}\right)^3 \tag{4.1}$$

Attenuation due to dust-storms is another propagation impairment, which may cause a noticeable power loss. Dust storms are really frequent on the Martian surface, especially in the south hemisphere, but they can extend on the whole planet [52]. During the storm, dust particles may rise high enough above the surface to lie within the radio path, causing a loss of signal energy. In addition, the change of polarization of the wave may occur due to the dust particles.
A valuable experimental model for dust storm attenuation on Mars surface has been proposed in [54] and detailed in the following equation:

$$A_{ds}(\lambda) = \frac{1.029 \times 10^6 \varepsilon''}{\lambda \cdot [(\varepsilon' + 2)^2 + \varepsilon''^2]} N_T \bar{r}^3 \tag{4.2}$$

where ε' and ε'' are, respectively, the real and imaginary part of the dielectric permittivity of dust particles [104], N_T, is the total particle density for

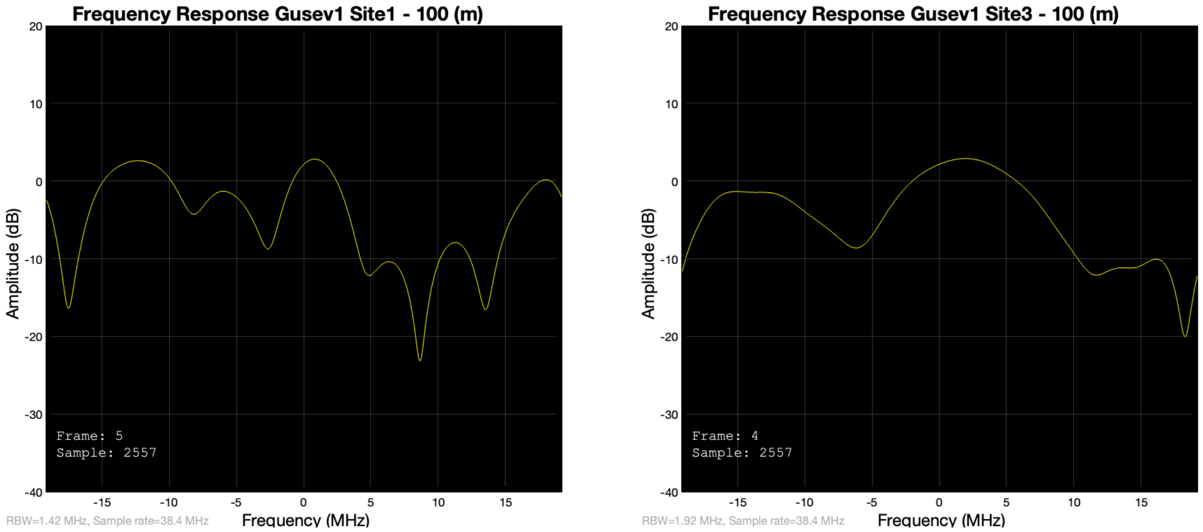

(a) “Gusev1, Site1” - 100m (b) “Gusev1, Site3 - 100m

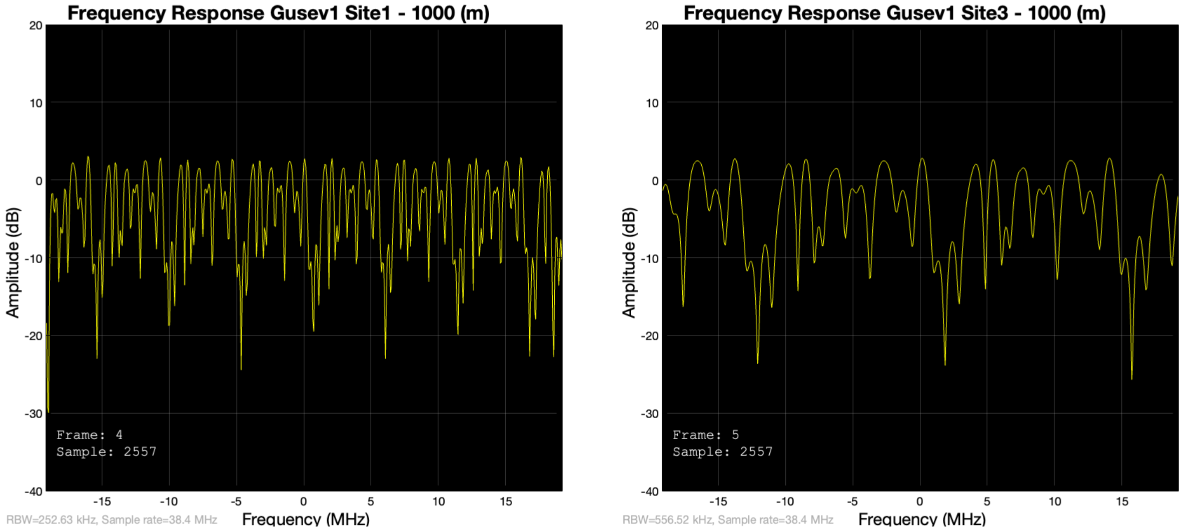

(c) “Gusev1, Site1” - 1000m (d) “Gusev1, Site3 - 1000m

Figure 4.4: (a) Frequency response of the “Gusev1, Site1” channel considering a distance d_{TX-RX} = 100m between transmitter and receiver. (b) Frequency response of the “Gusev1, Site3” channel considering a distance d_{TX-RX} = 100m between transmitter and receiver. (c) Frequency response of the “Gusev1, Site1” channel considering a distance d_{TX-RX} = 1000m between transmitter and receiver. (d) Frequency response of the “Gusev1, Site3” channel considering a distance d_{TX-RX} = 1000m between transmitter and receiver.

Table 4.2: E-LTE initialization

Parametrization	Value
Carrier Frequency f_c	2.4GHz
Number of Sub-Carriers N_{sc}	2048
Sub-carrier Spacing Δf	15kHz
Modulation Constellation	4-QAM, 16-QAM, 64-QAM
Baud-Rate	30.72MBaud/s
Number of Users N_{users}	4
Cyclic Prefix Length	16.67 μs
Occupied RF bandwidth f_{occ}	38.4MHz

m^3, and $\bar{r}$ is the mean particle radius expressed in m.

4.5 Simulating E-LTE Physical and Data-Link Layer

LTE transmission on Mars has been assessed by means of simulations in Simulink environment. We supposed to transfer on Mars a standard LTE equipment, with UEs and eNodeBs, like those actually working on Earth. We first simulated and tested the standard uplink and downlink transceivers, based on SC-FDMA with localized FDMA (L-FDMA) sub-carrier allocation and OFDMA, respectively. Then, we also simulated the uplink transmission based on the non-standard I-FDMA sub-carrier allocation.

For what concerns the parametrization of uplink and downlink transmission, we used the numerical values reported in Tab.4.2, related to terrestrial LTE setup [105]. In order to have symmetric bidirectional communication, the same baud-rate has been imposed to the uplink and the downlink, using all the available sub-carriers in both the communication directions. The CP length has been chosen in order to cope with the highest channel delay spread measured on the Martian surface.

4.5.1 Link performance evaluation

Link performance of LTE on Mars has been evaluated by plotting the “raw” channel BER vs. transmission $Eb/N0$, without introducing any channel coding. The impact of Turbo Forward Error Correction (FEC) coding on the available QoS will be analyzed in the next subsection. The BER results shown in the subsequent plots of Fig.4.5, Fig.4.6, and Fig.4.7 have been averaged over all the K transmitting users. Instead of assuming ideal Channel State Information (CSI) knowledge, Least-Square (LS) channel estimation using pilot symbols [99] has been adopted, according to LTE standard, in order to make simulations more realistic. As far as Frequency-Domain Equalization (FDE) is concerned, single-tap Zero-Forcing (ZF) equalization has been preferred to minimum mean square error (MMSE) in order to avoid estimation of noise variance. Also, this last choice is fully in agreement with the guidelines of LTE standard.

The analysis of uplink BER results of Fig.4.5a, Fig.4.5b, Fig.4.6a, and Fig.4.6b evidences three main outcomes:

- *an overall link performance degradation* can be noticed when 1000m transmission distance is considered. This is a confirmation of the more problematic multipath propagation encountered by long-range transmission in the Gusev region.
- *the uplink transmission attains better link performance in "Gusev1, Site3"*, than that achieved in "Gusev1, Site1".
- *I-FDMA seems to offer an augmented diversity* as compared to L-FDMA, with a noticeable performance gain that is noticed, in particular, for $Eb/N0 > 10$dB. As previously mentioned, I-FDMA pays a price in terms of increased computational complexity at the transmitter side.

The first two outcomes of the uplink analysis can be retained also for the downlink analysis of Fig.4.7 with a significant performance degradation noticed for long-distance transmission and, in general, for "Gusev1, Site1" area.

Some global considerations about the two different multi-carrier systems used by LTE in uplink and downlink should be pointed out. It is evident that SC-FDMA transmission performs better than OFDMA counterpart at equal $Eb/N0$. Such an improvement is indeed expected, as SC-FDMA exhibits augmented diversity as compared to OFDMA. In terrestrial LTE, such robustness is profitably exploited by uplink transmission (characterized by lower radiated power), together with the reduced Peak-to-Average Power Ratio (PAPR). As the SC-FDMA signal is detected by the eNodeB, the increased receiver complexity is not an issue. In the downlink, the lower complexity of the OFDMA receiver is welcome for low-cost and

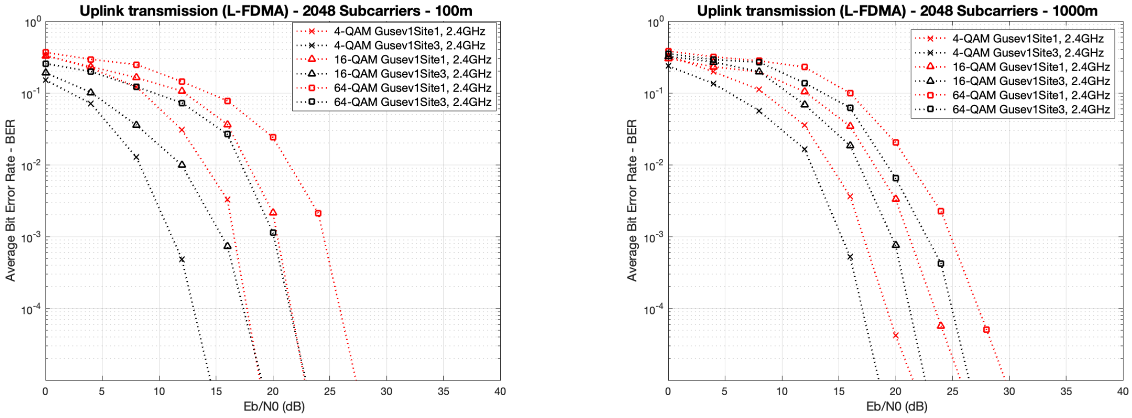

(a) BER vs Eb/N0

(b) BER vs Eb/N0

Figure 4.5: (a) SC-FDMA with localized allocation of the sub-carriers (L-FDMA) BER vs Eb/N0 for uplink communications considering a distance $d_{TX-RX} = 100$m between transmitter and receiver located on the Gusev crater. (b) SC-FDMA with localized allocation of the sub-carriers (L-FDMA) BER vs Eb/N0 for uplink communications considering a distance $d_{TX-RX} = 1000$m between transmitter and receiver located on the Gusev crater.

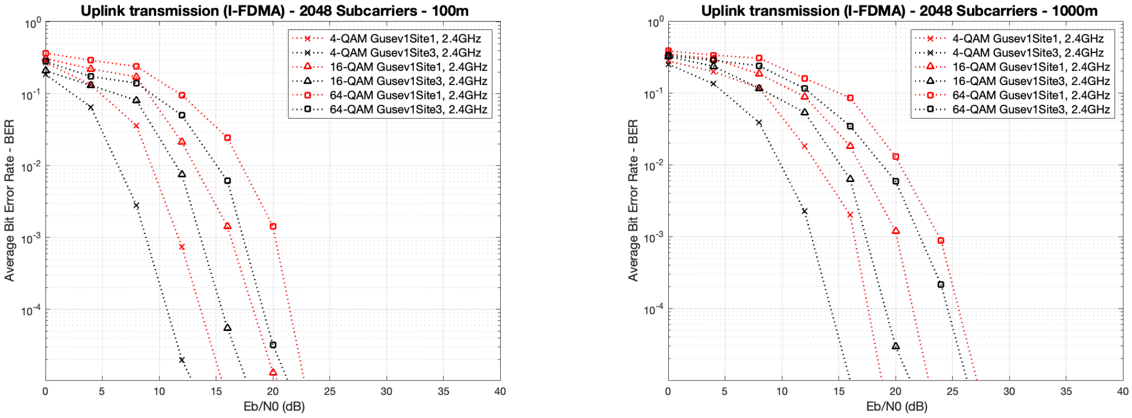

(a) BER vs Eb/N0

(b) BER vs Eb/N0

Figure 4.6: (a) SC-FDMA with interleaved allocation of the sub-carriers (I-FDMA) BER vs Eb/N0 for uplink communications considering a distance $d_{TX-RX} = 100$m between transmitter and receiver located on the Gusev crater. (b) SC-FDMA with interleaved allocation of the sub-carriers (I-FDMA) BER vs Eb/N0 for uplink communications considering a distance $d_{TX-RX} = 1000$m between transmitter and receiver located on the Gusev crater.

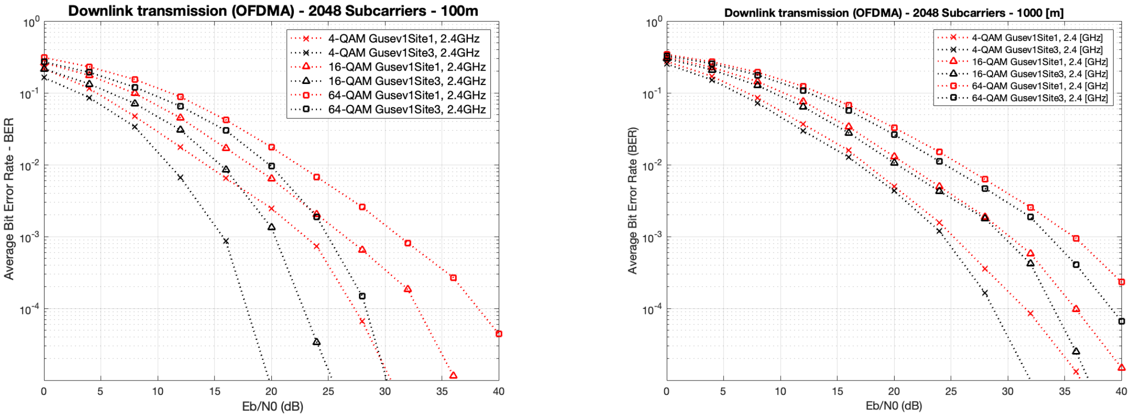

(a) BER vs Eb/N0

(b) BER vs Eb/N0

Figure 4.7: (a) OFDMA BER vs Eb/N0 for downlink communications, considering a distance $d_{TX-RX} = 100$m between transmitter and receiver located on the Gusev crater. (b) OFDMA BER vs Eb/N0 for downlink communications, considering a distance $d_{TX-RX} = 1000$m between transmitter and receiver located on the Gusev crater.

battery-operated portable terminals, while the higher power radiated by the eNodeB actually guarantees satisfactory performance also in presence of the power amplifier back-off, required to mitigate nonlinear distortion effects. The rationale of the uplink versus downlink trade-off, typical of terrestrial LTE, could be validated also for future applications of E-LTE on Mars. However, in our opinion, the door should be left open for (possible) different choices.

4.5.2 Link budget analysis and Quality-of-Service

Results shown in the previous subsection allow understanding how the PHY-layer of LTE standard - along with some non-standard improvements like uplink I-FDMA - might work on Mars. But, in order to quantify the actual QoS that we can achieve, we need to analyze the connection link budget and the impact of turbo FEC coding. It is commonly stated that a $BER \leq 10^{-5}$, measured after demodulation and turbo decoding, is good enough to guarantee the expected QoS to the entire LTE data transfer process [105].

Under the assumption of operating a terrestrial LTE equipment directly on Mars, we can report in Tab.4.3 the uplink and downlink link budgets, taking into account also the presence of dust storms on the Martian surface. The parameters related to the eNodeB and the UE are actually the

Table 4.3: Link budgets of LTE on Mars uplink and downlink

Parametrization	Downlink	Uplink
TX power P_{TX}^{max} (with OBO)	23dBmW	46dBmW
TX antenna gain G_{TX}	0dBi	18dBi
Cable loss L_{cable}	0dB	2dB
Receiver noise figure F	2dB	7dB
Environmental temperature T^{avg}	225K	225K
Interference margin $M_{interf.}$	1dB	4dB
Rx antenna gain G_{RX}	18dBi	0dBi
$\varepsilon^{'}$ ($f_c = 2.4$GHz)	4.56	4.56
$\varepsilon^{''}$ ($f_c = 2.4$GHz)	0.251	0.251
Particle density N_T (intense storm)	8×10^{-7}m^{-3}	8×10^{-7}m^{-3}
Cell radius d_{TX-RX}	100m, 1000m	100m 1000m
Carrier-to-noise $C/N0$ at cell border	93.0dBHz, 62.98dBHz	106.0dBHz, 75.97dBHz

same of terrestrial LTE. The values of $C/N0$ at cell border, reported in Tab.4.3, make evident that, in addition to worse multipath propagation, the long-distance transmission on Mars is impaired by severe large-scale path loss, with a consequential reduction of the available power resources. In order to evaluate the impact of turbo FEC coding on system performance and QoS, we have resorted to an off-line analysis that, from one hand, presents a certain degree of approximation, but, from the other, avoid lengthy Monte-Carlo simulations. First, we have drawn an analytical curve (obtained with MATLAB) showing the performance of 1/3-rate turbo coding in terms of BER after iterative decoding vs. channel "raw" BER.

We show here a plot representing the performance of 1/3-rate turbo coding in terms of BER after iterative decoding vs. channel "raw" BER. The different curves, obtained for a different number of decoding iteration k_{iter}, are presented in Fig.4.8. Assuming $k_{iter} = 4$, the uncoded BER required to achieve the expected turbo-coded BER (C-BER) value of 10^{-5} is 8.4×10^{-2}. The next step is to visually check on Fig.4.5a, Fig.4.5b, Fig.4.6a, Fig.4.6b, Fig.4.7a and Fig.4.7b the required $Eb/N0$ (namely: $[Eb/N0]^{req}$) that allows to obtain the aforesaid uncoded BER of 8.4×10^{-2}. Finally, we can compute the total useful system capacity $\mathbb{R}_b$ (bps) by applying the following formula:

$$\mathbb{R}_b = N_{alloc} B_{sub} r_{tc} log_2 \left(L_{mod} \right) \tag{4.3}$$

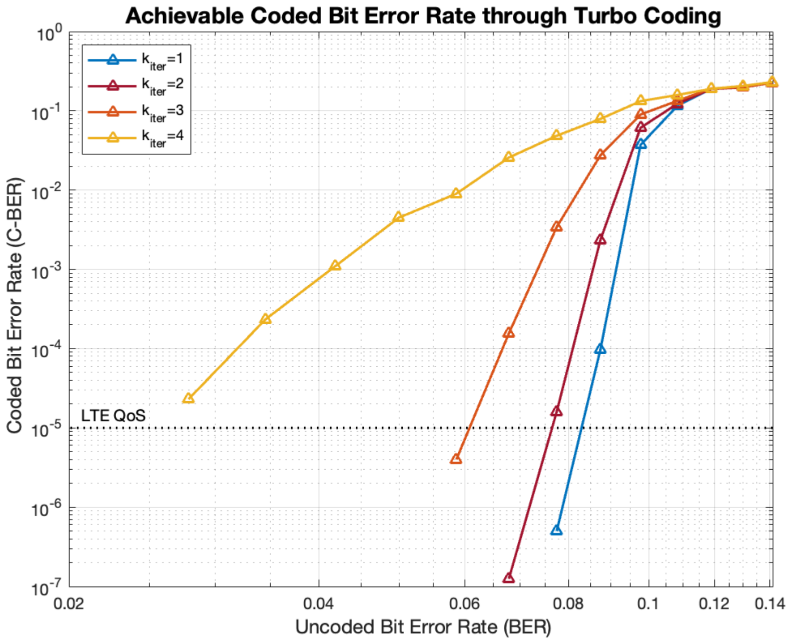

Figure 4.8: Analytical curves of BER after iterative turbo decoding vs. uncoded "raw" BER for different numbers of decoding iterations k_{iter}

where B_{sub} is the sub-carrier spacing of LTE, equal to $15KHz$ and L_{mod} is the number of levels of the adopted QAM modulation constellations (in our simulations, we have employed 4-QAM, 16-QAM and 64-QAM), r_{tc} is the 1/3 turbo coding rate and N_{alloc} is the maximum number of sub-carriers, that we can allocate to the overall user population in order to cope with the above-mentioned QoS requirements, namely:

$$N_{alloc} = min\left\{2048, \left\lfloor\frac{R_{gross}}{B_{sub}}\right\rfloor\right\} \tag{4.4}$$

where R_{gross} is the available gross baud-rate at the output of the multi-carrier detector (inclusive of turbo coding) that is expressed, in dBHz, as follows:

$$R_{gross}^{dBHz} = \left(\frac{C}{N_0}\right)_{dBHz} - \left[\frac{E_b}{N_0}\right]^{req} - 10log_{10}\left(log_2\left(L_{mod}\right)\right) \tag{4.5}$$

The values of $\left(\frac{C}{N_0}\right)_{dBHz}$ are the $C/N0$ at cell border shown in the last row of Tab.4.3. Please, note that in Eq.4.4, we explicitly imposed that the number of sub-carriers that can be allocated to the user population must

Table 4.4: Numerical results about $(Eb/N0)^{req}$ and total useful system capacity $\mathbb{R}_b$ of LTE uplink on Mars implemented by standard LTE SC-FDMA transmission with L-FDMA sub-carrier allocation.

($Eb/N0$ (dB),$\mathbb{R}_b$ (Mbps)	$d_{TX-RX} = 100$m			$d_{TX-RX} = 1000$m		
	4-QAM	16-QAM	64-QAM	4-QAM	16-QAM	64-QAM
"Gusev1, Site1"	$(11, 20.48)$	$(13.1, 32.56)$	$(17, 13.26)$	$(9, 0.080)$	$(13.5, 0.020)$	$(18.5, 0.000)$
"Gusev1, Site3"	$(3, 20.48)$	$(5.1, 40.96)$	$(12, 41.96)$	$(6, 0.160)$	$(11.5, 0.040)$	$(15, 0.000)$

Table 4.5: Numerical results about $(Eb/N0)^{req}$ and total useful system capacity $\mathbb{R}_b$ of LTE uplink on Mars implemented by non-standard LTE SC-FDMA transmission with I-FDMA sub-carrier allocation.

($Eb/N0$ (dB),$\mathbb{R}_b$ (Mbps)	$d_{TX-RX} = 100$m			$d_{TX-RX} = 1000$m		
	4-QAM	16-QAM	64-QAM	4-QAM	16-QAM	64-QAM
"Gusev1, Site1"	$(5.5, 20.48)$	$(9.5, 40.96)$	$(12.1, 40.98)$	$(8.5, 0.090)$	$(12, 0.040)$	$(12.1, 0.030)$
"Gusev1, Site3"	$(3, 20.48)$	$(8.25, 40.96)$	$(10.4, 60.63)$	$(5.25, 0.180)$	$(10, 0.060)$	$(10.4, 0.060)$

not exceed the total number of sub-carriers made available by LTE (2048, as shown in Tab.4.2). $N_{alloc} = 2048$ would make it feasible to transmit at a gross baud-rate of 30.72Mbaud/s (or 74.87dBHz). This would guarantee to achieve the maximum useful system capacity. Otherwise, the useful system capacity decreases due to the Martian propagation impairments. $N_{alloc} = 0$ means that the gross baud-rate achievable by the LTE Martian link is inferior to B_{sub}, which is the minimum baud-rate that the LTE PHY-layer can actually provide and, therefore, no useful capacity will be available for any user. It should be said that if $N_{alloc} < K$ (which corresponds to an available gross data rate lower than 60Kbaud/s), at least one user will obtain no useful capacity.

Tab.4.4, Tab.4.5 and Tab.4.6 show the numerical results in tabular format about $(Eb/N0)^{req}$ and the total useful system capacity $\mathbb{R}_b$ attained by standard L-FDMA-based LTE uplink, non-standard LTE uplink using I-FDMA instead of L-FDMA, and standard OFDMA downlink respectively. Results have been given for the two Martian sites considered in the simulations, the two assessed link distances and, finally, the three QAM modulation constellations employed. The most dramatic outcome of our analysis is the impossibility for the terrestrial LTE, transferred "as it is" on Mars, of supporting long-range connections. Indeed, for a link distance of 1000m, the results in terms of achievable useful capacity are some orders of magnitude below the maximum values achievable by terrestrial LTE. The big

Table 4.6: Numerical results about $(Eb/N0)^{req}$ and total useful system capacity $\mathbb{R}_b$ of LTE downlink on Mars implemented by standard LTE OFDMA transmission.

$(Eb/N0$ (dB),$\mathbb{R}_b$(Mbps)	$d_{TX-RX} = 100$m			$d_{TX-RX} = 1000$m		
	4-QAM	16-QAM	64-QAM	4-QAM	16-QAM	64-QAM
"Gusev1, Site1"	$(5.75, 20.48)$	$(9, 40.96)$	$(12.5, 61.44)$	$(8, 2.08)$	$(11, 1.04)$	$(14.8, 0.420)$
"Gusev1, Site3"	$(4, 20.48)$	$(7, 40.96)$	$(10.5, 61.44)$	$(7, 2.62)$	$(10, 1.30)$	$(14, 0.510)$

issue is related to the huge path loss attenuation, dramatically reducing the available power resources. In order to improve performance of long distance cellular connections on Mars, we should definitely increase the power resource availability by means of:

- *newly redesigned RF section characterized by superior gain* that substantially means to implement higher-gain antennas and/or more efficient power amplifiers for UEs and eNodeBs. This solution would be theoretically feasible, but the total RF gain increase should be of the order of 30dB. This might involve additional cost, weight, size and power consumption to the communication equipment. It should be understood if this is acceptable for future (manned) missions.

- *adaptive beamforming*, using, for instance, tunable antenna arrays at the eNodeB side. Such techniques have been successfully experimented in terrestrial environment and, in particular, in LTE applications. Their adaptability to the Martian context is still to be assessed.

- *cooperative relaying*. In the near future, much more transmitting devices may populate the Martian surface (new rovers, new landers, etc.). So, cooperative relaying scenarios, profitably experimented on Earth to increase coverage and QoS, should be concretely viable. But, at the present time, this is a futuristic research task that needs preliminary theoretical investigation.

As far as the shorter link distance 100m is concerned, the deployment of terrestrial LTE on Mars is much more feasible, even though some kind of upgrading should be anyway considered. As shown in Tab.4.6, the full LTE capacity is reached in the downlink in all the sites and for all modulation constellations. On the other hand, in the uplink, the standard transmission solution based on SC-FDMA with L-FDMA optimally performs in all the considered test sites only when 4-QAM modulation is used in combination with turbo coding. Turbo-coded 16-QAM achieves the maximum

capacity in the “Gusev1, Site3”, while in “Gusev1, Site1” the reached capacity is 79.5% of the total available capacity. The use of turbo-coded 64-QAM modulation for the Martian uplink is not advisable, at least with the standard transmission arrangement. In “Gusev1, Site1” only 21% of the available capacity is obtained, with an evident waste of radio resources. “Gusev1, Site3” shows better performance, but with an achieved capacity efficiency of 68.3% that is not very satisfactory.
A possible improvement for the uplink is the use of I-FDMA. Apparently, in short range, this improvement seems to fairly work. In our specific case, the numerical values of the total useful system capacity shown in Tab.4.5 evidence full LTE capacity achieved with turbo-coded 4-QAM and 16-QAM modulations both in “Gusev1, Site1” and “Gusev1, Site3”. Almost full capacity is reached by turbo-coded 64-QAM in “Gusev1, Site3” (98.7% of efficiency), while in “Gusev1, Site1”, the throughput efficiency of 64-QAM is still not satisfactory (66.7%) but anyway increased with respect to the L-FDMA counterpart.

4.6 Conclusions

The feasibility of the deployment of a mobile cellular network infrastructure on Mars, based on terrestrial LTE concepts, has been investigated by means of laboratory simulations. No *in-situ* installation is required, as the eNodeB can be hosted on a lander, while UEs are installed on the rovers and, in the future, also handled by human astronauts. The availability of such typology of infrastructure may be very beneficial, in particular in the perspective of future manned missions.
Data and models present in the literature, concerning the radio propagation on Mars, have been used in order to parameterize the simulators. However, a replicable model for a realistic characterization of the Martian channel is necessary for further analysis. Chapter 5 will deeply discuss it, thus proposing a ray tracing algorithm for 3D tile-based rendering of high resolution DEMs.
Two different Martian sites have been considered for assessment, both of them located in the Gusev crater. For each test site, two different transmission distances were assumed, namely 100m and 1000m. Simulation results demonstrate the overall viability of terrestrial LTE for short range connections or small cells, provided that some few upgrading in the radio interface design will be planned for the real installation of the infrastruc-

ture. The use of SC-FDMA with I-FDMA sub-carrier allocation might be one of these improvements.

More critical is the deployment of the LTE-based cellular infrastructure in larger areas. In such a case, the power resources made available by terrestrial LTE are absolutely insufficient to guarantee a minimally satisfactory QoS. In order to provide longer range mobile connectivity on Mars, without a substantial redesign of the LTE radio interface, in particular for what concerns the RF section, is required. The wide literature about terrestrial mobile communications already points out the solution to this issue (high gain antenna systems, adaptive beamforming, cooperative relaying etc.), but the deployability of such solutions on the "Red Planet" should eventually be carefully assessed by future research work.

Chapter 5

A Reliable and Replicable Martian Propagation Model based on 3D Ray Tracing and Digital Elevation Model

The RF propagation modelling is at the heart of our understanding of communication system performance on Mars. Thus, the essay below defines a complete methodology for large and small scale phenomena analysis through high resolution DEM and 3D ray tracing. First, we give an overview of our work, then, sect.5.2 organically details the simulator. Outage probability, path losses, shadowing, other attenuation and multipath propagation will be treated in sect.5.3. Finally, conclusions will be given in sect.5.4.
This part of the thesis is partly retrieved from published journals and conference papers [1].

5.1 Scenario and Further Motivations

ANALYZE the performance of deep-space communication systems and, by extension, network infrastructures, by means of simulations appears of paramount importance to support human personnel on Mars through efficient connectivity. Successfully deploying these futuristic architectures on the "Red Planet" is directly dependent on the accuracy of simulations and emulations, that we are able to achieve trough *ad-hoc* software. To this aim, the correct statistical modelling of the environment, that we are taking into account during the design phase of our system, is fundamental for realistic measurements. However, as we previously saw in Chapter 4, the state-of-the-art evaluations appear to be preliminary due

---

[1] Part of this chapter appears in [194, 196, 197]

to the lack of a model able to realistically estimate, with a small degree of freedom, the radio-frequency (RF) propagation over Mars terrains, i.e. the knowledge about Martian large-scale and small-scale phenomena.
Generally, software simulations are done to measure the performance of communication systems in terms of QoS and RMA metrics. Most of the commercial software, despite being different in their structures and workflows, are parameterized, in order to simulate a wireless environment, by characterizing the channel through path losses, shadowing, and path delays and gains for the multipath propagation. On Earth, such variables are easily measured by installing transceivers in urban, suburban, rural or mountainous areas and testing the RF propagation, thus gathering samples at the receiver side, from which we obtain the received power and delays of arrivals. Recently, these on-field tests were partially substituted by exploiting ray-tracing algorithms, as done in [106] for outdoor environment or in [107] for indoor situations, which uses as input a 3D representation of the area we want to study. However, when dealing with the Martian surface, on-field tests are not feasible, at least for our epoch - although it is possible to do approximated tests on Martian analog on Earth or reproducing a similar Martian environment as done by the Rover Operation Control Center (ROCC) in Turin [108]. As far as we know, the literature does not propose solutions to properly simulate the RF transmission over the surface of the planet along with in-depth analysis of the impairments affecting the propagation.

In the present chapter, we want to provide a technically meaningful analysis of large and small-scale phenomena over a realistic Martian environment by exploiting high resolution DEMs and 3D ray tracing for outdoor scenarios. Precisely, we assume the Gale crater as our scenario. NASA provided a high resolution DEM of the Gale crater (1 m/px). The Gale crater, which researchers believe to have been a salty iced lake in some Martian epochs [109], was the landing site of the Martian rover "Curiosity", as mentioned in sect.2.5. Thus, this is a particularly relevant area to be studied.

The model, that we designed, estimates through the Cole-Cole equations the electrical properties of a possible Martian replicant soil, i.e. JSC Mars-1, in order to later compute the amount of power lost/reflected into/from the medium, i.e. large rocks and cliffs. The DEM is processed in MATLAB to construct a 3D structure composed of tiles, whose side length is equal to the DEM's resolution. The closest vertices of the tiles are connected in

order to build the walls of the structure. A 3D ray-tracing algorithm is applied to the 3D tile-based Gale crater render to compute the first and second reflections of a RF signal. Then, each estimated signal replicas is analyzed in order to understand their carried power and delay of arrivals with respect to the Line-of-Sight (LOS) component.
The chapter will continue by studying the samples gathered from multiple simulations in terms of large-scale phenomena, i.e. path loss and shadowing, and small-scale phenomena, i.e. multipath propagation. Few considerations will be done about the outage probability and other kind of large-scale attenuation, such as dust-storms and atmosphere attenuation - no less important than the others. Our model will be explicitly treated and detailed in order to be fully replicable.

5.2 Simulator Walkthrough

In the next paragraph, the complex workflow for the design of a 3D ray tracing model for understanding the RF propagation impairments over Martian environments will be presented. Along with the in-depth narration about the simulator, we will discuss how to properly analyze the gathered data exiting from the simulator in order to statistically estimate large-scale and small-scale phenomena. Now, let us explain how to implement the core of this activity. As already mentioned before, we developed everything in MATLAB environment. It was chosen among other tools thanks to its reliability, its exorbitant number of usable *ad-hoc* built-in functions and its large community, that continuously helps the improvement of the software with external packages and integrable scripts.
Here below, we will follow the steps of our workflow, which will be resumed later on.

5.2.1 3D Martian structure from DEM

Few DEMs with a high resolution are available. One of them is, for sure, the “Mars MSL Gale Merged DEM 1m v3” with a resolution of 1m/px [110], which is surely enough when dealing with transmissions of hundreds or thousands of meters. It is the “elevation” photo of the Gale crater, an area probably formed 3.7 billion years ago from the downfall of a meteor, which was selected to be the landing site of the “Curiosity” rover in 2012. It is mostly characterized by flat areas made of layered sediments and a

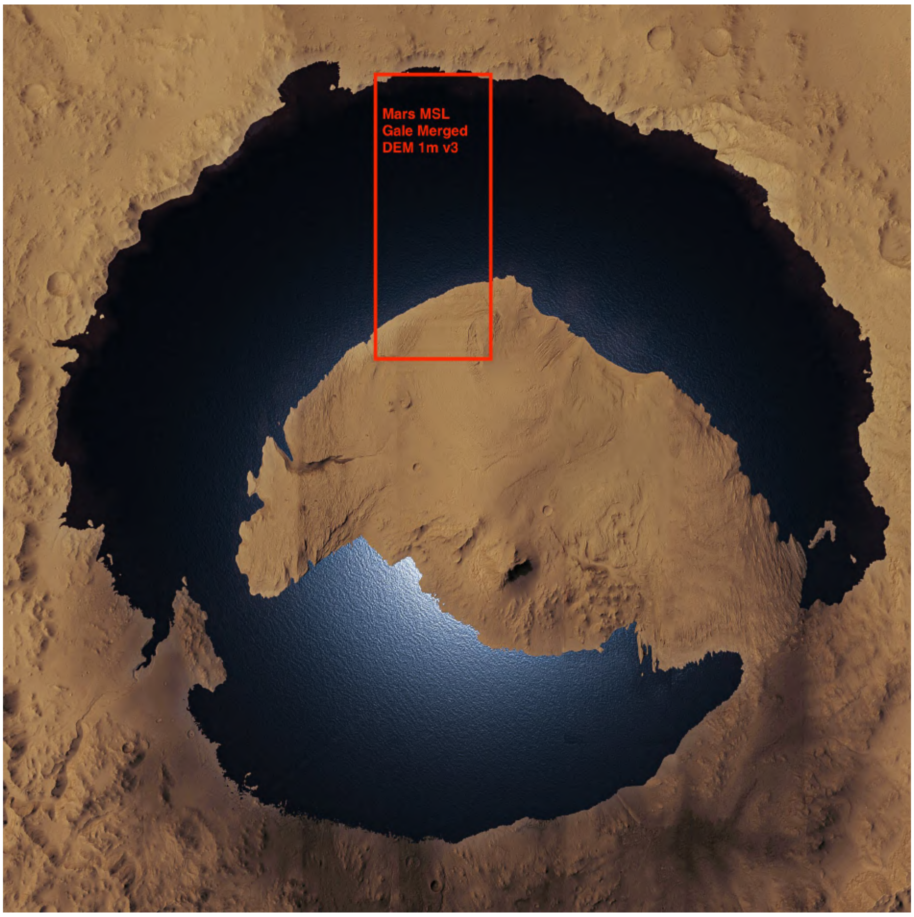

Figure 5.1: Hypothetic lake onto the Gale crater rendered thanks to the MRO Context Camera (CTX) orthoimagery, digital terrain model data and Blender with Cycles. Credit: Kevin Gill.

central peak, as correctly depicted by Kevin Gill in Fig.5.1. Researchers found that, with any luck, water flowed into the Gale crater from rivers fed by rains and melting snow. Thus, it became a lake, as in Fig.5.1. Its importance it is so justified by the probability of discovering signs of the presence of water, therefore, proof of possible lifeforms in some Martian era. However, for our purposes, this area has been exploited in order to construct a 3D structure upon which implementing our RF propagation simulator.

We cropped the DEM into two areas, strongly presenting differences in their morphological structure. The first area, which will be called for simplicity "Gale Crater - Area 1", is extruded from the center of the DEM. Consequently, its center point is the middle point of the entire DEM. The second area is obtained by dividing the DEM into three equally spaced

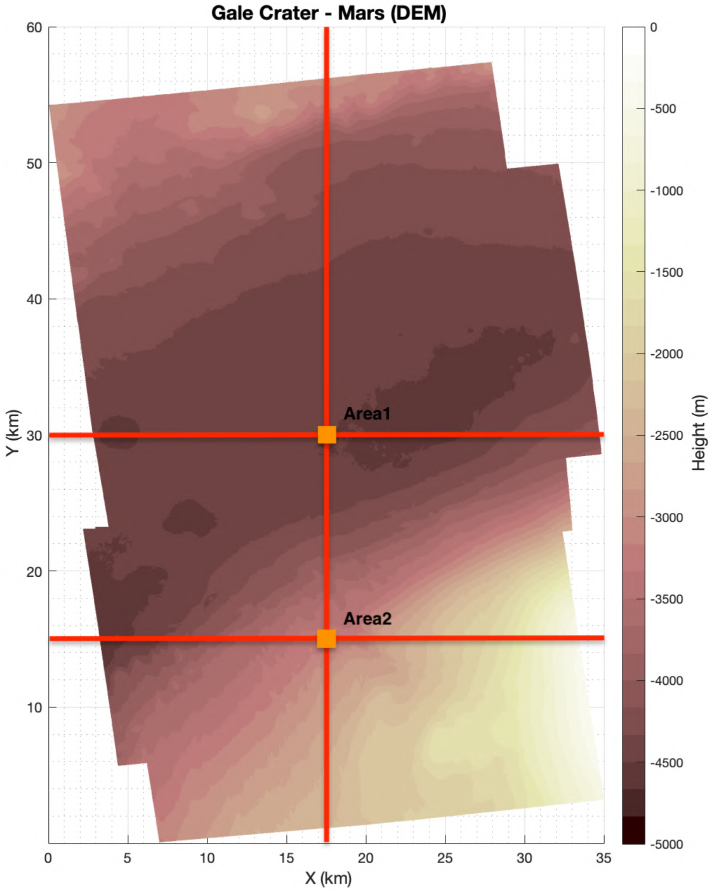

Figure 5.2: 2D-plot of the "Mars MSL Gale Merged DEM 1m v3" highlighting the slopes of the central peak, or mountainous area, which raises from the crater. The orange squares depict the cropped areas.

slices, where the center of the "Gale Crater - Area 2" is the intersection between the lowest red line and the vertical one in Fig.5.2. The two areas, both with side length of 1000m, represent, respectively, an almost flat area and a rocky yet steep one, as clearly visible from Fig.5.3, where the blue squares are the subdivision of the main areas along their diagonals. However, we will return to this when we will discuss the results in sect.5.3. Now, what is really demanding to point out is how to create the 3D areas in MATLAB.

A digital elevation model is an array of pixel, whose values are the quote of the area they are representing. Consequently, by defining a set of points $P = [p1, p2, p3, p4]$ in a three-dimensional space, each pixel can

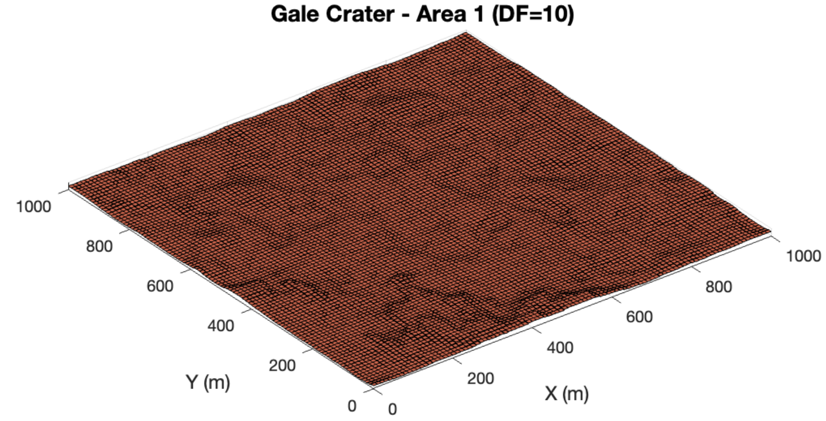

(a)
"Gale Crater - Area 1"

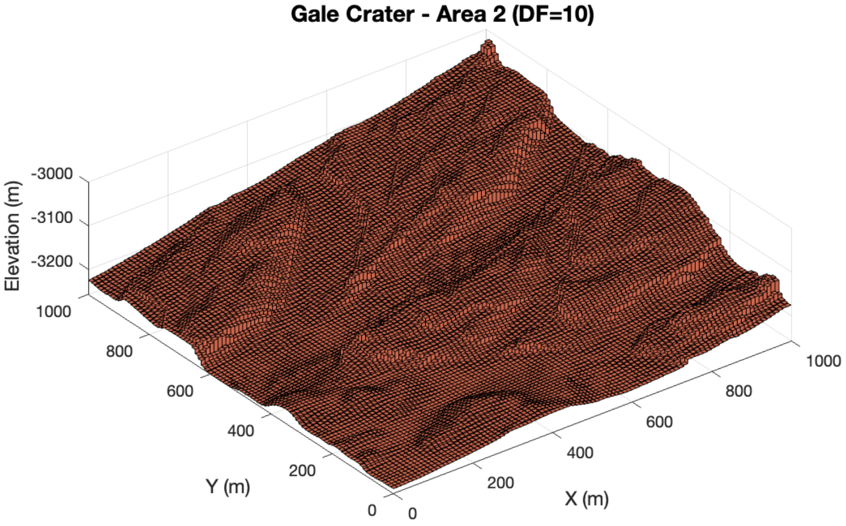

(b)
"Gale Crater - Area 2"

Figure 5.3: (a) Plot of the 3D tile-based structure of the "Gale Crater - Area 1". (b) Plot of the 3D tile-based structure of the "Gale Crater - Area 2".

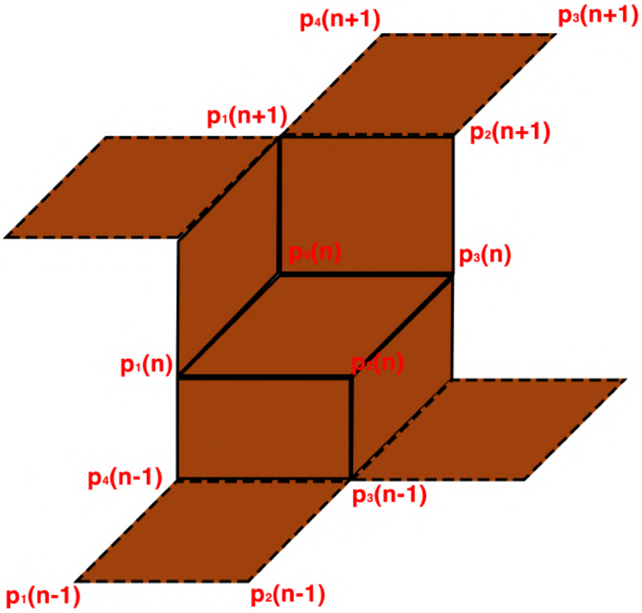

Figure 5.4: Pictorial representation of the interpolation between tiles constructing the 3D structure in MATLAB.

be modelled as a tile with side length equal to the DEM's resolution. With $n = [1, 2, ...N]$ the n^{th} pixel of the cropped area, the 3D structure is built by interpolating the closest vertices of the n^{th} tile along the z-axis. If we consider pixel n as in Fig.5.4, the walls between pixel n, $n-1$ and n, $n+1$ are easily obtained, respectively, by connecting $p_1(n)$ and $p_4(n-1)$, $p_2(n)$ and $p_3(n-1)$, $p_3(n)$ and $p_2(n+1)$, $p_4(n)$ and $p_1(n+1)$.

The repetition of this operation along the x-axis and y-axis direction, for the total number of pixel, lead to a floor matrix and a wall matrix, which are both used as input to the 3D ray-tracing algorithm. Thus, the Martian environment is, now, geometrically reproduced by the 3D tile-based structure.

5.2.2 Complex permittivity of Martian soil

The geometrical representation of the area is necessary when we estimate the reflections of the RF signal propagated over the structure. However, it is not enough to characterize the Martian environment. Indeed, as commonly known, the electrical characteristic of a material, in the form of complex permittivity, impacts on the amount of power transmitted/reflected into/from a medium made of the same material [111]. In order to support the scientific research, the international space agencies, e.g. NASA, replicated several Martian terrains thanks to some terrestrial analogs. An example of these studies is the JSC Mars-1, a Martian soil replicant obtained from the ash of the Pu'u Nene, which is a volcano located in Hawaii [112]. This was considered to be a Martian terrain analog due to its spectral similitude to the bright regions of Mars [113]. We considered it due to the huge amount of information in the literature about it, which has made possible a solid estimation of its complex permittivity. By expressing the complex permittivity as $\hat{\epsilon} = \epsilon_r^{'} - i\epsilon_r^{''}$, we can compute the real part $\epsilon^{'}$ and the imaginary part $\epsilon^{''}$ thanks to the Cole-Cole equations [114]:

$$\epsilon' = \epsilon_\infty + (\epsilon_{DC} - \epsilon_\infty)\frac{1 + (\omega\tau)^{1-\alpha}\sin\alpha\pi/2}{1 + 2(\omega\tau)^{1-\alpha}\sin\alpha\pi/2 + (\omega\tau)^{2(1-\alpha)}} \tag{5.1}$$

$$\epsilon'' = \frac{(\epsilon_{DC} - \epsilon_\infty)(\omega\tau)^{1-\alpha}\cos\alpha\pi/2}{1 + 2(\omega\tau)^{1-\alpha}\sin\alpha\pi/2 + (\omega\tau)^{2(1-\alpha)}} \tag{5.2}$$

with the angular velocity $\omega = 2\pi f$, the infinite and static dielectric permittivity defined as ϵ_∞ and ϵ_{DC}, the relaxation time constant τ and the Cole-Cole distribution α. The frequency dependence of this computation will be analyzed later through results by initializing the Cole-Cole equations with the parameters value in [115].

5.2.3 Fresnel coefficients

The estimate of the complex dielectric permittivity $\hat{\epsilon}$ is needed in order to understand the amount of power that will be "dissipated" during RF propagation. This is due to the scattering of the electromagnetic signal caused by the outdoor environment. Indeed, when the signal has a wavelength λ comparable to the dimension of an object, which is obstructing its propagation - a Martian rock or cliff, the so-called transmission and reflection phenomena happen. For transmission is meant the power transmitted T and lost into the medium, while reflection is the phenomena from which the incident power I is reflected (R) from the medium.

In this case of study, the reflected power characterizes the power of the signal replica generated from the collision with the terrain along with the increased distance with respect to the LOS. As we will see later, the ray travelling from TX to RX experiences a reflection when hitting a tile of the 3D structure. This means that only a percentage of the total amount of power incident to the interface will be redirected to another tile composing the terrain, while the transmitted power into the medium will be dissipated.

Thanks to the Fresnel coefficients and remembering the classical electromagnetic (EM) theory, where the incident power is $I = T + R$, we are able to compute the transmitted $T_{TE,TM}$ and reflected $R_{TE,TM}$ power - subscripts TE and TM refer to Transverse Electric and Magnetic modes, where the formulation is reported in the work provided in [116]:

$$T^{TE} = abs\left(\frac{\left(1-\gamma^2\right)\cdot e^{\left(-i\left(\frac{2\pi}{\lambda}\cdot w_{area}(\sqrt{\hat{\epsilon}-sin^2(\theta_I)}-1)\right)\right)}}{\left(1-\gamma^2 e^{-2i\left(\frac{2\pi}{\lambda}\cdot w_{area}\cdot\sqrt{\hat{\epsilon}-sin^2(\theta_I)}\right)}\right)}\right) \tag{5.3a}$$

$$\gamma = \left(\frac{cos(\theta_I)-\sqrt{\hat{\epsilon}-sin^2(\theta_I)}}{cos(\theta_I)+\sqrt{\hat{\epsilon}-sin^2(\theta_I)}}\right) \tag{5.3b}$$

$$T^{TM} = abs\left(\frac{\left(1-\kappa^2\right)\cdot e^{\left(-i\left(\frac{2\pi}{\lambda}\cdot w_{area}(\sqrt{\hat{\epsilon}-sin^2(\theta_I)}-1)\right)\right)}}{\left(1-\kappa^2 e^{-2i\left(\frac{2\pi}{\lambda}\cdot w_{area}\cdot\sqrt{\hat{\epsilon}-sin^2(\theta_I)}\right)}\right)}\right) \tag{5.4a}$$

$$\kappa = \left(\frac{\hat{\epsilon}\cdot cos(\theta_I)-\sqrt{\hat{\epsilon}-sin^2(\theta_I)}}{\hat{\epsilon}\cdot cos(\theta_I)+\sqrt{\hat{\epsilon}+sin^2(\theta_I)}}\right) \tag{5.4b}$$

where θ_I is the angle of incidence, $\lambda = c/f$ (m) the wavelength, c the speed of light and w_{area} is the thickness of the terrain. Indeed, we decided to compute the Fresnel coefficients by considering a thickness-dependence of the attenuation introduced by the medium in order to simulate the width of the area, which otherwise would be infinitesimal.

The transmission power lost into the medium, which is characterized by a thickness w_{area}, is simply subtracted from the unitary power, to reduce the increase of the computational load, thus obtaining the reflected one $R_{TE,TM} = 1 - T_{TE,TM}$.

5.2.4 3D ray tracing

We started from the work provided by Hosseinzadeh in [117] and well explained in [118]. Hosseinzadeh et al. studied the propagation of the Long Range (LoRa) modulation by considering an indoor environment. They compared the performance of non-deterministic models, such as ITU and log-distance, with deterministic ones, e.g. multi-wall and ray-tracing models. From the results, they found that for the estimation of the LoRa propagation the best choice was the multi-wall model in terms of accuracy, similar to the one obtained with the ray-tracing model, and reduced computational load with respect to ray-tracing. However, this is not true when dealing with strong small-scale fading, as correctly highlighted in [118]. Thus, a 3D ray-tracing algorithm is recommended when the objective is the overall characterization of propagation impairments, especially over outdoor environments, although the computational complexity is really high and can be a limit, especially thinking to the required simulation time. The ray tracing algorithm is based on geometrical optics as in [119] and it implements the procedures clearly shown in Fig.5.5. As briefly introduced before, it takes as input the 3D structure, or tile-area, modelled on the basis of the DEM. It is iterated for the number of RXs, that we choose to displace on the 3D tile-area. Furthermore, it would be possible to consider multiple transmitter simply by iterating the process for the number of TXs and adapting the various matrices dimensions. However, this will not be considered in this work, but it will be the subject of future analysis.

First, it traces the LOS with the aim of finding the received power of the signal in the location where the RX is placed. Obviously, between TX and RX there can be rocks or cliffs obstructing the LOS and dissipating power in the terrain. Thus, we find the intersection between TX-RX in order to account for the power lost, thanks to the Fresnel coefficients, into the medium as follows:

$$P_{LOS}^{dBW} = P_{TX}^{dBW} - 10log_{10}\left(\frac{4\pi d_{TX-RX}}{\lambda}\right)^2 + 10log_{10}(T_{TX,RX}^{TE,TM}) + G_{TX}^{dB} + G_{RX}^{dB} \tag{5.5}$$

where d_{TX-RX} is the distance between TX-RX, $10log_{10}(T_{TX,RX}^{TE,TM})$ is the power transmitted into the medium in dB with $0 < T < 1$ and G_{TX}^{dB}, G_{RX}^{dB} are the TX and RX antenna gains.

Now, the power of the first reflections and second reflections are needed to

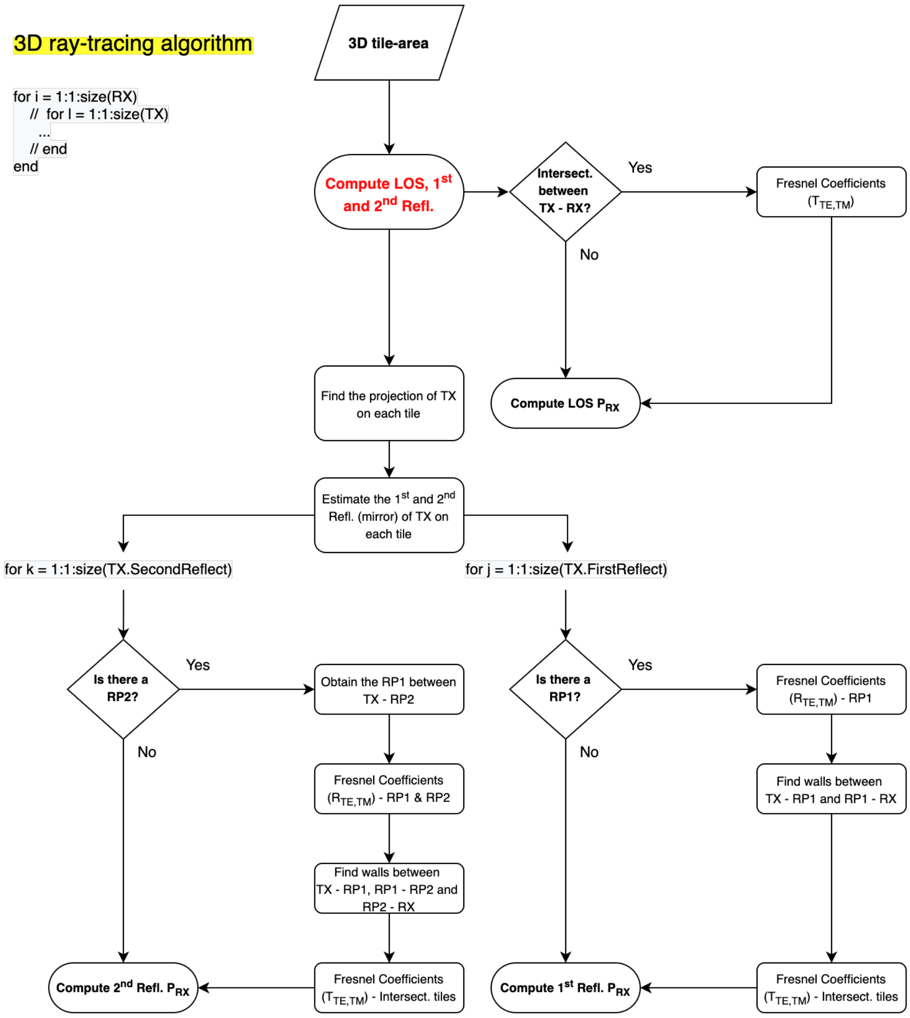

Figure 5.5: Flowgraph of the 3D ray-tracing algorithm for outdoor environment.

obtain the total received power at the RX side, and to analyze the effect of the small-scale phenomena on the propagation. For the sake of completeness, the first reflection means the path travelled by the signal which is reflected only one time from a reflection point (RP*) before reaching the RX, while the second reflection is the replica of the signal which arrives to the RX by reflecting on two RPs.
The algorithm finds the projection of TX on each tile, thus allowing to estimate the reflections, or mirrors, of the selected TX on each tile composing the 3D structure. The power of the 1^{st} reflection is computed by searching for the RP1 characterizing the path between TX and RX. If there is actually a RP1, the “ray tracer” proceeds to the computation of the reflection coefficients in order to estimate the amount of reflected power from the

RP1. Then, it finds the walls between the path TX-RP1 and RP1-RX by understanding the amount of power transmitted into each intersecting tiles. The received power due to the 1^{st} reflection is based on the following equation:

$$\begin{aligned} P^{dBW}_{1^{st}Refl} = P^{dBW}_{TX} - 20log_{10}\left(\frac{4\pi d_{TX,RP_n} + d_{RP_n,RX}}{\lambda}\right) + 10log_{10}(T^{TE,TM}_{TX,RP_n}) \\ + 10log_{10}(R^{TE,TM}_{RP_n}) + 10log_{10}(T^{TE,TM}_{RP_n,RX}) + G^{dB}_{TX} + G^{dB}_{RX} \end{aligned} \tag{5.6}$$

The 2^{nd} reflections are evaluated through the same process of the 1^{st} with the exception that, if there is a RP2, we need to obtain the RP1 between TX-RP2. Then, two RPs mean that we will have to compute the reflected power from the RP1 and RP2, as well as finding the tiles, or walls, intersecting the paths TX-RP1, RP1-RP2 and RP2-RX. The transmission coefficients are estimated for each intersection and the power of the second reflection is based on the following computation:

$$\begin{aligned} P^{dBW}_{2^{nd}Refl} = P^{dBW}_{TX} - 20log_{10}\left(\frac{4\pi d_{TX,RP_n} + d_{RP_n,RP_{n+1}} + d_{RP_{n+1},RX}}{\lambda}\right) \\ + 10log_{10}(T^{TE,TM}_{TX,RP_n}) + 10log_{10}(R^{TE,TM}_{RP_n}) + 10log_{10}(T^{TE,TM}_{RP_n,RP_{n+1}}) \\ + 10log_{10}(R^{TE,TM}_{RP_{n+1}}) + 10log_{10}(T^{TE,TM}_{RP_{n+1},RX}) + G^{dB}_{TX} + G^{dB}_{RX} \end{aligned} \tag{5.7}$$

5.2.5 Post-process and other propagation impairments

The knowledge coming out from the “ray tracer” allows us to process data for the analysis of large-scale and small-scale phenomena. Moreover, as introduced in sect.5.1, we can integrate the formulation representing other propagation impairments about atmosphere, cloud and fog, aerosol and dust storm attenuation, which are not directly studied through the main algorithm, in order to get a complete overview of the effect altering the RF propagation. The first analysis that should be made is the computation of the outage probability, which is the probability of having a completely blocked RF propagation due to big obstacles, such as big rocks and cliffs, obstructing the signal. This can be easily approximated by imposing a threshold on the minimum detectable signal (MDS) - noise floor plus a required SNR of 0dB, which is defined as follows:

$$MDS\,(dBm) = 10 \cdot log_{10}(k \cdot T \cdot 1000) + NF^{dB} + 10 \cdot log_{10}(B_w) \tag{5.8}$$

where k is the Boltzmann's constant, T is the temperature in K, NF is the noise figure expressed in dB and B_w is the receiver bandwidth. Then, by counting the occurrence of the samples below the threshold, in terms of received power P_{RX}, the percentage representing the blocking probability is obtained. From the data regarding the received power and the distance travelled from the LOS, 1^{st} and 2^{nd} reflections, we can estimate, in a first instance, the RMS delay spread σ_τ, which is defined as shown here below [120]:

$$\sigma_\tau = \sqrt{\bar{\tau^2} - (\bar{\tau})^2} \tag{5.9a}$$

$$\bar{\tau^2} = \frac{\sum P(\tau_k)\tau_k^2}{\sum P(\tau_k)} \tag{5.9b}$$

$$\bar{\tau} = \frac{\sum P(\tau_k)\tau_k}{\sum P(\tau_k)} \tag{5.9c}$$

where $\tau = \frac{d_{Refl.} - d_{LOS}}{c}$ is the path delay of the j^{th} signal replica, with c the speed of light, d_{LOS} the path travelled by the LOS and $d_{Refl.}$ the distance travelled by the j^{th} signal replica. For what concerns the PDP, in order to get the behavior for which the path replicas are attenuated as the delay with respect the LOS increases, the *Curve Fitting Toolbox* of MATLAB can be exploited to fit the attenuation of each path replica and estimate a PDP analytical model. The received power of the samples representing the LOS (P_{LOS}), for a certain distance between TX-RX and over precise Martian locations, can be used to derive a path loss exponent. By varying the path loss exponent p in the following equation, we can fit the gathered samples and estimate an average path loss exponent for our results:

$$L(d) = \left(\frac{4\pi d_{TX-RX}}{\lambda}\right)^p \tag{5.10}$$

Moreover, the standard deviation of the LOS received power gives us an indication of the fluctuation of the power, due to the morphology of the area in which we are simulating, around the mean, i.e. the shadowing effect.

Other kind of attenuation, i.e. the ones cited above, can be accounted by referring to the formulation and data found in [69] and [70]. For example, the attenuation due to cloud and fog can be accounted by applying the following equation:

$$k_i = 0.4343\frac{6\pi}{\lambda}Im\left[-\frac{K_c-1}{K_c+2}\right] \tag{5.11}$$

where k_i is the attenuation coefficient (dB/km/gm/m^3) and K_c is the complex dielectric permittivity of water or ice [69]. Instead, dust storms attenuation can be expressed as in Eq.4.2. Finally, by considering the International Telecommunication Union (ITU) model about large-scale atmospheric attenuation, which is implemented in MATLAB through the *gaspl* function, we can roughly estimate the attenuation on the propagation introduced by the Martian atmosphere [121].

5.2.6 Simulation workflow

The simulator follows various steps in order to finally estimate statistically relevant and solid Martian channels to be used for testing of network infrastructures and communication systems. Indeed, with this work we aim to provide a tool through which it will be possible to correctly initialize software, such as GNU Radio, LabVIEW, Simulink and MATLAB, mostly for the evaluation of performance at data link and PHY-layer side.

In Fig.5.6, we show how the simulator is designed. As visible, the first step was the selection of the DEM representing the Gale crater to be used as input for the 3D ray tracing algorithm. The DEM is modelled to construct a 3D structure in MATLAB to be used for simulating the RF propagation (*step.1*). Then, we estimated the permittivity of a possible Martian soil, e.g. the Martian replicant soil JSC Mars-1, thanks to the Cole-Cole equations in order to electrically characterize the 3D structure. The complex permittivity value coming out from *step.2* is imported in the computation of the Fresnel coefficients. Consequently, we are able to understand the amount of power transmitted/reflected into/from the medium, i.e. the Martian soil (*step.3*). At this time, the 3D ray tracing algorithm comes into play by tracing the LOS, first reflection and second reflection of an RF signal sent from one specific location to another over the 3D structure (*step.4*). The Fresnel coefficients allow considering not only the distance travelled by each signal replicas over the terrain, but also accounting for the power lost due to the incidence of the signal on the terrain. The information about the number of generated signal replicas, the received power of each signal replicas, as well as the LOS, the total received power in a

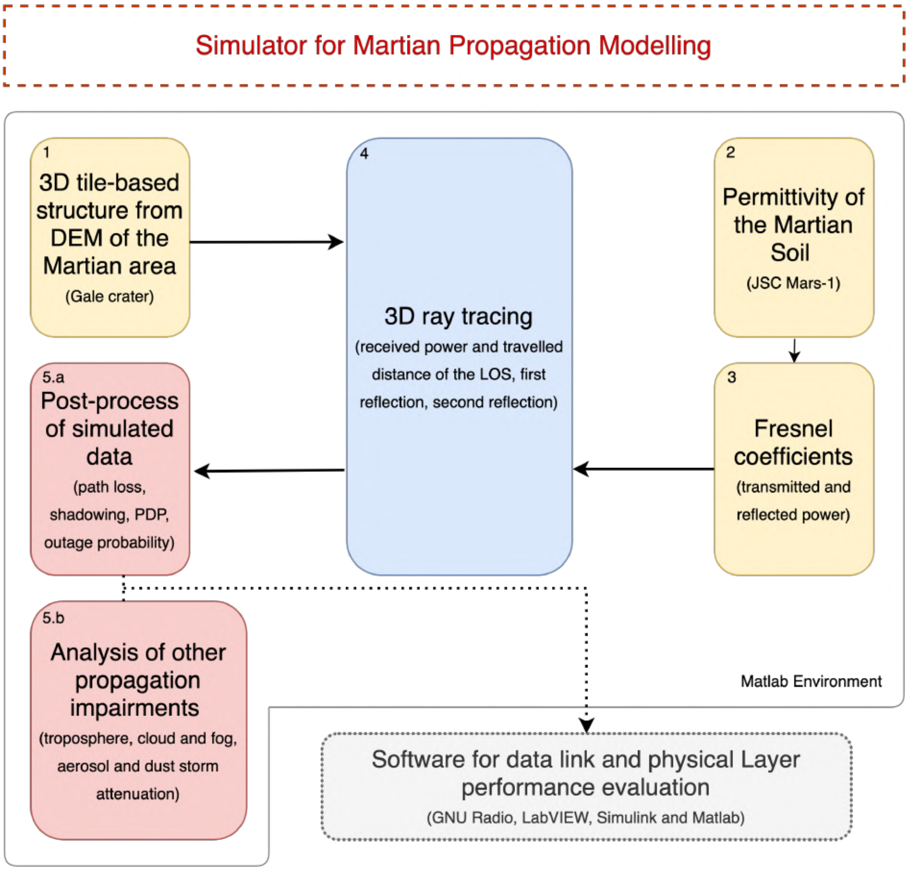

Figure 5.6: Flowgraph of the developed simulator showing all the steps from 1 to 5.a and 5.b for the evaluation of Martian propagation phenomena.

certain location and the path delays with respect to the LOS are put as input to the post-process script, which computes path losses, shadowing values, outage probability and PDPs. From both *step.5.a* and *step.5.b*, where we analyze through the propagation impairments due to the troposphere, clouds and fogs, aerosol and dust storms, we estimate a complete framework describing the effect of Mars on the RF propagation. These data become relevant when dealing with the modelling of statistical channels in commercial software as the ones cited above.

5.3 Data Acquisition, Processing and Findings

The implementation of the model, that we proposed in the previous section, will be accompanied by a collection of results spreading from the large-scale and small-scale phenomena to the computation of the outage probability, i.e. the probability of experimenting a blockage in the transmission. Moreover, to characterize the results, first, we will analyze the environment, thus the "Gale Crater - Area 1" and "Gale Crater - Area 2", from a statistical perspective. This will give us the dimension of the gathered data, in the sense that we will better understand and contextualize the results. We will start by showing the samples regarding the LOS and the estimated signal replicas for each sub-area. Then, we will compute the blocking probability for each sub-area, a discussion that will be linked to the intrinsic morphology of the sub-area. Large-scale phenomena and small-scale phenomena will be studied by averaging the whole amount of realization for each sub-area, thus focusing on the overall area. We considered transmissions with a Euclidean distance between TX-RX $d_{TX-RX} = \{100, 200\}$, which represents the radius of common terrestrial pico-cells. We selected all the possible locations distant d_{TX-RX} from the TX, which is located in the origins of the Cartesian coordinate system. To conclude, we initialized the model with the working frequencies $f = \{2.5, 39.0\}$GHz, i.e. S-band and EHF-band respectively, that are indicated by Verizon as carrier frequencies of the terrestrial 5G. Everything is designed, implemented and analyzed thanks to MATLAB.

5.3.1 Simulated testing environment

We took the DEM of the Gale crater with a resolution of $1m/px$. We cropped it into two areas of 1000×1000m, a flat one and a rocky one, called respectively "Gale Crater - Area 1" and "Gale Crater - Area 2", depicted in Fig.5.3a and Fig.5.3a. We down-sampled them in order to decrease the computational load, which is one of the major drawback of the 3D ray-tracing. We fixed the antenna height to $h = 1.5$m from the level of the ground - green dots in Fig.5.7a. The areas are divided along the diagonals into 8 sub-areas (SA), each one with a side length of 250m. It is interesting to characterize mathematically these sub-areas through common statistical measures, as mean and standard deviation, and the gradient operation, which is already shown in Fig.5.2 and better highlights the slopes of the Gale crater. From Tab.5.1 and Tab.5.2, it is easily demonstrated the deep heterogeneity of the areas, both globally and locally. The "Gale Crater - Area 1" (GA1) is situated -4500m below the "sea" level, while the "Gale Crater - Area 2" (GA2) is located on the rise of the Gale Crater central peak at more or less -3100m. However, the SAs of the GA2 extend from -3235.5m to -3071.8m. As we can see the maximum gradient for the GA2

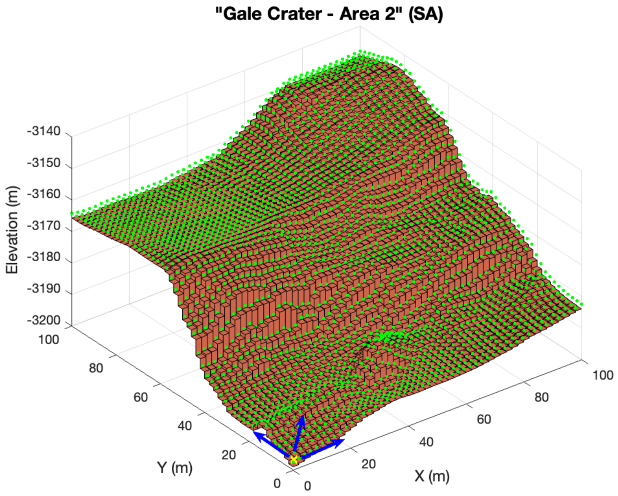

(a)
GA2 Generic Sub-Area

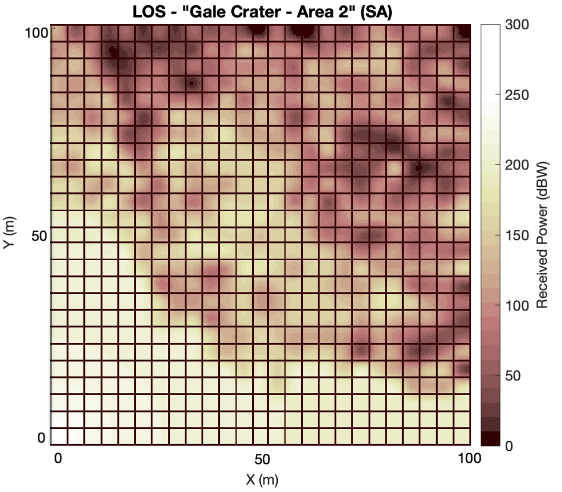

(b)
LOS over GA2 Sub-Area

Figure 5.7: (a) Tile-based structure representing a "trial" sub-area of the "Gale Crater - Area 2". The yellow cross represents the position of the TX, while the green dots show where the received power has been calculated. The blue arrows indicate the directions chosen for the computation of the received power (b) Line of sight over one testing sub-areas considered for the "Gale Crater - Area 2". In particular, this plot represents the LOS for the "trial" sub-area.

Table 5.1: Statistical representation of the “Gale Crater - Area 1” morphology.

Sub-Area — “Gale Crater - Area 1”	Mean Elevation (m)	Maximum Gradient (m)	Standard Deviation (dB)
Sub-Area 1	-4499.2	13.57	4.98
Sub-Area 2	-4500.3	10.18	2.25
Sub-Area 3	-4500.8	6.56	1.54
Sub-Area 4	-4499.0	11.80	3.84
Sub-Area 5	-4501.4	8.03	2.30
Sub-Area 6	-4502.9	5.86	1.23
Sub-Area 7	-4499.7	5.80	0.56
Sub-Area 8	-4497.1	10.50	3.68

Std Dev. stands for the fluctuation around the mean elevation.

Table 5.2: Statistical representation of the “Gale Crater - Area 2” morphology.

Sub-Area — “Gale Crater - Area 2”	Mean Elevation (m)	Maximum Gradient (m)	Standard Deviation (dB)
Sub-Area 1	-3235.5	34.44	8.15
Sub-Area 2	-3196.2	85.45	13.54
Sub-Area 3	-3149.2	98.64	13.98
Sub-Area 4	-3071.8	82.83	11.31
Sub-Area 5	-3193.7	88.01	12.69
Sub-Area 6	-3199.4	84.64	12.88
Sub-Area 7	-3157.6	84.00	12.77
Sub-Area 8	-3168.9	88.94	12.79

Std Dev. stands for the fluctuation around the mean elevation.

is the one of the SA3, which is 98.64m of excursion, while for the GA1 the maximum value is 13.98m of the SA1. From this and from the standard deviation of each SA for both the areas, we can expect severe alterations on the RF propagation for the GA2, which results to be really rocky and steep with respect the GA1. This will especially be evident in terms of path loss exponent, shadowing and overall outage probability, indeed big obstacles are the major contributions of these effects for what concerns the degradation of the signal.

5.3.2 Propagation impairments

We iterated 64 times the model in order to initialize the system with $f = \{2.5, 39.0\}$GHz and $d_{TX-RX} = \{100, 200\}$ for each SA composing GA1 and GA2. As discussed before and visible from Fig.5.6, we need to estimate the complex permittivity for the chosen frequency in order to compute the Fresnel coefficients and estimate the transmitted and reflected power into/from the terrain. In order to do that, we exploited the values in [115] for the JSC Mars1, where $\rho = 1.60$ (g/cm^3), $\epsilon_\infty = 5.30$, $\epsilon_{DC} = 2.86$, $\tau_\infty = 9.3 \times 10^-5$, $E = 0.175$(eV), $\alpha = 0.13$ and $\mu_r 1.00$.

From Fig.5.8a, the complex permittivity is $\hat{\epsilon}(2.5\text{GHz}) = 2.90 - 0.15i$ and $\hat{\epsilon}(39.0\text{GHz}) = 2.87 - 0.01i$.
Where demanded, we considered an average Martian temperature $T = 210$K, which is equal to -63°C [13]. Clearly, this is a generic assumption, which should be revised for further work by taking into account a certain fluctuation around the mean temperature. However, the noise floor variation due to the thermal excursion is within ≈ 1dB (see Fig.5.8b).
Now, let's see the gathered samples coming out from the "ray tracer". Fig.5.9 and Fig.5.10 show the samples obtained for each SA of the GA1 and GA2. The samples related to the GA1 shows, especially from Fig.5.9d, few samples with a really low received power P_{RX} with respect to a free space propagation. These values are concentrated on the SA2, SA3, SA5 and SA7. Very different is the situation of the GA2. Fig.5.10a shows samples well below the MDS (blue and red dotted lines), which will be defined in a while. For both the considered working frequencies, each SA presents very attenuated LOS propagation, except for the SA2, which from Tab.5.2 results to be the terrain with the highest standard deviation. However, the statistical analysis does not consider the TX elevation with respect to the RX. Indeed, if a TX is placed on a cliff and the RXs are situated on a valley, the transmission will not be affected by severe alterations due to the clearance of the Fresnel zone. This will be clear in the following discussion.

Outage probability

The blue dotted line and the red dotted line in Fig.5.9 and Fig.5.10 represent the MDS, where we considered for the $f = 2.5$GHz a receiver bandwidth $B_w = 100$MHz and for the $f = 39.0$GHz $B_w = 400$MHz [123]. These thresholds are $MDS(2.5GHz) = -117.23$dB and $MDS(2.5GHz) = -111.21$dB, which are used to count the samples of non-detectable signals at the RX side, thus computing the outage probability. Indeed, the outage probability is the phenomena describing the probability of not being able to detect the transmitted signal. Typically, it is mostly caused by the geometry of the environment in which the RF propagation happens, then, obviously, by the distance, which increasing increases also the probability of finding an obstruction, by the frequency (higher frequencies correspond to shorter wavelengths) and by the electrical properties of the environment. As expected, the distance acts on the probability of obstruction of the RF propagation, as well as the frequency. The data gathered for $f = 39.0$GHz exhibits lower power, as understandable, with respect to the $f = 2.5$GHz.

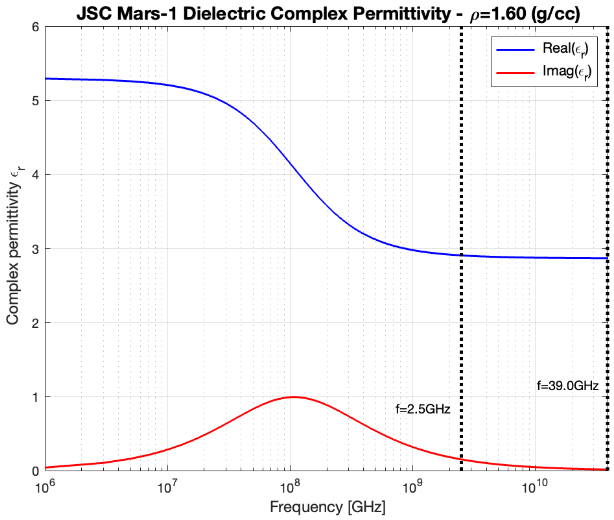

(a)

Complex Permittivity vs. Frequency

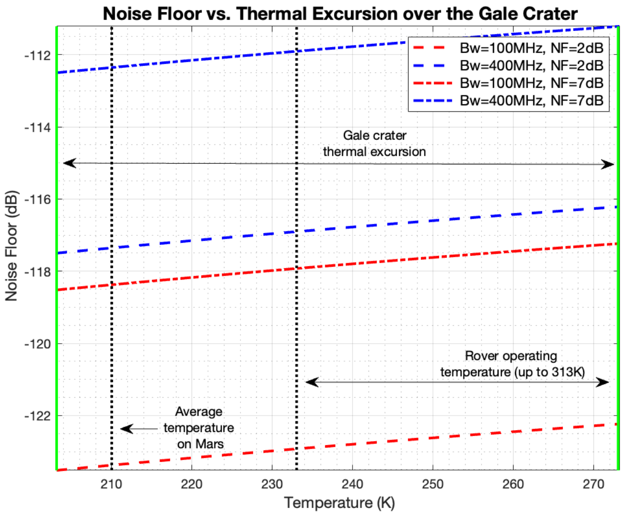

(b)

Noise Floor vs. Temperature

Figure 5.8: (a) JSC Mars-1 complex relative permittivity $\hat{\epsilon}$ in a frequency range $f_{min} = 1.0$MHz and $f_{max} = 39.0$GHz. (b) Noise floor with respect to the Gale crater thermal excursion. As visible the average Martian temperature does not represent the mean of the Gale crater thermal excursion. Rovers operate between [233, 313]K thanks to a temperature control shield (Spirit and Opportunity “heart” and “brain” were safe inside the Warm Electronics Box [122]).

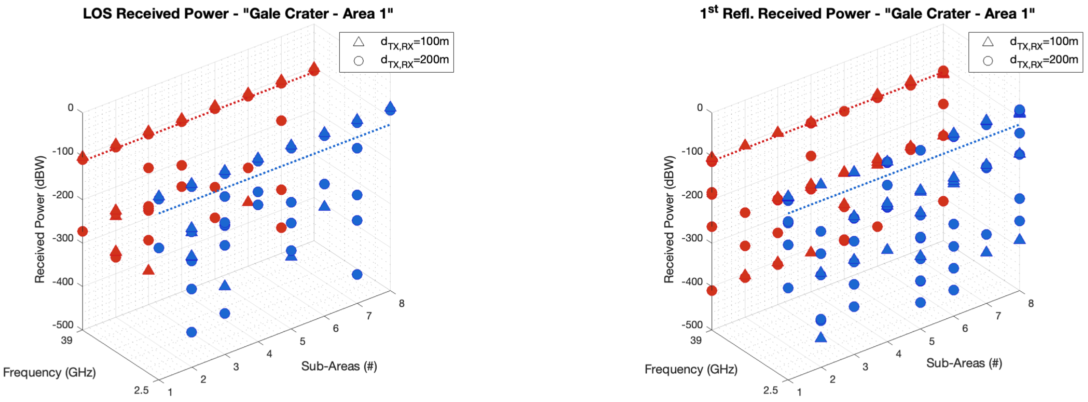

(a)
LOS Received Power

(b)
Received Power of the 1^{st} Refl.

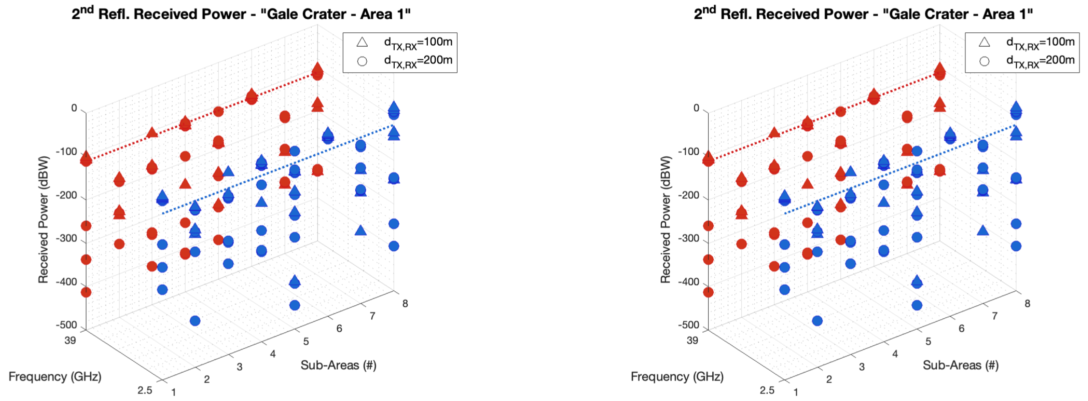

(c)
Received Power of the 2^{nd} Refl.

(d)
Total Received Power

Figure 5.9: (a) LOS received Power for the working frequency $f = \{2.5, 39.0\}$GHz vs. sub-areas composing the "Gale Crater - Area 1" (b) 1^{st} reflection received power for the working frequency $f = \{2.5, 39.0\}$GHz vs. sub-areas composing the "Gale Crater - Area 1" (c) 2^{nd} reflection received power for the working frequency $f = \{2.5, 39.0\}$GHz vs. sub-areas composing the "Gale Crater - Area 1" (d) Total received power for the working frequency $f = \{2.5, 39.0\}$GHz vs. sub-areas composing the "Gale Crater - Area 1"

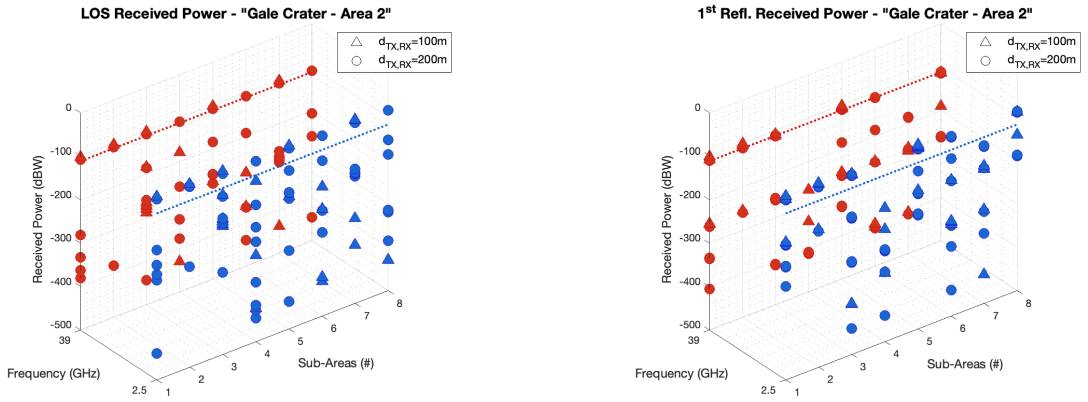

(a)
LOS Received Power

(b)
Received Power of the 1^{st} Refl.

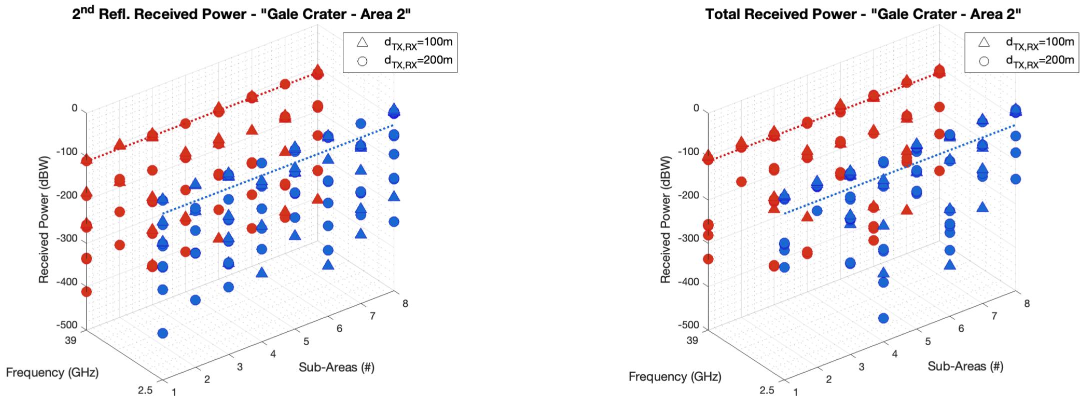

(c)
Received Power of the 2^{nd} Refl.

(d)
Total Received Power

Figure 5.10: (a) LOS received Power for the working frequency $f = \{2.5, 39.0\}$GHz vs. sub-areas composing the "Gale Crater - Area 2" (b) 1^{st} reflection received power for the working frequency $f = \{2.5, 39.0\}$GHz vs. sub-areas composing the "Gale Crater - Area 2" (c) 2^{nd} reflection received power for the working frequency $f = \{2.5, 39.0\}$GHz vs. sub-areas composing the "Gale Crater - Area 2" (d) Total received power for the working frequency $f = \{2.5, 39.0\}$GHz vs. sub-areas composing the "Gale Crater - Area 2"

The objects obstructing the RF propagation lead to higher amount of lost power for higher frequencies, thus lower wavelengths. However, the morphology of the terrain is the main actor on the increase of the outage probability. This is shown in Fig.5.11, where Fig.5.11d exhibits a blocking percentage of about 50% for the SA4. In the context of a communication system working on such an environment, we will have one out of two possibilities of not being able to even detect the signal at RX side for, more or less, both frequencies and $d_{TX-RX} = 200$m. Analyzing the SA8 of the GA2 for example, it is interesting to highlight that, despite the fact of showing low outage probability with respect to the other SAs, from Tab.5.2 we see its maximum gradient of about 89m and the standard deviation of 12.79dB, the third-highest between the other SAs. However, the TX is placed in this case at -3140m while the RXs at the two considered distances are displaced on a valley at -3200m and a hill at -3160m. This lead to that clearance of the Fresnel zone, that we briefly debated above, with respect to other cases, as for example the SA2 of the GA1, where we have lower gradient, lower standard deviation but still a higher outage probability.

Large-scale phenomena

Large-scale phenomena attenuate the signal constantly over the whole bandwidth. Among them, we can indicate the path loss, which is the attenuation due to the wavelength and the distance travelled by the signal, the shadowing, i.e. the fluctuation of the received power P_{RX} among the mean, and the atmospheric attenuation. As discussed before, for Mars we should consider also the attenuation due to the dust-storms and to the clouds or fogs. This last term will not be treated in this work, except for the brief introduction in sect.3.1.5, because it was extensively described in [69], while the other values will be analyzed in the following paragraphs.

Path loss and shadowing: We took the received powers P_{RX} for all signal samples acquired over the GA1 and GA2 and averaged them in order to characterize the propagation for each SA. The path loss exponents were then obtained by fitting the P_{RX} of the $i-th$ realization with the path loss value computed by iterating the exponent p in Eq.5.10 between $[1.8 : 0.01 : 4]$. Tab.5.3 and Tab.5.4 refer, respectively, to GA1 and GA2. Here, the morphology of the two areas strongly acts on the received power by heavily reducing it in the case of a rocky and steep environment, such as the GA2. Indeed, the GA1, from our estimation, is characterized by an average path

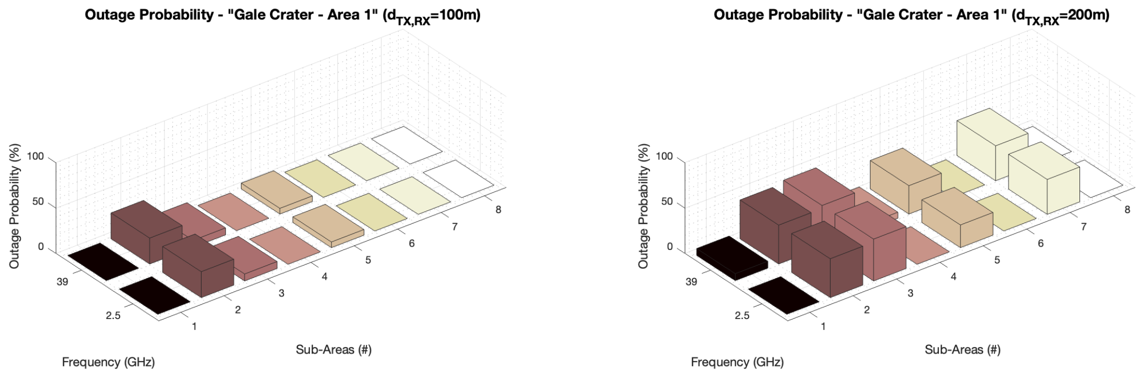

(a)
Outage probability for the GA1
(d_{TX-RX} = 100m)

(b)
Outage probability for the GA1
(d_{TX-RX} = 200m)

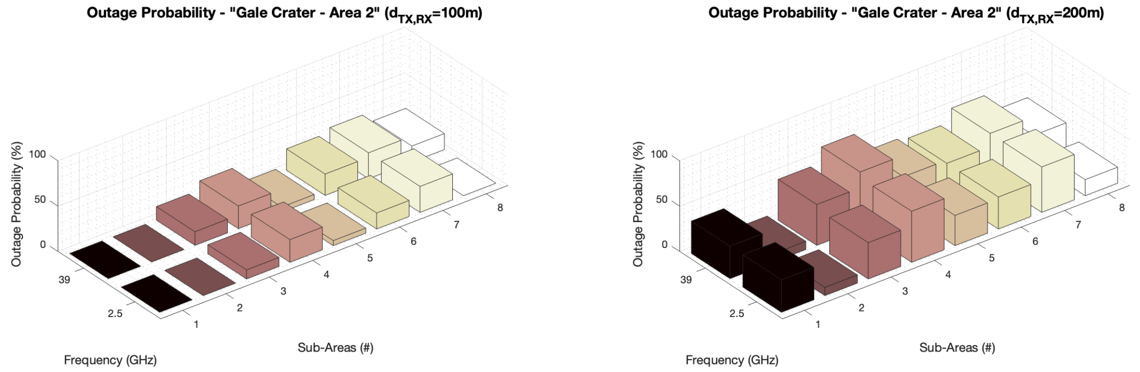

(c)
Outage probability for the GA2
(d_{TX-RX} = 100m)

(d)
Outage probability for the GA2
(d_{TX-RX} = 200m)

Figure 5.11: (a) LOS received Power for the working frequency $f = \{2.5, 39.0\}$GHz vs. sub-areas composing the "Gale Crater - Area 1" (b) 1^{st} reflection received power for the working frequency $f = \{2.5, 39.0\}$GHz vs. sub-areas composing the "Gale Crater - Area 1" (c) 2^{nd} reflection received power for the working frequency $f = \{2.5, 39.0\}$GHz vs. sub-areas composing the "Gale Crater - Area 2" (d) Total received power for the working frequency $f = \{2.5, 39.0\}$GHz vs. sub-areas composing the "Gale Crater - Area 2"

Table 5.3: Estimated path loss exponent and shadowing effect for the "Gale Crater - Area 1"

"Gale Crater - Area 1"	Mean PL Exponent	Maximum PL Exponent	Minimum PL Exponent	Standard Deviation (dB)
$f = 2.5$GHz	1.99	2.11	1.95	3.69
$f = 39.0$GHz	2.00	2.09	1.96	3.70

Std Dev. is computed on the logarithmic value of the LOS over each terrain.

Table 5.4: Estimated path loss exponent and shadowing effect for the "Gale Crater - Area 2"

"Gale Crater - Area 2"	Mean PL Exponent	Maximum PL Exponent	Minimum PL Exponent	Standard Deviation (dB)
$f = 2.5$GHz	2.63	4.56	1.96	11.79
$f = 39.0$GHz	2.57	3.87	1.97	11.99

Std Dev. is computed on the logarithmic value of the LOS over each terrain.

loss exponent of about 2, which basically is the free space path loss. This is something expected just by visualizing the area in Fig.5.3a. The lack of big rocks and cliffs lead to such kind of RF propagation. Instead, Tab.5.4 exhibits higher path loss exponents. The mean is around 2.6, which is near to the path loss exponent of a terrestrial urban area. Furthermore, with respect to the GA1, the shadowing value is way stronger reaching ≈ 12dB. The fluctuation of the received power, which is so really evident, is due to the big obstacles, in form of big rocks and cliffs, obstructing the free propagation.

Atmosphere and dust-storms: Regarding these kinds of attenuation, we exploited, first, the *gaspl* function, which is integrated in MATLAB. It performs the atmospheric gas attenuation model of ITU [121]. The atmospheric attenuation is primarily caused by oxygen and water vapor. Thus, by initializing the *gaspl* function with an average surface pressure of 610Pa [124] and the water vapor density of 0.0013g/m^3 [125], we can roughly estimate the spectral resonance of the atmospheric attenuation on Mars.

Fig.5.12a shows a peak at around 25GHz, which is mostly due to the water vapor, while between $60 - 70$GHz we have the highest attenuation caused by the oxygen molecules, as also similarly achieved in [126]. As we can see, as the distance between TX and RX increases, the attenuation increases too, following a logarithmic behavior.

Although this model is not perfectly fitted to the Martian environment - being a terrestrial model and not considering the most recurrent gas in the atmosphere of Mars (carbon dioxide, nitrogen), it gives us an in-

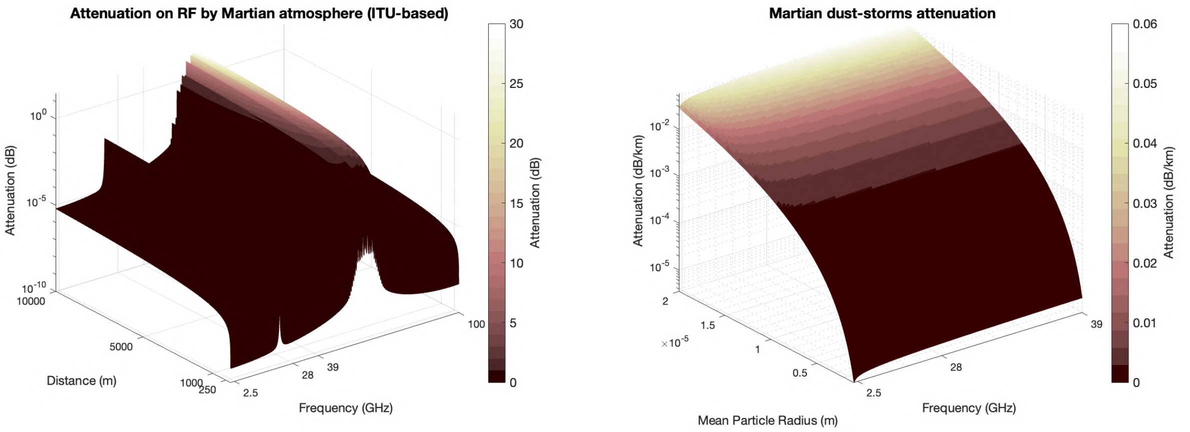

(a)
Atmospheric Attenuation

(b)
Dust-Storm Attenuation

(a) Attenuation due to Martian atmosphere for a frequency span between 1GHz and 100GHz vs. distance. (b) Attenuation due to Martian dust storms for a frequency span between 1GHz and 100GHz vs. mean particle radius N_T.

dication on the severe atmospheric attenuation for certain frequencies. $f = \{2.5,\ 39.0\}$GHz are not affected by the spectral resonance of the H20 and 02, which can cause 30dB of attenuation for a path of 10km and a working frequency between $60 - 70$GHz. Thus, they can be used as working frequencies of *ad-hoc* communication systems without particular problems for what concerns atmospheric attenuation. Moreover, for cellular networks with dimensions of hundreds of meters, the atmospheric attenuation are negligible.

The attenuation led by dust storms was computed upon the formulation of Eq.4.2 and considering the complex permittivity of the JSC Mars-1, which varies with frequency. Fig.5.12b shows that with the increase of frequency, the attenuation in dB/km remains, more or less, constant. However, as we consider a higher particle radius, we experiment a solid increase in the attenuation up to 0.055dB/km. For sizes of pico-cells, it should be irrelevant but for longer paths, and taking into account that dust-storms can cover the whole Mars, it is for sure a term that negatively affects the RF propagation.

Small-scale phenomena

The multipath fading refers to rapid fluctuations in the received signal, which causes constructive or destructive interference and shifts in the signal phase. This is due to the multiple paths that the signal travels in order

Table 5.5: Statistical representation of the path delays generated due to the 1^{st} and 2^{nd} signal reflections over the "Gale Crater - Area 1"

"Gale Crater - Area 1"	Mean Delay (s)	Maximum Delay (s)	Minimum Delay (s)	Standard Deviation
1^{st} Refl. ($d_{TX-RX} = 100$m)	5.47e-07	8.11e-07	3.40e-07	1.86e-07
2^{nd} Refl. ($d_{TX-RX} = 100$m)	9.85e-07	1.16e-06	7.79e-07	1.45e-07
1^{st} Refl. ($d_{TX-RX} = 200$m)	7.76e-07	8.34e-07	7.37e-07	3.50e-08
2^{nd} Refl. ($d_{TX-RX} = 200$m)	9.78e-07	1.11e-06	8.23e-07	1.05e-08

Std Dev. is computed on the mean path delays characterizing each sub-area.

Table 5.6: Statistical representation of the path attenuation generated due to the 1^{st} and 2^{nd} signal reflections over the "Gale Crater - Area 1"

"Gale Crater - Area 1"	Mean P_{RX} (W)	Maximum P_{RX} (W)	Minimum P_{RX} (W)	Standard Deviation
1^{st} Refl. ($d_{TX-RX} = 100$m, $f = 2.5$GHz)	1.76e-09	4.34e-09	2.73e-19	1.53e-09
2^{nd} Refl. ($d_{TX-RX} = 100$m, $f = 2.5$GHz)	2.82e-10	5.35e-10	4.08e-20	2.37e-10
1^{st} Refl. ($d_{TX-RX} = 200$m, $f = 2.5$GHz)	5.45e-10	1.31e-09	7.49e-21	6.12e-10
2^{nd} Refl. ($d_{TX-RX} = 200$m, $f = 2.5$GHz)	1.99e-10	4.62e-10	1.80e-15	2.16e-10
1^{st} Refl. ($d_{TX-RX} = 100$m, $f = 39.0$GHz)	8.33e-12	1.78e-11	2.28e-26	6.56e-12
2^{nd} Refl. ($d_{TX-RX} = 100$m, $f = 39.0$GHz)	2.64e-12	6.48e-12	9.39e-28	2.91e-12
1^{st} Refl. ($d_{TX-RX} = 200$m, $f = 39.0$GHz)	1.59e-12	3.70e-12	3.95e-27	1.37e-12
2^{nd} Refl. ($d_{TX-RX} = 200$m, $f = 39.0$GHz)	9.29e-13	2.24e-12	4.82e-20	9.88e-13

Std Dev. is computed on the mean path attenuation characterizing each sub-area.

to reach the RX. These paths are generated by the collisions of the signal with the environment surrounding it. Indeed, big obstacles reflect the propagation to other reflection points, which reflect the signal another time until, with a certain probability, it reaches its destination.
The multipath fading is then modelled through the formulation expressed by Eq.5.9c, where the RMS delay spread σ_τ expresses the difference in time between the first and last arrived signal replica. However, in this brief last discussion, we decided to concentrate on the needed values in order to model the multipath channel. Thus, in Tab.5.5 and Tab.5.7, we present the average, maximum and minimum delays experimented over the GA1 and GA2, while, in Tab.5.6 and Tab.5.8, we estimate the mean, maximum and minimum received power for the considered distances, frequencies and areas. Furthermore, the standard deviation depicts the dispersion of the sample delay and attenuation around the reported mean.

Comparing Tab.5.5 and Tab.5.7, we notice a stronger mean delay for what concerns the GA2 with respect to the GA1. The rocky area increases the possibility of having RPs between TX-RX, thus creating longer paths. The same behavior can be found when dealing with the received power $P(j)_{RX}$ of the $j-th$ replica. The nature of the GA2 impacts on the received power by, overall, lowering it, compared to the values gathered

Table 5.7: Statistical representation of the path delays generated due to the 1^{st} and 2^{nd} signal reflections over the "Gale Crater - Area 1"

"Gale Crater - Area 2"	Mean Delay (s)	Maximum Delay (s)	Minimum Delay (s)	Standard Deviation
1^{st} Refl. ($d_{TX-RX} = 100$m)	5.06e-07	8.41e-07	4.03e-07	1.73e-07
2^{nd} Refl. ($d_{TX-RX} = 100$m)	7.36e-07	9.09e-07	6.14e-07	1.14e-07
1^{st} Refl. ($d_{TX-RX} = 200$m)	7.60e-07	8.54e-07	7.02e-07	5.26e-08
2^{nd} Refl. ($d_{TX-RX} = 200$m)	9.77e-07	1.10e-06	9.10e-07	7.60e-08

Std Dev. is computed on the mean path delays characterizing each sub-area.

Table 5.8: Statistical representation of the path attenuation generated due to the 1^{st} and 2^{nd} signal reflections over the "Gale Crater - Area 2"

"Gale Crater - Area 2"	Mean P_{RX} (W)	Maximum P_{RX} (W)	Minimum P_{RX} (W)	Standard Deviation
1^{st} Refl. ($d_{TX-RX} = 100$m, $f = 2.5$GHz)	1.89e-09	3.55e-09	9.00e-21	1.65e-09
2^{nd} Refl. ($d_{TX-RX} = 100$m, $f = 2.5$GHz)	4.14e-10	1.28e-09	3.70e-15	4.82e-10
1^{st} Refl. ($d_{TX-RX} = 200$m, $f = 2.5$GHz)	9.64e-12	1.79e-11	1.69e-27	7.74e-12
2^{nd} Refl. ($d_{TX-RX} = 200$m, $f = 2.5$GHz)	2.13e-12	6.89e-12	1.44e-19	2.58e-12
1^{st} Refl. ($d_{TX-RX} = 100$m, $f = 39.0$GHz)	2.98e-10	7.21e-10	2.81e-30	2.84e-10
2^{nd} Refl. ($d_{TX-RX} = 100$m, $f = 39.0$GHz)	7.20e-11	1.22e-10	3.76e-15	4.39e-11
1^{st} Refl. ($d_{TX-RX} = 200$m, $f = 39.0$GHz)	1.36e-12	2.96e-12	9.84e-42	1.21e-12
2^{nd} Refl. ($d_{TX-RX} = 200$m, $f = 39.0$GHz)	4.40e-13	6.77e-13	8.36e-20	2.53e-13

Std Dev. is computed on the mean path attenuation characterizing each sub-area.

for the GA1. If we take a look at the $min(\overline{P}_{RX})$ (4-th column of Tab.5.6 and Tab.5.8), the values are generally well below the MDS. From this we get that such replicas do not impact on the demodulation process of the signal at the receiver side, because they are not even discernible, both for the GA1 and GA2.

The parameters on the tables can be exploited to model possible Martian channels. For example, it is possible to model channels made of 6 path replicas, divided into 3 first reflections and 3 second reflections from Tab.5.5 and Tab.5.7, which are associated to the received power values in Tab.5.6 and Tab.5.8. By normalizing the received power of the signal replicas, the PDP can be easily obtained for the two considered distances, frequencies and areas. The attention should be, however, put to the minimum received power, in order to take into account the MDS, previously detailed. This will not be covered by this work, but it will be a matter of study of future analysis.

5.3.3 Limitations

There are few limitations, which are fair to point out. First, the model has a sensible impact on the computational load. For this reason, we limited our analysis to few distances between TX-RX and we down-sampled by a factor of 5 the DEM's resolution. However, this was only a matter of time, indeed, further work will broaden the study by considering longer path lengths. Moreover, we put the thickness of the area equal to the DEM's resolution in order to give depth to our 3D structure. This is clearly an approximation for what concerns the computation of the Fresnel coefficients and the amount of transmitted and reflected power. However, it was done to not increase even more the complexity of the system, thus the time required for the simulations. To conclude, the electrical analysis, which characterizes the Martian soil in terms of frequency-dependent complex permittivity, is based on the JSC Mars-1, actually a replicant of a possible Martian sediment. Although a certain degree of approximation is introduced, this was the best choice from our perspective, as samples of Mars soil have not yet returned back to Earth. Further work will be addressed at improving and refining our simulator, while also optimizing the trade-off between complexity and performance.

5.4 Conclusions

This chapter has provided the tools for implementing a simulator for the understanding of the RF propagation over Mars thanks to high resolution DEMs and a 3D ray tracing algorithm. We deeply detailed each followed step for the design of the model, and the results were analyzed in terms of large-scale and small-scale phenomena. Moreover, we outlined a way for the computation of the outage probability, which is a really relevant term when developing and parameterizing ad hoc communication systems. Achieved results seem promising and cover the meaningful topic of providing a realistic and replicable RF propagation model on Mars, encompassing large-scale and small-scale phenomena in the presence of flat and rocky environments. The obtained parameterization of multipath propagation in terms of delays and power attenuation of the scattered replicas allows exploiting well-known channel models used in communication system simulations, like, e.g., the tapped delay one.

The discussion can be widened in future work, for instance, by cropping new and larger high resolution areas of the Martian surface and increasing the distance between transmit and receive antennas, thus experimenting longer paths, and, eventually, their height or by sweeping the working frequency. Moreover, a broadened analysis of the gathered data, also from a statistical point of view, could be helpful when selecting similar locations to test communication infrastructures to be deployed on Mars

Chapter 6

“Towards 6G” Martian Connectivity: a Space Ecosystem Providing Connectivity from Above

The main core of this thesis is represented by this chapter. 3D Networks implementing C-RAN will be extensively detailed, while trying to formulate a comprehensive framework for “Towards 6G” connectivity on Mars. After having introduced the scenario and further motivations in sect.6.1, we enter the definition of the layers composing 3D Networks in sect.6.2. Then, the implementation of C-RAN into 3D Networks is tackled in sect.6.3 and sect.6.4, where we discuss the advantages and methodologies for operating functional splits to divide the computational load between UAVs and Cubesats and optimize the utilization of resources. Sect.6.5 is devoted at analysing the computation of the session time and the optimal altitude selection, while sect.6.6 will reveal the UE-to-BS link performance in terms of spectral efficiency and expected C-BER. Trade-off occurring while designing C-RAN 3D Networks are shown in sect.6.7 and sect.6.8 presents the OAI model for network emulations, as well as results on E2E system performance. From here, we move to sect.6.9 with the resource allocation through SWaP-C metrics. Finally, thanks to an experimental testing on small PUs, we predict in sect.6.10 the amount of resources on-board of the UAV to absolve to PHY and data-link BBU tasks. Sect.6.10 will conclude the chapter, while pointing towards future developments.
This part of the thesis is partly retrieved from published journals and conference papers [1].

---

[1] Part of this chapter appears in [198–200, 202]

6.1 Scenario and Further Motivations

MARS services provided by mere satellite-based communications and solutions based on vehicles, such as landers and rovers, exhibit their limitations not only from the forward-looking perspective of settling bases on Mars but also in respect to the advancements in terrestrial communication infrastructures.

The main scope of previous generations of communication networks was to guarantee higher and higher data rates and reliability for the transmission of audiovisual information. On the other hand, 5G has been providing the infrastructure for interconnecting millions of “things” (e.g., sensors, robots, drones, etc) to realize the so-called Internet of Things (IoT). Furthermore, 5G has also been preparing a communication architecture for ultra-reliable low-latency communications in order to transmit not only audiovisual information but also haptic information for remote control and human-machine interactions. Another key aspect of 5G, which has been missing in satellite-based and space communication networks, is softwarization. The significantly greater flexibility and adaptability provided by the virtualization of hardware-based network functionalities has been fundamental to reduce Operational Expenditure (OPEX) and Capital Expenditure (CAPEX).

ITU has been writing the report entitled “International Mobile Telecommunications (IMT) Future Technology Trends Towards 2030 and Beyond”. This document will define the vision for future 6G networks. In Europe, the past year started the EU flagship on 6G called Hexa-x [127], which has the aim of shaping the future 6G objectives, architecture, technologies, and metrics towards its standardization. The current vision of 6G communication networks [128] includes the support for Augmented Reality (AR) and Virtual Reality (VR), towards the realization and deployment of holograms physically perceptible thanks to haptic data. This will imply the wide application of digital twins. Moreover, 6G will fully realize the concept of ML (3D) non-terrestrial networks (NTN). This has been changing the communication network architecture from two to three dimensions. In fact, 6G will seamlessly merge satellite, aerial and terrestrial networks in a unique dynamic and adaptive infrastructure.

On this perspective, in this chapter, we consider a new approach to tackle the fold of Martian mobile surface connectivity. The proposed solution is based on Martian C-RAN architecture for “Towards 6G” 3D Network made by four vertically and horizontally interconnected layers, namely: users equipment (UEs), fleets of drones, constellations of small satellites and orbiters at different altitudes operating in a futuristic 6G scenario. Such an architecture is fully appropriate for on-site Martian communications. This assumption is supported by various considerations:

- lower latency, which enables real-time remote control of vehicles operating on the planet [129].
- global coverage and increased RMA metrics with respect to on-ground infrastructures.
- higher throughput T_b as compared to 4G solutions and other old-fashioned technologies.
- efficient mobility management thanks to user authentication and defined handover protocols.
- improved energy efficiency attested around the 90% more than 4G one [130].
- dynamic splitting opportunities to provide guaranteed QoS for a plethora of heterogeneous applications.
- load balancing, thus better usage of energy resources and computational capabilities.
- lower outage probability thanks to the continuous presence of the LOS "from above"

In addition, both CubeSats and drones are way less bulky than eventual truss towers or BS-landers to be embarked on spacecrafts, DST vehicles. Moreover, space agencies like ESA are reasoning about the possibility of manufacturing, assembly and recycling space assets on orbit, even with a view on Mars [131]. The idea is that supplies for human deep-space explorations should be generated on orbit rather than delivered from Earth. Satellite and their payload sizes could strongly benefit from this, with their fairing not being limited by the transport vehicle. Next, possible upgrade of orbiters could be enabled, thus having a life extension, cost saving and improved space sustainability [131]. Few results, present in the literature, already suggested that in-space manufacturing (ISM) would compress the feedstock usage of more than the $\approx 78\%$ with respect to traditional spares, and, applying recycling strategies, this would reach the $\approx 98\%$ [132]. Even though we were not able to produce CubeSats, or other satellite platforms, directly on orbit, the escape velocity from Mars would make it easier to get out of the atmosphere, through something like a common space shuttle, with respect to being on Earth. To conclude, the thin Martian atmosphere could play a key role in the positioning of satellite into orbits. We will extensively talk about this in the prosecution of the chapter.

For all these reasons and suppositions, a concrete 'Towards 6G" scenario of Martian communications will be defined, along with the corresponding network architecture. To this aim, we followed a top-down approach for the realization of a framework characterizing 3D Networks implementing C-RAN, spreading from theory, simulations, emulations to conclude with hardware experimentation. A first preliminary analysis will assess the feasibility of splitting options by meeting stringent specification in terms of latency and bandwidth. We will compute the required CubeSat altitude with respect to the propulsion force needed to maintain the orbit. Next, the estimation of the elevation angle and the resulting session time available from CubeSat and the hovering UAV will be made, while fixing the altitude. Consequently, we will correlate drag force and session time to find the best CubeSat orbit altitude and provide the main architectural parameters.

Moving on, the CPRI compliance will be assessed by designing a communication system capable of achieving those large bandwidths imposed by the various splitting options. By referring to the RF model in Chapter 5, we will estimate the spectral efficiency for the UE-to-UAV (UE-to-RU) with respect to a selected QoS and a variable, in terms of decoding iterations and code rate, low-density parity-check (LDPC) channel coding.

Next, we will detail an in-depth analysis regarding numerous trade-offs to be accounted when selecting orbital altitudes, like designated lifetime, coverage, session time, latency etc. The system performance will be tested by means of an OpenAirInterface (OAI) emulator in order to compute the E2E throughput, delay, packet loss, computational burden and memory usage related to each single network node. Such an evaluation has been obtained by exploiting an LTE build on OAI, installed on three machines emulating the UE, the remote, distributed and centralized unit (RU, DU, CU) respectively, along with the Next Generation Core (NGC) network. More precisely, due to the lack of available servers, we virtualized the NGC in a docker inside the machine acting as DU and CU.

Last but not least, we will face the issues related to the computational burden inherent to the various available splitting options in 3D Networks from an experimental viewpoint. In particular, we focus our attention on the most critical point of the network chain: the UAV. Unfortunately, UAVs can host very limited resources and their service continuity represents a potential bottleneck for the entire system. A complete BBU-pool implementing all the required functionalities would require a power consumption of $1-2$kW, that is mostly unfeasible. Therefore, it is of paramount importance to move a proper amount of computational load to the upper-layer of the network. Our experimental setup consists of a laptop (MacBook Pro equipped with Apple M1 Pro chip), Raspberry Pi processors (3B+ and 4B series) and a multimeter, which is used to check the voltage swing and current flow. We take advantage from the NR DL-SCH and PDSCH implementation offered by the 5G toolbox of MATLAB 2021b version. We measure first the achievable throughput per slot and processing time to perform the whole NR DL-SCH and PDSCH transmission. We then deploy a 8 × 1-TX DL-SCH and PDSCH on low-budget PUs, namely the Raspberry Pi (RP) 3B+ and 4B with, respectively, $1\,GB$ and $2\,GB$ of RAM. The RPs are overclocked to visualize the processing improvement. Thanks to the *perf* command-line utility, we derive the instruction count (IC) per program, meaning the number of instructions composing the 8×1-TX functionalities chain. The mega instructions per second (MIPS), that should be assured by the PUs, are estimated upon an achievable clock frequency and expected processing time per single slot of the 5G NR frame. From this, the number of PUs needed to equip the UAV with is easily obtained by looking at some PU data sheets. Thus, we finally compare size, weight, power and cost (SWaP-C) metrics for a possible system design based on RPs and on Nvidia Jetson Nano, this last one used as benchmark.

In such a manner, an organic analysis for discussing the feasibility of 3D Networks for future 6G connectivity on Mars will be completed. Useful practical hints for the development of such complex systems will be provided. Of course, the same findings and concepts in this chapter could be reused and adapted for the next terrestrial 6G standard, suggesting an interesting technology dual-use (see Fig.6.1).

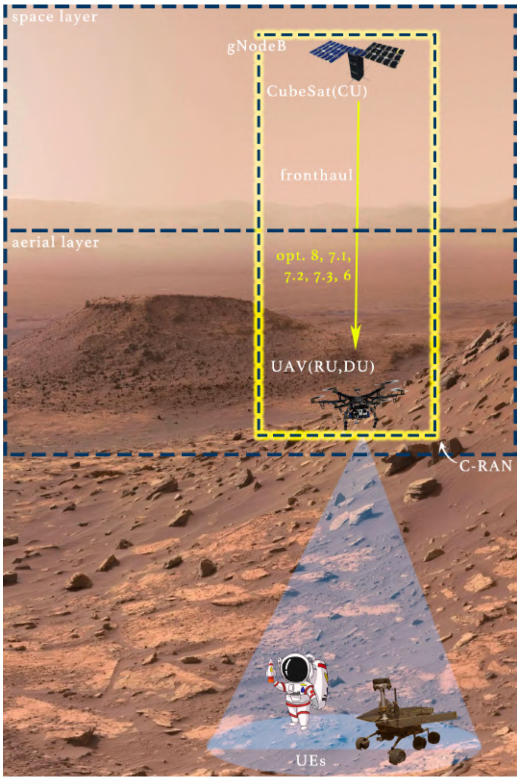

(a) Martian missions

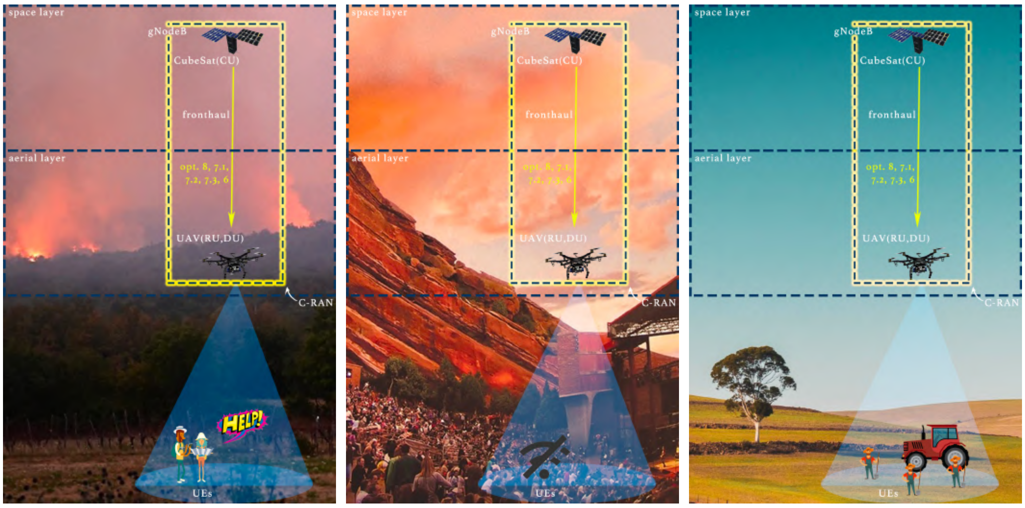

(b) Disaster areas (c) Massive events (d) Agricultural areas

Figure 6.1: Possible use-cases supported by 3D Network implementing C-RAN to bring efficient mobile connectivity. (a) Connectivity for future (human) activities on Mars. (b) Connectivity for disaster and high-priority areas. (c) Connectivity for massively populated events. (d) Connectivity for agricultural applications.

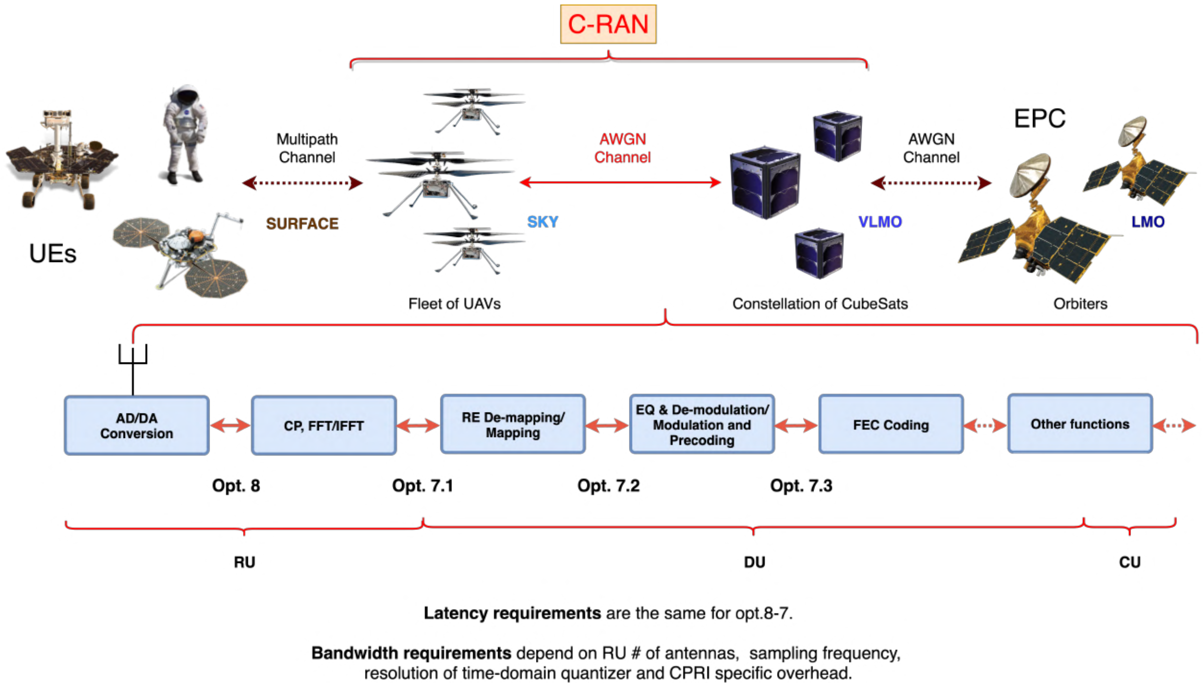

Figure 6.2: Pictorial representation of the 3D Network C-RAN architecture for "Towards 6G" Connectivity on Mars

6.2 3D Network Layers and Composition

Four main segments composes the whole network architecture by starting from the ground and reaching the orbits, as shown in Fig.6.2. The communication will vertically and horizontally happen between the independent segment. Horizontal communications, which are not the subject of this work, will guarantee dynamic failure recovery and virtualized functions distribution.

- *On-ground layer*: on the surface there will be, and already are present, static and dynamic machines, e.g. landers and rovers. These devices are equipped with a scientific payload, which is usually constituted by variegate sensors, to accomplish pre-defined missions. Usually, the equipment has to gather data from the soil and forward them through a direct link to the Earth. However, future missions will need to deliver data to a base or to astronauts to post-process it *in-situ*. Vice-versa, astronauts could need to remotely control in real-time vehicles to reach certain locations of interest. For these reasons, machines and astronauts are treated as end-users, thus UEs, of our architecture.

- *Aerial layer*: UEs will need low-latency, wideband anywhere-anytime, and robust connectivity, which will be provided by the binomial composed of UAVs, i.e. drones, and small satellites in the form of CubeSats, coordinately acting as gNodeB of the aerial-to-spatial network cell. Due to the lack of presence of high-altitude pseudo-satellites (HAPS) platforms, we will not insert HAPS in the proposed architectural design, although it cannot be excluded their future use on Mars. Fleets of UAVs will fly over sensible points to acquire data from the UEs. Eventually, they will be equipped with a scientific payload too to capture photo and videos of Martian areas. Dangerous or human-unreachable zones, such as the poles or mountainous locations, could be reached and investigated thanks to UAVs.
  Although they will embark solar panels and batteries to harvest and store energy, realistically, one of the main issues with their usage will be the power consumption. Thus, the scientific payload as well as the on-board transceiver should consume less as possible to save energy. We will detail later how to deal with the aforementioned trade-offs.

- *Very-LMO layer*: as we will suggest, it will be possible to exploit VLMO and deploy CubeSats at a very-low Martian altitude, while paying for the consumption of resources to counteract the drag force. Higher orbits would be preferable to increase satellite lifetime, coverage, thus reducing the cost. On the other hand, this would affect splitting operations that need to be performed within a narrow time window. We will touch these trade-offs later on. 1U CubeSats are $10x10x10$cm sized without considering the space occupied by solar panels and antennas. As shown in Tab.6.1, they can be arranged into multiple units, such as 6U, 12U, but also 1.5U, 2U, 3U and so on. Despite larger sizes cost more than low-sized, usually commercial, CubeSats, they can embark more weigh, which would guarantee to host a huger scientific payload, batteries and also really powerful PU units. This means that they could take on the responsibilities of performing the major part of the C-RAN virtualized functions. As drones will mostly be the RU of the BS, CubeSats will take charge of heavy DU and CU functions. Respectively for downlink and uplink communications, they will receive or forward data from/to the NGC, installed on orbiters in the higher LMOs.

- *LMO layer*: orbiters will reside in the LMO. They are way huger

Table 6.1: CubeSat Dimensions and Propulsion Systems

	Form Factor	Size	Weight	Nominal Thrust
Commercial CubeSat	1U	$10x10x10cm$	$1.33kg$	$1mN$ (off-the-shelf)
MarCO CubeSat	6U	$20x30x10cm$	$13.5kg$	$(10x4)mN$ (Vacco's MiPS)
Hybrid CubeSat	12U	$20x30x20cm$	$25.0kg$	$44.4N$ (JPL HT)

and heavier than CubeSats. Consequently, they will resent more from the drag force even if we increase their orbital altitude. However, as demonstrated by [133], electrical propulsion can express enough force to maintain orbits around 150km. In this regard, E2E delays will easily be managed to serve low-latency applications. Indeed, the propagation delay introduced by the UE-to-NGC path will roughly be half of a millisecond, if we consider an unlikely average elevation angle $\varepsilon = \pi/2$ between the nodes involved in the communication.

6.3 C-RAN Implemented on 3D Networks

C-RAN is the technology pooling baseband resources between the base stations (BSs) [134]. Contextualizing this sentence to our scenario, an aerial drone and an orbiting CubeSat will operate in accordance, and one after the other, in order to reproduce common 5G RU, DU and CU functionalities.

Fig.6.2 shows the functions operated at the lower layers of the C-RAN. At the PHY-layer side, depending on the direction of the data flow (downlink or uplink), first, an analog-to-digital or digital-to-analog operation is performed, as well as the insertion or removal of the cyclic prefix (CP), the mapping or demapping of the resource element (RE) and the modulation or demodulation plus the equalization happening in the frequency domain. Forward error correction (FEC) (de)coding is done at the data-link layer. This operation is particularly complex and time-consuming, especially for the iterative decoding. Indeed, from [135], it is fascinating to notice how the LTE encoding and, with a particular emphasis, the decoding operations are by far the most time-consuming ones in the PHY and data-link layer, thus the ones bringing in the heaviest computational load. Other processing time is due to the FFT/IFFT operation, while the (de)modulation takes less time to be performed [135].

The UAV and the CubeSat, that will mount software defined radio (SDR) transceiver and antennas for the transmitting and receiving phases, will host C-RAN virtualized functions by splitting the processing chain at low/high PHY layer side. 3GPP, in the latest releases, highlighted various splitting options to install C-RAN into non-dedicated hardware. Rather than virtualizing the whole C-RAN processing in a single node, which would need huge computational and energetic resources, it becomes feasible to divide the computational load into diversified hardware, such as a drone and a CubeSat. Due to the limited resources, that we imagine having on UAVs, we focus our attention towards low-level splitting options (opt.8-6). Reducing the computational load on UAVs means saving energy, which can be allocated to increase their limited flight time or use the on-board scientific payload. For this reason, we aim to move the most time-consuming operations on orbit, such as the FEC decoding. We will later see how this choice would impact on the system design.

However, this process is not straightforward as it implies tight requirements to be met. Indeed, as extensively described in [136], there are two main burdens that have to be accounted when implementing flexible C-RAN: *latency* and *bandwidth*. The front-haul (FH), i.e. the fiber connection between the RRH and BBU in terrestrial LTE, has to offer low-latency high-bandwidth links to forward the received traffic (for our case of study, the FH is dealt as a line-of-sight (LOS) wireless radio link between the drone and the CubeSat).

Precisely, C-RAN needs to deliver data from the UE to the BS, or vice-versa, within a limited amount of time, a delay budget T_{radio}, which varies accordingly to the application we want to serve. For 5G NR and low-latency applications, ITU fixes the one-way latency $T_{radio} = 0.5$ms [137]. Adapting the formulation of T_{radio} ([138]) to 3D Networks, the following relation holds:

$$T_{radio} = t_Q + t_{FA} + t_{tx} + t_{bsp} + t_{mpt} \tag{6.1}$$

$$t_{tx} = t_{tx}^{UE-UAV} + t_{tx}^{UAV-CS} \tag{6.2}$$

$$t_{bsp} = (t_{bsp}^{UAV} + t_{CPRIp}^{UAV}) + (t_{bsp}^{CS} + t_{CPRIp}^{CS}) \tag{6.3}$$

t_Q being the queuing delay, t_{FA} a delay contribution due to frame alignment, t_{tx} the transmission delay, t_{bsp} and t_{mpt} the baseband processing latency and the user processing latency, respectively. Referring to our nodes implementing C-RAN, under the hypothesis that all the delay terms are negligible except the transmission delay, the maximum allowed distance between UE and CubeSat would be $d_{UE-CS} = 150$km. Consequently, the CubeSats should orbit in the LMO. However, assuming the processing delay to be null is an unrealistic consideration, in particular, when dealing with complex functionalities, as the baseband processing, and limited resources available on UAV and CubeSats.

And that being the case, the altitude has to be decreased, thus impacting on lifetime and coverage, to save time for data processing, consequently improving the system QoS. Indeed, assuming the number of FEC decoding iterations k_{iter} inversely proportional to the BER, from the analytical formulation in [139], t_{bsp} can be expressed as follows:

$$t_{bsp} = T_{radio} - t_Q - t_{FA} - t_{tx} - t_{mpt} = \frac{L \cdot F \cdot k_{iter}}{pO} \tag{6.4}$$

where the other undefined terms are p the clock rate of the processor, O the processor efficiency in operations per cycle, L the code block length and F the decoder complexity [139]. It is now clear that as we reduce the transmission delays, we can sensibly increase the number of decoding iterations, which roughly means a desired decrease in the coded bit error rate (C-BER). However, the shorter is the distance d_{UAV-CS}, the higher will be the required force to be expressed by the propulsion system at CubeSat side to maintain a lower altitude. This will consume more energy resources to counteract the drag force, as we will see in the next sections. The optimal balancing of such a trade-off is a no trivial problem.

We just mentioned that the C-RAN architecture also requires a broadband front-haul link between the RRH and the cloudified BBU, especially in 3D Networks, where the front-haul must be wireless, and its QoS may be bounded by the CubeSat and UAV payload limitations. Again, this is why splitting operations have been introduced. Indeed, splitting the processing chain at different levels translates into a lowered mid-haul (front-haul when decoupling BS into RU-DU-CU) data rate and an optimized usage of computational and energy resources. This means that, as we split the computational load $\mathbb{L}$, we are also splitting the radio equipment size, weight and power consumption between the UAV and CubeSat. In Eq.6.3, t_{bsp} is the sum of $t_{bsp}^{UAV} + t_{CPRIp}^{UAV} + t_{bsp}^{CS} + t_{CPRIp}^{CS}$, which are the split baseband processing time and CPRI processing time at UAV and CubeSat side, respectively. The latter has been reported [140] to be $t_{CPRIp}^{UAV} + t_{CPRIp}^{CS} = 10\mu$s, considering the round-trip time of terrestrial fiber connections. Later on, t_{bsp}^{UAV} will be referred to the baseband processing per slot. As clearly understandable, the study regarding the delay terms in Eq.6.3 becomes fundamental for the proper design and functioning of 3D Networks. Saving time from the overall budget means to improve in a sense or in another the solidity of 3D Networks.

6.4 Splitting Options for C-RAN 3D Networks

3GPP identified eight possible functional split options (the low-layer ones are depicted in Fig.6.2). Here, split option 1 (i.e., opt.1) detaches the Packet Data Convergence Protocol (PDCP) from the network layer of Radio Resource Control (RRC), while opt.2 does the same between the Radio Link Control (RLC) and the PDCP. Opt.3 is operated within the RLC and opt.4 divides the Media Access Control (MAC) from the RLC, while opt.5 separates the Lower MAC from the Upper MAC. The last splitting operation within the data-link layer is opt.6, which is done before the Forward Error Correction (FEC). From opt.7-8 we move to the physical (PHY) layer. Opt.7.3 is performed between the detection, equalization, modulation, pre-coding and the FEC, while opt.7.2 goes deeper into the PHY-layer detaching the resource element (RE) mapping, or demapping, functions. The CP, insertion or removal, and Fast Fourier Transform (FFT), or Inverse FFT (I-FFT), are implemented in RU if opt.7.1 is considered. At the end, opt.8 is placed just after the analog-to-digital (AD), or digital-to-analog (DA), conversion. The above cited opt.8-6 are of particular interest, at least for our purposes, being focused on the implementation of C-RAN RU functions on UAVs to provide mobile connectivity with augmented energy efficiency. Indeed, power consumption will be a key aspect on Mars surface. Still in sect.1.1, we saw that energy will be a driving theme for the exploration of Mars. At the present time, for machines and drones such as the MHS, most of the time, energy is stored into batteries, which are recharged through solar panels. In the last few days, we have had news about the InSight lander, which is gradually shutting down due to dust covering its big solar panels, thus prohibiting the energy harvesting [141]. Thus, in order to maintain high usability of drones, for instance (but this is valid for each other devices on Mars), and make them fly for consistent time, we should consume less power as possible for any other kind of processing and general operations. As we will see, the low-PHY splitting options will have a high impact on our overall architecture by dividing the computational load between communicating nodes and optimizing the re-

source utilization.
Once again, strict latency and bandwidth requirements have to be met to correctly split the BBU processing chain and to not degrade the E2E system performance. Let us discuss them. *Latency requirement*: The Small Cell Forum (SCF) defines the one-way maximum latency, with $t_{tx=\tau}^{UAV-CS}$, $\tau_{ideal} = 0.25$ms as for the ideal case and $\tau_{near-ideal} = 2$ms for the near-ideal case (both valid for low-level functional splits), $\tau_{sub-ideal} = 6$ms and $\tau_{non-ideal} = 30$ms, respectively, for the sub-ideal and non-ideal case [142]. For the 3GPP [143], the latency for splitting opt.6-8 should be less than 0.25ms, while for opt.5 should be of the order of hundreds of microseconds, for opt.4 around 0.1ms, for opt.2-3 ranging from $1.5ms$ to $10ms$ and, finally, for opt.1, equal to 10ms. The authors of [144] state that, for opt. from 1 to 5, the requirements to be accounted for designing the architecture and the communication links are way relaxed with respect to the ones needed for opt.8-6. It seems, then, that the critical latency is $\tau_{ideal} = 0.25$ms [145]. This last will be assumed as our reference value.
To be noticed is that allowing splitting opt.8, which however could be unfeasible due to the prohibitive front-haul data rate, is meant to ensure the possibility of meeting most of the requirements of the other splitting operations. Depending on system requirements, there could be necessary to operate one or another splitting option.
Bandwidth requirement: Front-haul is not only latency constrained, but also bandwidth constrained. As pointed out in [145], the front-haul capacity is a C-RAN bottleneck. This is due to the required data rate, and for extension bandwidth, which does not correlate with the traffic load at the RU (RRH in the old LTE notation). Instead, it is formulated like this

$$D_{CPRI} = N_{ant} \cdot f_s \cdot N_{Q,opt.8} \cdot 2 \cdot (\psi_{CW} \cdot \psi_{LC}) \tag{6.5}$$

with $= N_{ant}$ the number of antennas at RU side, f_s the sampling frequency, $N_{Q,opt.8}$ the quantizer resolution in bits/samples, ψ_{CW} the CPRI control words overhead and ψ_{LC} the line-coding overhead [146].
Now, by comparing the data rate to be supported at the FH for the LTE 10MHz, LTE 20MHz and the Verizon 5G sampling frequency f_s of about $153.6MHz$, we can highlight an exponential increment plus a linear scaling if we increase the number of antennas N_{ant}, as visible in Fig.6.3a. We fix as commonly accepted values $N_{Q,opt.8} = 15$, $\psi_{CW} = 16/15$ and $\psi_{LC} = 10/8$ [145]. For example, $N_{ant} = 8$ would lead to $D_{CPRI} \approx 50$Gbps that for our wireless link and considering the modern technologies could

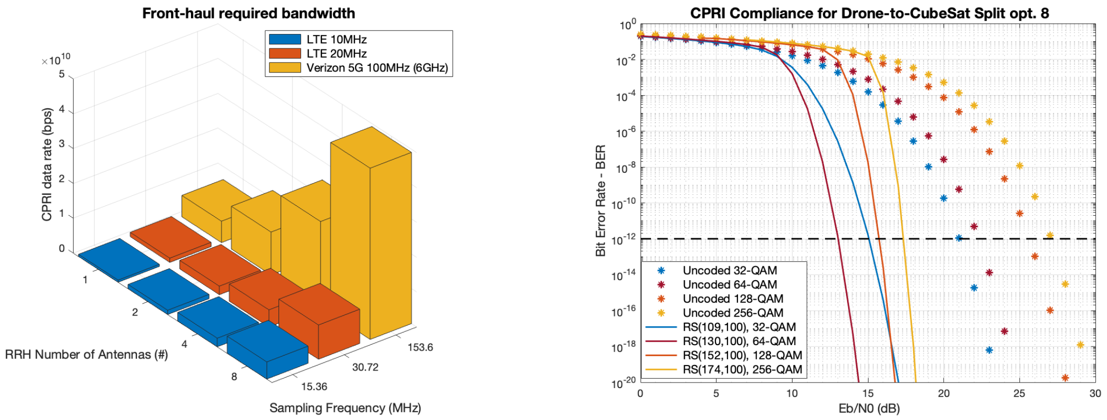

(a) Front-haul data rate (b) Coded BER vs Eb/N0

Figure 6.3: (a) LTE vs Verizon 5G required data rate at the front-haul (b) Plot showing the performance of various RS coded QAM configuration to reach the expected $QoS = 10^{-12}$

be prohibitive to be provided. Nevertheless, we suppose to have $N_{ant} = 1$ for the link evaluations in sect.6.6, which leads to $D_{CPRI} \approx 6.14$Gbps.
One might argue that by supporting higher-layer splitting options, it is possible to strongly reduce the mandatory data rate at the FH, thus lowering the overall complexity of the system required for $D_{CPRI} \sim 6.14$Gbps. Still assuming a single antenna at the UAV side and the typical Verizon 5G sampling frequency of 153.6MHz, the data rate to be transferred through the UAV-to-CubeSat link approximately equals 2.6Gbps for opt.7.1, 447Mbps for opt.7.2, 396Mbps for opt.7.3 and, finally, 104Mbps for opt.6 [145]. However, we aim to support the bandwidth for opt.8 to allow each possible splitting option, hence, to increase the degrees of freedom of future applications adopting this architecture.
The Common Public Radio Interface (CPRI), which on terrestrial mobile networks regulates the flow of traffic in the FH, despite indicating the Reed Solomon (RS) as a standard for FEC coding, does not provide information for the design of a RF wireless satellite link.

6.4.1 Meeting latency requirement to dimension C-RAN-based 3D Networks

The feasibility of the splitting opt.6-8 is assessed by meeting the latency requirement in terms of $\tau_{ideal} = 250\mu s$ [143]. Thus, to support low-latency applications in the order of 1-10 ms, τ_{ideal} should be our reference in the system design. This means that the distance d, lately referred to as slant

range, between UAV and CubeSat (CS), in a point-to-point communication, can range up to $d_{max} \sim 75$km, given that $d = c \cdot \tau_{ideal}$ with c the speed of light.
By starting from this assumption, the proposed methodology for this section can be resumed in the points listed below:

1. evaluating the Martian atmospheric density ρ by sweeping the altitude value.
2. computing the approximate drag force F_{drag} over 1U, 6U, 12U CubeSat, thus understanding the needed propulsion force F_{prop} to correct and maintain the orbit.
3. analyzing the acceptable elevation angle ϵ, while computing the slant range d between the hovering UAV and the orbiting CubeSat, to assure τ_{ideal}.
4. obtaining the maximum session time t_s between UAV and CubeSat.

First of all, we estimate the Martian atmospheric density $\rho(h_{CS})$ through the model in [133], i.e.:

$$\rho(h_{CS}) = \rho_0 \cdot e^{\frac{-h_{CS}}{H}} \tag{6.6}$$

where $H = 11.1$km the atmosphere's scale height [13], h_{CS} the CubeSat actual altitude and ρ_0 two reference densities, a low one $\rho_0 = 0.0001\text{kg/m}^3$ and a high one $\rho_0 = 0.001\text{kg/m}^3$. The drag force F_{drag} is expressed as below [133]:

$$F_{drag}(h_{CS}) = \frac{1}{2}\Bigg(\rho(h_{CS}) \cdot v_{CS}(h_{CS})^2 \cdot C_D \cdot A_{CS}\Bigg) \tag{6.7}$$

and computed accordingly to different size of CubeSat. Indeed, v_{CS} stands for the circular velocity of CubeSat, which is the following [147]:

$$v_{CS}(h_{CS}) = \sqrt{\frac{G \cdot M_{Mars}}{h_{CS} + R_{Mars}}} \tag{6.8}$$

with $G = 6.67 \times 10^{-11}\text{Nm}^2/\text{kg}^2$ the gravitational constant, $M_{Mars} = 6.39 \times 10^{23}$kg and $R_{Mars} = 3389.5 \times 10^3$m, respectively, the planet mass and radius [13], $C_D = 2.0$ is the drag coefficient, A_{CS} is the CubeSat cross-section obtained by the formulation, valid for parallelepiped-shaped spacecraft, in [148]:

$$A_{CS} = \frac{1}{2}\Bigg(S_1 + S_2 + S_3\Bigg) \tag{6.9}$$

with S_1, S_2, S_3 the mean area of the visible CubeSat surfaces, which, however, does not consider the area occupied by the possible presence of the solar array. The considered dimensions are $10x10x10cm$ for 1U, $20x30x10cm$ for 6U and $20x30x20cm$ for 12U.

At this point in order to evaluate the minimum orbital altitude of CubeSat, under which it would be impossible to counteract the drag force and maintain the orbit, it is necessary to know the force F_{prop}, expressed by the thruster installed on the small satellite platform. F_{prop} should be, at least, equal to F_{drag} to be able to continuously correct the satellite orbit. In Tab.6.1, we show some commercial and non-commercial thrusters and their impact on the minimum allowed altitude.

As briefly introduced in the list at the beginning of this section, the minimum altitude is the minimum acceptable distance d_{min} between UAV and CubeSat. Indeed, while we consider for simplicity the UAV hovering on the Martian surface, CubeSat is circularly orbiting, in LMO or VLMO, around Mars at the velocity described in Eq.6.8. Consequently, CubeSat will be in the nearest point to the UAV only when the elevation angle, i.e. the angle between the line of sight (LOS) connecting CubeSat and UAV and the relative horizontal plane, is $\epsilon = \frac{\pi}{2}$. The LOS length d is also called slant range and it is formulated by starting from the law of cosines, and customized to fit our problem, as follows [149]:

$$\begin{aligned}(R_{Mars}+h_{CS})^2 = \\ (R_{Mars}+h_{UAV})^2+d^2-2(R_{Mars}+h_{UAV})cos(90+\epsilon)\end{aligned} \tag{6.10a}$$

$$\begin{aligned}(R_{Mars}+h_{CS})^2 = \\ (R_{Mars}+h_{UAV})^2+d^2+2(R_{Mars}+h_{UAV})sin(\epsilon)\end{aligned} \tag{6.10b}$$

$$\begin{aligned}\frac{(R_{Mars}+h_{CS})^2}{(R_{Mars}+h_{UAV})^2} = \\ \left(1+\frac{d^2}{(R_{Mars}+h_{UAV})^2}+2\frac{sin(\epsilon)}{(R_{Mars}+h_{UAV})}\right)\end{aligned} \tag{6.10c}$$

$$\begin{aligned}\frac{(R_{Mars}+h_{CS})^2}{(R_{Mars}+h_{UAV})^2} = \\ \left(cos^2(\epsilon)+sin^2(\epsilon)+\frac{d^2}{(R_{Mars}+h_{UAV})^2}+2\frac{sin(\epsilon)}{(R_{Mars}+h_{UAV})}\right)\end{aligned} \tag{6.10d}$$

$$\frac{(R_{Mars}+h_{CS})^2}{(R_{Mars}+h_{UAV})^2}-cos^2(\epsilon)=\left(sin(\epsilon)+\frac{d}{(R_{Mars}+h_{UAV})}\right)^2 \tag{6.10e}$$

$$d=\left[\sqrt{\frac{(R_{Mars}+h_{CS})^2}{(R_{Mars}+h_{UAV})^2}-cos^2(\epsilon)}-sin(\epsilon)\right]\cdot(R_{Mars}+h_{UAV}) \tag{6.10f}$$

where h_{UAV} is the drone height, as visible from Fig.6.4, and the elevation angle ϵ is defined in the range $[0,\, \frac{\pi}{2}]$. The minimum allowed elevation angle ϵ_{min} is found by searching, in the matrix representing the slant range d, the maximum LOS distance $d_{max} = c \cdot \tau_{ideal}$ between UAV and CubeSat for each h_{CS} and h_{UAV}.

Thanks to trigonometric functions, the session time between UAV and CubeSat, i.e. the time that elapses between having $\epsilon = [\frac{\pi}{2},\, \pi - \epsilon_{min}]$, can be estimated. Such a range is inherent to the slow handover mode, where a UAV re-connects to a new CubeSat close to the Zenith when the distance from the previous CubeSat exceeds d_{max}. First, the angle θ in (rad) subtended by the circular minor arc, representing the orbit within $\epsilon = [\epsilon_{min},\, \frac{\pi}{2}]$ with radius $r = h_{CS} + R_{Mars}$ and center in the Earth's core,

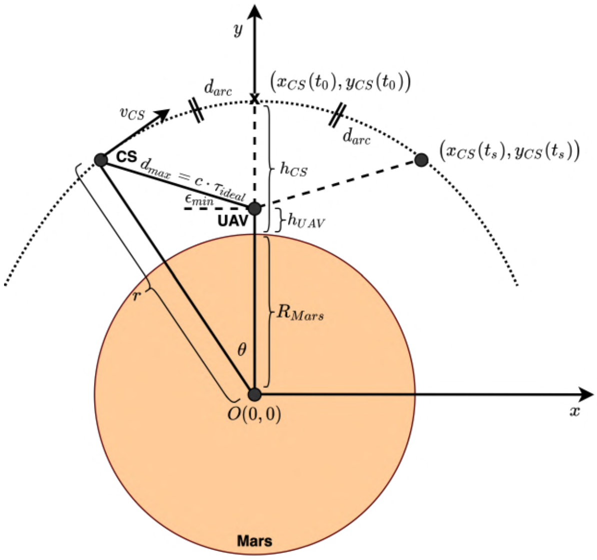

Figure 6.4: 2D geometrical representation of the circular arc in which communication happens in session time t_s between CubeSat and UAV.

is found in the following manner:

$$(R_{Mars} + h_{CS}) sin(\theta) = d_{max} cos(\epsilon_{min}) \tag{6.11a}$$

$$\theta_{max} = asin\left(\frac{d_{max} \cdot cos(\epsilon_{min})}{R_{Mars} + h_{CS}}\right) \tag{6.11b}$$

Then, the session time t_s in which UAV and CubeSat can communicate is given by the distance d_{arc}, i.e. the circular arc travelled by CubeSat divided by the orbital speed v_{CS}, i.e.:

$$d_{arc} = \Big(\theta \cdot (R_{Mars} + h_{CS})\Big) \tag{6.12a}$$

$$t_s = \frac{d_{arc}}{v_{CS}} \tag{6.12b}$$

To conclude and further clarify, t_s is the session time achievable if we suppose to establish a communication between UAV at a certain altitude and CubeSat exactly moving from Zenith to the loss-of-signal position, where $d = d_{max}$. Thus, this estimate accepts a certain degree of approximation, which, however, seems reasonable for our purpose of assessing the feasibility of functional split in 3D Networks.

6.4.2 Meeting bandwidth requirement to design the front-haul of C-RAN-based 3D Networks

In sect.6.4, we computed the required data rate $D_{CPRI} = 6.14Gbps$ for the wireless front-haul, i.e. the drone-to-satellite link. Thus, we need to provide our nodes involved in the communication with analog front-end (AFE) components able to generate a suitable sampling rate in output of the transceiver. If we invert the equation correlating the achievable bit-rate $R_b = D_{CPRI}$ in bps with the AFE sampling rate S_R in Msamples/s, we obtain the required spectral efficiency γ [192]:

$$\gamma = \left(\frac{R_b \cdot f_{ov}}{S_R} \right) \tag{6.13}$$

which is expressed in bits/symbol. f_{ov} is the oversampling factor usually expressed by the producer. To the aim of reducing as much as possible γ, which impacts on the number of levels of the chosen modulation technique and thus on the BER, the commercial AFE reported in [192] are not enough to produce the desired bit-rate. Now, being an application for *ad-hoc* deep space missions, we can adopt high-cost non-commercial AFE, such as the AD9081BBPZ-4D4AC from Analog Devices Inc., which can support $S_R = 4000$MSPS with $f_{ov} = 3$.

The resulting spectral efficiency becomes $\gamma = 4.61$bit/symbol, which is an appropriate value to later parameterize the link budget. Once we estimate the spectral efficiency, we can dimension the RS code-rate η by formulating the following

$$\eta = \frac{\gamma}{\gamma_{ideal}} \tag{6.14}$$

where $\gamma_{ideal} = log_2(M)$ with M the modulation levels. By considering M-QAM, which as stated in [99] is more suitable and leads to better performance with respect M-PSK for $\gamma > 3$, it is finally possible to obtain the configuration of coding and modulated bits per symbol lowering the energy per bit to noise power spectral density ratio $Eb/N0$. By fixing $m = [5, 6, 7, 8] > \gamma$ with $M = 2^m$ and 100 information bits, the total number of bit per frame is $n = [109, 130, 152, 174]$, which leads to a correction capability $t = [4, 15, 26, 37]$ of each configuration. The BER results were estimated through the use of the analytical formulation in [150]. They are then presented in Fig.6.3b. From this figure, the RS(130,100) 64-QAM is by far the choice showing the best performance for the expected quality of

service (QoS) identified by the CPRI as $BER = 10^{-12}$. Consequently, the link budget parametrization will need to guarantee $Eb/N0 \geq 13.04$dB.
First of all, for the next considerations, we will assume an average receiver temperature $T = 273$K both for downlink and uplink communications [151]. The required bandwidth B_w around the X-band carrier frequency $f_c = 8.4$GHz is expressed as in [152]

$$B_w = \left(\frac{R_b}{\gamma}\right) \cdot (1 + r) \tag{6.15}$$

where a common $r = 0.3$ is the roll-off factor of the pulse-shaping filter. To the best of authors' knowledge, the state-of-the-art does not suggest particular antennas to be mounted on UAV for X-band radio communications. For this reason, we decided to dimension the drone antenna's gain by computing:

$$\begin{aligned} G_{UAV}^{TX,RX} &= SNR_{dB} + L_p + A_{dB} + 10log_{10}(k \cdot T) \\ &\quad + 10log_{10}(B_w) + F_{dB} - P_{dB}^{TX} - G_{CS}^{TX,RX} \end{aligned} \tag{6.16}$$

with $SNR = Eb/N0 + 10log_{10}(\gamma)$, L_p the free-space path loss, A_{dB} demodulation losses, k the Bolztmann's constant, F the receiver noise figure and $G_{CS}^{TX,RX}$ the CubeSat antenna's gain.
As written in Tab.6.2, we consider $P_{TX} = 5$W for the transmitter onboard of CubeSats [153], while $P_{TX} = 1$W for the drone transmitter is a reasonable parametrization to save energy resources. For what concerns antennas to equip CubeSat with, the literature shows many possible solutions. However, most of them are for commercial purposes, thus they do not provide huge TX-RX gains, which are of paramount importance in such a scenario. Instead, the already cited 6U MarCO CubeSats mounted reflectarray antennas, shown in Fig.2.7a, able to guarantee, in the X-band, 28dBi of gain [153]. Nevertheless, 12U CubeSats are huger than 6U ones, thus, the authors of [154] proposed a deployable mesh reflector, under construction at Tyvak [155], with an aperture of 1m, which assure a gain of $\sim$ 36dBi for the X-band.
In Fig.6.5, the $\star$ markers represent the intersection between the required $Eb/N0 = 13.04$dB and the sweeping of UAV antenna's gain. As clearly highlighted, providing a higher antenna's gain at CubeSat side means a lower dimensioning of the UAV antenna's gain. Uplink communications, due to the reduced transmitted power from the drone, will need at least

Table 6.2: Link budget for the drone-to-CubeSat link

	Downlink	Uplink
Required Eb/N0	13.04dB	
Temperature (T)	273K	
Carrier Frequency (f_c)	8.4GHz	
Occupied Bandwidth (B_w)	1.73GHz	
Path Loss (L_p)	148.43dB	
Receiver Noise Figure (F)	1.23dB	
Demodulation Losses (A)	2.5dB	
TX Power (P_{TX})	1W	5W
CubeSat Gain ($G_{CS}^{TX,RX}$)	[28, 36.8]dBi	[28, 36.1]dBi
UAV Gain ($G_{UAV}^{TX,RX}$)	[32.0, 23.2]dBi	[25.0, 16.02]dBi

23.2dBi by adopting the Tyvak X-band mesh reflector, otherwise, as shown in Tab.6.2, the MarCO reflectarray will require $G_{UAV}^{TX} = 32.0$dBi, which is unfeasible from a design point of view. The other terms considered in the link budget evaluation are the ones proposed in Tab.6.2, where the receiver noise figure F and the demodulation losses A comes from [192] and the free-space path loss is estimated for the maximum distance $d_{UAV-CS}^{max} = 75$km. To conclude this section, just some notes about the choice of the nonlinear RF amplifier that is always critical in the front-haul design and link budget definition. In the literature, some real Solid-State Power Amplifier (SSPA) components for small satellite transmission in the X-band have been proposed in [156] and [157]. Despite their indubitable efficiency, these components are characterized by an insufficient band pass (both of them around 300MHz) as compared to the value of 1.73GHz required by the link budget. For this reason, *ad-hoc* components should be designed and characterized by a good trade-off between band pass, saturation gain, reduced input back-off and high power-added efficiency. This will represent a challenging open issue for RF designers.

6.5 Session Time and Optimal Altitude Selection

As previously mentioned in sect.6.4.1, by comparing the drag force F_{drag} and the thruster force F_{prop}, we are able to estimate the minimum allowed altitude for the 1U, 6U and 12U CubeSats. From the literature, we found that propulsion systems for 1U commercial CubeSats can roughly

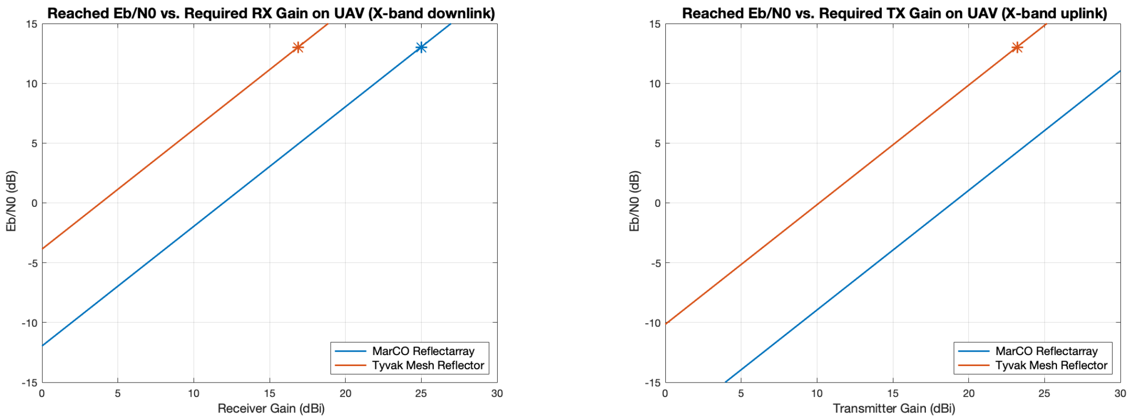

(a) Needed RX gain

(b) Needed TX gain

Figure 6.5: (a) Dimensioning of the RX gain for the drone's antenna to provide the required downlink X-band Eb/N0 while considering the MarCO reflectarray and Tyvak mesh reflector gain at CubeSat side. (b) Dimensioning of the TX gain for the drone's antenna to provide the required uplink X-band Eb/N0 while considering the MarCO reflectarray and Tyvak mesh reflector gain at CubeSat side.

express $F_{prop} = 1$mN. For what concerns 6U CubeSats, we took as reference MarCO's platforms, whose size well fits with the 6U model. MarCO satellites have been equipped with eight Vacco's thrusters, but only four of them have been used for trajectory correction. Thus, from the data sheet of [158] detailing the "Micro Propulsion System" (MiPS) adopted by MarCOs, we fixed $F_{prop} \approx 4 \times 10$mN. However, thinking to Martian deep space missions with such a relevance, it would be useful to have more capacity for scientific payload. In this context, 12U CubeSat are the largest platforms from the considered ones. Without going much into the details, the authors in [159] presented a 12U CubeSat, weighing about 25kg, with a single main hybrid rocket motor able to produce $F_{prop} = 44.4$N, while occupying the 76% of the total volume. This is more than 3 orders of magnitude above the mentioned F_{prop} for 6U CubeSat. Fig.6.6 shows, in a first instance, that such a system, with the current technologies, is not suitable for Earth. Indeed, by parametrizing Eq.6.6 with $H_{Earth} = 8.5$km and $\rho_0 = 1.217$kg/m^3, we understand that the selected thruster for the 1U, 6U and 12U CubeSat cannot provide enough force to correct trajectories and altitudes under, respectively, [163.5, 143.0, 86.5]km. This is quite interesting, but also expected due to the thinner Martian atmosphere with respect to Earth. This suggests that the atmosphere and the environment of the Red planet can be regarded as advantageous for the future *in-situ*

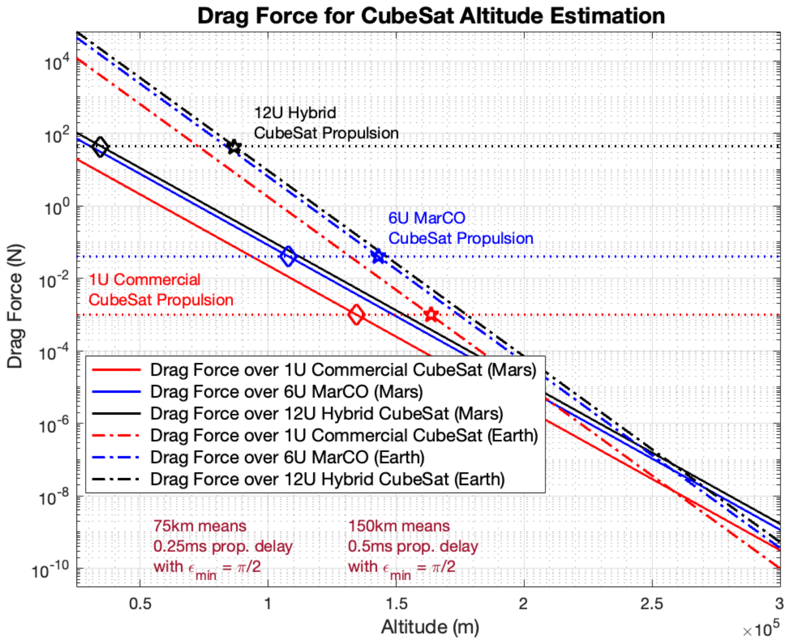

Figure 6.6: Drag force F_{drag} over 1U, 6U and 12U CubeSats on VLMO with respect to the low Earth orbit (LEO). The dotted lines stand for the propulsion force F_{prop} expressed by off-the-shelf, Vacco's MiPS and JPL hybrid thrusters (HT).

deployment of B5G networks. However, it is evident from Fig.6.6 that common commercial thrusters for 1U CubeSat, or the Vacco's MiPS for 6U CubeSat, cannot be used to guarantee Martian orbits with altitudes under $[134.5, 108.0] km$, where our upper bound is $h_{max} \sim 75km$. Instead, the JPL hybrid thruster can allow decreasing the minimum acceptable orbit well below $h_{max} \sim$ 75km, thus meeting the fundamental latency requirement of the splitting options 7.3, 7.2, 7.1 and 8. 12U hybrid CubeSat can support a minimum altitude $h_{min} \sim$ 35km. Clearly, it is not necessary to place constellations of CubeSats at such a low altitude, thinking also that it is almost impossible to maintain the thrusters always active to not consume the whole energy or propellant resources in a while. When dealing with the OAI emulator, we will realize that there are few degrees of freedom that allow to relax the latency requirement to raise the constellation altitude. However, this gives us a consistent indication on the fact that in the next future, there could be Martian missions with extremely low altitudes.

Our analysis proceeds by showing in Fig.6.7a the minimum acceptable elevation angle ϵ_{min} for altitudes ranging from the lower h_{min} = 35km and

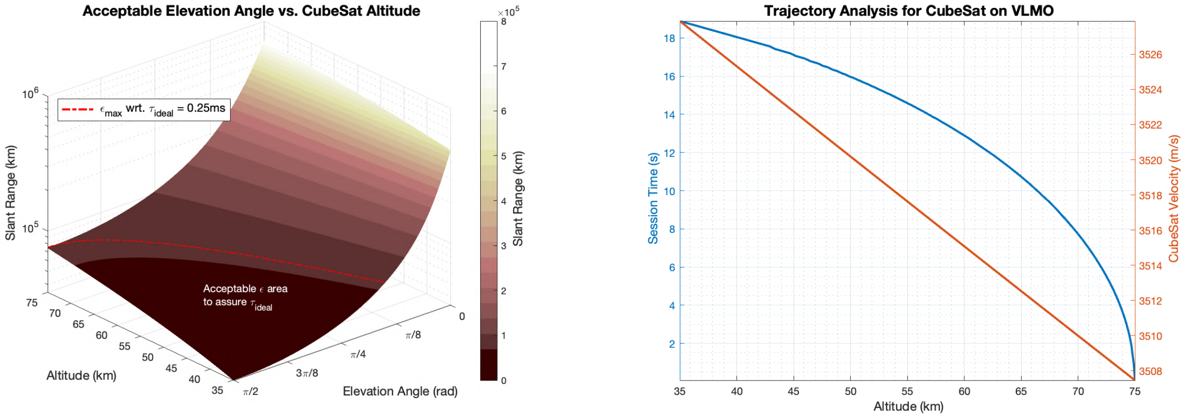

(a) Acceptable Elevation Angle (b) Session Time

Figure 6.7: (a) 3D plot representing the slant range vs. the altitude and the elevation angle. The red dotted line identifies the minimum elevation angle for each selected altitude. (b) For an altitude ranging from h = [35, 75]km, the variation of CubeSat velocity and the available communication window, or session time, from UAV to CubeSat.

maximum $h_{max} = 75$km bound. As we can see by following the red dotted line, the slant range is fixed at $d_{max} = 75$km to respect $\tau_{ideal} = 250\mu$s, i.e. the ideal latency case. The lower elevation angle ϵ is found when $h_{min} \sim 35$km, while for $h_{max} = 75$km it would be possible a communication only at $\epsilon = \frac{\pi}{2}$, thus leading to a session time $t_s \sim 0$.

Now, Fig.6.7b depicts, for each altitude h_{CS}, the eventual session time between UAV and CubeSat, which is roughly moving at a speed v_{CS} of about ~ 3.5km/s. If we lower the altitude of CubeSat, we are able to sensibly increase the session time up to more or less $t_s = 18$s for really low altitudes, where we have to pay the price in terms of resources consumed to correct the trajectory of CubeSat.

To conclude, Fig.6.8 directly correlates through a Pareto front the drag force and session time. As we go higher with the CubeSat altitude h_{CS}, we decrease the drag force F_{drag} but also the possible session time t_s. Vice-versa, a lower h_{CS} means higher t_s but also higher F_{drag} to be counteracted by F_{prop} and the on-board resources. If we normalize the two terms, while giving them the same weights, and search for the altitude which minimizes the error, we obtain

$$E = min\Bigg(abs\Big(t_s(i+1) - t_s(i)\Big) + abs\Big(F_{drag}(i+1) - F_{drag}(i)\Big)\Bigg) \tag{6.17}$$

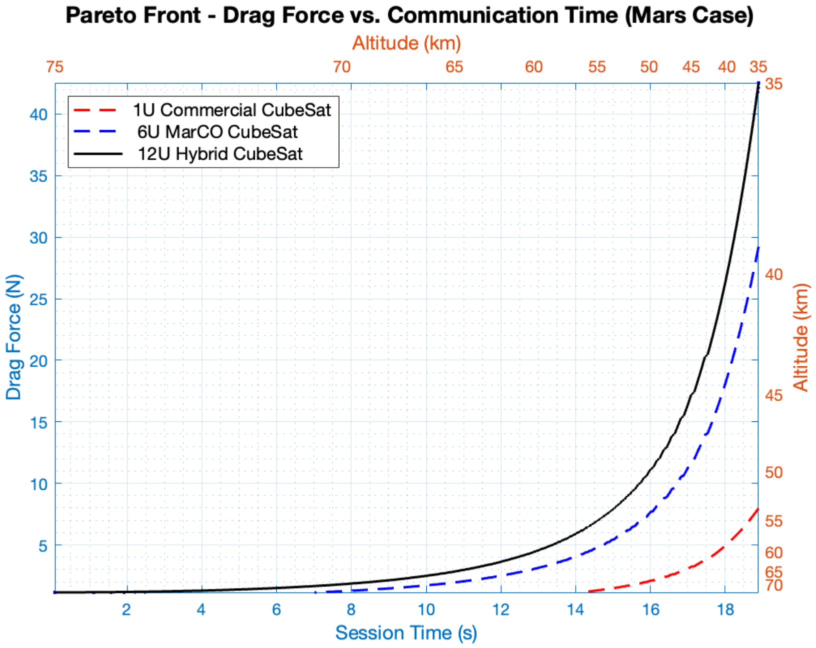

Figure 6.8: Pareto front of the drag force F_{drag} vs. session time t_s. The dotted lines refer to 1U and 6U CubeSats, while the black one is the 12U CubeSat.

with i the index running the vectors, the optimal altitude is $h_{opt} = 67.1$km with $F_{drag} = 2.34$N (the 5.2% of the maximum F_{prop} expressed by the JPL hybrid CubeSat) and $t_s = 9.6$s. However, the selection of the best altitude should be done by unevenly weighing multi-objectives with respect to precise scientific requirements.

6.6 Physical and Data-Link Layer Evaluations

Low-density parity-check coding (LDPC) offers equal or better performance than the turbo coding at the price of lower complexity [160]. This is the reason behind its choice for the 5G NR [161]. Optimum ML decoding for LDPC has a prohibitive computational complexity, but iterative sub-optimum decoding can provide results very close to the theoretical Shannon bound and can be efficiently supported by low-cost application-specific integrated circuit (ASIC) implementations [162]. As commonly known, the increase of the number of allowed decoding iterations k_{iter} for FEC operations, which depends also on the available processing time $t_{bsp} = T_{radio} - t_Q - t_{FA} - t_{tx} - t_{mpt}$ at the baseband unit (from Eq.6.3), guarantees an improvement in the C-BER performance. Thus, let us remember that we fixed $T_{radio} = 0.5$ms, which is the ideal latency requirement identified by 3GPP. The parameter $t_J = 33.34\mu$s accounts for other delays brought by the baseband processing [163]. In particular, we assume to be due to FFT processing, since demodulation tasks are done in negligible time [164]. For what concerns the queuing delay, we suppose $t_Q = 20\mu$s for each node between UE and BBU, i.e. the drone representing the RU and the CubeSat embarking DU and CU functionalities. Although we considered $t_{tx} = t_{UAV-CS} = t_{split} = 0.25$ms to perform low-layer splitting options (opt.8-6), accordingly to what we said in sect.6.4, the distance between drone and CubeSat can even be decreased at the price of a higher propulsion force to be produced. For example, with $d_{UAV-CS} = [50, 75]$km so $t_{tx} = [0.25, 0.17]$ms, the available processing time at the baseband unit becomes $t_{bsp} = [0.18, 0.26]$ms. However, it should be kept in mind that the less is the CubeSat constellation altitude, the less is the coverage provided on-ground. Approximately and considering the optimal altitude of about 67.1km, suggested in sect.6.5, a single CubeSat is able to provide a maximum coverage of 0.01% of the whole planet surface. Thus, a CubeSat constellation made of 10000 nodes would be required to guarantee the 100% coverage. Despite being a feasible number for terrestrial applications, e.g. see Starlink, on Mars this deployment could be tough to achieve in this decade. That is the reason why the ideal latency t_{split} could be relaxed of tenths of a millisecond to higher the altitude of the CubeSat constellation, consequently the coverage on-ground. To this aim, investigations in sect.6.7 will evaluate E2E delay and packet loss through network emulations to estimate the price to be paid for such an operation.

Before going deep into data-link and PHY-layer assessment, some notes should be spent about the issue of Doppler shift. 3GPP Release 15 shows an allowed maximum Doppler shift for S-band LEO NTN of about 48.0KHz, and way higher values for $f_c = [20, 30]$GHz communications [165]. Due to the reduced CubeSat speed, which is ~ 3.5km/s, the maximum Doppler shift results equal to 43.4KHz for the optimal altitude of 67.1km and the chosen carrier frequency of $f_c = 8.4$GHz. Signal acquisition might be negatively affected by this. For this reason, the receiver should be pre-trained to acquire the absolute maximum value of the Doppler shift for this specific application. The Doppler variation, estimated through a continuous resampling of the CubeSat position with respect to the UAVs, is then easily corrected thanks to a closed-loop compensator (phased locked loop) [192]. Coming back of few steps, by sweeping the number of processing units

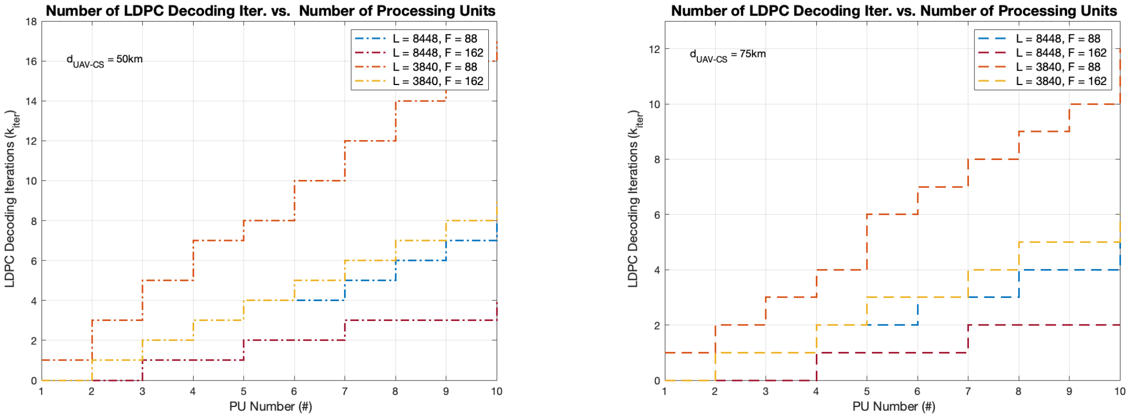

(a) Number of decoding iterations k_{iter}

(b) Number of decoding iterations k_{iter}

Figure 6.9: (a) Number of achievable decoding iterations vs. processing units for d_{UAV-CS} = 50km. (b) Number of achievable decoding iterations vs. processing units for d_{UAV-CS} = 75km.

(PU), where we suggest the use of the Leopard data processing unit (DPU) having a clock rate $p = 2.32$GHz, we are able to finally estimate k_{iter}. It is of simple understanding that, as we install more PU on CubeSat side, we are adding processing capabilities. From Fig.6.9, we clearly see the effect of this, which increases k_{iter} for both cases in (a) and (b).

3GPP defined two block sizes for the 5G NR: $L = 8448$bit and $L = 3840$bit. Putting these values in Eq.6.4 along with $F = [88, 162]$bit, which are taken from [166], we appreciate that the reduction in the block size and in the LDPC decoding complexity is directly proportional to the increase in the number of k_{iter}. Last but not least, more processing time t_{bsp} means more k_{iter}. This is achieved, as introduced before, by decreasing the slant range from drone to CubeSat, i.e. the FH length, thus reducing the session time and making more frequent the handover.

In order to obtain an estimation of the coded BER, depending on the number of allowed decoding iterations k_{iter}, we developed a Simulink model. The results in Fig.6.10 are obtained by selecting M-QAM constellations, with $M = [4, 16, 64]$, as modulation format. The channel related to the link drone-UE is, so far, assumed to be Additive White Gaussian Noise (AWGN). Such a hypothesis may be realistic in some particular configurations where LOS connection is guaranteed and obstacles do not produce wave reflection and scattering. A more detailed analysis considering Martian multipath propagation will be matter for future work.

From the plots of Fig.6.10, we can notice a performance gain between

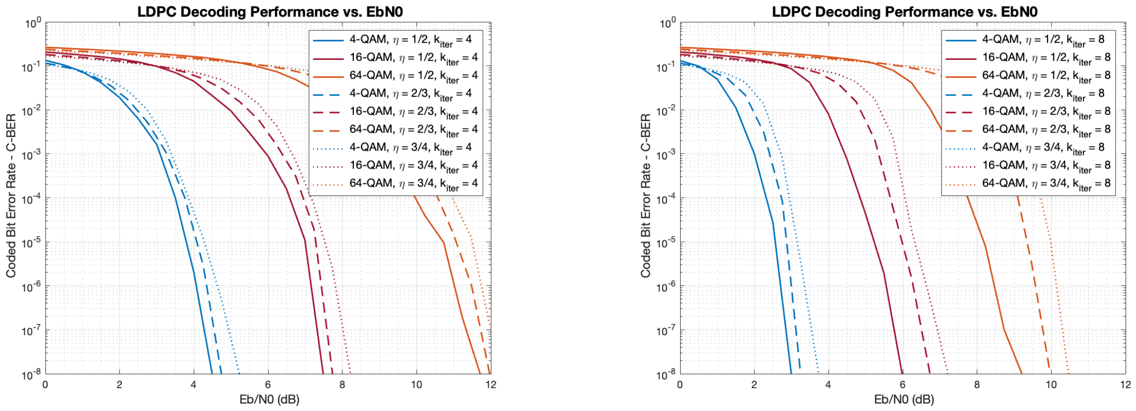

(a) BER vs. Eb/N0 with LDPC $k_{iter} = 4$

(b) BER vs. Eb/N0 with LDPC $k_{iter} = 8$

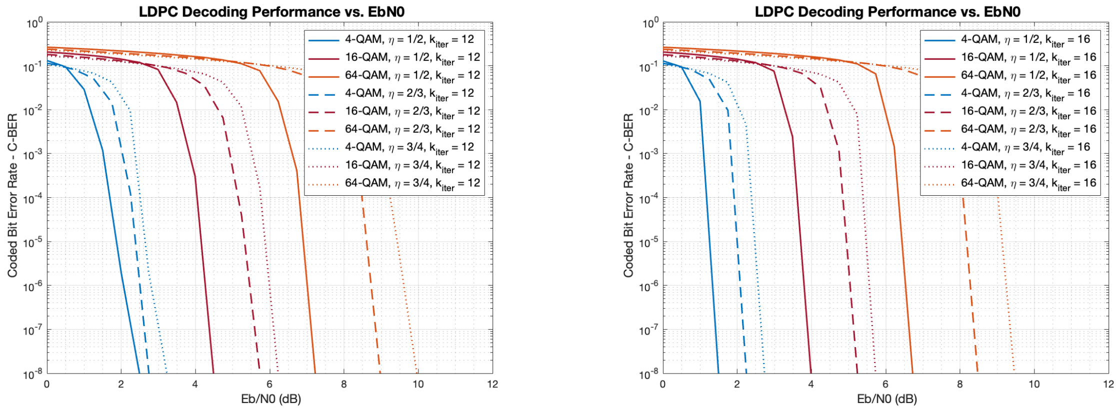

(c) BER vs. Eb/N0 with LDPC $k_{iter} = 12$

(d) BER vs. Eb/N0 with LDPC $k_{iter} = 16$

Figure 6.10: (a) LDPC Performance for a 4, 16, 64-QAM with a variable code-rate $\eta = [\frac{1}{2}, \frac{2}{3}, \frac{3}{4}]$ and number of decoding iterations $k_{iter} = 4$. (b) LDPC Performance for a 4, 16, 64-QAM with a variable code-rate $\eta = [\frac{1}{2}, \frac{2}{3}, \frac{3}{4}]$ and number of decoding iterations $k_{iter} = 8$. (c) LDPC Performance for a 4, 16, 64-QAM with a variable code-rate $\eta = [\frac{1}{2}, \frac{2}{3}, \frac{3}{4}]$ and number of decoding iterations $k_{iter} = 12$. (d) LDPC Performance for a 4, 16, 64-QAM with a variable code-rate $\eta = [\frac{1}{2}, \frac{2}{3}, \frac{3}{4}]$ and number of decoding iterations $k_{iter} = 16$.

Table 6.3: Link budget for the UE-to-drone (RU) link

	B5G Parameterization
Modulation	4-QAM, 16-QAM, 64-QAM
LDPC code-rate (η)	$[\frac{1}{2}, \frac{2}{3}, \frac{3}{4}]$
Temperature (T)	273K
Carrier Frequency (f_c)	2.5GHz
Occupied Bandwidth (B_w)	153.6MHz
Cell Radius ($d_{UE-UAV/RU}$)	[500, 1000]m
Path Loss Exponent	[2.07; 2.22] (GA1, GA2)
Path Loss (L_p)	[103.92, 110.15] (GA1) [111.45, 118.13] (GA2)
Shadowing (χ)	[6.71, 9.80]dB (GA1, GA2)
Receiver Noise Figure (F)	2.0dB
Demodulation Losses (A)	2.5dB
Aviation Margin (Avt_{mrg})	6.0dB
TX Power (P_{TX})	23dBmW
RU Gain ($G_{UAV/RU}$)	18dBi
RU SNR	[18.97, 12.74]dB (GA1) [8.80, 2.12]dB (GA2)

each curve representing different modulation levels, which becomes more evident for $k_{iter} = 4$ decoding iterations. Considering an extremely low $BER = 10^{-8}$ and fixed code-rate, 4dB of gain are appreciable between all curves related to the 4-QAM, 16-QAM and 64-QAM.

For what concerns the code-rate $\eta = [1/2, 2/3, 3/4]$ and taking into account a precise modulation (see Tab.6.3), we can highlight an added gain brought to system performance as we augment k_{iter}. For $k_{iter} = 4$ and a 64-QAM, less than 1dB is gained passing from $\eta = 3/4$ to $\eta = 1/2$, which also decreases the spectral efficiency $\gamma = \eta \cdot log_2(M)$. Instead, for $k_{iter} = 16$ and the same configuration as before, $Eb/N0^{64-QAM}_{BER=10^{-8}}(\eta = 3/4) \sim 9.5$dB and $Eb/N0^{64-QAM}_{BER=10^{-8}}(\eta = 1/2) \sim 7.5$dB, which means 2dB of gain. Despite this analytical considerations, what really matters is the $Eb/N0$ obtained at the RU side, that then will assure a certain coded BER for k_{iter} decoding iterations. To estimate it, we formulated the equation below

$$\begin{aligned} SNR_{dB} = P^{TX} + G_{UAV/RU} - L_p^{GA1,GA2} - A - F \\ - Avt_{mrg} - 10log_{10}(k \cdot T) - 10log_{10}(B_w) - \zeta \end{aligned} \tag{6.18}$$

where, among the other parameters defined in Tab.6.3, Avt_{mrg} is an aviation margin taken from [167]. A, F and the transmitted power P_{TX} from UE were found in [192] and the carrier frequency $f_c = 2.5$GHz and occupied bandwidth $B_w = 153.6$MHz are the parameterization of the Verizon 5G sub-6GHz.

In sect.5.3.2, we propose different path loss exponent and shadowing values, i.e. the fluctuations of the signal power due to obstacles in between the straight path from TX to RX, for two Martian areas, i.e. "Gale Crater - Area 1" (GA1) and "Gale Crater - Area 2" (GA2). Recalling what we discussed in Chapter 5, GA1 is a flat area where RF propagation is affected by a quasi free-space path loss, while GA2 presents a rocky environment with steep cliffs. Few preliminary results over differently sampled Gale areas ([194]) slightly underestimated the path loss exponent around 2.22 and the shadowing value of 9.80dB for GA2. Further analysis should correct GA2 measurements upwards. The shadowing increases accordingly to the nature of the area, that we are taking into account. GA2, being characterized by huge cliffs, leads to a higher probability of obstructing the LOS between TX and RX. We decided to integrate these considerations into our link budget evaluation to better represent the Martian environment. Although we modelled the Martian channel supposing TX and RX antennas at 1.5m above the ground, we can approximate that for a RU at $3-5$m, which is the height at which the Mars Helicopter Scout was able to fly, the path loss and shadowing would be roughly the same.

The outcomes shown in Tab.6.3 propose a GA1 SNR at RU side of [18.97, 12 .74]dB and a GA2 SNR of [8.80, 2.12]dB, respectively, for a cell radius of 500m and 1000m, meaning with this the actual distance between UE and UAV acting as RU. More than 10dB of gain are lost moving from the GA1 to GA2. This, as anticipated before, is due to the morphological features which are poles apart for the GA1 and GA2. From sect.5.3, while for the 1×1km GA1 the maximum gradient between the lowest and highest point is ~ 17m, the GA2 one is equal to ~ 239m, thus showing big cliffs and rocks, which largely justify the differences in the path loss exponent and shadowing.

Now, to conclude the discussion, we lack only to visualize the reachable $Eb/N0$ for the various configurations mixing the 4, 16 and 64-QAM with the code-rate η, the distances $d_{UE-UAV/RU}$ with the Gale crater areas. From the formulation below

$$Eb/N0_{dB} = SNR_{dB} - 10log_{10}(\eta) \tag{6.19}$$

Table 6.4: Achievable $Eb/N0$ and γ for Gale Crater - Area 1 and cell radius $d_{UE-UAV/RU}$ = 500m

$(Eb/N0, \gamma)$	$\eta = \frac{1}{2}$	$\eta = \frac{2}{3}$	$\eta = \frac{3}{4}$
4-QAM	(18.97dB, 1.00bit/s/Hz)	(17.72dB, 1.33bit/s/Hz)	(17.21dB, 1.50bit/s/Hz)
16-QAM	(15.96dB, 2.00bit/s/Hz)	(14.71dB, 2.67bit/s/Hz)	(14.20dB, 3.00bit/s/Hz)
64-QAM	(14.20dB, 3.00bit/s/Hz)	(12.95dB, 4.00bit/s/Hz)	(12.44dB, 4.50bit/s/Hz)

Table 6.5: Achievable $Eb/N0$ and γ for Gale Crater - Area 1 and cell radius $d_{UE-UAV/RU}$ = 1000m

$(Eb/N0, \gamma)$	$\eta = \frac{1}{2}$	$\eta = \frac{2}{3}$	$\eta = \frac{3}{4}$
4-QAM	(12.74dB, 1.00bit/s/Hz)	(11.49dB, 1.33bit/s/Hz)	(10.98dB, 1.50bit/s/Hz)
16-QAM	(9.73dB, 2.00bit/s/Hz)	(8.48dB, 2.67bit/s/Hz)	(7.97dB, 3.00bit/s/Hz)
64-QAM	(7.97dB, 3.00bit/s/Hz)	(6.72dB, 4.00bit/s/Hz)	(6.21dB, 4.50bit/s/Hz)

we can estimate the $Eb/N0$ at the RU to, eventually, map the values in Fig.6.10 and obtain the expected coded BER. Finally, Tab.6.4, Tab.6.5, Tab.6.6 and Tab.6.7 conclude the section by giving us the information regarding the $Eb/N0$ at the RU. First, it is clearly evident that the results seem dramatic only when trying to provide connectivity to a UE distant 1000m from the UAV over the GA2. Only with a (2,1) 4-QAM, we reach an $Eb/N0$ of about 2.12dB, that mapped onto Fig.6.10c and Fig.6.10d will mean, respectively, a BER well lower than 10^{-6} and 10^{-8} with $k_{iter} = 12$ and $k_{iter} = 16$. Instead, for $k_{iter} = 4$ and $k_{iter} = 8$, the BER would be much higher than 10^{-2} and 10^{-4}. Thus, if we assume $k_{iter} = 12$ to provide a consistent BER, by linking to Fig.6.9a we would necessitate 7PU on-board of the CubeSat, where we would also be forced to reduce the distance $d_{UAV-CS}^{max} = 50$km to achieve a spectral efficiency of just 1bit/s/Hz. This is obviously an unfeasible solution, which however gives us an idea of the many trade-offs to be accounted to build 3D Network-based 6G architecture for Martian global connectivity.

Coming back to the previous point, Tab.6.4 provides excellent results in terms of $Eb/N0$. Indeed, for each tried configuration, the reachable $Eb/N0$ at RU allows reducing the BER to values lower than 10^{-8}, even allowing just $k_{iter} = 4$ decoding iterations. With $L = 3840$ and $F = 88$, we can mount 4PU to guarantee, for instance, a $BER \leq 10^{-8}$ and a $\gamma = 4.50$bit/s/Hz for $d_{UAV-CS}^{max} = 75$km. In Tab.6.5 the results appear to be a bit more stringent, especially for what concerns the 64-QAM. For the lowest code-rate considered, an $Eb/N0 = 6.21$dB is not enough to

Table 6.6: Achievable $Eb/N0$ and γ for Gale Crater - Area 2 and cell radius $d_{UE-UAV/RU} =$ 500m

$(Eb/N0, \gamma)$	$\eta = \frac{1}{2}$	$\eta = \frac{2}{3}$	$\eta = \frac{3}{4}$
4-QAM	(8.81dB, 1.00bit/s/Hz)	(7.56dB, 1.33bit/s/Hz)	(7.04dB, 1.50bit/s/Hz)
16-QAM	(5.79dB, 2.00bit/s/Hz)	(4.55dB, 2.67bit/s/Hz)	(4.03dB, 3.00bit/s/Hz)
64-QAM	(4.03dB, 3.00bit/s/Hz)	(2.78dB, 4.00bit/s/Hz)	(2.27dB, 4.50bit/s/Hz)

Table 6.7: Achievable $Eb/N0$ and γ for Gale Crater - Area 2 and cell radius $d_{UE-UAV/RU} =$ 1000m

$(Eb/N0, \gamma)$	$\eta = \frac{1}{2}$	$\eta = \frac{2}{3}$	$\eta = \frac{3}{4}$
4-QAM	(2.12dB, 1.00bit/s/Hz)	(0.87dB, 1.33bit/s/Hz)	(0.36dB, 1.50bit/s/Hz)
16-QAM	(-0.89dB, 2.00bit/s/Hz)	(-2.14dB, 2.67bit/s/Hz)	(-2.65dB, 3.00bit/s/Hz)
64-QAM	(-2.65dB, 3.00bit/s/Hz)	(-3.90dB, 4.00bit/s/Hz)	(-4.41dB, 4.50bit/s/Hz)

achieve a good BER. This does not happen for a 16-QAM exploiting the same $\eta = 3/4$, which, with an $Eb/N0 = 7.97$dB, assures a $BER \leq 10^{-6}$ and a $\gamma = 3.00$bit/s/Hz. As understandable, the worst results come for the GA2 bringing into the SNR computation the higher path loss exponent and shadowing. Given our parameterization, for such an environment, it is preferable to adopt the 4-QAM, while paying for a reduced spectral efficiency. At most, a (2,1) 16-QAM providing $\gamma = 2.00$bit/s/Hz and an $Eb/N0 = 5.79$dB would guarantee a $BER \sim 10^{-6}$ for $k_{iter} = 8$.

6.7 Feasibility and trade-off analysis

The 3D Network design is directly dependent on the chosen orbital altitudes, both for the CubeSat and Orbiter constellations. Indeed, as we will see in sect.6.8, the E2E measures are obtained in relation to the distance between each node involved in the communication. However, in order to lower the overall system complexity, we assume to have UAVs, as well as on-ground UEs, at a negligible height with respect to the satellites in the space around Mars. This means that our attention will focus on the UAV-CubeSat and CubeSat-Orbiter links (later referred to as UAV-CS and CS-OB links). We rely on statistical distributions to model the link distances, as a simple 2D geometrical analysis would not be realistic. Thus, we assume two constellations of about $N_{CS} = 100$ and $N_{OB} = 100$. Despite the fact that it will take many years to have such constellations on Mars, a hundred of nodes per constellation is relatively a small number when compared to terrestrial applications. For instance, SpaceX had the possibility to deploy around Earth more than 4000 low Earth orbit (LEO) CubeSats to provide global low-latency internet access [168]. Moreover, such assumption raise up an interesting discussion on the occurrence probability of a certain link distance.

In [169], the cumulative distribution function (CDF) of the contact distance (CD) between an observer on Earth and a cloud of satellites located on a sphere following a binomial point process (BPP) has been outlined. The authors also defined the CDF of nearest-neighbor (NN) distance between a point in an inner BPP sphere and a constellation of satellites in an outer one. Adapting these findings to our test case (i.e., two concentric orbits over the sphere representing the Earth), we can model the CDF $F_{D_{UAV-CS}}(d)$ as in the following. The product series of [169] can be simplified by supposing that $n = 1$ (i.e. one spherical orbit) for the constellation of CubeSat over the fleet of UAVs on Mars surface:

$$F_{D_{UAV-CS}}(d) \triangleq \mathbb{P}(D_{UAV-CS} < d) = 1 - \mathbb{P}\left(D_{UAV-CS} \geq d\right) \tag{6.20}$$

with the complementary cumulative function (CCDF) of D_k given by

$$\begin{gathered}\mathbb{P}\left(D_{UAV-CS} \geq d\right) = \\ \begin{cases} 1, & d < h_{CS} \\ \left[1 - \frac{1}{\pi}\arccos\left(1 - \frac{d^2 - h_{CS}^2}{2R_{Mars} r_{CS}}\right)\right]^{N_{CS}}, & h_{CS} \leq d \leq d_{\max}(CS,0) \\ \left[1 - \frac{1}{\pi}\arccos\left(\frac{R_{Mars}}{r_{CS}}\right)\right]^{N_{CS}}, & d > d_{\max}(CS,0) \end{cases}\end{gathered} \tag{6.21}$$

where: $d_{\max}(CS,0) = \sqrt{2R_{Mars}h_{CS} + h_{CS}^2}$, $R_{Mars} = 3.389,5 \times 10^3$m is the mean Mars radius, h_{CS} is the CubeSats orbital altitude, and $r_{CS} = R_{Mars} + h_{CS}$. The parameter d is an arbitrary distance swept in certain range as shown in Fig.6.11. The CDF of the nearest-neighbor (NN) distance is $F_{D_{CS-OB}}(d)$. Similarly to the previous case:

$$F_{D_{CS-OB}}(d) \triangleq \mathbb{P}(D_{CS-OB} < d) = 1 - \mathbb{P}\left(D_{CS-OB} \geq d\right) \tag{6.22}$$

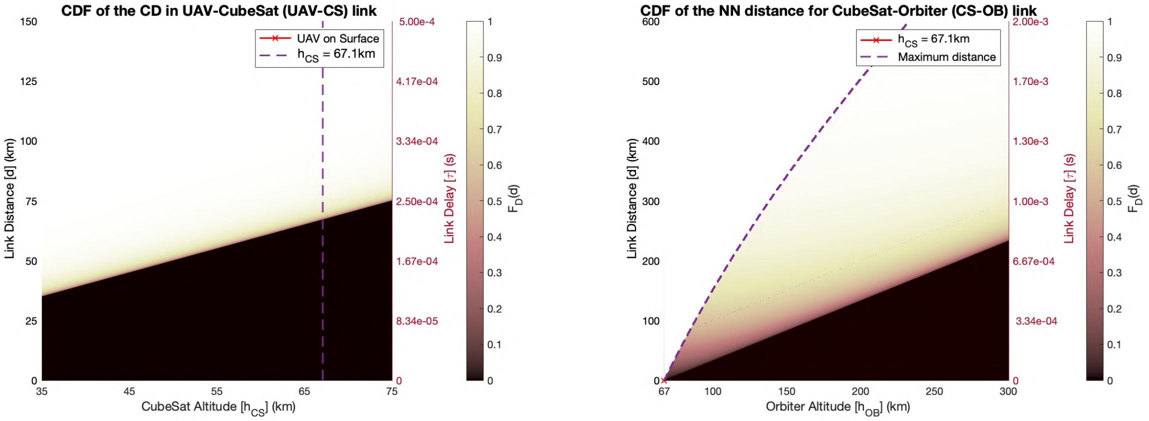

(a) CDF of the CD for the UAV-CS link (b) CDF of the NN for the CS-OB link

Figure 6.11: (a) Cumulative distribution function of the contact distance between a CubeSat constellation, with $N_{CS} = 100$, deployed into the V-LMO and a UAV on-ground. (b) Cumulative distribution function of the nearest-neighbor distance between an orbiter constellation, with $N_{OB} = 100$, deployed into the LMO and a CubeSat on V-LMO.

If we assume a CubeSat, as observation point, located on an inner spherical orbit with respect to the Orbiters one, i.e. $k \neq i$, we derive $\mathbb{P}\left(D_{CS-OB} \geq d\right)$

$$\begin{cases} 1, & d < |h_{OB} - h_{CS}| \\ \left[1 - \frac{1}{\pi}\arccos\left(1 - \frac{d^2 - (h_{CS} - h_{OB})^2}{2 r_{CS} r_{OB}}\right)\right]^{N_{OB}}, & |h_{OB} - h_{CS}| \leq d \leq d_{\max}(OB, CS) \\ \left[1 - \frac{1}{\pi}\arccos\left(1 - \frac{(r_{CS} + r_{OB})^2 - d_{\max}^2(OB,CS)}{2 r_{CS} r_{OB}}\right)\right]^{N_{OB}}, & d > d_{\max}(OB, CS) \end{cases} \tag{6.23}$$

where $d_{\max}(OB, CS) = \sqrt{r_{OB}^2 - R_{Mars}^2} + \sqrt{r_{CS}^2 - R_{Mars}^2}$. For the eventuality of having an observer over the same orbital sphere containing the satellite, i.e. with $k = i$, we suggest referring to [169]. For our purposes, it is sufficient to point out $k \neq i$.

In Fig.6.11, the CDF of the contact distance (CD) and nearest-neighbor (NN) distance is shown by sweeping the allowed altitude range between [35, 75]km for the UAV-CubeSat link, and between [67.1, 300]km, where the lower bound is the optimal orbital altitude described in sect.6.5. These evaluations are particularly useful to get, for an orbital altitude h_{CS} or h_{OB}, the probability link distance. Indeed, as introduced in sect.6.4, we should be aware of the maximum distance of about 75km between UAV and CubeSat to respect the ideal front-haul latency case imposing $\tau_{ideal} = 250\mu$s. However, if we fix $h_{CS} = 67.1km$, the probability of occurrence of the contact distance $d_{UAV-CS} = 75km$ is of about 89.7%. This means that for a

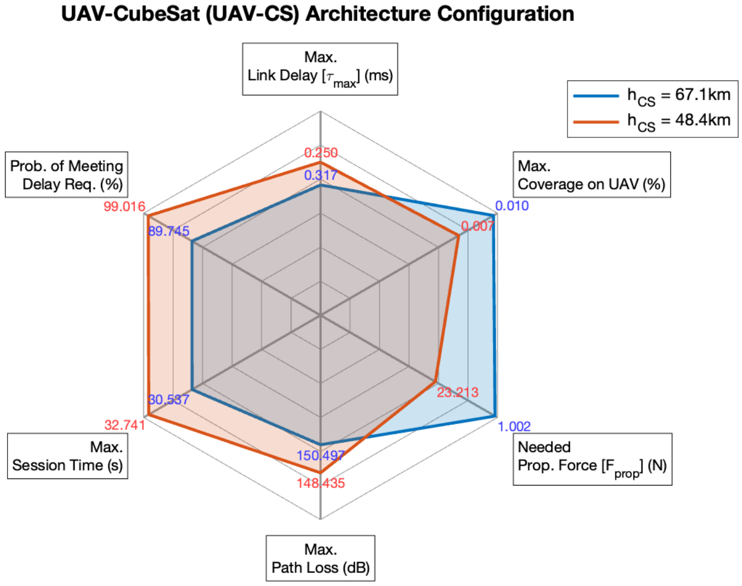

Figure 6.12: Spider web plot of the trade-offs introduced by the selection of the altitude for a CubeSat constellation placed at h_{CS} = [48.4, 67.1]km with respect to a fleet of UAVs at negligible altitude over the Martian surface.

10.3%, the UAV will experience $d_{UAV-CS} > 75km$ considering $N_{CS} = 100$, thus not respecting the imposed latency. This first consideration opens up to the following discussion.

The thoughtful altitude selection, both for what concerns the CubeSats and orbiters constellation, leads to several trade-offs to be accounted. Despite coming from multi-domain fields, such as aerospace, mechanics, and communication/networking ones, their behavior is directly correlated through the orbital altitude. As specified above, h_{CS} = 67.1km leads to a certain probability of not respecting the Common Public Radio Interface (CPRI) requirements defined previously. Thus, our computations estimated that for more than the 99% of the times, we are able to find $d_{UAV-CS} < 75km$ by placing the CubeSat constellation at h_{CS} = 48.4km, as shown in Fig.6.12. Such a low orbit translates into a reduced maximum link delay τ_{Conf2} = 250μs (*Conf2* means the configuration with $h_{CS} = 48.4km$), thus a theoretical lower bit error rate (BER) [192] and, generally, packet error rate (PER). However, to the best of authors' knowledge, the state-of-the-art lacks of a precise evaluation of the PER when dealing with augmented splitting latencies with respect to the ideal 3GPP case.

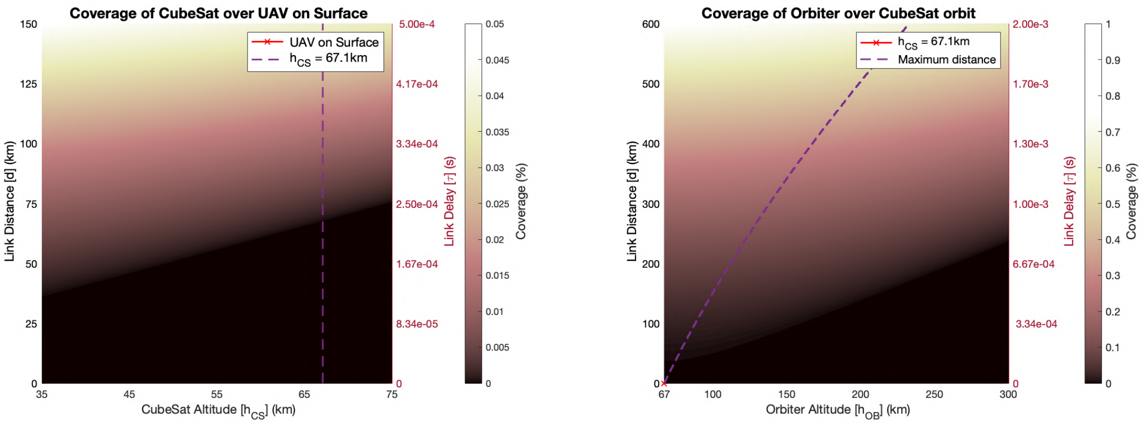

(a) Coverage of CS over Mars (b) Coverage of OB over CS spherical orbit

Figure 6.13: (a) Percentage of coverage from a single CubeSat deployed into the V-LMO to a UAV on-ground. (b) Percentage of coverage from a single orbiter deployed into the LMO to a CubeSat on V-LMO.

This is meaningful because, with $h_{CS} = 48.4km$ we are also increasing the propulsion force, up to $F_{prop} = 23.2N$, to counteract the drag force over the CubeSat. This side effect is of major importance because it would be required to install on CubeSat a hybrid propulsion system, which are usually used for orbit insertion and not for trajectory corrections [159], while strongly paying in terms of on-board weight, available space, power consumption and even missions costs. For *Conf1* — meaning the configuration with $h_{CS} = 67.1km$ — an electrical propulsion can be exploited to provide $F_{prop} = 1.0N$. In such a case, the energy would come from large solar panels but the lifetime of the CubeSat, which is crucial, would sensibly be augmented. Another key point is also the coverage, as shown in Fig.6.13. The coverage can be deterministically estimated thanks to the following equation [149]:

$$\text{Coverage}(\%) = \frac{1}{2}\left(1 - \cos\beta_0\right) \tag{6.24}$$

where β_0 is the central angle subtended by the straight lines connecting the Mars center with the observer on surface and the satellite on orbit. VLMO objects cannot provide a huge footprint on Mars, due to their relatively small distance from the "Red Planet" surface, as visible from Fig.6.13a. Thus, by gaining height we can improve the coverage for a single CubeSat over the UAV, from an area of 84x84km for *Conf2* to one equal to

120x120km for *Conf1.* A constellation of $N_{CS} = 100$ would then lead to a 1% of Mars coverage per instant, which is fair for this application given the deep space context.
Other aspects for *Conf1* with respect to *Conf2* are an increased path loss and lowered session time between UAV and CubeSat. However, as shown in Fig.6.12, path loss gradient of 2dB can easily be managed as well as the session time, where just $\approx$ 2.2s more of connectivity are not sufficient to justify the choice of *Conf2*.
An analysis quite similar to the one we have detailed as shown in Fig.6.14. Just by visualizing the plots, it is evident the predominant *red* area in Fig.6.14b, which places a constellation of orbiter at an altitude $h_{OB} =$ 300km. This is especially true for what concerns the average lifetime of orbiters, which was obtained by following the methodology in [170], suggested by IPS Radio & Space Services and computing the Mars atmospheric density ρ thanks to Eq.6.6 with the reference density $\rho_0 = 0.001 \text{kg/m}^3$. The lifetime is of about 2.5years for $h_{OB} = 250$km, while it reaches more than 200 years for $h_{OB} = 300$km. Despite the fact that usually satellites last no more than 15-20 years, it is important to notice that this estimate does not consider the use of propulsion to correct trajectories. This means that we would not require propulsion to maintain the orbit, thus saving energy for the on-board processing as core network. Coherently, an augmented propagation delay will be evident in the E2E latency and packet loss.

6.8 OAI Model Development and End-to-End Network Emulation

Fig.6.15 shows the considered OpenAirInterface (OAI) 5G [171] emulation platform. Here, OAI provides emulation of different RAN components and also virtualized core network components. The OAI supports different split nature of C-RAN components: RU, DU, and CU. Similarly, the OAI NGC supports different functional components: the Mobility Management Entity (MME), the Home Subscriber Server (HSS), the Serving Gateway (S-GW) and the Packet Gateway (P-GW). In addition, the OAI open source platform also supports different functional split interfaces such as opt.8, opt.7.1, and opt.2 as described in 3GPP [172]. As shown in Fig.6.15, the opt.7.1 split is exploited between the DU and the CU components. The radio frequency (RF) and the lower-PHY functions such as FFT, IFFT and cyclic prefix (CP) add/removal are considered for UAV (SKY), and

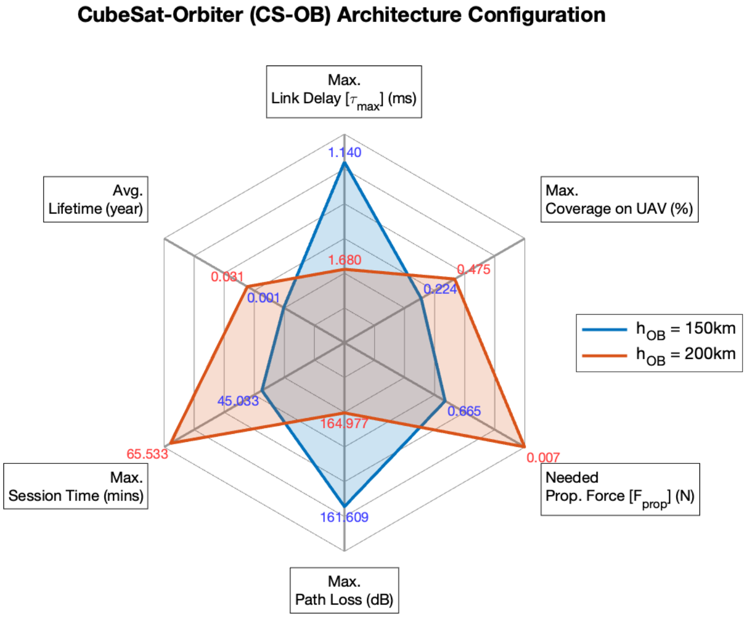

(a) Trade-offs for $h_{OB} = [150, 200]$km

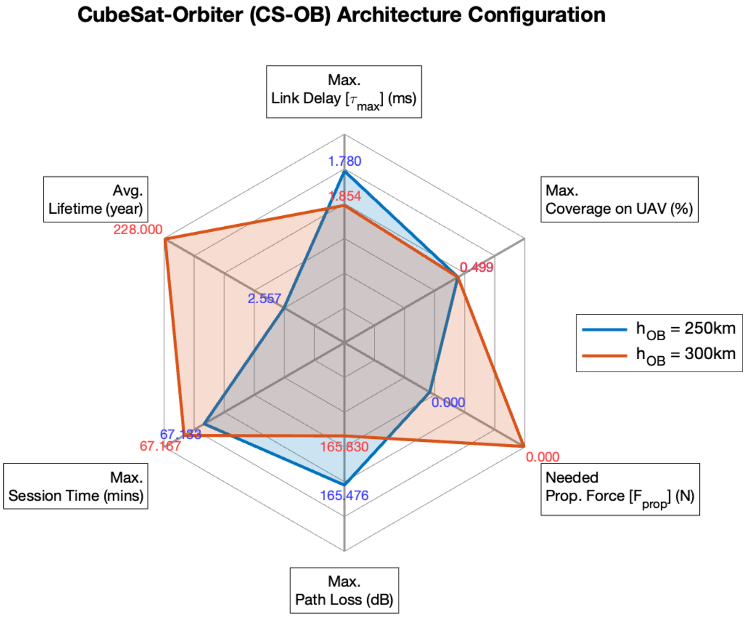

(b) Trade-offs for $h_{OB} = [250, 300]$km

Figure 6.14: (a) Spider web plot of the trade-offs introduced by the selection of the altitude for an orbiter constellation placed at $h_{OB} = [150, 200]$km with respect to a CubeSat constellation at $h_{CS} = 67.1$km. (b) Spider web plot of the trade-offs introduced by the selection of the altitude for an orbiter constellation placed at $h_{OB} = [250, 300]$km with respect to a CubeSat constellation at $h_{CS} = 67.1$km.

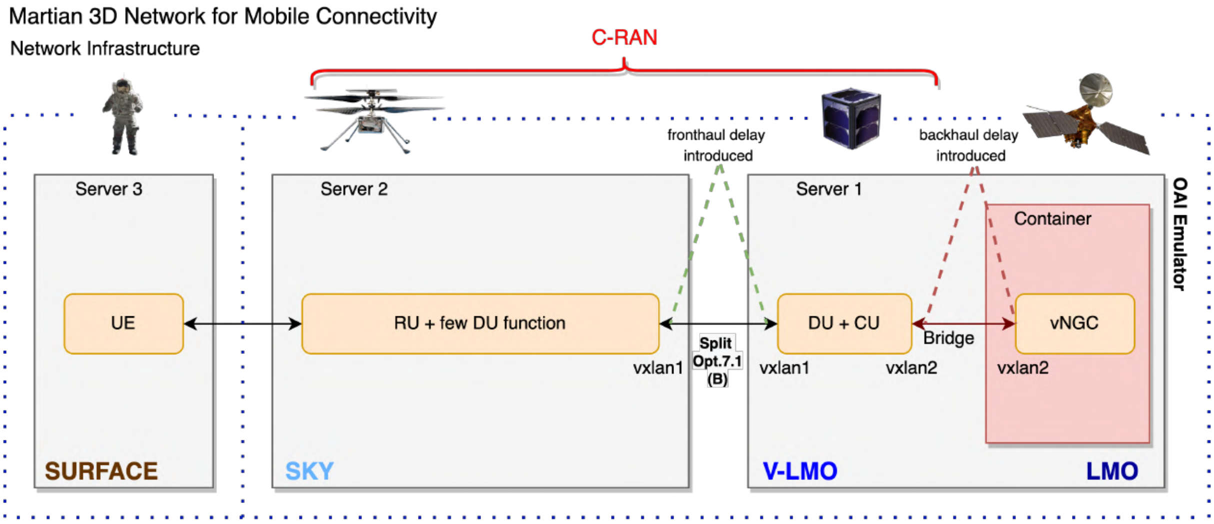

Figure 6.15: The considered OAI deployment mapped to 6G connectivity on Mars.

emulated at the Server2. The higher-PHY and above functions are deployed at the Server 1, and considered as CubeSat (V-LMO). The OAI UE is considered to emulate the user (SURFACE) and the docker-container based virtulized NGC (vNGC) is deployed in server2 to evaluate as Orbiter (LMO). The connections between DU and CU, CU and NGC are exploited by using Virtual Extensible LAN (VXLAN). In order to emulate the considered 6G connectivity on Mars, the obtained simulation delays are introduced in the OAI emulator at "VXLAN" interfaces for front-haul and back-haul as shown in Fig.6.15. The delay at the VXLAN links are introduced by using the linux utility *traffic control (tc)*. The *tc* utility follows a token bucket filter implementation, and it is capable of increasing the delay on a link by strong packets for the given amount of time at the output interface before its transmit on the link [173, 174]. The emulation platform is mapped with 6G connectivity on Mars by considering the link between DU and CU as the link between UAV and CubeSat (UAV-CS) and the link between CU and NGC as the link between CubeSat and Orbiter (CS-OB).

6.8.1 E2E Performance

As noticed in the legend in Fig.6.16, four network emulation configurations have been considered by selecting maximum distances between the CD and NN. From Fig.6.11a and Fig.6.11b, we obtain the upper bound

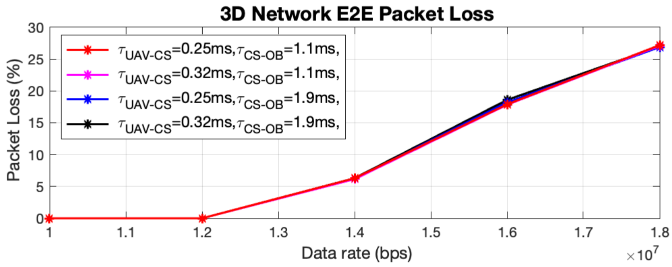

(a) E2E Packet Loss

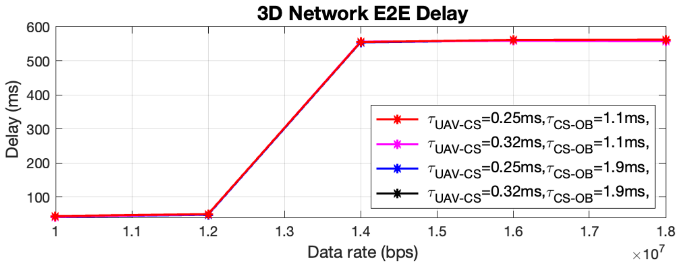

(b) E2E Delay

Figure 6.16: (a) End-to-end packet loss in percentage, considering τ_{UAV-CS} = [0.25, 0.32]ms and τ_{CS-OB} = [1.1, 1.9]ms. (b) End-to-end delay in milliseconds, considering τ_{UAV-CS} = [0.25, 0.32]ms and τ_{CS-OB} = [1.1, 1.9]ms.

Table 6.8: Contact distance for UAV-CubeSat link.

	Contact Distance	Propagation Delay
$h_{CS} = 48.4$km	$d^{max}_{UAV-CS} \approx 75$km	$\tau^{max}_{UAV-CS} \approx 0.25$ms
$h_{CS} = 67.1$km	$d^{max}_{UAV-CS} \approx 95$km	$\tau^{max}_{UAV-CS} \approx 0.32$ms

of link distances, ensuring more than 99% of occurrence, both for UAV-CubeSat (*UAV-CS*) and CubeSat-orbiter (CS-OB) links.

However, the emulated configurations are based on the observed best and worst cases between the emulated components. In the worst scenario, the maximum contact distance between the UAV and the CubeSat, placed at $h_{CS} = 67.1$km, is around 95km, and the corresponding delay is $\tau_{UAV-CS} = 0.32$ms (see Tab.6.8). The best case scenario is taken into account by placing CubeSat at $h_{CS} = 48.4$km, and consequently the corresponding delay is $\tau_{UAV-CS} = 0.25$ms as specified in 3GPP [172]. Similarly, the delays between the CubeSat and orbiter are for the best scenario $\tau_{CS-OB} = 1.1$ms and for the worst one $\tau_{CS-OB} = 1.9$ms (see Tab.6.9).

The above specified delays are introduced at the various VXLAN interface (as shown in Fig.6.15) with help of *tc* utility. E2E packet loss and

Table 6.9: Contact distance for UAV-CubeSat link.

	Contact Distance	Propagation Delay
$h_{OB} = 150.0$km	$d_{CS-OB}^{max} \approx 341.8$km	$\tau_{UAV-CS}^{max} \approx 1.1$ms
$h_{OB} = 200.0$km	$d_{CS-OB}^{max} \approx 503.7$km	$\tau_{UAV-CS}^{max} \approx 1.7$ms
$h_{OB} = 250.0$km	$d_{CS-OB}^{max} \approx 533.5$km	$\tau_{UAV-CS}^{max} \approx 1.8$ms
$h_{OB} = 300.0$km	$d_{CS-OB}^{max} \approx 555.7$km	$\tau_{UAV-CS}^{max} \approx 1.9$ms

delays are computed by taking advantage of the *iperf*, and *ping* utility, respectively. The user datagram protocol (UDP) traffic transmitted from client (i.e. UEs) to server (i.e. NGC) - or orbiter constellation, is in the range $T_b = (10 : 2 : 20)$Mbps. During the *iperf* transmission from the UE to NGC, the E2E delay (round-trip-time - RTT) is measured between UE and NGC, thanks to the *ping* command and the averaged delays are considered for plotting. The E2E packet loss is determined from the *iperf* output.

Fig.6.16 shows packet loss and delay as a function of the link rate transmitted between the UE and NGC. For a link rate less than 12Mbps, the achieved packet loss tightly approaches the zero value as shows Fig.6.16a, and the E2E delay is about $40-50$ms (see Fig.6.16b). Such a latency with the proposed throughput would be suitable to support critical applications, for instance real-time drone government, which require data rates around $300-600$Kbps and $RTT < 60$ms to not affect the maneuverability, and also video calls, where the requirements for high definition are: $T_b = 1.8$Mbps and one-way latency below 100ms. For the evaluation purpose only, the channel bandwidth is set to 25MHz (i.e., 25 resource blocks).

Note that changes in the back-haul delay for few milliseconds maintain the system able to perform well, however the same cannot be said for the front-haul latency due to tight synchronization required between the C-RAN components. However, for our purposes, the link distance between UAV (RU) and CubeSat (DU and CU) has a strong impact on coverage and lifetime, as shown in sect.6.7. Fig.6.17 shows the packet loss and the delay as function of front-haul delay, which indeed represents the distance between the UAV and the CubeSat. Here, the fixed back-haul delay is introduced and set to $\tau_{CS-OB} = 1.9$ms, and the link rate is set to 12Mbps between the UE and NGC. The obtained results show that there is an inflection point towards $\tau_{fh} = \tau_{UAV-CS} = [0.6,\ 0.7]$ms, where the packet loss and delays changes. More specifically, the worse E2E packet loss and delay

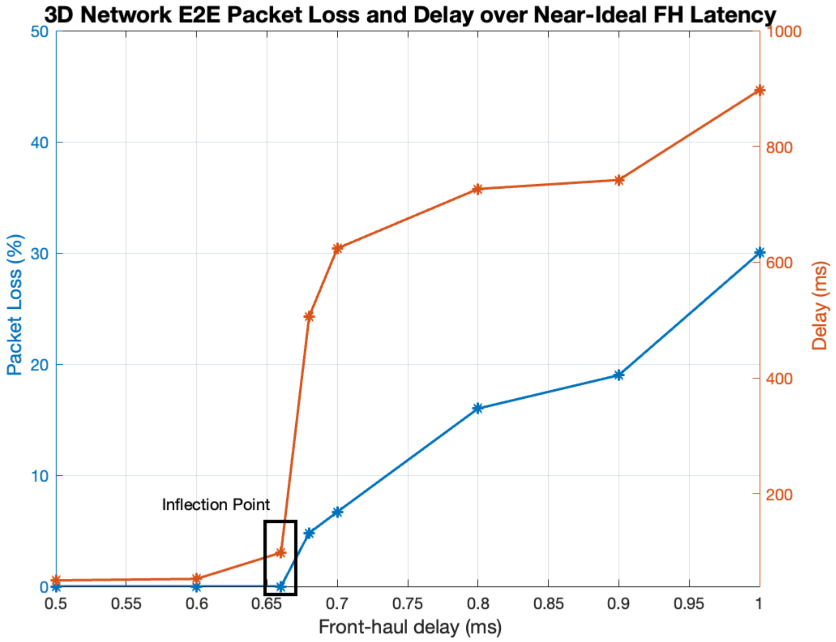

Figure 6.17: E2E packet loss and delay obtained by varying the front-haul near-ideal latency in the range $\tau_{fh} = \tau_{UAV-CS} = [0.5, 1.0]$ms.

behaviour starts from the inflection point $\tau_{UAV-CS} = 0.66$ms. This leads to $d^{max}_{UAV-CS} \approx 200$km, which show the possibility of increasing the orbital altitude of many kilometers, thus providing a higher degree of freedom to the whole architectural design.

6.8.2 Distribution of computational burden through the various network nodes

To conclude this section, just a few considerations regarding the computational load on the UAV and CubeSat nodes. We emulated RU, DU and CU functions on two identical HP servers mounting an Intel Core i7-10700 processor with a base clock frequency of 2.9GHz, 16MB of cache, and 8 cores. The emulations were measured through *sar* command. The computational load is almost flat in the $T_b = (10 : 2 : 20)$Mbps range for each tested case. However, 1.31% is the load of the RU task on the UAV processing unit, while 4.13% is the load of DU plus CU functions on the CubeSat processing unit. If we consider the whole load and do a simple proportion, it results that we moved the 75.82% of the baseband processing on CubeSat, while the remaining 24.18% should be accomplished at the

UAV side. Thus, despite next sections will deepen the knowledge around energy resources to be available especially on-board of UAVs, we can claim that power consumption will be higher at CubeSat side, as it was desired to save energy for drone operations.

6.9 SWaP-C for Resource Allocation

The previous subsection roughly demonstrated the computational load distribution over UAV and CubeSat for the implementation of C-RAN functionalities. However, to dimension computational and energy resources to be hosted on communicating nodes is a non-trivial task, that cannot be superficially addressed. More in detail, t_{bsp} is a function of $\mathbb{R}$, thus $t_{bsp}(\mathbb{R}, IC)$, with IC the Instruction Count per program. The amount of resources to be made available on the UAV or CubeSat is dependent, on one side, on the targeted processing time, on the other side, on the number of instructions per program to be run. In our case, IC varies with the performed splitting operations. As we choose lower splitting options, the IC will decrease. More precisely, $IC^{dynamic}_{split\,opt.}$ is the dynamic number of instruction per splitting option to be executed. The dynamic IC takes into account all those instructions repeatedly computed within, for instance, loops.

$$IC^{dynamic}_{split\,opt.} = IPC^{PU}_{split\,opt.} \cdot t^{PU}_{split\,opt.} \cdot f^{PU}_{CPU} \tag{6.25}$$

The instructions per cycle $IPC^{PU}_{split\,opt.}$ depend on the PU and the workload [175]. As we shall see later, we measured it on hardware to retrieve $IC^{dynamic}_{split\,opt.}$. The PU processing time for the considered splitting option is $t^{PU}_{split\,opt.}$, while f^{PU}_{CPU} is the achievable PU clock frequency. Being $IC^{dynamic}_{split\,opt.}$ a constant, by inverting the equation and varying the objective processing time $t^{obj}_{split\,opt.}$, we estimate the required $IPC^{obj}_{split\,opt.}$ as follows:

$$IPC^{PU-obj}_{split\,opt.} = \frac{IC^{dynamic}_{split\,opt.}}{t^{PU-obj}_{split\,opt.} \cdot f^{PU}_{CPU}} \tag{6.26}$$

From here, it is straightforward to predict the needed $MIPS^{PU-obj}_{split\,opt.}$ with respect to the required processing time per splitting option:

$$MIPS^{PU-obj}_{split\,opt.} = \frac{IPC^{PU-obj}_{split\,opt.} \cdot f^{PU}_{CPU}}{10^6} \tag{6.27}$$

Now, let’s assume to parallelize the workload on PUs. Under such assumption, we obtain the $N^{PU-obj}_{split\,opt.}$ necessary PUs to be mounted and available, for instance, on a UAV:

$$N^{PU-obj}_{split\,opt.} = \frac{MIPS^{PU-obj}_{split\,opt.}}{(MIPS^{PU}_{max})} \tag{6.28}$$

where $MIPS^{max}_{PU}$ is the PU maximum reachable MIPS value.

$$V^{PU-obj}_{split\,opt.} = N^{PU-obj}_{split\,opt.} \cdot V^{PU} \tag{6.29}$$

$$m^{PU-obj}_{split\,opt.} = N^{PU-obj}_{split\,opt.} \cdot m^{PU} \tag{6.30}$$

$$P^{PU-obj}_{split\,opt.} = N^{PU-obj}_{split\,opt.} \cdot P^{PU} \tag{6.31}$$

$$c^{PU-obj}_{split\,opt.} = N^{PU-obj}_{split\,opt.} \cdot c^{PU} \tag{6.32}$$

Finally, $N^{PU-obj}_{split\,opt.}$ allow us to provide guidelines regarding the volume $V^{PU-obj}_{split\,opt.}$ (m^3), weight $m^{PU-obj}_{split\,opt.}$ (kg), power $P^{PU-obj}_{split\,opt.}$ (W) and cost $c^{PU-obj}_{split\,opt.}$ (USD). (SWaP-C) metrics for the system design. V^{PU}, m^{PU}, P^{PU} and c^{PU} refers to the volume, mass, power consumption and cost of a single PU. SWaP-C is a common set of metrics for the optimization of hardware and software systems. The knowledge about SWaP-C is a priority for dimensioning complex systems like the one presented in this work.

6.10 Experimental Testing

The first step of the experimental analysis is to simulate the DL-SCH and PDSCH processing chain on a 2021 MacBook Pro equipped with an Apple M1 Pro chip and a 16GB RAM. Our aim is to obtain, through these simulations, data about the achievable throughput with respect to the system parameter setting and the variation of the execution time depending on the considered splitting options and the number of antennas both at TX and RX sides. On the other hand, the analysis regarding the system dimension-

Table 6.10: Raspberry Pi Data Sheet

	3B+	**4B**
Processor	Broadcom BCM2837B0 (4 Cores)	Broadcom BCM2711 (4 Cores)
Clock Frequency (Operative) f^{w}_{CPU}	1.4GHz	1.5GHz
Clock Frequency f^{MIN}_{CPU}	0.6GHz	0.6GHz
Clock Frequency f^{MAX}_{CPU}	1.4GHz	2.1GHz
Mega Instructions Per Second (MIPS)	~ 527	~ 2037
RAM	1GB	2GB
Power Supply	5V/2.5A DC via micro-USB	5V DC via USB-C (min 3A*)
Temperature (Operative)	45°	50°
Power Consumption (400% CPU Load)	5.1W	6.4W
Weight	45g	46g
Volume	80.92cm^3g	99.53cm^3g

ing through SWaP-C metrics has been performed starting from low-cost PU architectures. In particular, two Raspberry Pi (RP) boards have been used as external PUs to test on hardware with the NR splitting functionalities. The details about these devices are shown in Tab.6.10 [176, 177]. The RPs 3B+ and 4B mount an ICE Tower Cooling Fan from S2Pi, i.e. a liquid cooling, as shown in Fig.6.18b. This was necessary to overclock the PUs and to avoid unexpected crashes or even damages to the electronic board. The RPs are fed by a micro-USB and a USB-C respectively, assuring an input voltage of about $5V$. A Ruideng UM25 USB multimeter is used to check the possible voltage swings. It allows measuring voltage with a time step of one second, as well as for the current flowing in the RPs, through a simple graphical user interface receiving data via Bluetooth. An Ethernet cable connects the PC with the RPs for data and Wi-Fi sharing. An Ethernet-to-USB-C adapter has been employed due to the lack of a Gigabit Ethernet port on the MacBook. The program has been developed in MATLAB 2021b environment by exploiting the "5G Toolbox" and following 3GPP specifications about 5G NR. Deploying functions on Raspberry Pi is allowed thanks to the MATLAB Support Package for Raspberry Pi Hardware, which is a collection of functions to interface MATLAB and the RPs, and the *codegen* command. Through *codegen* it is possible to generate C++ code starting from MATLAB code. Most of the functions are supported by *codegen* for the C++ code generation. The remaining functions have been *ad-hoc* customized to be exclusively composed of functions

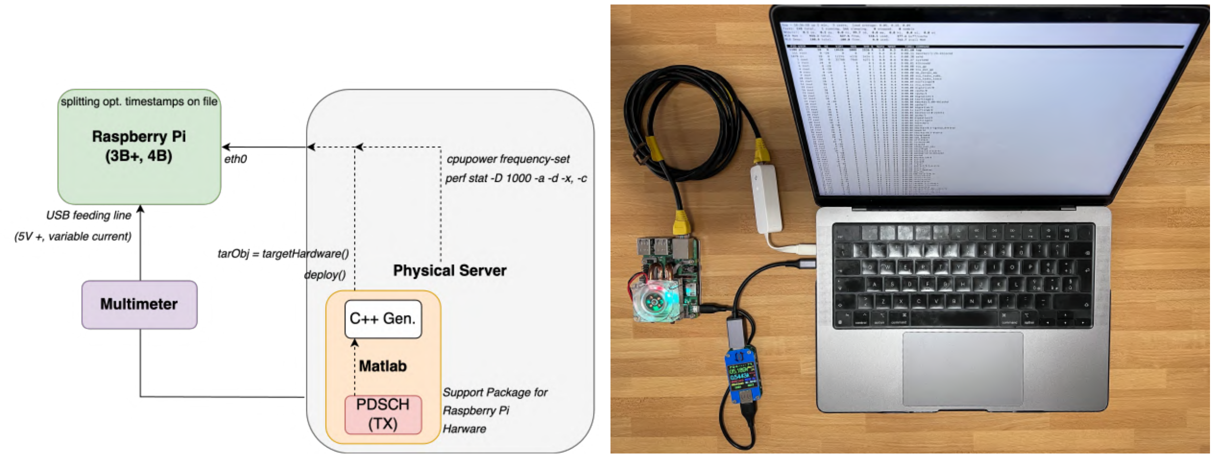

(a) Flow-graph (b) Setup photo

Figure 6.18: (a) Setup flow-graph detailing the deployment of PDSCH functionalities from MATLAB over external hardware, which is controlled by the physical server through *ssh*, by converting the program into C++ code. (b) Setup photo showing the deployment of PDSCH functionalities over a Raspberry Pi 3B+ (Raspberry Pi 4B was used as well) through MATLAB® Support Package for Raspberry Pi™ Hardware installed on a Macbook Pro with Apple M1 Pro chip. The feeding line is connected by a Ruideng UM25 USB multimeter for power measurements. The RPs mount the ICE Tower Cooling Fan from S2Pi to cool down themselves during the overclock process.

already supported by *codegen*. RPs are controlled by the PC through *ssh* and overclocked by launching *cpupower frequency-set* with *–min* and *–max* field to fix the working clock frequency f^{w}_{CPU}. The timestamps for each splitting opt. are printed on text file and then post-processed. Information about the IC per program have been retrieved by exploiting *perf stat*, which allows visualizing the IPC depending on the workload. As it is difficult to isolate the IPC per splitting option, we averaged the gathered data between 25 realizations of the same test, running the whole DL-SCH and PDSCH chain per slot.

6.10.1 Software implementation of New Radio processing functionalities

Fig.6.19 shows the processing chain, implemented by making use of the MATLAB 5G toolbox, namely: NR Downlink Shared Channel (DL-SCH) and Physical Downlink Shared Channel (PDSCH). Here, the implemented system is primarily subdivided into three different modules: *Transmitter*, *Propagation channel & Noise*, and *Receiver*. As shown in Fig.6.19,

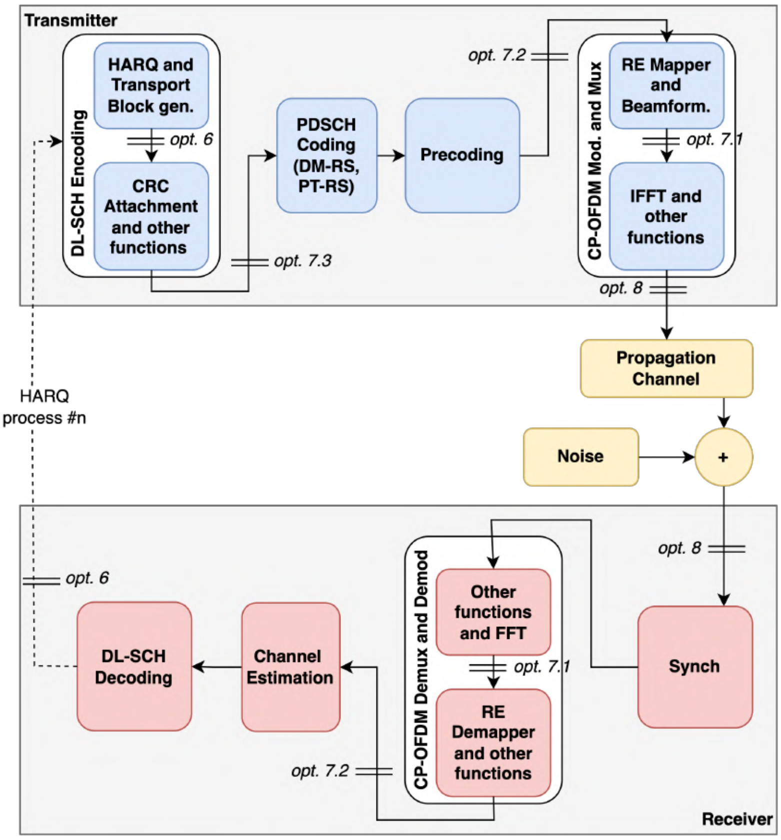

Figure 6.19: Encoding, modulating, demodulating and decoding functionalities composing the DL-SCH and PDSCH.

Transmitter module provides DL-SCH transport channel encoding, which internally performs Hybrid ARQ (HARQ), transport block generation, and Cyclic Redundancy Check (CRC) attachment along with other functions. The transport channel is used for the transmission of user data, dedicated control bits, user-specific and downlink system information. The PDSCH is the physical channel carrying the DL-SCH coded data. Here, Demodulation Reference Signal (DM-RS) and Phase Tracking Reference Signal (PT-RS) are associated with the PDSCH. The DM-RS is used to estimate the channel at demodulator side, and the PT-RS is used to compensate the Common Phase Error (CPE). Upon obtaining the perfect channel estimation for the considered sub-frames and averaging all the allocated resource blocks over time and frequency, pre-coding is obtained using Singular Value Decomposition (SVD). The output of the pre-coding is passed to the Cyclic-Prefixed Orthogonal Frequency Division Multiplexing (CP-OFDM) modulator and multiplexer, which manages the transmis-

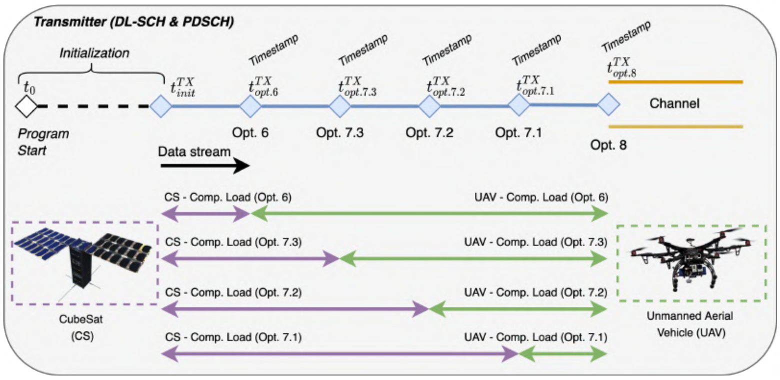

(a) Computational Load - Splitted TX

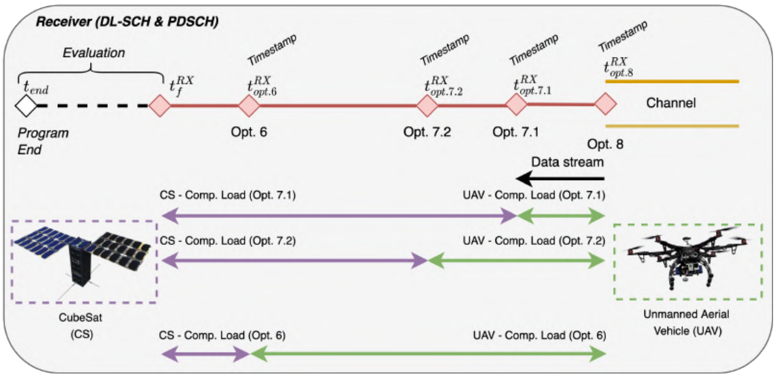

(b) Computational Load - Splitted RX

Figure 6.20: (a) Pictorial representation of the TX processing chain splitted up by opt.6, 7.3, 7.2, 7.1 and 8. In violet, the segments showing the computational load for TX processing moved to the CubeSat constellation, in green, the segments showing the computational load for TX moved to the UAV fleet. Opt.8 is not depicted because it assigns all the load to the CubeSat's PUs. (b) Pictorial representation of the RX processing chain splitted up by opt.8, 7.1, 7.2, and 6. In violet, the segments showing the computational load for RX moved to the CubeSat constellation, in green, the segments showing the computational load for RX moved to the UAV fleet. Opt.8 is not depicted because it assigns all the load to the CubeSat's PUs.

sion by supporting variable sub-carrier spacing, e.g., 15kHz, 30kHz, 60kHz, 120kHz. Clustered Delay Line (CDL) and Tapped Delay Line (TDL) are the two channel models supported in the considered implementation. The *Receiver* module, finally, performs PDSCH and DL-SCH demultiplexing, demodulation and decoding functions.

Fig.6.19 also shows the different splitting options (namely: opt.6, 7.3, 7.2, 7.1 and 8) that can be performed at transmitter and receiver side. Fig.6.20a shows the corresponding computational load distributed between CubeSat and UAV at the transmitter side. The computational load and the required corresponding PUs at the UAV might change based on the selected split option. Hence, it is important to know which resources are required to

perform the considered functions. Similarly, Fig.6.20b shows the computational load offloaded at the CubeSat and UAV for the receiver. Finally, the HARQ process either transmits new transport data or re-transmits the previously delivered transport data depending on Acknowledgement (ACK) or Negative Acknowledgement (NACK) determined by the CRC check. The above implementation is realized by setting some basic parameter values. As per 3GPP specifications, we consider the "Numerology 1", thus $N_{slot} = 20$ within a radio frame of 10ms (the selection of one between the 6 numerologies depends on the physical channel conditions). This means that the slot duration is $t_{slot} = 0.5ms$ with a sub-frame composed of 2 slots. Each slot contains 14 OFDM symbols. An OFDM symbol lasts in 33.33μs and the CP length is 2.34μs, leading to an overall symbol duration of 35.68μs. The slot is divided into two segments. We fixed DL-SCH transport channel coding code words to 1, as well as the number of transmission layers. The frequency domain sub-carrier spacing is set to $\Delta f = 30$KHz and 12 sub-carriers are contained in a resource block (RB). With a signal bandwidth of about 20MHz, 51 RBs are taken into account. Other significant parameters are the 16 HARQ processes, the LDPC code-rate $k/n = 490/1024$ with $k_{iter} = 6$ fixed as the maximum number of decoding iterations. The selected modulation constellation is the 16-QAM.
While for the simulations on PC we changed the number of N_{ant}^{TX} transmitting and N_{ant}^{RX} receiving antennas, for testing purposes over RPs we kept $N_{ant}^{TX} = 8$. For obvious reasons, i.e. due to the processing of 8 data streams, on a hand, this was the more time-consuming scenario, on the other, it is feasible to assume to mount more antennas to take advantage from the spatial diversity. To conclude this subsection, just a couple of words on the channel parametrization. We assumed to adopt a Clustered Delay Line channel model of type C (CDL-C), which is defined by 3GPP in Release 14 as a statistically realistic representation of a non-line-of-sight (NLOS) urban environment [143]. The delay spread is $\tau = 0.3\mu$s and the Doppler spread is $f_{shift} = 5$Hz, that could correspond to a relative speed of 2.5Km/h at a carrier frequency $f_c = 2.4$GHz.

6.10.2 Guidelines for Splitting Options Selection

The simulation results average data coming from the transmission of 5 slots. For each slot, the channel is re-initialized. First of all, we acquired the E2E throughput for the gNodeB-to-UE link, where the gNodeB is the binomial composed by Cubesat and UAV. For the CubeSat-to-UAV

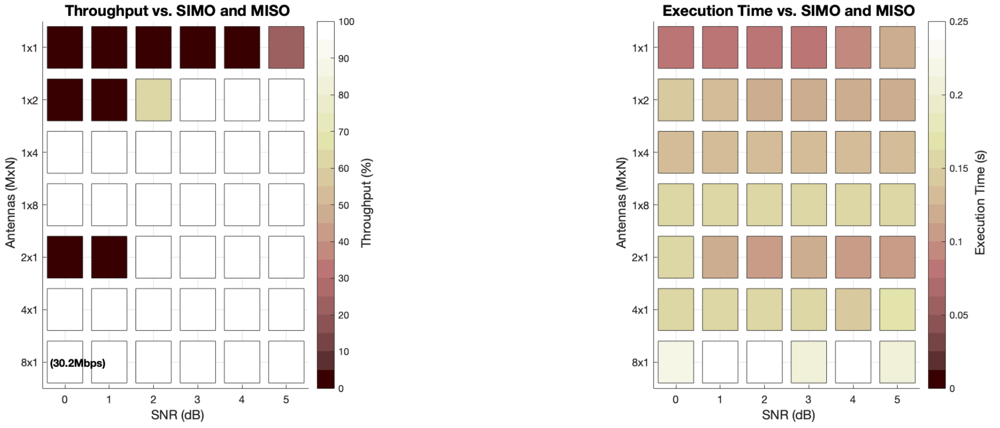

(a) Achievable throughput

(b) Execution time

Figure 6.21: (a) 5G NR PDSCH achievable throughput in percentage for MISO and SIMO systems. (b) 5G NR PDSCH execution time over an Apple M1 Pro chip for MISO and SIMO systems.

link we have considered a transparent channel. Indeed, this evaluation is simply aimed at visualizing the signal-to-noise ratio (SNR) improvement yielded by an increase of N_{ant}^{TX} or N_{ant}^{RX} antennas number. By adding antenna units, the SNR required to assure the same throughput decreases, as clearly visible in Fig.6.21a. Assuming the configuration described above - thus a maximum achievable throughput $T_b^{MAX} \approx 30.2Mbps$ - for single-input single-output (SISO) system and $SNR = 5$dB, we reach a 20% of T_b^{MAX}, while by doubling the TX or RX antennas, we obtain an important gain of 3dB to achieve 100% of throughput performance. This is due to the spatial diversity guaranteed by MISO and SIMO systems.

As expected, we can verify, from Fig.6.21b, that there is not any significant correlation between the execution time, i.e. $t_{bsp}^{UAV} = (t_f^{RX} - t_{opt.8}^{RX}) + (t_{opt.8}^{TX} - t_{init}^{TX})$, and the required SNR. We cannot verify the same for what concerns a higher number TX or RX antennas. Indeed, the amount of processing yielded by DL-SCH and PDSCH to the multiple streams transmitted by the physical antennas justifies a higher execution time t_{bsp}^{UAV}, and, consequentially a higher computational load $\mathbb{L}$ assuming $\mathbb{L} \propto t_{bsp}^{UAV}$. Again from Fig.6.21b, it is remarkably noticed that the execution time for a 2×1 or 1×2 system is almost twice that of the SISO system. Moreover, looking at the 1×8 versus 8×1 configurations, the former configuration takes 69% of the time taken by the latter one to complete the simulation.

From Fig.6.22, assuming a DL communication between the UAV-based RRH and an on-ground UE, it is important to notice how much the execution time increases as far as N_{ant}^{TX} increases, if we split the TX processing. Vice-versa, as N_{ant}^{RX} increases, the execution time ramps up to perform demodulation, demapping and decoding operations at RX side. As already mentioned above, the linear increase in the number of data streams (therefore in the baseband processing functionalities to be run) is the main cause of an increased execution time. Consequently, still considering the UAV-to-UE scenario, it appears that, as we add complexity to the TX, some splitting options become more prone to be exploited. In general, opt.6 yields, both for MISO and SIMO systems, to a $\sim 60-70\%$ reduction of the execution time with respect to not exploiting any splitting opportunities. However, this does not occur for a 8×1 configuration, where opt.6 carries a reduction of about 47%. Hence, opt.7.2 lowers down the processing latency of another 43.4%, as shown in Fig.6.22d. This is due to pre-coding and mapping operations left at Cubesat side. The formed PDSCH grid is a 3D matrix, whose third dimension is equal to N_{ant}^{TX}. From here, we can deduce that the more N_{ant}^{TX} we mount on the communicating node, e.g. UAV, the more is the importance of opt.7.2, at least in terms of saved computational and energy resources at UAV side. Other reasoning in this sense should take care of the communication system dimensioning according to the midhaul data rate to be maintained between UAV and CubeSat.

The analysis provided here about RX split processing is made upon the use of DL-SCH and PDSCH. To estimate RX processing at UAV side, physical uplink shared channel (PUSCH) should have been implemented for the uplink communication. However, with a small degree of approximation, we assume DL-SCH and UL-SCH very similar in their basic functionalities, as stated in [178]. Thus, the evaluations made about DL-SCH and PDSCH apply also to UL-SCH and PUSCH. From Fig.6.22b, it is clear that an increase in N_{ant}^{RX} corresponds to a higher execution time t_{bsp}^{UAV}, and, consequently, to a heavier processing load. Apparently, opt.7.2 is the operation leading to the major variations of the execution time at UAV or CubeSat side. In particular, the execution time reduction ranges between $\sim 70-80\%$ for all the simulated configurations. The gradient ∇ increases also in correspondence of opt.8 for 2×1, 4×1 and 8×1 MISO systems. However, opt.8, which would set to zero the processing time at UAV side (Fig.6.22a and Fig.6.22b do not depict opt.8 for this reason), is mostly prohibitive for the data rate in the order of Gbps required to the fronthaul link, as clearly understandable from our discussion in the previous

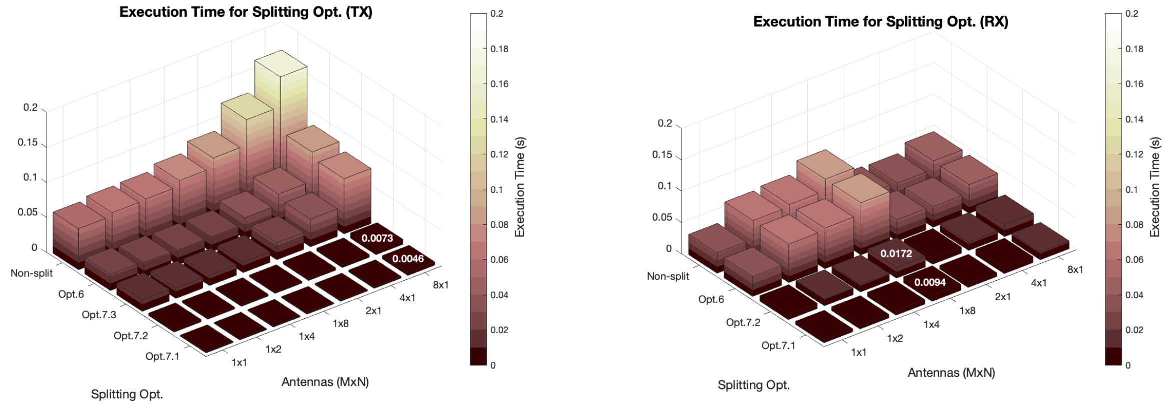

(a) TX execution time performing low-level splitting opt.

(b) RX execution time performing for low-level splitting opt.

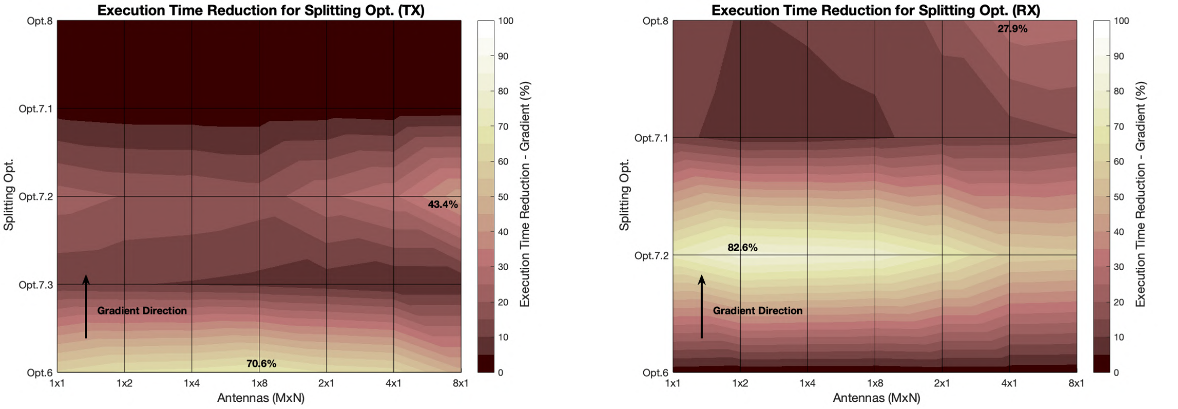

(c) TX execution time (∇) performing low-level splitting opt.

(d) RX execution time (∇) performing low-level splitting opt.

Figure 6.22: (a) Execution time of a 5G NR TX in percentage over an Apple M1 Pro chip to perform opt.6, opt.7.3, opt.7.2, opt.7.1, opt.8. (b) Execution time of a 5G NR RX in percentage over an Apple M1 Pro chip to perform opt.6, opt.7.3, opt.7.2, opt.7.1, opt.8. (c) Discrete gradient (∇) showing the saved amount of computational load by performing opt.6, opt.7.3, opt.7.2, opt.7.1, opt.8 at TX side with respect to the whole PDSCH computation. (d) Discrete gradient (∇) showing the saved amount of computational load by performing opt.6, opt.7.3, opt.7.2, opt.7.1, opt.8 at RX side with respect to the whole PDSCH computation.

sections. To conclude this subsection, we should highlight that opt.7.3 is not present for RX splitting, because 3GPP standardized it only for DL transmission [85, 143].

6.10.3 On-hardware results

To perform on-hardware evaluations, we have deployed the TX processing chain of a 8 × 1 MISO system on the external PUs, namely RP 3B+ and 4B. This choice was done to test the worst case scenario. As visible from the comparison of Fig.6.22a with Fig.6.22b, the 1 × 8 SIMO RX requires 49% less time than the 8 × 1 MISO TX to be executed.

The program runs over a single core, which led to a power consumption of about 3.72W (multimeter computation). The task parallelization is assumed for the SWaP-C analysis. We followed the methodology presented in sect.6.9 to acquire data related to RP 3B+ and 4B performance. In Fig.6.23a, with regard to splitting options 6, 7.3, 7.2 and 7.1, we evaluated the execution time on RPs against the clock frequency f^{w}_{CPU}. On the RP 3B+ and 4B, the execution time for the DL-SCH and PDSCH is in the order of seconds. More precisely, for a $f^{w}_{CPU} = 1$GHz, the processing power $\mathbb{P}\,^{UAV(RP\,3B+)}_{bsp}$ of a RP 3B+ allows executing the whole series of functions within $t^{UAV(RP\,3B+)}_{bsp} = 4.86$s, while the RP 4B decreases the execution time to $t^{UAV(RP\,4B)}_{bsp} = 2.47$s. This is due to the augmented processing capabilities $\mathbb{P}$ of the RP 4B with respect to the 3B+, i.e. $\mathbb{P}\,^{UAV(RP\,4B)}_{bsp} >> \mathbb{P}\,^{UAV(RP\,3B+)}_{bsp}$, at the price of a higher power consumption, as visible from Tab.6.10. As in the previous simulation series, shown in Fig.6.22c, opt.6 dramatically reduces the execution time to $t^{UAV(RP\,3B+)}_{opt.6} = 0.24$s and $t^{UAV(RP\,4B)}_{opt.6} = 0.22$s. An increase of the clock frequency f^{w}_{CPU}, while it solidly impacts on the execution time as clearly noticeable from Fig.6.23a, however, does not seem to cause a variation in the gradient ∇ characterizing the benefits of a splitting option with respect to another one. The number of instruction per cycle (IPC) is directly related to the choices of the processor and to the clock frequency. Practically, it is retrieved through *perf-stat*, which we have launched on the overclocked RP 4B ($f^{w}_{CPU} = 1.5$GHz) through *ssh*.

The achieved averaged value is $IPC^{RB\,4B}_{bsp} = 0.8152$, as shown in Fig.6.23b., which led to $IC^{dynamic}_{opt.6} = 159.6 \times 10^6$, $IC^{dynamic}_{opt.7.3} = 110.5 \times 10^6$, $IC^{dynamic}_{opt.7.2} = 68.4 \times 10^6$ and $IC^{dynamic}_{opt.7.1} = 40.2 \times 10^6$. Obviously, reducing the number

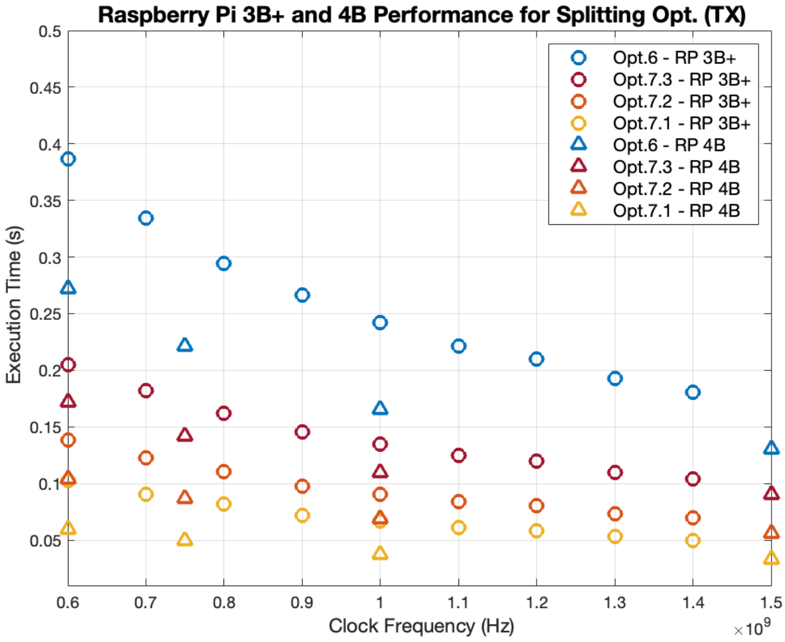

(a) Execution Time vs. Overclocked RP

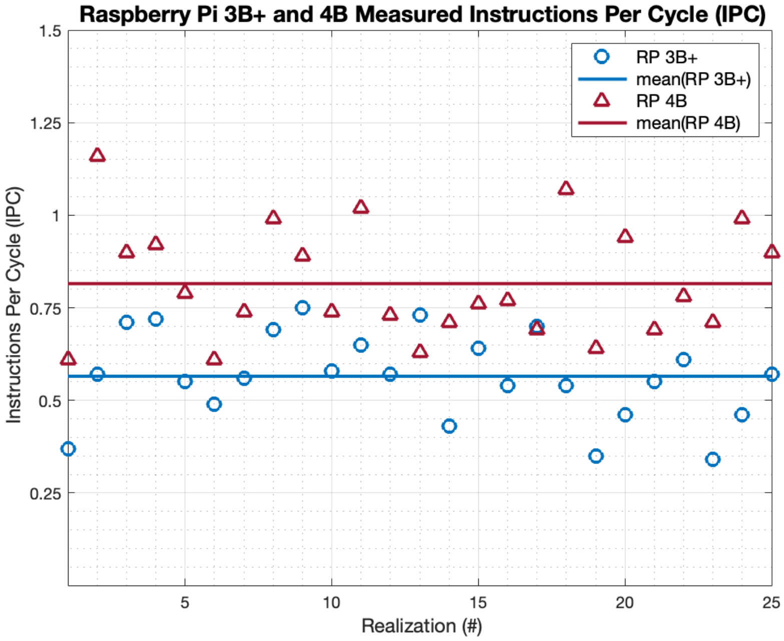

(b) Measured IPC for RPs

Figure 6.23: (a) Execution time of a 5G NR split TX over a Raspberry Pi 3B+ and Raspberry Pi 4B vs. various clock frequencies $f_{CPU} = [0.6, 1.5]$GHz reached by overclocking the RPs. (b) Measured IPC while running the whole DL-SCH and PDSCH chain on Raspberry Pi 3B+ and 4B.

of functions to be operated means to reduce the information count per program, which largely justifies the important gap between $IC^{dynamic}_{opt.6}$ and $IC^{dynamic}_{opt.7.1}$. From here, we have searched for the MIPS reachable by the RP 4B and comparing them with those of Nvidia Jetson Nano to estimate the number of PUs needed on-board of the UAV to execute the splitting options within a time span $t^{UAV}_{bsp} = [0.5,\ 1.5]$ms. This range was empirically selected, however, the slot duration is $t_{slot} = 0.5$ms, thus it is feasible to assume an added processing time per slot of the same order of magnitude. Obviously, by accepting a higher execution time and keeping in mind that for generic applications 5G commonly accepts T_{radio} around a couple of milliseconds, as written above in sect.6.4, we will incur in a lower distance between UAV and CubeSat, thus lower CubeSat lifetime, coverage and increased energy demand to correct the orbits.

In order to estimate the SWaP-C metrics, we fix $MIPS^{RP\,4B} = 2037$ and $MIPS^{JN} = 3900$ [179,180]. Although, these are not precise values as they come from benchmarking the PUs, we assume them as a feasible and easily achievable MIPS. Nvidia Jetson Nano is a small, powerful PU, whose envelope dimensions are $0.100 \times 0.080 \times 0.029$m. The maximum power consumption is around $10W$ and the list price for the “Jetson Nano Developer Kit” is 99$ with respect to 55$ for a RP 4B with 2GB of RAM [181]. The weight is 250g per board [182].

Finally, we shall point out how splitting options will impact on the system dimensioning. Indeed, size or volume, weight, power consumption and cost are strongly linked with the IC and t_{bsp} achieved per splitting option. This behavior is shown in Fig.6.24 and Fig.6.25. Requiring a tighter execution time turns into much more resources to be embarked on the UAV. Consequently, a system designer may think to assure enough computational and energy resources to perform one of the proposed splitting option. On average, by looking at the plots in Fig.6.24d and Fig.6.25d, we can say that in order to achieve the same system performance the required volume and the overall cost to host the RP 4B PUs or JN PUs on UAV will be almost the same. To be fair, costs depend on many factors. For instance, the latest chip shortage brought the cost of RPs to a 400% markup [183]. However, our aim is to provide a rough costs estimate. On the other hand, the weight to deploy RP-based or JN-based PUs on UAV is of particular interest. A single JN unit weighs the 543% more than the RP 4B. This is obviously reflected on the results in Fig.6.24b and Fig.6.25b. Assuring the processing capabilities $\mathbb{P}$ to perform opt.6 by RP 4B within $t^{UAV(RP\,4B)}_{opt.6} = 0.5$ms

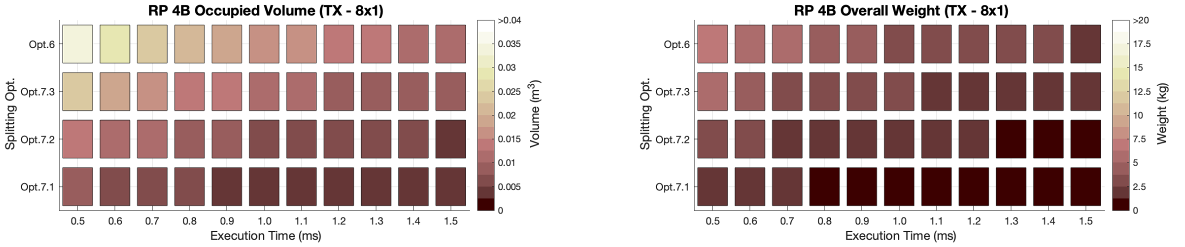

(a) Required RPs volume to assure the needed 5G NR TX execution time

(b) Required RPs weight to assure the needed 5G NR TX execution time

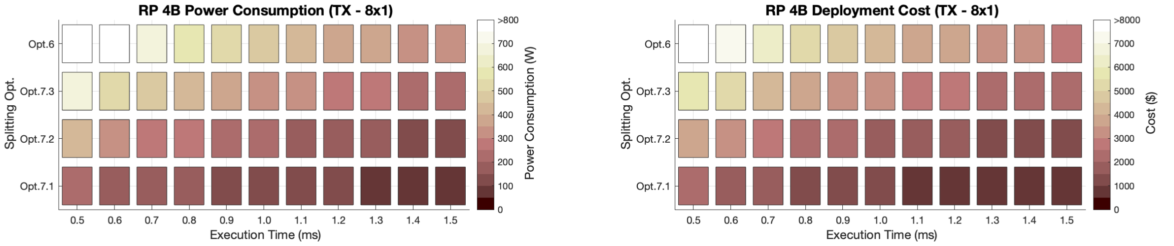

(c) Required RPs energy resources to assure the needed 5G NR TX execution time

(d) Required RPs cost to assure the needed 5G NR TX execution time

Figure 6.24: SWaP-C analysis for Raspberry Pi 4B split 5G NR TX. (a) Volume required to host RPs 4B on nodes implementing C-RAN to perform splitting opt.6, opt.7.3, opt.7.2 and opt.7.1 at TX side. (b) Weight required to host RPs 4B on nodes implementing C-RAN to perform splitting opt.6, opt.7.3, opt.7.2 and opt.7.1 at TX side. (c) Power consumption to host RPs 4B on nodes implementing C-RAN to perform splitting opt.6, opt.7.3, opt.7.2 and opt.7.1 at TX side. (d) Approximated deployment costs to host RPs 4B on nodes implementing C-RAN to perform splitting opt.6, opt.7.3, opt.7.2 and opt.7.1 at TX side.

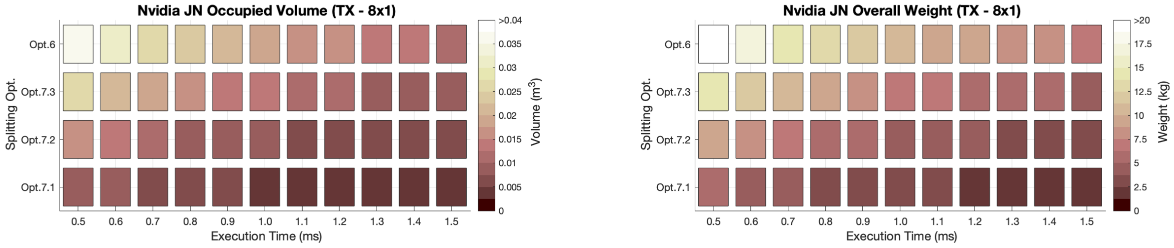

(a) Required JNs volume to assure the needed 5G NR TX execution time

(b) Required JNs weight to assure the needed 5G NR TX execution time

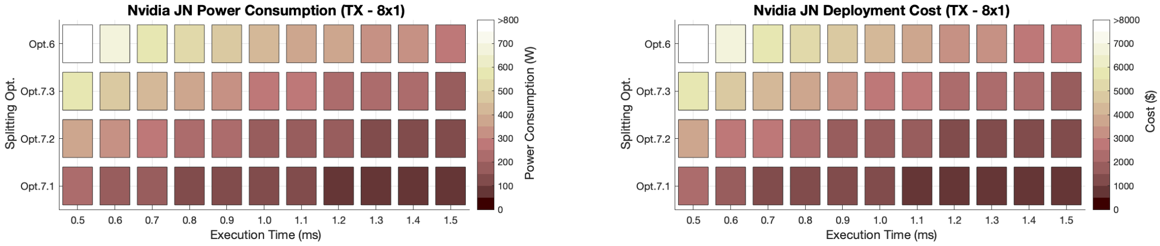

(c) Required JNs energy resources to assure the needed 5G NR TX execution time

(d) Required JNs cost to assure the needed 5G NR TX execution time

Figure 6.25: SWaP-C analysis for Nvidia Jetson Nano split 5G NR TX. (a) Volume required to host JNs on nodes implementing C-RAN to perform splitting opt.6, opt.7.3, opt.7.2 and opt.7.1 at TX side. (b) Weight required to host JNs on nodes implementing C-RAN to perform splitting opt.6, opt.7.3, opt.7.2 and opt.7.1 at TX side. (c) Power consumption to host JNs on nodes implementing C-RAN to perform splitting opt.6, opt.7.3, opt.7.2 and opt.7.1 at TX side. (d) Approximated deployment costs to host JNs on nodes implementing C-RAN to perform splitting opt.6, opt.7.3, opt.7.2 and opt.7.1 at TX side.

involves a weight $m \approx 7.5$Kg, while $m \approx 20$Kg would be the added weight for a JN-based UAV, and $P_{opt.6}^{UAV(RP4B)} = 820$W of power consumption with respect to $P_{opt.6}^{UAV(JN)} = 942$W.
Once we highlighted the macro differences between RP-based and JN-based systems, it is important to notice how a system design would change upon a static splitting option choice at the UAV side. Let us consider hosting JNs on UAV for their lower total power consumption and set a required slot processing time $t_{opt.6}^{UAV(JN)} = 0.5$ms. The required weight would be $m_{opt.6}^{UAV(JN)} = 20$Kg, as said before, and $m_{opt.7.3}^{UAV(JN)} = 14$Kg for opt.7.3, $m_{opt.7.2}^{UAV(JN)} = 5.5$Kg for opt.7.2 and $m_{opt.7.1}^{UAV(JN)} = 2$Kg for opt.7.1. Roughly speaking, there is an order of magnitude between $m_{opt.7.1}^{UAV(JN)}$ and $m_{opt.6}^{UAV(JN)}$. The same applies for costs, where from more than $cost_{opt.6}^{UAV(JN)} \approx 8000\$$ we move to $cost_{opt.6}^{UAV(JN)} \approx 2000\$$, which for mass production is for sure a great saving. The volume decreases too as well as the power consumption, which from opt.6 and opt.7.1 is reduced of ≈ 600W. The amount of saved energy resources would be then dedicated to the maximization of the flight time and, above all, service continuity.

6.11 Conclusions

This part of the thesis has discussed the motivation and the feasibility of a 6G 3D Network on Mars in order to provide connectivity to humans and machines. This represents an innovative, advantageous and flexible solution to set up a future generation network infrastructure in an extraterrestrial environment, where no infrastructure and reliable ground power supply are present. To the best of the authors' knowledge, this is the first work discussing 6G 3D Networks provisioning in an extraterrestrial scenario, showing a key bridge between the advancement in space exploration and the way to future generation communication networks. Moreover, the literature lacked of an integrated model detailing C-RAN 3D Networks from multi-perspectives. We tried to address this gap with a comprehensive analysis, moving from theory to simulations emulations and testing on hardware.
The chapter has principally analyzed the implementation of C-RAN into 3D Networks for 6G connectivity on Mars. Operating functional splits

is made possible by meeting strict requirements. Thus, we proposed a methodology to design 3D Networks and the C-RAN front-haul in compliance with latency and bandwidth requirements. Session time and optimal altitudes are computed with respect to the needed propulsion force to maintain the orbit. What is clear is that the Martian atmosphere could largely favor the deployment of a constellation of V-LEO CubeSats with respect to the terrestrial atmosphere by reducing the drag force, hence guaranteeing lowered altitudes.

Then, the antenna gains for the UAV-to-CubeSat wireless broadband link are dimensioned, accordingly to the required QoS imposed by the CPRI standard. Moreover, simulations and results about PHY and data-link layer performance shows the feasibility of network cells with radius of 500m and 1000m, obviously encountering decreased system performance as we enlarge the cell radius. Trade-off raising to design C-RAN 3D Networks are extensively studied. The important aspect of this part is to notice the inversely proportional behavior of the mechanical and aerospace parameters versus the communication and networking ones. As we go higher with the altitude of an orbiting node, we increase its lifetime and coverage while reducing the need for propulsion force to perform station keeping. On the other hand, by doing so, the service time will be worsened, as well as delays and attenuation, with a consequential impact on QoS performance.

Emulations via OpenAirInterface make possible to examine the E2E throughput, packet loss, latency and computational load. It is of particular interest the inflection point found by performing such evaluations. The analysis of the gathered data at the end user, or at the NGC side, allows computing the precise thresholds imposed by throughput and front-haul delays, above which E2E delay and packet loss become unacceptable. Starting from this achievement, we can increment the degrees of freedom of the 3D Network design. For instance, the more front-haul delay the network can accept, the higher lifetime and coverage of CubeSats is enabled, as well as the less would be the number of CubeSats to be deployed, thus reducing the overall costs of the whole system.

To conclude, we presented a methodology for the resource allocation of 3D Networks implementing C-RAN from the UAV perspective. First, we detailed the impact of baseband processing on the radio transmission delay and E2E delay. Then, we addressed the issue concerning the UAV on-board resources required to execute the baseband functionalities. Later on, we discussed splitting opportunities to save UAV-based RRH resources, while moving to the CubeSats, or other sky platforms, the major part of the computational load. Finally, we derived a methodology to predict the required resources, i.e. size weight power and cost (SWaP-C), on UAV to perform splitting options in an advantageous time window. Results firmly demonstrated the impact and benefits of baseband splitting operations over system design and performance.

This whole narration can be regarded as a starting point for future research work. First, it should be assessed the impact on E2E system performance of non-transparent front-haul links introducing errors, and non-ideal radio propagation on the Martian surface. Then, the analysis carried out for point-to-point connections should be extended to point-to-multipoint and multipoint-to-multipoint configurations. Handover strategies should also be an important theme to be opened up.

As repeatedly affirmed, we focused our attention towards the UAV resource dimensioning, being one of the most visible potential bottleneck of 3D Networks (considering the current drone technologies). For what concerns CubeSats, providing guidelines about the design of a satellite platform able to efficiently execute the assigned C-RAN functions will be a matter of future analysis.

Chapter 7

Advanced Relaying Techniques for Mars-to-Earth Long Haul

Providing connectivity on Mars is a two-fold task. While we already discussed the problem of in-situ Martian connectivity, we still need to deal with the Mars-Earth broadband data transfer. Here below, in sect.7.1 we contextualize the proposed decode-and-forward (DF) optical wireless multi-relay network (OWmRN) based on LPs, then, in sect.7.2 the solution will be detailed moving from the LPs motion, to the network modelling and link budget computation. Sect.7.3 will present results on the achievable data rate over a wide time span, depending on the relay-node characterizing the minimum-cost signal's path. Sect.7.4 will discuss delay management techniques and sect.7.5 will conclude the chapter proposing further improvements to the network.
This part of the thesis is partly retrieved from a conference paper [1].

7.1 Scenario and Further Motivations

RADIO-Frequency direct transmission (DT) from Mars to Earth is not likely to assure the required channel capacity for such high data rates. This, both in terms of bandwidth B_w, where the RF spectrum to be used is limited, and in terms of total received power P_{RX} at the receiver (RX). Indeed, for RF transmission, P_{RX} is extremely dispersed for long distances, especially due to the distance and the large beam divergence ϕ_{div}, which makes the geometric loss L_G a really significant term [184]. On the other hand, optical communications seems a good choice to deliver data to and

---

[1] Part of this chapter appears in [201]

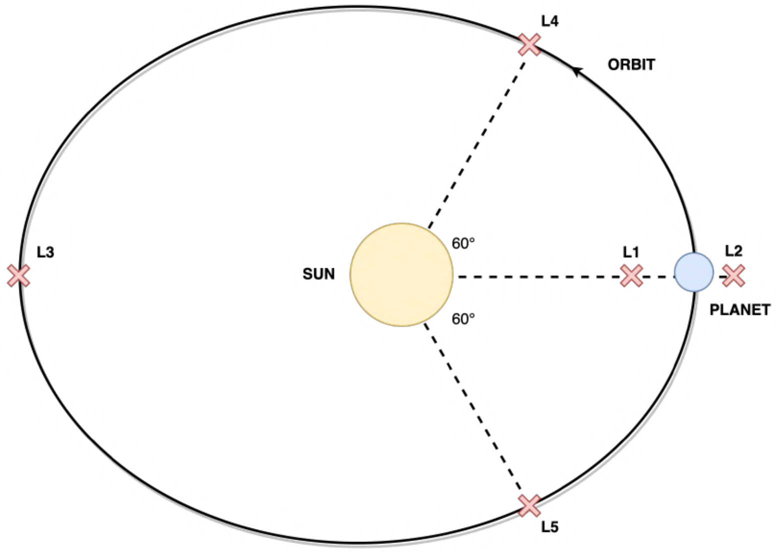

Figure 7.1: Lagrangian points for a generic satellite-planet-Sun interplanetary systems.

from Mars. This depends on the really small wavelength $\lambda_{opt} << \lambda_{RF}$ and the incredible available spectrum to be occupied. The narrow beam divergence is $\phi_{div} \sim \frac{\lambda}{D_{TX}}$, where D_{TX} is the transmitter (TX) aperture diameter [184]. Indeed, as we lower the wavelength, the ϕ_{div} will decrease as well as the geometrical loss L_G induced by it. What comes out is that the power consumption as well as the size and weight of the optical transceiver are way lower with respect to the RF counterparts [185]. Thus, it becomes easier to mount such a payload on orbiters or spacecraft to be sent in the deep space. For what concerns the bandwidth, it is approximately in the order of Terahertz (THz), which is 10^5 times the usable spectrum for typical RF carriers [185].
Although it could be feasible, for the data rates mentioned above, to design a suitable direct optical link from Mars to Earth based on orbiters, the reliability of such a network would be influenced just by the few nodes orbiting the two planets. Thus, a failure on one of this would hopelessly compromise the continuity of service and information would get lost. Moreover, and no less important, the solar conjunction between Mars and Earth happens every two terrestrial years. It roughly lasts two weeks, and it completely blocks communications, as also introduced in sect.1.1. To overcome such drawbacks, several studies were carried out detailing the deployment of network nodes to relay data from and to the so-called Lagrangian points (see Fig.7.1).

The Lagrangian points (LPs) are solutions to the restricted three-body

problem, where two heavy orbiting masses are close to a third whose mass is negligible [186]. Five of them can be found in each considered system, meaning, for instance, Mercury-Sun (Mr-S), Venus-Sun (V-S), Earth-Sun (E-S) and Mars-Sun (Ms-S). Usually, the Lagrangian points L4 and L5 are good spot to "park" orbiters and spacecraft, while L1, L2 and L3 are known as unstable points, where station-keeping should be adopted to counteract to the perceptible gravitational forces. However, by taking the necessary countermeasures, it is possible to conceptually formulate and analyze an optical wireless multi-relay network (OWmRN) based on Lagrangian points for Mars-to-Earth communications.
To the best of the author's knowledge, a OWmRN for interplanetary connectivity has not been simulated yet. Thus, we will try to fill this gap by estimating, first, the positions of the LPs in the deep space for the various orbiting systems. The communicating nodes are assumed to decode-and-forward (DF) the received frame. Then, the network will be modelled as a *digraph*, i.e. directed graph, where the shortest-path is weighted by selecting the route able to maximize the overall link capacity. The optical transceivers and their design parameters will be dimensioned accordingly to the system requirements, which will be related to data rate, BER and link distance d. The latter will, obviously, sensibly increase the propagation latency τ_{prop}. To this aim, few considerations about possible delay-hiding techniques will be raised to improve the QoE of end-users.

7.2 Designing Optical Relay Networks for Deep Space

The deployment of a decode-and-forward optical wireless multi-relay network (DF-OWmRN) based on Lagrangian points for Mars-to-Earth communications passes, first, through the computation of the LPs motion around the Sun as well as the motion of the inner planets of the Solar System. We suppose to “park” in the deep space orbiters orbiting in the vicinity of the LPs and mounting an FSO transceiver. Each network node, or orbiters, is meant to receive data from another node, decode and re-encode it to then forward everything to the next node. The outer planets and their LPs are not taken into account as parking spot for other relaying nodes. Indeed, not being in between Mars and Earth, there is no reason to increase the length of the path followed by the signal to reach the RX. This would cause higher delays and loss of power. A typical FSO transmitter for space application is mainly composed of a laser source, such as master oscillator power amplifier (MOPA)-based lasers or solid state laser communications in Space (SOLACOS), a modulator, which translates a low-frequency signal into an optical carrier [184], and a telescope directing the optical signal towards the receiver. The most popular modulation, thanks to its simplicity and robustness, is the On-Off Keying (OOK), which encodes each bit into a "on" or "off" light pulse. Thus, a data bit 1 is an emitted light, whereas a 0 is the absence of light [184]. For what concerns the receiver, it is usually constituted by another telescope collecting the optical radiation, an optical band pass filter (BPF), which reduces the background noise, and an optical amplifier. After these stages, we find a photodetector converting the optical signal into electrical one. High receiver sensitivity is a key factor for deep space communications, which is enabled by the choice of avalanche photodiodes (APDs). Finally, the demodulator retrieves the information sent by the transmitter. The choice of the best path from Earth to Mars, or viceversa, able at conveying the maximum possible amount of data is done by modelling the network as a *digraph*, where each edge is directed towards a new node. As mentioned above, the nodes are all the LPs related to the Earth-Sun, Venus-Sun, Mercury-Sun and Mars-Sun three-body systems, where the third mass is an orbiter parked on a chosen LP. The edges are weighted by the bit error probability P_b of a Reed-Solomon (RS) coded OOK transmission. At this point, the optimal path is the one given as output by the *shortestpath* function integrated in MATLAB, which maximizes the average capacity $\overline{\mathcal{C}}_{opt}$ by searching for the overall path with the lowest weight. Since the choice of the inter-link of the *shortestpath* depends on $max(\overline{\mathcal{C}}_{opt})$, the propagation delay τ_{prop} will be slightly increased with respect to the DT. However, there are applicable techniques that helps to conceal the delay at the end-user side. The most promising of them will be discussed in sect.7.4.

7.2.1 Lagrangian points motion

The motion of LPs in a certain time span t can be computed by taking advantage of the uniform motion of the material point over a circumference with radius r, i.e.:

$$x = a \cdot cos(\omega t) \tag{7.1a}$$

$$y = b \cdot sin(\omega t) \tag{7.1b}$$

where a is the semi-major axis of the ellipse representing the orbit, b is the semi-minor axis and $\omega = \frac{2\pi}{T}$ with T is the orbital period. The above equations are used to estimate the motion around the Sun per day of a given planet and its LPs, whose Euclidean distance with respect to the position of the same planet is always constant. By considering a reference planet position with Cartesian coordinates ($x = a, y = 0$), as for instance in Fig.7.2a, the LPs will be located at the following pairs of points [186]:

$$L1 : \left(x = R\left[1 - \left(\frac{\alpha}{3}\right)^{1/3}\right], y = 0\right) \tag{7.2a}$$

$$L2 : \left(x = R\left[1 + \left(\frac{\alpha}{3}\right)^{1/3}\right], y = 0\right) \tag{7.2b}$$

$$L3 : \quad \left(x = -R\left[1 + \frac{5}{12}\alpha\right], y = 0\right) \tag{7.2c}$$

$$L4 : \quad \left(x = \frac{R}{2}\left(\frac{M_1 - M_2}{M_1 + M_2}\right), y = \frac{\sqrt{3}}{2}R\right) \tag{7.2d}$$

$$L5 : \quad \left(x = \frac{R}{2}\left(\frac{M_1 - M_2}{M_1 + M_2}\right), y = -\frac{\sqrt{3}}{2}R\right) \tag{7.2e}$$

where $R \sim a$ and $\alpha = \frac{M}{M_{Sun}+M}$ with M the planet mass. It becomes straightforward to move the LPs accordingly to the revolution of their reference planet around the Sun, at least for L1, L2 and L3. Through proper manipulation of the arrays describing the planet orbital period and knowing that the distance from the LPs and the planet is always constant, the motion of L4 and L5 is, then, easily found. An example is shown in Fig.7.2a and Fig.7.2b, where starting from the planetary conjunction at time $t = 0$, after one Martian year all the LPs are displaced onto Cartesian coordinates determined by the planet orbital period of the various three-body systems.

7.2.2 Network modelling

The *digraph* object contained in MATLAB is a powerful tool to model the possible paths from a network node to another one, with an efficient control over accidental loops. The nodes are the LPs moving accordingly to their three-bodies reference system. Each node is associated with a table

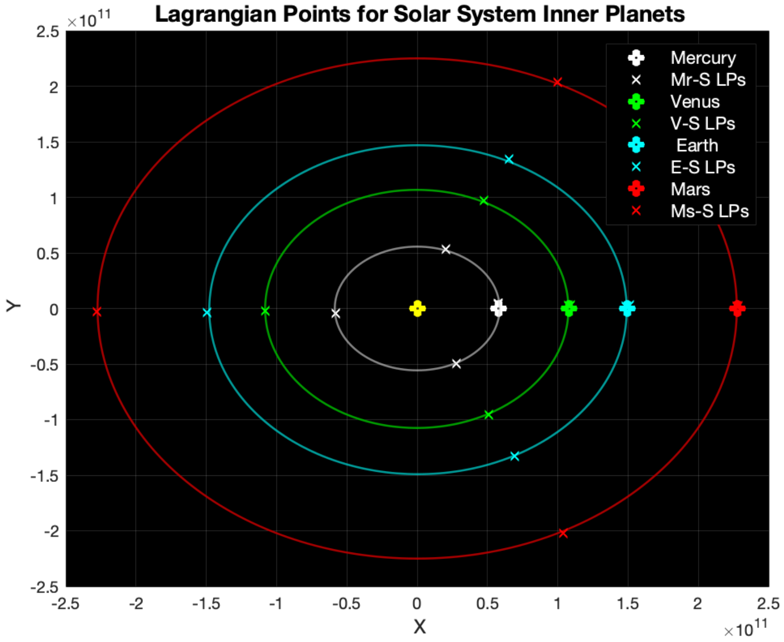

(a) Inferior Conjunction

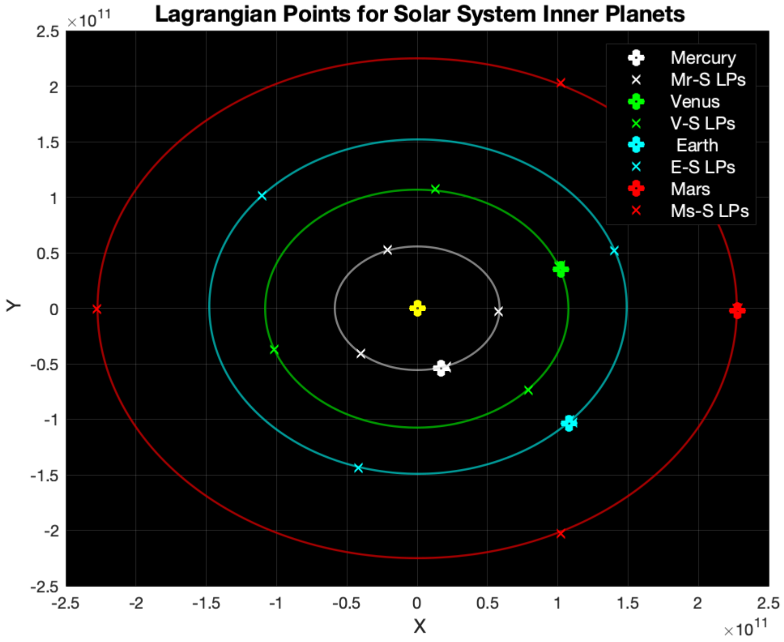

(b) Orbiting Planets

Figure 7.2: (a) Lagrangian points relative to the inner planets of the solar system in inferior conjunction. (b) Lagrangian points relative to the inner planets of the solar system after one Martian year from the inferior conjunction.

of directed edges. Path weights are then the bit error probability Pb of the RS coded OOK at each node k. We consider the use of APD direct detection, also known as intensity modulated/direct detection (IM/DD). The uncoded bit-error-probability $Pb_{unc}(k)$ is thus given by the following equation:

$$Pb_{unc}(k) = Q\left(\sqrt{\frac{S}{N}}\right) \tag{7.3}$$

where $\frac{S}{N}$ is given by the formulation here below [184]

$$\frac{S}{N} = \frac{R_0^2 \mathcal{M}^2 P_{RX}^2(k)}{(\sigma_1^2 + \sigma_0^2)} \tag{7.4}$$

The detector responsivity is $R_0 = \frac{\eta q}{hv}$, η being the detector quantum efficiency and q the electronic charge in Cb, h is the Planck's constant and v the working frequency. While $\mathcal{M}$ stands for the multiplication gain, which is given by

$$\mathcal{M} = \left(\frac{4K_BTF_n/R_L}{xqR_0P_{RX}(k)}\right)^{\frac{1}{x+2}} \tag{7.5}$$

with K_B the Boltzmann's constant, T the temperature in K, F_n is the noise figure, R_L the load resistance in Ω, x is a constant dependent on the material composing the photodetector and $P_{RX}(k)$ is the received power in W at the node k.

What is still missing is the definition of noise $N = \left(\sigma_1^2 + \sigma_0^2\right)$ as the sum of σ_1^2 plus σ_0^2, i.e.:

$$\sigma_1^2 = 2qI_{dc}B + 4K_BTBF_n/R_L \tag{7.6a}$$

$$\sigma_0^2 = 4K_BTBF_n/R_L \tag{7.6b}$$

where $I_{dc} = \mathcal{M}^2FR_0P_{RX}$ is the DC current and B is the overall bit-rate of the OOK. Finally, the coded $Pb_{cod}(k) = RS(n, k, Pb_{unc}(k), M)$, with $M = 2^l$ and l the number of bit per symbol, can be found by taking advantage of the common analytical expression in [150]. On a side note, it is correct to point out that we neglected the background noise, thus the formulation above comes from the removal of the terms dependent on such an impairment. However, we kept the thermal and shot noise as major contributor of noise in the computation.

The *shortestpath* function determines the shortest route providing the lowest total weight, thus lowest Pb_{cod}. The field *positive*, chosen for our weighted graph, employees the Dijkstra algorithm.

7.2.3 Link budget computation

The received power P_{RX} at a node k depends on many factors. They are shown as follows:

$$P_{RX}(k) = \frac{P_{TX} \cdot G_{TX} \cdot G_{RX} \cdot \eta_{TX} \cdot \eta_{RX} \cdot L_{TX}^{pnt} \cdot L_{RX}^{NBF}}{L_{TX-RX}^{path}} \tag{7.7}$$

where, for sake of space, we could not highlight that the terms with subscript TX are referred to $k-1$, while the ones with RX are related to the node k, i.e. the current destination where we want to estimate P_{RX} and the Pb_{cod}. P_{TX} is the power transmitted from the previous node $k-1$. G_{TX} is the transmitter gain defined as follows [184]:

$$G_{TX} = \left(\frac{4\pi A}{\lambda^2}\right) \left[\frac{2}{\alpha_{TX}^2} \left\{e^{-\alpha_{TX}^2} - e^{-\alpha_{TX}^2 \gamma_{TX}^2}\right\}^2\right] \tag{7.8}$$

where $A = \pi D_{TX}^2/4$ is the aperture area, $\alpha_{TX} \approx 1.07$ is the truncation ratio depending on the transmitter obscuration ratio $\gamma_{TX} = 0.2$. Clearly, $\lambda = c/f$ is the signal wavelength. The telescope receiver gain G_{RX} is given as follows [184]:

$$G_{RX} = \left(\frac{\pi D_{RX}}{\lambda}\right)^2 \left(1 - \gamma_{RX}^2\right) \tag{7.9}$$

where D_{RX} is the telescope diameter. Among the losses, we have the narrowband filter loss, that we assumed as a constant, and the free-space path loss, that given the extremely high frequency and distance, is playing a major role in reducing the received power at the destination on the node k. For sake of completeness:

$$L_{TX-RX}^{path} = \left(\frac{\lambda}{4\pi d}\right)^2 \tag{7.10}$$

d being, as already mentioned in the introduction, the link distance, i.e. the length of the straight path between nodes k and $k-1$. To conclude the link budget parameter analysis, L_{TX}^{pnt} represents the pointing loss, taken into account as a fixed value.

Table 7.1: System Parametrization

Parameters	Value
Laser power (P_{TX})	[150, 200]W
Operating wavelength (λ)	1550nm
TX Telescope Diameter (D_{TX})	1m
TX Obscuration Ratio (γ_{TX})	0.2
TX Optics Efficiency (η_{TX})	0.65
TX Pointing Loss (L^{pnt})	0.9
RX Telescope Diameter (D_{RX})	1m
RX Obscuration Ratio (γ_{RX})	0.35
RX Optics Efficiency (η_{RX})	0.7
Narrow Band Filter Loss (L_{RX}^{NBF})	0.7
Quantum Efficiency (η)	0.7
$x(InGaAs)$	0.7
Noise Figure (F_n)	1dB

7.3 OWmRN Achievable Data Rate and LP Utilization

This section will assess the behavior of the relaying network by estimating the achievable C-BER at final destination, meaning for instance Mars or Earth, with respect to a data rate swept in the range $[10, 100]$Mbps and a quite large time window of about five terrestrial years. Due to the huge distances between each node, we decided to exploit a robust RS(127,71) coding with a code rate of 0.56 compared to a lighter RS(256,224) leading to 0.88, in order to reduce the redundancy, increase the goodput, while paying in terms of C-BER. Another interesting point will consider the utilization of each orbiter on a particular LP within the deep space relaying network. Indeed, our simulations consider 20 usable nodes to relay the information from Mars to Earth, or vice-versa. For each planet-Sun system, we have 5 LPs possibly involved in the communication, for a total of 20 LPs. In Tab.7.1, we show the parametrization of the optical transceiver as well as the operating wavelength λ [184].

In order to estimate the achievable data rate within our time window, we fixed a $BER \leq 10^{-}9$ to guarantee the required QoS. As shown in Fig.7.3, with the configuration mentioned in Tab.7.1, it is always possible to provide at least 10Mbps of data exchanged from Mars to Earth. However, if we average in the time frame the data rates able to guarantee the expected QoS, what we obtain is an average data rate for the configuration $P_{TX} = 150$W - RS(128,71) of about 29.47Mbps, for $P_{TX} = 150$W - RS(256,224) the lowest 12.52Mbps, for $P_{TX} = 200$W - RS(128,71) the highest 44.63Mbps, and with $P_{TX} = 150$W - RS(256,224) 17.66Mbps. Of course, this variation is expected, although for such an application it should be better to reduce the power consumption, thinking to the limited energy resources in the deep space, rather than increasing the RS code-rate for an augmented goodput. However, as suggested by the blue pattern in Fig.7.3, each configuration of the OWmRN allows a data rate evidently outperforming common DT which, at most, are able to provide 4Mbps [187].

Another important aspect to be analyzed is the frequency of utilization of each node within the OWmRN. As mentioned above, we decided to simulate all the LPs of all the inner three-body systems of the Solar System. Despite this, averaging between the four configurations in Fig.7.4, the LPs of the Mars-Sun systems are not chosen to construct the optimal path, except for L1 which is located in between Mars and Sun and whose frequency of occurrence is around the $\approx 83 - 84\%$. Interesting is that the L2 is the less probable LP in the shortest-path for the Mr-S, V-S, and E-S three-body systems. This probably due to the outer position with respect to its reference planet (see Fig.7.1).

Picking the best and worst pair in terms of provided results, i.e. $P_{TX} = 200$W - RS(128,71) $P_{TX} = 150$W - RS(256,224), L1 Venus and L4 Venus are utilized the 47.06% and 41.84% of the times, respectively. These considerations suggest that some LPs should be preferable with respect to others, depending on the available power resources and the robustness of the RS channel coding. From a system design point of view, this means that the network could be constructed just with few orbiters placed in the most frequent LPs within the shortest-path to relay considerable amount of data from Mars to Earth and vice-versa, thus minimizing mission costs.

7.4 Delay Management Techniques

One of the most trivial objections against the Mars-to-Earth communications is the huge delay involved by the interplanetary distance, that would

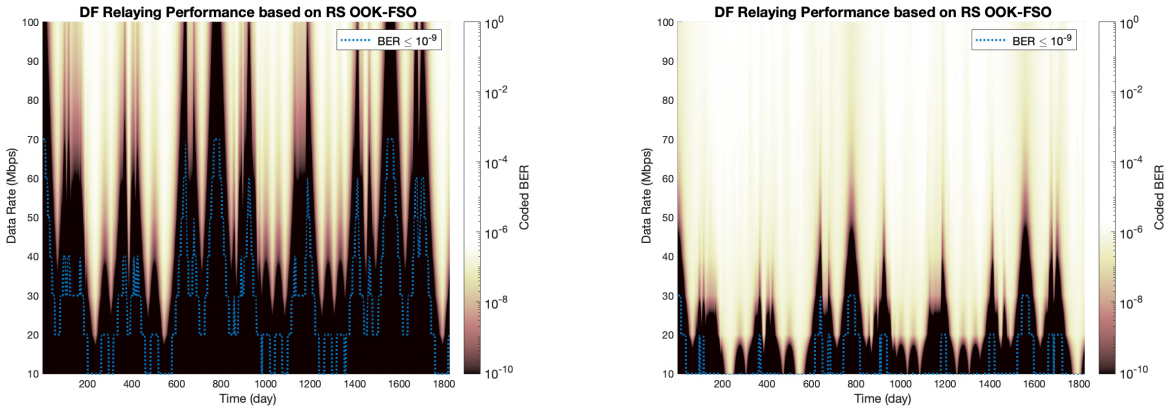

(a) $P_{TX} = 150\text{W}$ - RS(128,71)　　(b) $P_{TX} = 150\text{W}$ - RS(256,224)

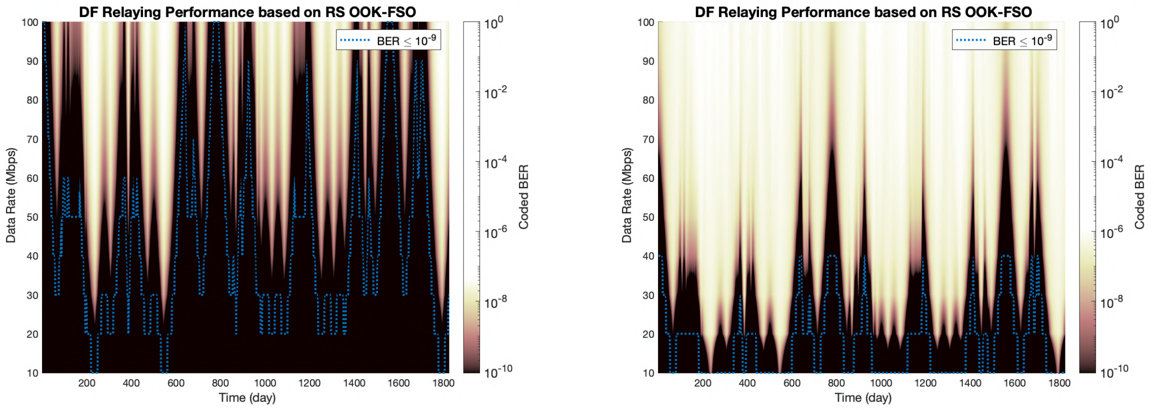

(c) $P_{TX} = 200\text{W}$ - RS(128,71)　　(d) $P_{TX} = 200\text{W}$ - RS(256,224)

Figure 7.3: (a) Performance assured by the DF relaying network based on OOK-FSO assuming $P_{TX}(k) = 150\text{W}$ and RS(127,71). (b) Performance assured by the DF relaying network based on OOK-FSO assuming $P_{TX}(k) = 150\text{W}$ and RS(256,224). (c) Performance assured by the DF relaying network based on OOK-FSO assuming $P_{TX}(k) = 200\text{W}$ and RS(127,71). (d) Performance assured by the DF relaying network based on OOK-FSO assuming $P_{TX}(k) = 200\text{W}$ and RS(256,224).

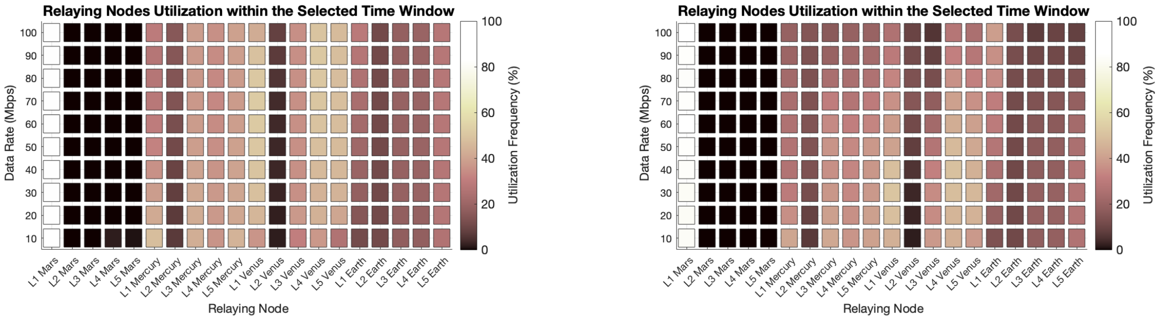

(a) $P_{TX} = 150\text{W}$ - RS(128,71)

(b) $P_{TX} = 150\text{W}$ - RS(256,224)

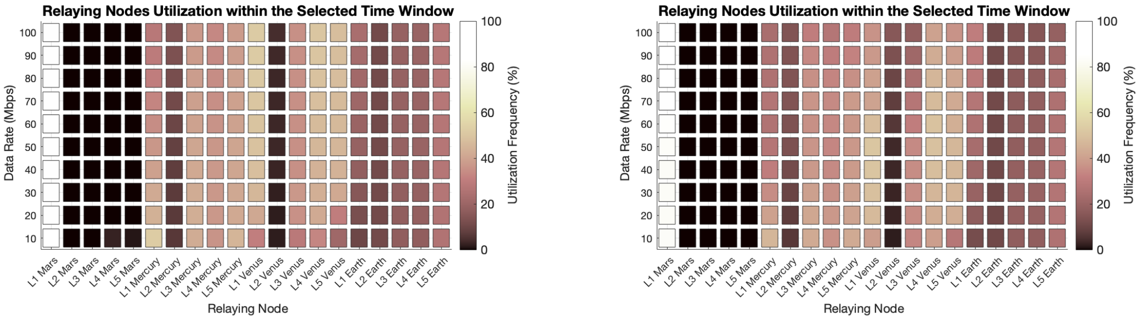

(c) $P_{TX} = 200\text{W}$ - RS(128,71)

(d) $P_{TX} = 150\text{W}$ - RS(256,224)

Figure 7.4: (a) Frequency of utilization of each network node within a time window of five terrestrial years assuming $P_{TX}(k) = 150\text{W}$ and RS(127,71). (b) Frequency of utilization of each network node within a time window of five terrestrial years $P_{TX}(k) = 150\text{W}$ and RS(256,224). (c) Frequency of utilization of each network node within a time window of five terrestrial years $P_{TX}(k) = 200\text{W}$ and RS(127,71). (d) Frequency of utilization of each network node within a time window of five terrestrial years $P_{TX}(k) = 200\text{W}$ and RS(256,224).

hinder real-time voice and data exchange. This objection would be reasonable if we have in mind the real-time constraints of terrestrial communications. However, in an interplanetary framework, the concept of "real-time" is not measured with the scale used in the terrestrial one. For instance, a delay of $6 - 7$ minutes in a voice communication is completely outside any concept of QoE measured on Earth.

If we consider a Martian scenario, such a delay may be acceptable. Remember that, many years ago, the telephone service was not so diffused on the territory and in some places, even close to big towns, there was only a single fixed telephone line and device available for communities of few thousands of people. In such a situation, people accepted very favorably a delay of few minutes before calling home.

Anyway, recent developments in interplanetary networking are considering solutions to improve performance also in presence of long delay. For instance, in [188] the authors analyzed an interplanetary overlay network in the presence of a long link delay, highly asymmetric channel rates and varying data loss rate. The main conclusion of [188] was that hybrid of TCP and Licklider transmission protocol (LTP) convergence layer protocols has significant goodput advantage over other protocol options as the ratio of data channel rate to Acknowledgment (ACK) channel rate increases. Other works [189] discuss the Interplanetary Internet and Delay Tolerant Networking (DTN) concepts, along with the various space networks.

In our view, we think that the issue of the long delay in the Mars-to-Earth link can be effectively faced at application layer level. The Earth station exactly knows the delay due to the long path, at least in terms of its first order (mean) and second order (variance) statistics.

For what concerns the transmission of data from Mars, it can be considered a synchronous application protocol that coordinates the exchange of data with the Martian hub in predefined time slots, encompassing the long delay. For what concerns voice transmission coming from astronauts exploring Mars, the issue is more complicated, because voice services are typically asynchronous. However, we can think to some sort of mechanism, based on periodical voice messaging that is expected to be received by the Earth station during reserved slots. Such an approach can be reasonable for the ordinary management of the mission. In case of emergency situations, the protocol for voice transmission should be, of course, reconsidered and redesigned. This will be a matter of future work.

7.5 Conclusions

We discussed how to take advantage of Lagrangian points and optical communications to provide efficient relaying in long-distance trunking from Mars to Earth. The relay network has been modelled as a directed graph where the shortest-path is weighted by selecting the route able to maximize the overall link capacity. Numerical results evidenced that the proposed methodology is efficient and viable, providing goodput values clearly outperforming conventional solutions based on direct optical transmission. Future work may increase the level of the analysis at PHY-layer level, considering possible link impairments both due to turbulence, space phenomena, hardware impairments, etc. Other typologies of channel coding might be considered as alternative to RS coding (e.g.: Low-Density Parity Check, LDPC codes). Finally, possible future analysis may concern with the optimized distribution of LP connections on the basis of their frequency of utilization.

As far as the huge delay inherent to interplanetary long-haul is concerned, this issue is not avoidable. However, it can be concealed at application layer level by studying appropriate QoE-oriented information management mechanisms comprehensive of the transmission delay. This will be another interesting argument for future research works.

Part III

Conclusion and Bibliography

Chapter 8

Final Considerations and Future Trends: What Comes Next?

We finally arrived at the conclusion of this thesis. The narration around NGC-M was wide and deeply detailed. Let us resume everything here, while fixing the findings of most interest and trying to critically compare them, their strengths and weaknesses in relation to what we saw throughout the essay. Sect.8.1 will summarize the main findings and contributions of this thesis, sect.8.2 will fairly compare the proposed solutions and sect.8.3 will comprehensively discuss further works to progress with the conducted research.

8.1 Summary of Findings

The road towards the human exploration of Mars is still impervious and demands joint efforts from all the international scientific community. To support and ease life in the deep space, envisioning future colonies on Mars, means bringing there efficient and reliable connectivity through complex architectures, among other technologies to be developed that we discussed in sect.1.1. In our small way, therefore, we tried to address the above by treating Martian communications as a twofold problem: assuring on-ground low-latency, broadband and robust connectivity and allowing to continuously transfer huge amount of data between Mars and Earth. However, the obstacles behind our goals were multiple and arduous to be solved. Indeed, little was published in the state-of-the-art, thus we aimed at constructing our own organic and integrated vision of technologies for Martian communications. First, we preliminarily analyzed in Chapter 4 a LTE porting on Mars, namely: Extraterrestrial LTE (E-LTE), by equipping machines, such as landers and rovers, with radio equipment and resources to deploy local mobile networks on the planet surface. Through Simulink and MATLAB simulations, we evaluated the physical and data-link layer performance reflected by the imposed E-LTE quality-of-service (QoS). We suggested here the introduction of single-carrier frequency division multiple access with interleaved allocation of the sub-carriers (I-FDMA) to benefit from an added diversity gain with respect to localized frequency division multiple access (L-FDMA). The results were encouraging, showing the feasibility of a small local network cell, while highlighting the negative impact of longer distances on the achievable throughput. Throughout this introductory work, we realized the need of a model for better understanding the radio-frequency (RF) propagation impairments over precise Martian locations. Even though the literature was quite rich about terrestrial measurements for assessing large and small-scale phenomena, for the Martian case, few data were available in the literature, thus not allowing a realistic and statistical modelling of Martian channels. For this reason in Chapter 5, we take advantage from a high resolution digital elevation model (DEM) to construct a tile-based structure on MATLAB of the Gale crater, that we used as representation of the Martian environment. We derived the electrical properties of a possible Martian soil, namely: JSC Mars-1, to characterize the tiles and to compute the Fresnel coefficients. A 3D ray tracing algorithm was implemented to estimate the line-of-sight (LoS), first and second reflections of a RF signal emitted by an isotropic antenna over 3D Martian areas. Thanks to the received power and the delay of arrivals of the signal replicas with respect to the LOS, we enlarged the knowledge around the RF propagation on Mars, acquiring data regarding the path loss exponent, shadowing, outage probability, and multipath fading occurring on flat and rocky areas of the planet. We also discussed a few limitations of our model in sect.5.3.3.

E-LTE represented the beginning of our approach to a networked Martian environment, however, allowing more degrees of freedom in-situ has driven us to the conception of an autonomous yet reconfigurable space ecosystem on the “Red Planet”, constituted of a 3D Network implementing C-RAN for a disruptive “Towards 6G” connectivity. This infrastructure has been designed by detaching the monolithic chain of 5G functionalities, which are virtualized on heterogeneous nodes, such as UAVs and CubeSats. We dug into Non Terrestrial Networks (NTN) to shed light on multi-layered networks on Mars. To begin with, we described the layers composing the

3D Network. Then, we discussed C-RAN implemented in 3D Networks thanks also to splitting options, allowing to detach radio unit, distributed unit and centralized unit functions of the 5G New Radio (NR). We proposed a methodology to meet latency and bandwidth requirements when dimensioning the 3D Network and designing the C-RAN front-haul. Next, a strategy for picking the optimal altitude to deploy the constellations of CubeSats is formulated and physical and data-link layer performances are estimated after having assured the compliance with the Common Public Radio Interface (CPRI) standard for the wireless connection between CubeSat and UAV thanks to a link budget analysis. After that, we found the inflection point, before which we can relax the latency requirement for splitting the baseband processing, that allows to increase the altitude of the orbiting small satellite platforms, thus reaching satisfying coverage, lifetime, and a sensible decrease of network nodes, without paying in terms of end-to-end quality-of-service. Finally, through a SWaP-C analysis based on hardware testing, we predicted the energy and computational resources to be hosted on-board of UAVs. Although such a complex architecture could seem way to bulky for interconnecting human personnel and machines on Mars, we qualitatively and quantitatively demonstrated its necessity and advantages to successfully accomplish future (un)manned missions in Chapter 6. Further considerations on this will come in the following section.

Just as importantly, it is obvious that delivering data on and from Mars is an enabler of deep space explorations. In anticipation of tens of machines gathering samples from the planet surface, tens of people exchanging critical information between themselves, downloading media for entertainment, expecting instructions from Earth, but also contacting families from there, we propose a decode-and-forward (DF) optical wireless multi-relay network (OWmRN) supported by orbiters “parked” in the Lagrangian points (LP). The satellites embark free space optics (FSO) transceivers to relaying data on the shortest-path from Mars to Earth, the one maximizing the channel capacity while meeting an expected QoS. Results demonstrated that OWmRN outperforms direct transmissions (DT), depending on the selected configurations. Due to the application, we suggest improving the robustness of the Reed-Solomon channel coding rather than increasing the transmitting power from each node. To conclude, the frequency of utilization of the various LPs within the shortest-path opens the door to the design of an optimized OWmRN, where just few LPs are picked to deploy the network while reducing the costs of the system.

8.2 On-Ground versus From-Above Connectivity

It is ethically mandatory to compare the E-LTE architecture with the C-RAN 3D Network for “Towards 6G” connectivity. The E-LTE generates a local network with a radius of hundreds of meters. For sure, it instantiates efficient connectivity within the network cell, as we saw in sect.4.5. However, the network relies on a base station (BS) fixed on-ground, precisely, the lander has not motion capabilities. In addition, the antenna height over the lander could be of few meters, thus not assuring the clearance of the first Fresnel zone. Again, the LTE remote radio head (RRH) and baseband unit (BBU) processing leads to a power consumption that can easily reach few kW. Thus, the energy resources could be not sufficient to consistently reuse landers as BSs and continuously networking the environment. Such a solution could fit the early stages of manned missions, where few people will live and work within a bounded area. On the contrary, an anywhere-anytime available space ecosystem can guarantee on-demand connectivity. Despite their limited flight time, once charged through solar arrays, UAVs can provide wider coverage, an improved QoS with an always present LOS, and more in general extremely broadband connections. Higher carrier frequencies with respect to E-LTE translates into broader spectrum portions to be allocated, thus extremely raised data rate. Moreover, let us remember that the spectrum on Mars is unlicensed, thus it can be widely exploited for future connectivity. As pretty clear, UAVs can fly, thus following people for space walks, acquiring data from human-unreachable zones through a dedicated payload, and also providing connectivity to faraway machines in need of sending data. If we point to a solid and safe human future on Mars, although it will require, at least, an enormous capital expenditure (CAPEX) to be sustained from space agencies and private companies, C-RAN 3D Network seems a feasible and reliable choice.
Other comparisons will be made in future works.

8.3 Future Trends

Each chapter’s own conclusion gave micro hints about possible further works to improve the analysis, algorithms, infrastructures etc. Here, we recall them while adding also macro visions and trends that could follow parallel branches of research. The E-LTE porting could be better studied in light of a more detailed Martian channel. Another step ahead could be to implement the 5G NR functionalities to appreciate the QoS improvement with respect to the E-LTE. An energy budget could also help to precisely understand the amount of energy resources to be harvested for the BBU processing.

The 3D ray tracing model based on DEM should be refined by minimizing the degrees of approximation, such as the down-sampling operation for the huge computational complexity, or again, introducing a variable permittivity to better electrically characterize the tiles and giving realistic depth to the 3D structure Up to now, we modelled C-RAN 3D Networks simulating and emulating point-to-point connections. Instead, further works should take into account constellations of CubeSats and fleets of UAVs accordingly operating and horizontally exchanging data. For sure, this is an open issue to be addressed. We still lack of knowledge for what concerns the resource allocation at CubeSat side within C-RAN 3D Networks. As said in sect.6.10, UAVs can be a potential network bottleneck for their limited resources, however, on the other hand, CubeSats are limited by their reduced sizes, thus volume to be occupied by processing units (PUs). A complete softwarization of their radio equipment could be another interesting theme, in line with what has been done in [195]. On these perspectives, we aim at collecting the knowledge gained around C-RAN 3D Networks to develop a multi-objective optimization problem for the remote and space manufacturing and deployment of CubeSats. The objectives will be the altitude selection, thus the number of orbiting nodes to achieve $> 99\%$ of network availability, the shape and size of CubeSats, then the energy and computational resources to be embarked on them with respect to the E2E system performance to be achieved. This will provide useful guidelines, giving a nod to a completely autonomous manufacturing typical of Industry 4.0.

Again, UAVs could be rather seen as a transparent relaying node forwarding data to the constellation of CubeSats, taking in charge the whole baseband processing. Most probably, to do so, CubeSats should be replaced with huger orbiters to host more equipment, thus assuring a certain QoS. In addition to everything we proposed here above, one idea could be to host variegate payload on the same CubeSat, being part of the C-RAN 3D Network, for furnishing positioning, navigation and timing (PNT) services. Finally, the DF-OWmRN could be compared with amplify-and-forward

(AF), compress-and-forward (CF) or other more complex cooperative relaying strategies. Non-Keplerian orbits could also be introduced in the network and later assessed. One last proposals and then the discussion will come to an end. Personally, we see drones still limited with respect to their huge potentiality. As the market will invest more and more into their production, a mobile network made of mere UAVs could be possible. A kind of artificial intelligence could be distributed into fleets of UAVs. Drones could be agents capable of operating functions on the basis of requests from other agents. The agent-based aerial network could become a dynamically adaptive C-RAN dependent on inter-link distances, users density and vicinity, and covered areas to provide ultra-efficient connectivity.

Bibliography

[1] R. Lea, "New images of ancient waterways of Mars could unlock the secrets of planet's past." https://www.space.com/photos-mars-holden-basin-past-water, 2022. (Date last accessed on October 25, 2022).

[2] J. Green, "Inventions we use every day that were actually created for space exploration." https://eu.usatoday.com/story/money/2019/07/08/space-race-inventions-we-use-every-day-were-created-for-space-exploration/39580591/. (Date last accessed on October 20, 2022).

[3] NASA, "How long would a trip to Mars take?." https://image.gsfc.nasa.gov/poetry/venus/q2811.html. (Date last accessed on October 21, 2022).

[4] J. Crusan and NASA, "Evolvable Mars Campaign." https://www.nasa.gov/sites/default/files/files/NextSTEP-EMC-Reference.pdf, 2016. (Date last accessed on October 21, 2022).

[5] T. D. Haws, J. S. Zimmerman, and M. E. Fuller, "Space launch system: Near term missions on the journey to mars," in *2018 IEEE Aerospace Conference*, pp. 1–10, 2018.

[6] T. Cichan, S. A. Bailey, S. D. Norris, R. P. Chambers, S. D. Jolly, and J. W. Ehrlich, "Mars base camp: An architecture for sending humans to mars by 2028," in *2017 IEEE Aerospace Conference*, pp. 1–18, 2017.

[7] R. Potter, S. Saikia, and J. Longuski, "Resilient architecture pathways to establish and operate a pioneering base on mars," in *2018 IEEE Aerospace Conference*, pp. 1–18, 2018.

[8] NASA, "6 Technologies NASA is Advancing to Send Humans to Mars." https://www.nasa.gov/directorates/spacetech/6_

Technologies_NASA_is_Advancing_to_Send_Humans_to_Mars, 2020. (Date last accessed on October 21, 2022).

[9] T. Percy, M. McGuire, and T. Polsgrove, “Combining solar electric propulsion and chemical propulsion for crewed missions to mars,” in *2015 IEEE Aerospace Conference*, pp. 1–10, 2015.

[10] P. Chai, R. Merrill, and M. Qu, “Mars hybrid propulsion system trajectory analysis part i: Crew missions,” 08 2015.

[11] NASA, “Journey to Launch: NASA’s Inflatable Heat Shield Ready for Demonstration.” https://www.nasa.gov/feature/goddard/2021/nasa-confirms-thousands-of-massive-ancient-volcanic-eruptions-on-mars, 2022. (Date last accessed on October 23, 2022).

[12] NASA, “Solar Electric Propulsion (SEP).” https://www.nasa.gov/mission_pages/tdm/sep/index.html, 2020. (Date last accessed on October 21, 2022).

[13] NASA, “Mars Fact Sheet.” https://nssdc.gsfc.nasa.gov/planetary/factsheet/marsfact.html, December 2021. (Date last accessed on September 30, 2022).

[14] ESA, “ESA presents new generation of astronauts.” https://www.esa.int/Science_Exploration/Human_and_Robotic_Exploration/ESA_presents_new_generation_of_astronauts, 2022. (Date last accessed on December 6, 2022).

[15] T. J. Disher, K. M. Anglin, E. C. Anania, and J. P. Kring, “The seed colony model: An approach for colonizing space,” in *2017 IEEE Aerospace Conference*, pp. 1–8, 2017.

[16] NASA, “NASA is Laser-focused on Deep Space Communication.” https://www.nasa.gov/mission_pages/station/research/news/comm_delay_assessment, 2021. (Date last accessed on October 21, 2022).

[17] NASA, “Communications.” https://mars.nasa.gov/mars2020/spacecraft/rover/communications/. (Date last accessed on October 22, 2022).

[18] A. Vanelli-Coralli, A. Guidotti, T. Foggi, G. Colavolpe, and G. Montorsi, "5g and beyond 5g non-terrestrial networks: trends and research challenges," in *2020 IEEE 3rd 5G World Forum (5GWF)*, pp. 163–169, 2020.

[19] A. Guidotti, A. Vanelli-Coralli, V. Schena, N. Chuberre, M. Jaafari, J. Puttonen, and S. Cioni, "The path to 5g-advanced and 6g non-terrestrial network systems." 09 2022.

[20] NASA, "NASA Confirms Thousands of Massive, Ancient Volcanic Eruptions on Mars." https://www.nasa.gov/feature/goddard/2021/nasa-confirms-thousands-of-massive-ancient-volcanic-eruptions-on-mars. (Date last accessed on October 23, 2022).

[21] K. Zawieska and B. R. Duffy, "Social exploration: Mars rovers," in *2014 9th ACM/IEEE International Conference on Human-Robot Interaction (HRI)*, pp. 324–325, 2014.

[22] NASA, "The Red Planet." https://mars.nasa.gov/#red_planet. (Date last accessed on October 27, 2022).

[23] NASA, "What is the habitable zone or "Goldilocks zone"?." https://exoplanets.nasa.gov/faq/15/what-is-the-habitable-zone-or-goldilocks-zone/#:~:text=The%20habitable%20zone%20is%20the,the%20surface%20of%20surrounding%20planets. (Date last accessed on October 27, 2022).

[24] C. P. McKay, "Requirements and limits for life in the context of exoplanets," *Proceedings of the National Academy of Sciences*, vol. 111, no. 35, pp. 12628–12633, 2014.

[25] M. Greshko, "Planet Mars, explained." https://www.nationalgeographic.com/science/article/mars-1, 2021. (Date last accessed on October 29, 2022).

[26] NASA, "In Depth." https://solarsystem.nasa.gov/planets/mars/in-depth/, 2021. (Date last accessed on October 29, 2022).

[27] NASA, "Earth Fact Sheet." https://nssdc.gsfc.nasa.gov/planetary/factsheet/earthfact.html, December 2021. (Date last accessed on September 30, 2022).

[28] E. Creecy, L. Li, X. Jiang, M. Smith, D. Kass, A. Kleinböhl, and G. Martínez, "Mars’ emitted energy and seasonal energy imbalance," *Proceedings of the National Academy of Sciences*, vol. 119, no. 21, p. e2121084119, 2022.

[29] A. D. Gilbert, "Chapter 9 - dynamo theory," vol. 2 of *Handbook of Mathematical Fluid Dynamics*, pp. 355–441, North-Holland, 2003.

[30] V. U. Nwankwo, N. N. Jibiri, and M. T. Kio, "The impact of space radiation environment on satellites operation in near-earth space," in *Satellites Missions and Technologies for Geosciences* (V. Demyanov and J. Becedas, eds.), ch. 5, Rijeka: IntechOpen, 2020.

[31] G. Leone, P. J. Tackley, T. V. Gerya, D. A. May, and G. Zhu, "Three-dimensional simulations of the southern polar giant impact hypothesis for the origin of the martian dichotomy," *Geophysical Research Letters*, vol. 41, no. 24, pp. 8736–8743, 2014.

[32] R. Burnham, "Gusev Crater once held a lake after all, says ASU Mars scientist." https://news.asu.edu/content/gusev-crater-once-held-lake-after-all-says-asu-mars-scientist, 2014. (Date last accessed on October 28, 2022).

[33] C. J. Gallagher and R. Bahia, "Chapter 2 - outflow channels on mars," in *Mars Geological Enigmas* (R. J. Soare, S. J. Conway, J.-P. Williams, and D. Z. Oehler, eds.), pp. 13–40, Elsevier, 2021.

[34] N.-C. of Arizona, "HiRISE Spots the Mouth of a Martian Lava Tube." https://mars.nasa.gov/resources/26349/hirise-spots-the-mouth-of-a-martian-lava-tube/, 2021. (Date last accessed on October 28, 2022).

[35] A. Daga, C. Allen, M. Battler, J. Burke, I. Crawford, R. Leveille, S. Simon, and L. Tan, "Lunar and martian lava tube exploration as part of an overall scientific survey," *LPI Contributions*, 11 2009.

[36] E. Howell, "A brief history of mars missions." https://www.space.com/13558-historic-mars-missions.html, 2019 (accessed October 19, 2020).

[37] L. Dajose, "A planet painted by hand." https://magazine.caltech.edu/post/mars-first-photo-jpl. (Date last accessed on October 26, 2022).

[38] NASA, "Mars 3 Lander." https://nssdc.gsfc.nasa.gov/nmc/spacecraft/display.action?id=1971-049F. (Date last accessed on October 26, 2022).

[39] NASA, "The mars rovers: Spirit and opportunity." https://spaceplace.nasa.gov/mars-spirit-opportunity/en/, (accessed October 22, 2020). (Date last accessed on October 25, 2022).

[40] A. K. Misra and T. E. Acosta-Maeda, "Hematite spherules on mars," in *Mineralogy* (A. I. Al-Juboury, ed.), ch. 1, Rijeka: IntechOpen, 2018.

[41] NASA, "Sam's top 5 discoveries aboard nasa's curiosity rover at mars." https://mars.nasa.gov/news/9239/sams-top-5-discoveries-aboard-nasas-curiosity-rover-at-mars/?site=msl, 2022. (Date last accessed on October 26, 2022).

[42] NASA, "Mars cube one demo." https://www.jpl.nasa.gov/news/press_kits/insight/launch/appendix/mars-cube-one/, 2021. (Date last accessed on October 26, 2022).

[43] NASA, "Marco (mars cube one)." https://solarsystem.nasa.gov/missions/mars-cube-one/in-depth/, 2021. (Date last accessed on October 26, 2022).

[44] NASA, "Mars helicopter flight log." https://mars.nasa.gov/technology/helicopter/, 2022. (Date last accessed on December 10, 2022).

[45] NASA, "Foreign object debris seen during helicopter's 33rd flight." https://mars.nasa.gov/technology/helicopter/status/409/foreign-object-debris-seen-during-helicopters-33rd-flight/, 2022. (Date last accessed on October 26, 2022).

[46] NASA, "Ingenuity mars helicopter landing press kit." https://www.jpl.nasa.gov/news/press_kits/ingenuity/landing/, 2022. (Date last accessed on October 26, 2022).

[47] T. Tzanetos, J. Bapst, G. Kubiak, L. P. Tosi, S. Sirlin, R. Brockers, J. Delaune, H. F. Grip, L. Matthies, J. Balaram, S. Withrow-Maser, W. Johnson, L. Young, and B. Pipenberg, "Future of mars rotorcraft - mars science helicopter," in *2022 IEEE Aerospace Conference (AERO)*, pp. 1–16, 2022.

[48] J. Delaune, J. Izraelevitz, S. Sirlin, D. Sternberg, L. Giersch, L. Tosi, E. Skliyanskiy, L. Young, M. Mischna, S. Withrow-Maser, J. Mueller, J. Bowman, M. Wallace, H. Grip, L. Matthies, W. Johnson, M. Keennon, B. Pipenberg, H. Patel, and Balaram, "Mid-air helicopter delivery at mars using a jetpack." (Date last accessed on October 27, 2022), 03 2022.

[49] S. Withrow, W. Johnson, L. A. Young, H. Cummings, J. Balaram, and T. Tzanetos, *An Advanced Mars Helicopter Design.*

[50] SpaceX, "Spacex home." https://www.spacex.com/, 2022. (Date last accessed on October 26, 2022).

[51] B. Origin, "Blue origin for the benefit of earth." https://www.blueorigin.com/, 2022. (Date last accessed on October 26, 2022).

[52] R. Pucci, L. S. Ronga, E. Del Re, and D. Boschetti, "Performance evaluation of an ieee802.15.4 standard based wireless sensor network in mars exploration scenario," in *2009 1st International Conference on Wireless Communication, Vehicular Technology, Information Theory and Aerospace Electronic Systems Technology*, pp. 161–165, 2009.

[53] A. Daga, G. R. Lovelace, D. K. Borah, and P. L. De Leon, "Terrain-based simulation of ieee 802.11a and b physical layers on the martian surface," *IEEE Transactions on Aerospace and Electronic Systems*, vol. 43, no. 4, pp. 1617–1624, 2007.

[54] V. Chukkala and P. De Leon, "Simulation and analysis of the multipath environment of mars," in *2005 IEEE Aerospace Conference*, pp. 1678–1683, 2005.

[55] Xiaoyan Hong, M. Gerla, R. Bagrodia, Taek Jin Kwon, P. Estabrook, and Guangyu Pei, "The Mars sensor network: efficient, energy aware communications," in *2001 MILCOM Proceedings Communications for Network-Centric Operations: Creating the Information Force (Cat. No.01CH37277)*, vol. 1, pp. 418–422 vol.1, Oct 2001.

[56] M. Prathaban and J. Kohlenberg, "Buffer Management Policy for Mars Intelligent Proximity Network," in *2008 Second Asia International Conference on Modelling Simulation (AMS)*, pp. 309–314, May 2008.

[57] T. Hook and A. Barhorst, "Probability of data loss between mars tumbleweed rovers," in *2015 11th International Conference on the Design of Reliable Communication Networks (DRCN)*, pp. 197–202, 2015.

[58] A. Babuscia, D. Divsalar, and K. Cheung, "CDMA communication system for mars areostationary relay satellite," in *2017 IEEE Aerospace Conference*, pp. 1–10, March 2017.

[59] D. Bell, R. Cesarone, T. Ely, C. Edwards, and S. Townes, "Mars network: a mars orbiting communications and navigation satellite constellation," in *2000 IEEE Aerospace Conference. Proceedings (Cat. No.00TH8484)*, vol. 7, pp. 75–88 vol.7, 2000.

[60] K. Hill and K. Gagneja, "Concept network design for a young mars science station and trans-planetary communication," in *2018 Fourth International Conference on Mobile and Secure Services (MobiSecServ)*, pp. 1–8, 2018.

[61] M. Marcozzi and M. Ottavi, "Evaluation of a multi-access communication architecture for future mars exploration," *38th International Communications Satellite Systems Conference (ICSSC 2021)*, 2022.

[62] NASA, JPL-Caltech, Arizona State University, "Meridiani planum." https://mars.nasa.gov/resources/5260/meridiani-planum/, 2012. (Date last accessed on November 5, 2022).

[63] NASA Science, "Destination: Gusev crater." https://science.nasa.gov/science-news/science-at-nasa/2003/30dec_gusevcrater, 2003. (Date last accessed on November 5, 2022).

[64] ATDI, "Htz communications replaces ics telecom." https://atdi.com/ics-telecom/, 2021. (Date last accessed on November 5, 2022).

[65] L. J. Greenstein, V. Erceg, Y. S. Yeh, and M. V. Clark, "A new path-gain/delay-spread propagation model for digital cellular channels," *IEEE Transactions on Vehicular Technology*, vol. 46, no. 2, pp. 477–485, 1997.

[66] P. I. Lazaridis, S. Kasampalis, Z. D. Zaharis, J. P. Cosmas, L. Paunovska, and I. A. Glover, "Longley-rice model precision in case of multiple diffracting obstacles," in *2015 1st URSI Atlantic*

Radio Science Conference (URSI AT-RASC), (Gran Canaria (SP)), pp. 1–1, 2015.

[67] E. Del Re, R. Pucci, and L. S. Ronga, “Ieee802.15.4 wireless sensor network in mars exploration scenario,” in *2009 International Workshop on Satellite and Space Communications*, (Siena (I)), pp. 284–288, 2009.

[68] Americans Meteorological Society, “atmospheric attenuation.” https://glossary.ametsoc.org/wiki/Atmospheric_attenuation, 2021. (Date last accessed on November 5, 2022).

[69] NASA, “Martian atmosphere and its effects on propagation 3 . 1.” https://descanso.jpl.nasa.gov/propagation/mars/MarsPub_sec3.pdf, 2002. (Date last accessed on November 5, 2022).

[70] NASA, “Martian dust storms and their effects on propagation.” https://descanso.jpl.nasa.gov/propagation/mars/MarsPub_sec5.pdf, 2002. (Date last accessed on November 5, 2022).

[71] de Looper, Christian and Martonik, Andrew, “What is 5g? speeds, coverage, comparisons, and more.” https://www.digitaltrends.com/mobile/what-is-5g/, 2022. (Date last accessed on November 5, 2022).

[72] M. Giordani, M. Polese, M. Mezzavilla, S. Rangan, and M. Zorzi, “Toward 6g networks: Use cases and technologies,” *IEEE Communications Magazine*, vol. 58, no. 3, pp. 55–61, 2020.

[73] A. Guidotti, A. Vanelli-Coralli, M. Caus, J. Bas, G. Colavolpe, T. Foggi, S. Cioni, A. Modenini, and D. Tarchi, “Satellite-enabled lte systems in leo constellations,” in *2017 IEEE International Conference on Communications Workshops (ICC Workshops)*, pp. 876–881, 2017.

[74] O. Kodheli, A. Guidotti, and A. Vanelli-Coralli, “Integration of satellites in 5g through leo constellations,” in *GLOBECOM 2017 - 2017 IEEE Global Communications Conference*, pp. 1–6, 2017.

[75] M. Giordani and M. Zorzi, “Non-terrestrial networks in the 6g era: Challenges and opportunities,” *IEEE Network*, vol. 35, no. 2, pp. 244–251, 2021.

[76] A. Guidotti, A. Vanelli-Coralli, A. Mengali, and S. Cioni, "Non-terrestrial networks: Link budget analysis," in *ICC 2020 - 2020 IEEE International Conference on Communications (ICC)*, pp. 1–7, 2020.

[77] R. Bassoli, "Chapter 7 - network function virtualization," in *Computing in Communication Networks* (F. H. Fitzek, F. Granelli, and P. Seeling, eds.), pp. 119–132, Academic Press, 2020.

[78] J. Yusupov, A. Ksentini, G. Marchetto, and R. Sisto, "Multi-objective function splitting and placement of network slices in 5g mobile networks," in *2018 IEEE Conference on Standards for Communications and Networking (CSCN)*, pp. 1–6, 2018.

[79] B. S. Rawal, G. Manogaran, R. Singh, P. M, and M. Hamdi, "Network augmentation by dynamically splitting the switching function in sdn," in *2021 IEEE International Conference on Communications Workshops (ICC Workshops)*, pp. 1–6, 2021.

[80] Arzo, Sisay Tadesse, Scotece, Domenico, Bassoli, Riccardo, Barattini, Daniel, Granelli, Fabrizio, Foschini, Luca, and Fitzek, Frank H. P., "Msn: A playground framework for design and evaluation of microservices-based sdn controller," *Journal of Network and Systems Management*, vol. 30, no. 1, pp. 1573–7705, 2021.

[81] F. W. Murti, S. Ali, and M. Latva-aho, "Deep reinforcement based optimization of function splitting in virtualized radio access networks," in *2021 IEEE International Conference on Communications Workshops (ICC Workshops)*, pp. 1–6, 2021.

[82] S. T. Arzo, R. Bassoli, F. Granelli, and F. H. P. Fitzek, "Multi-agent based autonomic network management architecture," *IEEE Transactions on Network and Service Management*, vol. 18, no. 3, pp. 3595–3618, 2021.

[83] E. Amiri, N. Wang, M. Shojafar, and R. Tafazolli, "Optimizing virtual network function splitting in open-ran environments," in *2022 IEEE 47th Conference on Local Computer Networks (LCN)*, pp. 422–429, 2022.

[84] B. M. Khorsandi, F. Tonini, E. Amato, and C. Raffaelli, "Dedicated path protection for reliable network slice embedding based on func-

tional splitting," in *2019 21st International Conference on Transparent Optical Networks (ICTON)*, pp. 1–4, 2019.

[85] L. M. P. Larsen, A. Pruski, H. L. Christiansen, S. Ruepp, and M. S. Berger, "Xhaul latency dimensioning of 5g drone control," in *2022 International Conference on Unmanned Aircraft Systems (ICUAS)*, pp. 762–771, 2022.

[86] R. Bassoli, C. Sacchi, F. Granelli, and I. Ashkenazi, "A virtualized border control system based on uavs: Design and energy efficiency considerations," in *2019 IEEE Aerospace Conference*, pp. 1–11, 2019.

[87] D. L. Bekker, T. A. Werne, T. O. Wilson, P. J. Pingree, K. Dontchev, M. Heywood, R. Ramos, B. Freyberg, F. Saca, B. Gilchrist, A. Gallimore, and J. Cutler, "A cubesat design to validate the virtex-5 fpga for spaceborne image processing," in *2010 IEEE Aerospace Conference*, pp. 1–9, 2010.

[88] S. Cakaj, B. Kamo, A. Lala, and A. Rakipi, "The coverage analysis for low earth orbiting satellites at low elevation," *International Journal of Advanced Computer Science and Applications*, vol. 5, 07 2014.

[89] T. Iida, Y. Arimoto, and Y. Suzuki, "Earth-Mars communication system for future Mars human community: A story of high speed needs beyond explorations," *IEEE Aerospace and Electronic Systems Magazine*, vol. 26, no. 2, pp. 19–25, 2011.

[90] D. Boroson, C.-C. Chen, and B. Edwards, "The Mars laser communications demonstration project: truly ultralong-haul optical transport," in *OFC/NFOEC Technical Digest. Optical Fiber Communication Conference, 2005.*, vol. 3, pp. 3 pp. Vol. 3–, 2005.

[91] A. Biswas, J. Kovalik, and M. W. Regehr, "Future planetary optical access links," in *2011 International Conference on Space Optical Systems and Applications (ICSOS)*, pp. 384–388, 2011.

[92] R. Macdonald, M. Frescheville, M. Mcinnes, C. Biggs, R. Mckay, M. Macdonald, F. Frescheville, M. Vasile, C. Mcinnes, and J. Biggs, "Non-Keplerian orbits using low thrust, high ISP propulsion systems," *60th International Astronautical Congress 2009, IAC 2009*, vol. 6, 01 2009.

[93] B. Du, F. Gao, and J. Xu, “The analysis of topology based on Lagrange points L4/L5 of Sun-Earth system for relaying in Earth and Mars communication,” in *2017 IEEE 9th International Conference on Communication Software and Networks (ICCSN)*, pp. 533–537, 2017.

[94] M. Bappy, M. Rahman, and R. Huq, “Deep Space Communication and Exploration of Solar System through Inter-Lagrangian Data Relay Satellite Constellation,” 05 2019.

[95] “Release 13.” https://www.3gpp.org/specifications-technologies/releases/release-13. (Date last accessed on October 31, 2022).

[96] H. G. Myung and D. J. Goodman, *Single Carrier FDMA*. Wiley, 2008.

[97] 3GPP, “Scenarios and requirements for small cell enhancements for E-UTRA and E-UTRAN (3GPP TR 36.932 version 12.1.0 Release 12) .” https://www.etsi.org/deliver/etsi_tr/136900_136999/136932/12.01.00_60/tr_136932v120100p.pdf. (Date last accessed on October 31, 2022).

[98] C. Schlegel and L. Perez, *Trellis and Turbo Coding.* Wiley, 2003.

[99] Proakis, *Digital Communications 5th Edition.* McGraw Hill, 2007.

[100] E. Mioso, M. Bonomi, F. Granelli, and C. Sacchi, “An SDR-based reconfigurable multicarrier transceiver for terrestrial and satellite communications,” in *2017 IEEE Aerospace Conference*, pp. 1–13, March 2017.

[101] R. E. Arvidson, R. C. Anderson, P. Bartlett, J. F. Bell, D. Blaney, P. R. Christensen, P. Chu, L. Crumpler, K. Davis, B. L. Ehlmann, R. Fergason, M. P. Golombek, S. Gorevan, J. A. Grant, R. Greeley, E. A. Guinness, A. F. C. Haldemann, K. Herkenhoff, J. Johnson, G. Landis, R. Li, R. Lindemann, H. McSween, D. W. Ming, T. Myrick, L. Richter, F. P. Seelos, S. W. Squyres, R. J. Sullivan, A. Wang, and J. Wilson, “Localization and Physical Properties Experiments Conducted by Spirit at Gusev Crater,” *Science*, vol. 305, no. 5685, pp. 821–824, 2004.

[102] O. N. Rzhiga, “Distortions of the low frequency signal by Martian ionosphere at vertical propagation,” *IEEE Transactions on Antennas and Propagation*, vol. 53, pp. 4083–4088, Dec 2005.

[103] W. C. Jakes and D. C. Cox, eds., *Microwave Mobile Communications.* Wiley-IEEE Press, 1994.

[104] J. Goldhirsh, “A parameter review and assessment of attenuation and backscatter properties associated with dust storms over desert regions in the frequency range of 1 to 10 ghz,” *IEEE Transactions on Antennas and Propagation*, vol. 30, pp. 1121–1127, November 1982.

[105] H. Holma and A. Toskala, *LTE for UMTS: Evolution to LTE-Advanced.* Wiley Publishing, 2nd ed., 2011.

[106] F. Fuschini, H. El-Sallabi, V. Degli-Esposti, L. Vuokko, D. Guiducci, and P. Vainikainen, “Analysis of multipath propagation in urban environment through multidimensional measurements and advanced ray tracing simulation,” *Antennas and Propagation, IEEE Transactions on*, vol. 56, pp. 848 – 857, 04 2008.

[107] S. Hosseinzadeh, H. Larijani, K. Curtis, A. Wixted, and A. Amini, “Empirical propagation performance evaluation of lora for indoor environment,” in *2017 IEEE 15th International Conference on Industrial Informatics (INDIN)*, (Emden (D)), pp. 26–31, 2017.

[108] C. Mascia, “A torino nasce il rover operation control center per exomars 2020.” https://www.astronomia.com/2019/05/30/a-torino-nasce-il-rover-operation-control-center-per-exomars-2020/, 2019. (Date last accessed on November 5, 2022).

[109] P. S. Anderson, “Curiosity just learned that gale crater may once have held a vast salty lake.” https://earthsky.org/space/mars-curiosity-rover-ice-covered-lake-gale-crater, 2020. (Date last accessed on November 8, 2022).

[110] T. Parker and F. J. C. III, “Mars MSL Gale Merged DEM 1m v3.” https://astrogeology.usgs.gov/search/map/Mars/MarsScienceLaboratory/Mosaics/MSL_Gale_DEM_Mosaic_10m, 2016. (Date last accessed on June 3, 2021).

[111] B. I. Bleaney, *Electricity and Magnetism.* Oxford University Press., 1976.

[112] C. C. Allen, R. V. Morris, D. J. Lindstrom, M. M. Lindstrom, and J. P. Lockwood, “JSC Mars-1: Martian Regolith Simulant,” in *Lunar and Planetary Science Conference*, Lunar and Planetary Science Conference, (Houston (TX)), p. 27, Mar. 1997.

[113] R. Morris, T. Graff, D. Ming, Bell, L. le, S. Mertzman, and P. Christensen, “Palagonitic mars: A basalt centric view of surface composition and aqueous alteration,” 02 2004.

[114] K. Cole and R. H. Cole, “Dispersion and absorption in dielectrics i. alternating current characteristics,” *Journal of Chemical Physics*, vol. 9, pp. 341–351, 1941.

[115] D. Stillman and G. Olhoeft, “Frequency and temperature dependence in electromagnetic properties of martian analog minerals,” *Journal of Geophysical Research: Planets*, vol. 113, no. E9, 2008.

[116] A. Fourlis, “Reflection transmission coefficient.” https://www.mathworks.com/matlabcentral/fileexchange/36531-reflection-transmission-coefficient, 2012. (Date last accessed on November 8, 2021).

[117] S. Hosseinzadeh, “3D Ray Tracing For Indoor Radio Propagation.” https://www.mathworks.com/matlabcentral/fileexchange/64695-3d-ray-tracing-for-indoor-radio-propagation, 2020. (Date last accessed on June 3, 2021).

[118] S. Hosseinzadeh, H. Larijani, K. Curtis, A. Wixted, and A. Amini, “Empirical propagation performance evaluation of LoRa for indoor environment,” in *2017 IEEE 15th International Conference on Industrial Informatics (INDIN)*, (Emden (D)), pp. 26–31, 2017.

[119] J. W. McKown and R. L. Hamilton, “Ray tracing as a design tool for radio networks,” *IEEE Network*, vol. 5, no. 6, pp. 27–30, 1991.

[120] G. L. Stüber, *Principles of Mobile Communication (2nd Ed.)*. USA: Kluwer Academic Publishers, 2001.

[121] ITU-R, “Reference standard atmospheres.” https://www.itu.int/dms_pubrec/itu-r/rec/p/R-REC-P.835-6-201712-I!!PDF-E.pdf, 2017. (Date last accessed on November 8, 2021).

[122] NASA, “Rover temperature controls.” https://mars.nasa.gov/mer/mission/rover/temperature/#:~:text=Like%20the%20human%20body%2C%20the,Fahrenheit%20to%20104%C2%B0%20Fahrenheit). (Date last accessed on November 8, 2021).

[123] 3GPP, “Nr; user equipment (ue) radio transmission and reception; part 2: Range 2 standalone.” https://portal.3gpp.org/desktopmodules/Specifications/SpecificationDetails.aspx?specificationId=3284. (Date last accessed on November 9, 2022).

[124] NASA, “Sequence of events.” https://mars.nasa.gov/MPF/mpf/realtime/mars2.html#:~:text=At%20ground%20level%20the%20Martian,atmospheric%20pressure%20of%2014.7%20psi. (Date last accessed on November 9, 2022).

[125] R. T. Clancy, F. Montmessin, J. Benson, F. Daerden, A. Colaprete, and M. J. Wolff, *Mars Clouds*, p. 76–105. Cambridge Planetary Science, Cambridge University Press, 2017.

[126] NASA, “Martian atmospheric gaseous attenuation.” https://descanso.jpl.nasa.gov/propagation/mars/MarsPub_sec4.pdf, 2009. (Date last accessed on November 9, 2022).

[127] Hexa-X, “D1.2 – Expanded 6G vision, use cases and societal values — including aspects of sustainability, security and spectrum,” 2 2021. (Date last accessed on November 11, 2022).

[128] R. Bassoli, F. H. Fitzek, and E. Calvanese Strinati, “Why do we need 6G?,” *ITU Journal on Future and Evolving Technologies*, vol. 2, no. 6, 2021.

[129] IOT Solution World Congress, “Advantages of 5g and how will benefit iot.” https://www.iotsworldcongress.com/advantatges-of-5g-and-how-will-benefit-iot/, 2019. (Date last accessed on November 11, 2022).

[130] R. Cardone, “Achieving sustainability with energy efficiency in 5g networks.” https://www.ericsson.com/en/blog/3/2021/1/achieving-sustainability-with-energy-efficiency-in-5g-networks, 2021. (Date last accessed on November 11, 2022).

[131] A. Makaya, "Out of Earth Manufacturing Context and Recent Advancements." https://bsgn.esa.int/wp-content/uploads/2022/07/Manufacturing-in-Space-Space4Inspiration_13-07-2022.pdf. (Date last accessed on November 10, 2022).

[132] A. Owens and O. de Weck, "Systems analysis of in-space manufacturing applications for the international space station and the evolvable mars campaign," 09 2016.

[133] K. Wickhusen, J. Oberst, and F. Damme, "A Proposed Mission to Very Low Mars Orbit - Supported by an Electric Propulsion System," in *European Planetary Science Congress*, pp. EPSC2018–364, Sept. 2018.

[134] A. Checko, H. L. Christiansen, Y. Yan, L. Scolari, G. Kardaras, M. S. Berger, and L. Dittmann, "Cloud ran for mobile networks—a technology overview," *IEEE Communications Surveys Tutorials*, vol. 17, no. 1, pp. 405–426, 2015.

[135] S. Bhaumik, S. Chandrabose, M. Jataprolu, G. Kumar, A. Muralidhar, P. Polakos, V. Srinivasan, and T. Woo, "Cloudiq: A framework for processing base stations in a data center," *Proceedings of the Annual International Conference on Mobile Computing and Networking, MOBICOM*, 08 2012.

[136] M. Peng, C. Wang, V. Lau, and H. V. Poor, "Fronthaul-constrained cloud radio access networks: insights and challenges," *IEEE Wireless Communications*, vol. 22, no. 2, pp. 152–160, 2015.

[137] P. K. Agyapong, M. Iwamura, D. Staehle, W. Kiess, and A. Benjebbour, "Design considerations for a 5g network architecture," *IEEE Communications Magazine*, vol. 52, no. 11, pp. 65–75, 2014.

[138] I. Parvez, A. Rahmati, I. Guvenc, A. I. Sarwat, and H. Dai, "A survey on low latency towards 5g: Ran, core network and caching solutions," *IEEE Communications Surveys and Tutorials*, vol. 20, no. 4, pp. 3098–3130, 2018.

[139] M. A. Marotta, H. Ahmadi, J. Rochol, L. DaSilva, and C. B. Both, "Characterizing the relation between processing power and distance between bbu and rrh in a cloud ran," *IEEE Wireless Communications Letters*, vol. 7, no. 3, pp. 472–475, 2018.

[140] H. J. Son, S. M. Shin, “Fronthaul size: Calculation of maximum distance between rrh and bbu.” https://www.netmanias.com/en/post/blog/6276/c-ran-fronthaul-lte/fronthaul-size-calculation-of-maximum-distance-between-rrh-and-bbu, 2014.

[141] Witze, Alexandra, “Nasa spacecraft records epic ‘marsquakes’ as it prepares to die.” https://www.nature.com/articles/d41586-022-03447-4, 2022. (Date last accessed on November 12, 2022).

[142] Small Cell Forum, “Small cell virtualization functional splits and use cases,” 2015. Document 159.05.1.01.

[143] 3GPP, “Study on new radio access tech- nology: Radio access architecture and interfaces (release 14).” https://portal.3gpp.org/desktopmodules/Specifications/SpecificationDetails.aspx?specificationId=3056, 2017. (Date last accessed on November 11, 2022).

[144] L. M. P. Larsen, A. Checko, and H. L. Christiansen, “A Survey of the Functional Splits Proposed for 5G Mobile Crosshaul Networks,” *IEEE Communications Surveys and Tutorials*, vol. 21, no. 1, pp. 146–172, 2019.

[145] J. K. Chaudhary, *Analysis of Bandwidth and Latency Constraints on a Packetized Cloud Radio Access Network Fronthaul.* PhD thesis, Technische Universität Dresden, Dresden, 2020.

[146] U. Dötsch, M. Doll, H.-P. Mayer, F. Schaich, J. Segel, and P. Sehier, “Quantitative analysis of split base station processing and determination of advantageous architectures for lte,” *Bell Labs Technical Journal*, vol. 18, no. 1, pp. 105–128, 2013.

[147] J. Lissauer and I. de Pater, *Fundamental Planetary Science: Physics, Chemistry and Habitability.* Cambridge University Press, 2013.

[148] T. Coail-Fourrier, “Evaluation and correction of the orbital decay, deorbit calculation for a 3u cubesat in low earth orbit.,” 09 2017.

[149] S. Cakaj, B. Kamo, A. Lala, and A. Rakipi, “The coverage analysis for low earth orbiting satellites at low elevation,” *International Journal of Advanced Computer Science and Applications*, vol. 5, no. 6, 2014.

[150] B. Sklar, *Digital Communications: Fundamentals and Applications.* Prentice-Hall, Inc., 1988. Upper Saddle River, NJ, USA.

[151] N. W. Service, "The planet mars." https://www.weather.gov/fsd/mars#:~:text=Temperatures%20on%20Mars%20average%20about,lower%20latitudes%20in%20the%20summer. (Date last accessed on November 11, 2022).

[152] J.-D. Gayrard, "Terabit satellite: Myth or reality?," in *2009 First International Conference on Advances in Satellite and Space Communications*, pp. 1–6, 2009.

[153] R. E. Hodges, N. Chahat, D. J. Hoppe, and J. D. Vacchione, "A deployable high-gain antenna bound for mars: Developing a new folded-panel reflectarray for the first cubesat mission to mars.," *IEEE Antennas and Propagation Magazine*, vol. 59, no. 2, pp. 39–49, 2017.

[154] N. Chahat, J. Sauder, M. Mitchell, N. Beidleman, and G. Freebury, "One-meter deployable mesh reflector for deep space network telecommunication at x- and ka-band," in *2019 13th European Conference on Antennas and Propagation (EuCAP)*, pp. 1–4, 2019.

[155] N. Chahat, E. Decrossas, D. Gonzalez-Ovejero, O. Yurduseven, M. J. Radway, R. E. Hodges, P. Estabrook, J. D. Baker, D. J. Bell, T. A. Cwik, and G. Chattopadhyay, "Advanced cubesat antennas for deep space and earth science missions: A review," *IEEE Antennas and Propagation Magazine*, vol. 61, no. 5, pp. 37–46, 2019.

[156] L. Xianfeng, G. Hao, J. Yaxiang, X. Chunjian, C. Xiaomin, and S. Huixian, "An x-band transmitter for small satellites," in *2007 International Conference on Microwave and Millimeter Wave Technology*, pp. 1–3, 2007.

[157] H. Watanabe, O. Ceylan, H. Saito, A. Tomiki, H. Nunomura, O. Shigeta, N. Iwakire, T. Shinke, and T. Fukami, "High-efficiency x band gan power amplifier for small satellite downlink system," in *2013 IEEE MTT-S International Microwave Symposium Digest (MTT)*, pp. 1–4, 2013.

[158] V. Industries, "Standard micro propulsion system." https://www.vacco.com/images/uploads/pdfs/MiPS_standard_0714.pdf, . (Date last accessed on November 11, 2022).

[159] E. T. Jens, A. C. Karp, J. Rabinovitch, A. Conte, B. Nakazono, and D. A. Vaughan, *Design of Interplanetary Hybrid CubeSat and SmallSat Propulsion Systems.*

[160] R1-164182, "Comparison of coding schemes for nr." https://www.3gpp.org/DynaReport/TDocExMtg--R1-85--31662.htm, 2016. (Date last accessed on November 11, 2022).

[161] 3GPP, "Release 17." https://www.3gpp.org/release-17, 2020. (Date last accessed on November 11, 2022).

[162] S. Shao, P. Hailes, T.-Y. Wang, J.-Y. Wu, R. G. Maunder, B. M. Al-Hashimi, and L. Hanzo, "Survey of turbo, ldpc, and polar decoder asic implementations," *IEEE Communications Surveys Tutorials*, vol. 21, no. 3, pp. 2309–2333, 2019.

[163] S. Liu and D. Liu, "A high-flexible low-latency memory-based fft processor for 4g, wlan, and future 5g," *IEEE Transactions on Very Large Scale Integration (VLSI) Systems*, vol. 27, no. 3, pp. 511–523, 2019.

[164] S. Bhaumik, S. Chandrabose, M. Jataprolu, G. Kumar, A. Muralidhar, P. Polakos, V. Srinivasan, and T. Woo, "Cloudiq: A framework for processing base stations in a data center," *Proceedings of the Annual International Conference on Mobile Computing and Networking, MOBICOM*, 08 2012.

[165] 3GPP, "Study on new radio (nr) to support non terrestrial networks (release 15). r 38.811." https://portal.3gpp.org/desktopmodules/Specifications/SpecificationDetails.aspx?specificationId=3234, 2018. (Date last accessed on November 11, 2022).

[166] Z. Wu, C. Gong, and D. Liu, "Computational complexity analysis of fec decoding on sdr platforms," *Journal of Signal Processing Systems*, vol. 89, 11 2017.

[167] J. Kakar, "Uav communications: Spectral requirements, mav and suav channel modeling, ofdm waveform parameters, performance and spectrum management." https://vtechworks.lib.vt.edu/handle/10919/53512, 2015. Master's thesis, Virginia Polytechnic Institute and State University, VA, USA, (Date last accessed on November 11, 2022).

[168] M. Handley, “Delay is Not an Option: Low Latency Routing in Space,” in *Proceedings of the 17th ACM Workshop on Hot Topics in Networks*, HotNets ’18, (New York, NY, USA), p. 85–91, Association for Computing Machinery, 2018.

[169] A. Talgat, M. A. Kishk, and M.-S. Alouini, “Nearest neighbor and contact distance distribution for binomial point process on spherical surfaces,” *IEEE Communications Letters*, vol. 24, no. 12, pp. 2659–2663, 2020.

[170] J. Kennewell, “Satellite Orbital Decay Calculations.” https://www.sws.bom.gov.au/Category/Educational/Space%20Weather/Space%20Weather%20Effects/SatelliteOrbitalDecayCalculations.pdf, 1999. (Date last accessed on November 12, 2022).

[171] OAI, “OpenAirInterface: The Faster Growing Community and Software Assets in 5G Wireless.” (Date last accessed on November 12, 2022).

[172] 3GPP, “3GPP TR 21.916 – 3rd Generation Partnership Project; Technical Specification Group Services and System Aspects; Release 16 Description; Summary of Rel-16 Work Items (Release 16).” https://portal.3gpp.org/desktopmodules/Specifications/SpecificationDetails.aspx?specificationId=3056, 2021. (Date last accessed on November 12, 2022).

[173] H. Gupta, D. Manicone, F. Giannone, K. Kondepu, A. Franklin, P. Castoldi, and L. Valcarenghi, “How much is fronthaul latency budget impacted by RAN virtualisation ?,” in *2017 IEEE Conference on Network Function Virtualization and Software Defined Networks (NFV-SDN)*, pp. 315–320, 2017.

[174] F. Giannone, K. Kondepu, H. Gupta, F. Civerchia, P. Castoldi, A. Antony Franklin, and L. Valcarenghi, “Impact of virtualization technologies on virtualized ran midhaul latency budget: A quantitative experimental evaluation,” *IEEE Communications Letters*, vol. 23, no. 4, pp. 604–607, 2019.

[175] Shaban, Muhammad, “Cpu performance evaluation.” http://meseec.ce.rit.edu/eecc550-winter2011/550-12-6-2011.pdf. (Date last accessed on November 12, 2022).

[176] L. Hattersley, “Raspberry pi 4 vs raspberry pi 3b+.” https://magpi.raspberrypi.com/articles/raspberry-pi-4-vs-raspberry-pi-3b-plus, 2019. (Date last accessed on November 12, 2022).

[177] Raspberry Pi Dramble, “Power consumption benchmarks.” https://www.pidramble.com/wiki/benchmarks/power-consumption. (Date last accessed on November 12, 2022).

[178] X. Lin, J. Li, R. Baldemair, J.-F. T. Cheng, S. Parkvall, D. C. Larsson, H. Koorapaty, M. Frenne, S. Falahati, A. Grovlen, and K. Werner, “5g new radio: Unveiling the essentials of the next generation wireless access technology,” *IEEE Communications Standards Magazine*, vol. 3, no. 3, pp. 30–37, 2019.

[179] R. Longbottom, “Raspberry pi 3b+ 32 bit and 64 bit benchmarks and stress tests,” 09 2018. (Date last accessed on November 12, 2022).

[180] R. Graves, “Benchmarking the brand new nvidia jetson nano: 4gb, usb 3, $99!.” https://www.sevarg.net/2019/04/07/benchmarking-nvidia-jetson-nano/, 2019. (Date last accessed on November 12, 2022).

[181] A. Lele, “Nvidia jetson nano is a $99 raspberry pi rival for ai development.” https://itsfoss.com/nvidia-jetson-nano/#:~:text=NVIDIA%20Jetson%20Nano%20is%20a%20%2499%20Raspberry%20Pi%20Rival%20for%20AI%20Development&text=At%20the%20GPU%20Technology%20Conference,the%20Jetson%20Nano%20Developer%20Kit., 2020. (Date last accessed on November 12, 2022).

[182] K. Yurkova, “Make the most of your jetson’s computing power for machine learning inference.” https://deci.ai/blog/jetson-machine-learning-inference/#:~:text=You%20can%20buy%20a%20Jetson,250%20g%20(~9%20ounces)., 2021. (Date last accessed on November 12, 2022).

[183] L. Pounder, “Raspberry pi 4 in short supply, being scalped at 400% markup (updated).” https://www.tomshardware.com/news/raspberry-pi-4-supply-issues, 2022. (Date last accessed on November 12, 2022).

[184] H. Kaushal, V. Jain, and S. Kar, *Free Space Optical Communication.* Springer Publishing Company, Incorporated, 1st ed., 2017.

[185] H. Kaushal and G. Kaddoum, “Free Space Optical Communication: Challenges and Mitigation Techniques,” 06 2015.

[186] Neil J. Cornish, “The Lagrange Points.” https://map.gsfc.nasa.gov/ContentMedia/lagrange.pdf, 1998. (Date last accessed on March 14, 2022).

[187] NASA, “NASA Mars Curiosity Rover: Communications with Earth.” https://mars.nasa.gov/msl/mission/communications/. (Date last accessed on May 20, 2022).

[188] R. Wang, V. Dave, B. Ren, R. Bhavanthula, Q. Zhang, J. Hou, and L. Zhou, “Interplanetary Overlay Network (ION) for Long-Delay Communications with Asymmetric Channel Rates,” in *2011 IEEE International Conference on Communications (ICC)*, pp. 1–5, 2011.

[189] J. Mukherjee and B. Ramamurthy, “Communication Technologies and Architectures for Space Network and Interplanetary Internet,” *IEEE Communications Surveys Tutorials*, vol. 15, no. 2, pp. 881–897, 2013.

List of Publications

[190] C. Sacchi and S. Bonafini, “From LTE-A to LTE-M: a Futuristic Convergence between Terrestrial and Martian Mobile Communications,” 2019 IEEE International Black Sea Conference on Communications and Networking (BlackSeaCom), 2019, pp. 1-5, doi: 10.1109/BlackSeaCom.2019.8812825.

[191] R. Bassoli, F. Granelli, C. Sacchi, S. Bonafini and F. H. P. Fitzek, “CubeSat-Based 5G Cloud Radio Access Networks: A Novel Paradigm for On-Demand Anytime/Anywhere Connectivity,” in IEEE Vehicular Technology Magazine, vol. 15, no. 2, pp. 39-47, June 2020, doi: 10.1109/MVT.2020.2979056.

[192] S. Bonafini, R. Bassoli, F. Granelli, F. H. P. Fitzek and C. Sacchi, “Virtual Baseband Unit Splitting Exploiting Small Satellite Platforms,” 2020 IEEE Aerospace Conference, 2020, pp. 1-14, doi: 10.1109/AERO47225.2020.9172316.

[193] S. Bonafini and C. Sacchi, “Building Cellular Connectivity on Mars: A Feasibility Study,” 2020 IEEE Aerospace Conference, 2020, pp. 1-12, doi: 10.1109/AERO47225.2020.9172518.

[194] S. Bonafini and C. Sacchi, “Evaluation of Large Scale Propagation Phenomena on the Martian Surface: A 3D Ray Tracing Approach,” 2020 10th Advanced Satellite Multimedia Systems Conference and the 16th Signal Processing for Space Communications Workshop (ASMS/SPSC), 2020, pp. 1-8, doi: 10.1109/ASMS/SPSC48805.2020.9268846.

[195] S. Bonafini, C. Bianchi, F. Granelli and C. Sacchi, “A Reconfigurable Multi-Modal SDR Transceiver for CubeSats,” 2021 IEEE Aerospace Conference (50100), 2021, pp. 1-12, doi: 10.1109/AERO50100.2021.9438235.

[196] S. Bonafini and C. Sacchi, “3D Ray-tracing Analysis of Radio Propagation on Mars Surface,” 2021 IEEE Aerospace Conference (50100), 2021, pp. 1-10, doi: 10.1109/AERO50100.2021.9438180.

[197] S. Bonafini and C. Sacchi, “Design of a 3D ray-tracing model based on digital elevation model for comprehension of large- and small-scale propagation phenomena over the Martian surface,” Int J Satell Commun Network. 2022; 40(6): 408- 427. doi:10.1002/sat.1423

[198] S. Bonafini, C. Sacchi, R. Bassoli, F. Granelli, K. Kondepu and F. H. P. Fitzek, “An Analytical Study on Functional Split in Martian 3D Networks,” in IEEE Transactions on Aerospace and Electronic Systems, 2022, doi: 10.1109/TAES.2022.3187668.

[199] S.Bonafini, C.Sacchi, R.Bassoli, F.Granelli, K.Kondepu and F.H.P.Fitzek “End-to-end performance assessment of a 3D network for 6G connectivity on Mars surface” Computer Networks, vol. 213, p. 109079, 2022. [Online]. Available: https://www.sciencedirect.com/science/article/pii/S1389128622002171

[200] S. Bonafini, C. Sacchi, F. Granelli, R. Bassoli, F. H. P. Fitzek and K. Kondepu, “3D Cloud-RAN Functional Split to Provide 6G Connectivity on Mars,” 2022 IEEE Aerospace Conference (AERO), 2022, pp. 1-13, doi: 10.1109/AERO53065.2022.9843703.

[201] S. Bonafini, N. Satriano and C. Sacchi, “Study on Relay Networks based on Lagrangian Points for Optical-based Mars-to-Earth Communications,” 2022 IEEE 9th International Workshop on Metrology for AeroSpace (MetroAeroSpace), 2022, pp. 152-157, doi: 10.1109/MetroAeroSpace54187.2022.9856020.

[202] S. Bonafini, S. T. Arzo, C. Sacchi and M. Devetsikiotis, ”HW/SW Development of Cloud-RAN in 3D Networks: Computational and Energy Resources for Splitting Options,” submitted to 2023 IEEE Aerospace Conference (AERO), in review.

[203] J. C. B. Borromeo, S. Bonafini, K. Kondepu, N. Andriolli, F. H. P. Fitzek, C. Sacchi and L. Valcarenghi,“5G NR Analysis for Satellite-UAV Communication in Three-Dimensional Networks”, submitted to 2023 IEEE International Conference on Communications (ICC), in review.

DOCTORAL PROGRAM IN INFORMATION AND COMMUNICATION TECHNOLOGY

Doctoral candidate
Stefano Bonafini

Cycle	**35**
Thesis	**Next-Generation Space Communications Technologies for Building Future Mars Connectivity**
Advisor	**Claudio Sacchi (University of Trento)**
Co-advisor	

1. List of publications

Published Journals

- R. Bassoli, F. Granelli, C. Sacchi, S. Bonafini and F. H. P. Fitzek, ``CubeSat-Based 5G Cloud Radio Access Networks: A Novel Paradigm for On-Demand Anytime/Anywhere Connectivity," in IEEE Vehicular Technology Magazine, vol. 15, no. 2, pp. 39-47, June 2020, doi: 10.1109/MVT.2020.2979056.
- S. Bonafini and C. Sacchi, ``Design of a 3D ray-tracing model based on digital elevation model for comprehension of large- and small-scale propagation phenomena over the Martian surface," Int J Satell Commun Network. 2022; 40 (6): 408- 427. doi:10.1002/sat.1423
- S. Bonafini, C. Sacchi, R. Bassoli, F. Granelli, K. Kondepu and F. H. P. Fitzek, ``An Analytical Study on Functional Split in Martian 3D Networks," in IEEE Transactions on Aerospace and Electronic Systems, 2022, doi: 10.1109/TAES.2022.3187668 (early view access).
- S.Bonafini, C.Sacchi, R.Bassoli, F.Granelli, K.Kondepu and F.H.P.Fitzek “End-to-end performance assessment of a 3D network for 6G connectivity on Mars surface” Computer Networks, vol. 213, p. 109079, 2022. [Online]. Available: \url{https://www.sciencedirect.com/science/article/pii/S1389128622002171}

Published Conference Papers

- C. Sacchi and S. Bonafini, ``From LTE-A to LTE-M: a Futuristic Convergence between Terrestrial and Martian Mobile Communications," 2019 IEEE International Black Sea Conference on Communications and Networking (BlackSeaCom), 2019, pp. 1-5, doi: 10.1109/BlackSeaCom.2019.8812825.
- S. Bonafini, R. Bassoli, F. Granelli, F. H. P. Fitzek and C. Sacchi, ``Virtual Baseband Unit Splitting Exploiting Small Satellite Platforms," 2020 IEEE Aerospace Conference, 2020, pp. 1-14, doi: 10.1109/AERO47225.2020.9172316.
- S. Bonafini and C. Sacchi, ``Building Cellular Connectivity on Mars: A Feasibility Study," 2020 IEEE Aerospace Conference, 2020, pp. 1-12, doi: 10.1109/AERO47225.2020.9172518.
- S. Bonafini and C. Sacchi, ``Evaluation of Large Scale Propagation Phenomena on the Martian Surface: A 3D Ray Tracing Approach," 2020 10th Advanced Satellite Multimedia Systems Conference and the 16th Signal Processing for Space Communications Workshop (ASMS/SPSC), 2020, pp. 1-8, doi: 10.1109/ASMS/SPSC48805.2020.9268846.

- S. Bonafini, C. Bianchi, F. Granelli and C. Sacchi, ``A Reconfigurable Multi-Modal SDR Transceiver for CubeSats," 2021 IEEE Aerospace Conference (50100), 2021, pp. 1-12, doi: 10.1109/AERO50100.2021.9438235.
- S. Bonafini and C. Sacchi, ``3D Ray-tracing Analysis of Radio Propagation on Mars Surface," 2021 IEEE Aerospace Conference (50100), 2021, pp. 1-10, doi: 10.1109/AERO50100.2021.9438180.
- S. Bonafini, C. Sacchi, F. Granelli, R. Bassoli, F. H. P. Fitzek and K. Kondepu, ``3D Cloud-RAN Functional Split to Provide 6G Connectivity on Mars," 2022 IEEE Aerospace Conference (AERO), 2022, pp. 1-13, doi: 10.1109/AERO53065.2022.9843703.
- S. Bonafini, N. Satriano and C. Sacchi, ``Study on Relay Networks based on Lagrangian Points for Optical-based Mars-to-Earth Communications," 2022 IEEE 9th International Workshop on Metrology for AeroSpace (MetroAeroSpace), 2022, pp. 152-157, doi: 10.1109/MetroAeroSpace54187.2022.9856020.

Under Review

- S. Bonafini, S. T. Arzo, C. Sacchi and M. Devetsikiotis, "HW/SW Development of Cloud-RAN in 3D Networks: Computational and Energy Resources for Splitting Options," submitted to 2023 IEEE Aerospace Conference (AERO), in review.
- J. C. B. Borromeo, S. Bonafini, K. Kondepu, N. Andriolli, F. H. P. Fitzek, C. Sacchi and L. Valcarenghi,``5G NR Analysis for Satellite-UAV Communication in Three-Dimensional Networks", submitted to 2023 IEEE International Conference on Communications (ICC), in review.

2. Research/study activities

Period Abroad

- Short-term Scholar at the University of New Mexico (UNM), department of Electrical and Computer Engineering (ECE), under supervision of prof. Michael Devetsikiotis (April, 1 – July 31, 2022)

Teaching Activities

- Co-supervised two master’s thesis, one bachelor’s thesis
- Successfully attended the PhD Summer School entitled “Frontier Technologies for Space 2.0 Communications”, sponsored by the Aerospace and Electronic System Society (AESS) and the Italian Space Agency (ASI)
- Teaching assistant for the master’s course “Communication Systems” (A.Y. 2020-21, A.Y. 2021-22, A.Y. 2022-23)

Research Project

- Participated in the development of the Dynamic Architecture based on UAVs Monitoring for Border Security and Safety (DAVOSS) funded by the NATO Science for Peace and Security Programme

Studying Activities

- Courses offered by the Information Engineering and Computer Science (IECS) doctoral programme. More precisely:
    a. Academic Writing for the Sciences and Engineerings
    b. AI Ethics Today

    c. Computing in Communication Networks
    d. PhD Summer School detailed in the following point
- Successfully attended the PhD Summer School entitled “Frontier Technologies for Space 2.0 Communications”, sponsored by the Aerospace and Electronic System Society (AESS) and the Italian Space Agency (ASI)

Reviewer

- Reviewed several articles for IEEE conferences and journals. More precisely:
    a) IEEE Transactions on Aerospace and Electronic Systems
    b) European Wireless (November 10-12, 2021, Verona, Italy)
    c) IEEE Global Communications Conference (GLOBECOM, December 4-8, 2022, Rio de Janeiro, Brazil)

Science Communications

- ICT Days 2021 (presentation about in-lab activities)
- Video interviewed for sponsoring DISI and IECS (brief speech about in-lab activities)